Metrology of Additive Manufactured Lattice Structures

by

Younes Chahid

2021

A thesis submitted to the University of Huddersfield in partial fulfilment of the requirements for the degree of Doctor of Philosophy

Supervisors: Dr. Radu Racasan, Dr. Paul Bills, Prof. Liam Blunt

Copyright statement

Acknowledgments

I would like to start by thanking my parents, family, brother Zakaria and brother-in-law Ahmed for being my mentors and the reason I am in an engineering career in the UK. I would like to express my gratitude and appreciation to Radu and Paul who trusted me and guided me thorough this research experience since the BEng final year project and especially during the challenging pandemic. My gratitude and appreciation for Liam for offering solid feedback, advice, and encouragement since being your analysis of materials student and thorough my research. I would also deeply thank Andy and Ahmed for being great office mates and for addressing my thousands and one questions at the start and during my PhD journey. Thank you to Alexander for assisting in AM samples, Luca for guidance and assistance in data analysis, Philip Sperling for assisting in the licensing and use of volume analysis software and to Paras Shah for being the first international student I met undertaking a PhD in AM. Thanks to Chris.D and Katie for answering my infinite number of questions and it is my pleasure to be Chris.J, Ameer, Karl, Joe and Johnny companion in this journey. Special thanks to Eirini, Olga, Gio, Fenia, Bill and Stephan for the company and Greek food. Also special thanks to Damianos for the support and encouragement all the way from Cyprus. The author gratefully acknowledges the UK's Engineering and Physical Sciences Research Council (EPSRC) funding of the Future Metrology Hub (Grant Ref: EP/P006930/1).

Abstract

Additive Manufacturing (AM) has proved efficient in many medical, aerospace, and automotive applications. While most critical AM parts still require a case-by-case verification, medium size productions have been proven successful and future plans of mass customisation and quality inspection protocols are being drawn. AM is beneficial and cost effective to use in low volumes or when parts have highly functional complex features like topology optimised shapes or lattice structures. While AM has been existing for more than three decades, the usual high cost, especially of Powder Bed Fusion (PBF) means that the use of advanced design techniques, like the incorporation of functional lattice structures, is necessary to capitalise on the technology investment. However, while design and manufacturing capabilities has significantly increased in the last decade, especially with methods like design for AM (DfAM), the metrology side is still falling behind, especially when it comes to internal features or complex geometries like lattices. This challenge has led further academic and industrial research in metrology related to AM, which is sometimes referred to as “design for metrology”. This has been done by understanding the quality measurement tools, considering them from the beginning of AM process and also by using AM benchmark artefacts followed by adequate measurement strategies. The lack of standards related to AM and to non-destructive evaluation (NDE) tools like X-ray Computed Tomography (XCT) meant that further research still has to be done in this field. XCT still currently lacks from the challenge of being heavily relying on user experience, which increases chances of human error. Another current challenge in the AM field is the lack of tools allowing for considering or designing the expected manufacturing defects like dimensional deviation or surface topography in the design phase, making most current design simulations inaccurate as they are done on perfect computer-aided design (CAD). Finally, and since there is still no unique AM benchmark artefact that is standardised and can be used for all processes, multiple designs are currently suggested in literature, although, none of them being mainly focused on lattices with clear and appropriate measurement strategy. This thesis reports on development of novel protocol that can assist XCT users to optimise scan process settings in a cost effective and timely manner using 2D image analysis prior to reconstruction. This is especially critical when using lattice structures since XCT is the only tool that can give a holistic analysis as well as reach internal features or re-entrant ones. The technique has been initially tested on machined parts and further developed to work for lattice structures. This work has increased the efficiency and optimised the dimensional metrology process of lattices. After proposed method related to dimensional metrology, a method was developed to extract surface data of AM lattices using XCT alongside a script developed to allow the design of AM PBF like surfaces on any CAD using areal surface parameters as inputs. The method was then further optimised and adapted to work for the CAD of lattice structures which have different up skin and down skin surface values. Subsequent to proposed dimensional

and surface research studies, an AM lattice benchmark artefact design and measurement strategy has also been developed, which was an ideal way to complete the overall research study. The novel design has a gradual strut diameter and is the first AM benchmark artefact suggested in literature that is solely made for lattices. The measurement strategy has used ISO/ASTM 52902:2019 as a guideline to develop lattice specific measurement methods using XCT. This sequence of connected research experiments has been designed to focus specifically on AM lattice structures, providing adequate and efficient methods in dimensional and surface metrology fields using XCT. The research is completed by a novel AM lattice benchmark artefact that is parametric and not process specific, which was printed in this research in both PBF and Fused Deposition Modelling (FDM) processes. The developed research has been chosen to be relevant in industrial scenarios where cost effectiveness is essential. The work presented in this thesis represents a milestone in research related to XCT dimensional and surface metrology linked to lattices as well as research related to AM benchmark artefacts. Further research in this field can accelerate the transition and use of efficient AM protocols and adoption of lightweight and highly functional lattice structures, accompanied by reliable processes from the design stage to metrology one.

Table of Contents

List of Figures

List of Tables

Glossary

3MBIC	3M Buckley Innovation Centre.
3MF	3D Manufacturing format is a file format developed for additive manufacturing and can include information like the 3D model, colours and materials.
ABS	Acrylonitrile Butadiene Styrene is a polymer material commonly used in FDM process.
ACOs	Aircraft certification offices.
AM	Additive manufacturing is defined as the process of joining materials to make parts from 3D model data, usually layer upon layer, as opposed to subtractive manufacturing and formative manufacturing methodologies [1].
AMSC	America Makes & ANSI Additive Manufacturing Standardization Collaborative.
ANSI	American National Standards Institute.
ASTM	American Society for Testing and Materials.
B-rep	Boundary representation is a collection of surface elements used to represent a geometry in a CAD environment.
Bit depth	Bit depth is the range or number of grey levels that can be assigned to each pixel as an exponent of 2.
BCC	Body Centred Cubic is a crystal molecular body structure used as a lattice structure unit cell.
CAD	Computer Aided Design.
CFD	Computational fluid dynamics.
CLI	Common Layer Interface is an AM format that is unambiguous and represents the multiple cross sections forming the 3D volume part, where the space between the cross sections is the layer thickness [2].
CMM	Coordinate Measuring Machine.
CNC	Computer numerical control.
Contouring	The melt strategy followed in the outer region or outline of the part during the AM process.
CPU	Central processing Unit.
CT	Computed Tomography.

DLF Direct laser forming, an AM process.

Downskin Additive manufactured geometry of a product can be divided to the core part, up skin and downskin areas. The areas with no underlying layers are named downskin.

FAA Federal aviation administration.

FCC Face Centred Cubic is a crystal molecular body structure used as a lattice structure unit cell.

FDA Food and Drug Administration.

FDM Fused Deposition Modelling, an AM process.

FE Finite element.

FEA Finite element analysis.

GD&T Geometric dimensioning and tolerancing.

Gyroid A type of TPMS discovered by Schoen in 1970 [3].

Hatch spacing The spacing between two parallel laser passes in the LPBF process.

Hatching The melt strategy followed in the central region of the part during the AM process.

ISO International Organization for Standardization.

Kelvin cell Based on kelvin model proposed by Sir William Thomson (Lord Kelvin) in 1887 used to describe the equal sized bubble foam. The kelvin cell is a tetrakaidecahedron (polyhedron with 14 faces) consisting of 6 squares and 8 hexagons [4].

LPBF Laser Powder Bed Fusion, an AM process.

Melt pool Melt pool is the interaction result between the LPBF process material and laser. The melt pool size affects the size of the created geometry.

MIDOs Manufacturing inspection district offices.

MPE Maximum Permissible Error.

NASA National Aeronautics and Space Administration.

NDE Non-destructive evaluation.

NIST National Institute of Standards and Technology.

NPL National Physical Laboratory.

OD Outer Diameter.

PBF Powder Bed Fusion, an AM process.

PLA Polylactide thermoplastic is a polymer material commonly used in FDM process.

PPE Personal protective equipment.

Radiograph A 2D digital representation using grayscale of the X-ray imaged part.

ROI Region Of Interest.

SDF Signed distance field.

SEM Scanning Electron Microscope.

STL Stereo Lithography format is a file format used to describe the surface geometry of a 3D model.

TC Technical committee.

TIFF Tagged Image File Format is an image file format commonly used for its lossless compression capability [5].

TPMS Triply periodic minimal surfaces are a category of lattice structures where the geometry of the surfaces have a mean curvature of zero.

Up skin Additive manufactured geometry of a product can be divided to the core part, up skin and downskin areas. The areas with no further upper layers are named up skin.

V&V Verification and validation.

XCT X-ray Computed Tomography.

List of Publications and Awards

Journal papers

Y. Chahid, R. Racasan, L. Pagani, A. Townsend, A. Liu, P. Bills, L. Blunt, parametrically designed surface topography on CAD models of additively manufactured lattice structures for improved design validation, Addit. Manuf. 37 (2021) 101731. https://doi.org/10.1016/j.addma.2020.101731.

- Contribution: Planned and performed experiments, analysis, and drafted manuscript.

Conferences

Y. Chahid, A. Townsend, T. Ahmed, P. Bills, C. Dawson, R. Racasan, Method to choose X-ray computed tomography settings for dimensional metrology using 2D image analysis prior to reconstruction, 2019 4th Dimensional X-ray Computed Tomography Conference
(Huddersfield, UK)

- Contribution: Planned and performed experiments, analysis, and drafted manuscript.

Y. Chahid, A. Townsend, A. Liu, P. Bills, R. Racasan, Ranking of X-CT settings for dimensional metrology of additive manufactured lattice structures using image analysis of minimum 2D projections, 2019 4th ASTM Symposium on Structural Integrity of Additive Manufactured Materials and Parts
(Maryland, USA)

- Contribution: Planned and performed experiments, analysis, and drafted manuscript.

Y. Chahid, R. Racasan, P. Bills, L. Blunt, Design and measurement strategy of additive manufacturing lattice benchmark artefact , 2021 Euspen Advancing Precision in Additive Manufacturing
(St Gallen, Switzerland)

- Contribution: Planned and performed experiments, analysis, and drafted manuscript.

Book chapter

Y. Chahid, A. Townsend, A. Liu, P. Bills, P. Sperling, and R. Racasan, "Optimizing X-Ray Computed Tomography Settings for Dimensional Metrology Using 2D Image Analysis." In *STP1631-EB Structural Integrity of Additive Manufactured Materials and Parts*, ed. N. Shamsaei and M. Seifi, (pp. 88-101). West Conshohocken, PA: ASTM International, 2020. doi: https://doi.org/10.1520/STP163120190141

- Contribution: Planned and performed experiments, analysis, and drafted manuscript.

Articles

Y. Chahid, How to Design and Optimize a Patient Specific Additively Manufactured Hip Implant Stem, 2020 Ntopology, https://ntopology.com/blog/2020/12/16/design-of-surface-roughness-on-cad-of-am-lattices/

Y. Chahid, Design of surface roughness on CAD of AM lattices using areal surface parameters for better design validation, 2020 Ntopology, https://ntopology.com/blog/2020/12/16/design-of-surface-roughness-on-cad-of-am-lattices/

Y. Chahid, Design for Metrology in Additive Manufacturing, 2020 Ntopology,
https://ntopology.com/blog/2020/12/16/design-of-surface-roughness-on-cad-of-am-lattices/

Y. Chahid, AM brings a new dawn to surgical procedures, 2021 MTD magazine,
https://mtdcnc.com/magazines/mtdcnc/am-brings-a-new-dawn-to-surgical-procedures

P. Sperling, Y. Chahid, Les implants passé aux rayons X, 2021 CEM magazine

Awards

_ Winner of Additive World 2020 DfAM Challenge organised by Additive Industries
_ Winner of 2020 Society of the year award as founder of Huddersfield 3D printing society
_ Selected in IMechE 2019 Rising Star - 25 under 35

1. Chapter: Introduction

1.1. Background Motivation

Additive manufacturing (AM) adoption has been constantly increasing in the recent years. During the last decade, the AM industry grew by $10.8 billion and is expected to reach $47.7 billion, four times the progress done in the last 10 years by 2025 [6]. A major reason for this has been the innovations reached in the design stage using design for AM (DfAM), as well as advancements in the manufacturing and post processing phases, making AM machines more affordable and efficient.

To take advantage of AM, engineers would usually have to justify the cost by increasing their component efficiency, reducing weight in addition to production times [7]. This usually leads to using the mentioned DfAM technique which can include lattice structures, topology optimisation and more [8]. Lattice structures have been applied to lightweight parts, for thermal dissipation, damping, osseointegration of implants and more [9,10].

However, in a global economy of $80 trillion, manufacturing represents 16% of it, and AM account for less than 1% of that. If AM was to reach 5% of global manufacturing, it would reach a $640 billion industry [6]. High cost of AM technology is usually justified by increasing the efficiency of the parts by incorporating lattice structures, which can allow for increased manipulation of material properties. Advances in this field led to state-of-the-art and new design approach called "architected materials" [11], with boundless possibilities. The use of lattices in medical has for example allowed for the manufacturing of implants that have closer mechanical properties to the human bone [12], reducing the stress shielding effect [13] and increasing chances of osseointegration [14]. Lattice structures have also been combined with superalloys like Inconel which are challenging to machine, to produce significant lightweight parts with remarkable properties, attractive for aerospace applications [15]. Applications related to heat exchangers have also benefited from the use of lattice structures [16], especially triply periodic minimal surfaces like gyroids which significantly increase the surface area [17]. The impact of these lattice heat exchangers is expected to be significant, especially with the increasing research in AM copper [18].

However, while AM enables us to design and manufacture better functioning lattice structures in medical, automotive, aerospace and more, it also creates bigger challenges when it comes to metrology and quality control of these complex geometries. This challenge is emphasised by lack of methods developed for inspection and holistic evaluation of AM lattice structures as well as lack of standards in use of ideal non-destructive evaluation (NDE) tools like X-ray Computed Tomography (XCT) which are often suitable for these kinds of complex geometries. These gaps have been thoroughly highlighted both in literature [19] and organisations like America Makes & ANSI Additive Manufacturing Standardization Collaborative (AMSC), which names Gap NDE4 the one related to XCT, Gap P4 the one related to surface metrology of complex geometries and AM lattices and GAP D26, the one related to developing metrology methods optimised for lattice structures [20]. Due to the challenges currently hindering further adoption of AM, especially advanced lattice structures and alongside the mentioned research gaps, the following aim and objectives summarise the work presented in this PhD study.

1.2. Aim

The aim of this project is to lay a clear approach in providing **defining parameters** and **measurement techniques** for the metrology process of additive manufactured lattice structures from design to inspection. This aim will enable a clear, repeatable, and reliable approach of measuring or comparing produced lattice structures to **further accelerate the mass adoption of AM and use of lattice structures in industry**.

1.3. Objectives

The objectives set to reach the aim of the project are:

- Objective 1: Holistic review of AM lattices regarding the latest advances and current research gaps in design, manufacturing using laser powder bed fusion (LPBF) and material extrusion as well as metrology using XCT.
- Objective 2: Develop a non-destructive method to optimise the XCT dimensional metrology of lattice structures, additive manufactured in Aluminium using LPBF process.
- Objective 3: Develop method to extract areal surface parameters of both up and down skin of Aluminium lattice structures, additive manufactured using LPBF process. Also optimise the metrology process of lattices by exploring possibility of incorporating dimensional and surface defects in design stage.
- Objective 4: Develop a novel design of AM lattice benchmark artefact, additive manufactured in Titanium using LPBF process and polylactide thermoplastic (PLA) using material extrusion as well as the non-destructive measurement strategy of both internal and external features using XCT.

2. Chapter: Additive Manufacturing

2.1. Commercial beginnings

AM is defined by the International Organisation for Standardisation (ISO) as “process of joining materials to make parts from 3D model data, usually layer upon layer, as opposed to subtractive manufacturing and formative manufacturing methodologies” [1].

The odyssey of AM commercialisation started in 1987, with SLA-1, the first stereolithography (SLA) machine introduced by 3D Systems [21]. Electro Optical Systems (EOS), another giant in the AM industry, was founded in 1989 and sold their first stereolithography machine in 1990 [6]. A year later, new technologies like fused deposition modelling (FDM), solid ground curing (SGC) and laminated object manufacturing (LOM) were commercialised by Stratasys, Cubital and Helisys respectively [6]. In 1998, Extrude Hone (currently named ExOne) commercialised the industry’s first metal AM machine, the ProMetal RTS-300 [6].

Early 2000s saw the rise and fall of many companies, acquisition and mergers, as well as a number of lawsuits and patent agreements. The stirred and fierce competition in this period started to lead to slightly more affordable AM machines like for example the ZPrinter 310 from Z Corp in 2003 priced at $29,900 later reduced in 2006 to $19,900, this drop in price was however not general to all AM technologies [6].

In 2009, a key FDM patent held by Stratasys expired, making way to multiple low cost FDM manufacturers to enter the AM market [22], mainly in the FDM market and more specifically the desktop based versions. This scenario led to the first truly affordable desktop AM machines, which were mostly based on the open-source FDM Replicating Rapid Prototyper Project (RepRap). The low cost RepRap desktop AM machine, was shared by Dr. Adrian Bowyer, formerly an academic at the University of Bath who obtained multiple awards for his considered outstanding contribution to 3D printing[23,24]. RepRap machines went to inspire some of the biggest FDM companies today like Makerbot, Prusa or Ultimaker who’s co-founders recently testified that his company would not have existed today if it was not for the RepRap project. The proliferation of desktop AM manufacturers of FDM machines meant that in April 2009, a RepRap based kit was sold for around $1000 by Bits from Bytes [6]. It is possible today to buy RepRap based 3D printers for as less as $200, a first in FDM AM community [25].

2.2. Different types and trends of AM processes

AM is split into seven different type of processes as categorised by BS EN ISO/TC 261 and ASTM F42 in the Terminology for AM Technologies Standard [1]. These processes include powder bed fusion, binder jetting, directed energy deposition, material extrusion, material jetting, sheet lamination and vat photopolymerization. Industry adoption percentages of different AM process types can be seen in Figure 1 where Powder Bed Fusion (PBF) process is clearly dominant with a value of 54%.

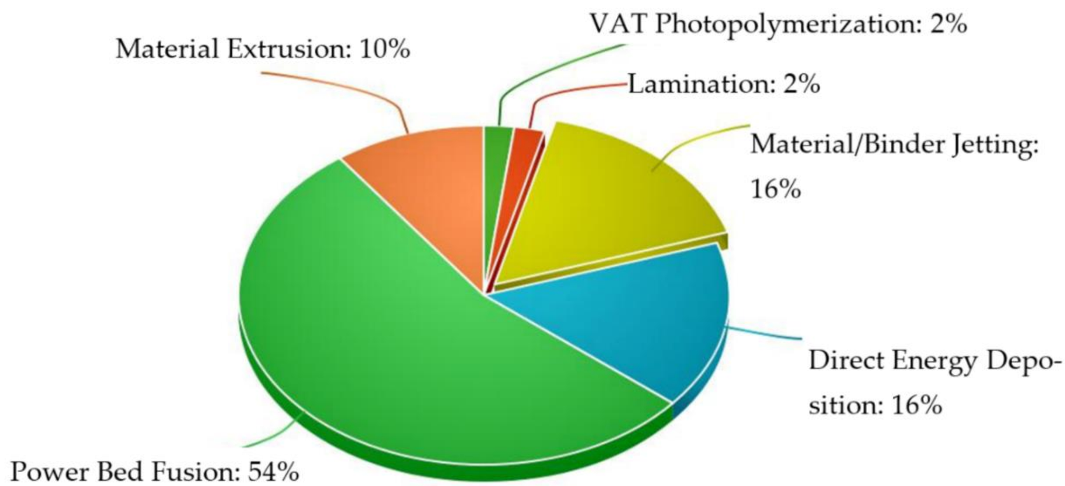

Figure 1: Industry adoption of different AM processes in 2020 [26]

a) LPBF metal AM process

Powder bed fusion (PBF) represents 54% of the AM industry adoption in 2020 as seen in Figure 1. PBF is further categorised depending on the heat source like laser or electron beam, both with a powder based material supply [27]. LPBF is considered the method with the best dimensional accuracy and reproducibility of a part production [28]. The LPBF process is sometimes referred to by other names like Direct Metal Laser Melting (DMLS) or Selective Laser Melting (SLM) which are terms coined by different AM companies[26].

The process usually starts by a layer of metal powder with a defined thickness to be spread across the machine build platform as seen in Figure 2. The area of interest is then melted using the laser beam, subsequently, the build plate moves down, and another layer of powder is spread followed by further melting of the next cross section of the part. The process is repeated until the build is complete, layer per layer hence the additive naming of the process.

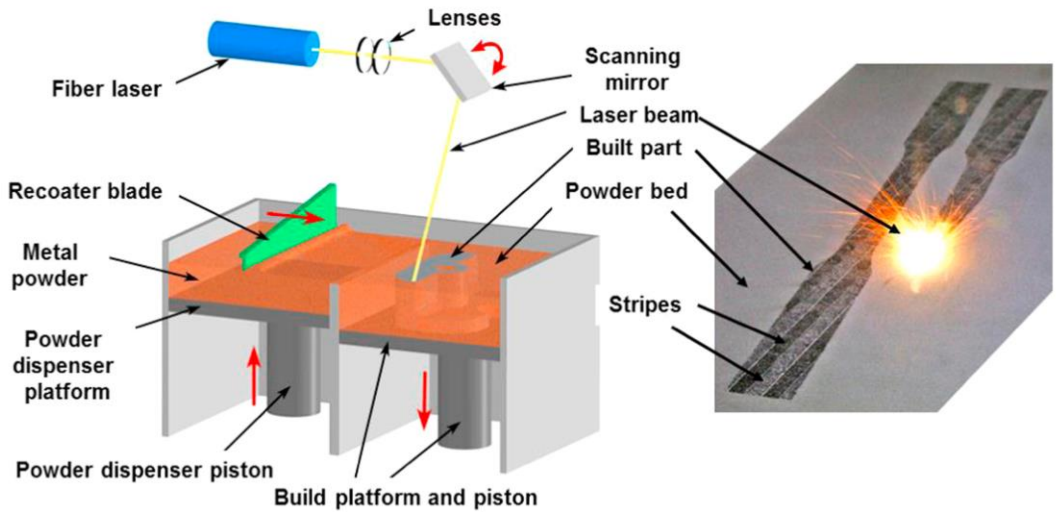

Figure 2: Example of an AM LPBF system [29].

Different process parameters can be set prior to starting the printing process. The parameters include for example the laser beam power, the hatch scanning strategy spacing, the scan velocity and layer thickness [28]. Different printing process parameters can lead to different part characteristics like microstructure, dimensional deviation, surface roughness and more. Structural integrity can be affected by these defects, in some cases, fatigue performance of LPBF additive manufactured Ti-6Al-4V part can be 77% less than its wrought material equivalent [30]. In another study done by Masuo et al. the process defects reduced the fatigue performance of the as fabricated LPBF AM Ti-6Al-4V by a third compared to its wrought alloy equivalent [31]. The PBF process in general is relatively more expensive than its AM process counterparts and with a size limitation. The process also sometimes suffers from some levels of distortions and coarse surface finish, especially in overhangs. The quality of “as built” components may not be satisfactory to product requirement, necessitating post processing techniques. For example, hot isostatic pressing (HIP) has been shown to be effective in reducing part porosity [32], with limitations depending on pore connectivity, proximity to surface and sometimes the reopening of pores, when annealing after HIP [32,33]. The reduction of part porosity lead to a decrease of internal stress concentrations, allowing for an increased fatigue life [34]. However, HIP process can also lead to decreased yield strength and ultimate tensile strength due to the recrystallisation and microstructure changes caused by the process [35]. Improvements in HIP process can allow for the sealing of pores as well as preserving yield and ultimate tensile strength properties [36]. Chemical etching can be used to reduce surface roughness of complex geometries like lattice structures, leading to removal of critical surface defects that might also act as crack initiators [37].

b) Material extrusion

Material extrusion or FDM process represents 10% of the industry adoption in 2020 as seen in Figure 1. This AM process is usually dominated by polymer materials and considered a good entry level due to its low cost and ease of use. The FDM process relies on the melting and rapid cooling of a material usually in a filament tube form layer per layer as seen in Figure 3. Recent innovations and trends in this process include the infusion of metal powder in the commonly used (PLA) or acrylonitrile butadiene styrene (ABS) with varying quantities. This has opened the door to manipulate the mechanical properties of the printed part while reducing chances of warping due to increased thermal conductivity [38]. Another recent development in the material extrusion process type is the capability to manufacture metal parts. The raw material this time is metal powder mixed with a polymer binding agent that is still extruded through a nozzle in a close way to the FDM process. After printing the post processing includes a solvent and thermal debinding to remove the binder agent and producing mechanically stable parts in a material like 316 L steel parts with 95% density [39].

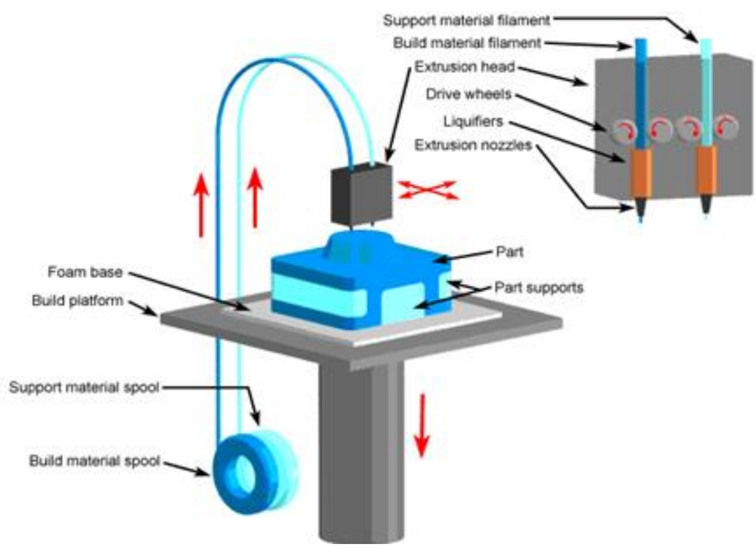

Figure 3: Example of AM FDM system [40].

An example of a part made using this process can be seen in Figure 4. Material extrusion can be a great entry level and low-cost way to enter the AM field, although recent advancement in producing metal parts can see even more adoption from small batch AM applications or especially machine shops. However, the process is relatively slower when compared to other AM processes and often requires the use of supports, limiting the complexity and accuracy of produced parts. Nevertheless, the process has low maintenance costs, low material costs and can be considered simpler to use [26].

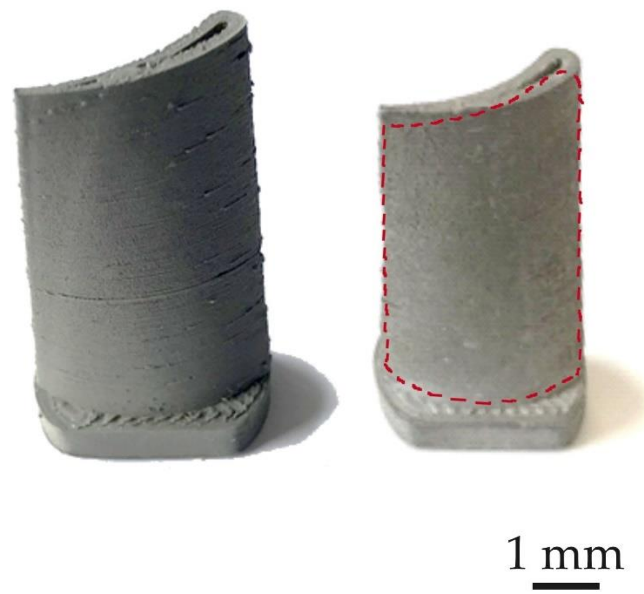

Figure 4: Additive manufactured 316L steel blade done using material extrusion process combined with solvent and thermal debinding leading to a 17% shrinkage shown from the left image to the right one [39].

2.3. Applications of AM

AM was initially used for prototyping or to make cosmetic models [41]. These models were usually used for communicating design intent or shown to clients for limited demonstrations [6]. However, it can be seen how in Figure 5 AM cosmetic models only represent 10.5% and falls fourth in the most common application of AM. Also, Figure 5 shows how more than half of AM applications are used for end use parts (30.9%) followed by functional prototypes (24.6%). End use parts include components that are sold and used directly by the customer. The difference between cosmetic models and functional prototypes is that the latter are used by designers and engineers to assess the function capability of the part and its fit in into an assembly. This application heavily assists users of AM in removing any ambivalence about the tolerances or functional issues of a part before any batch production.

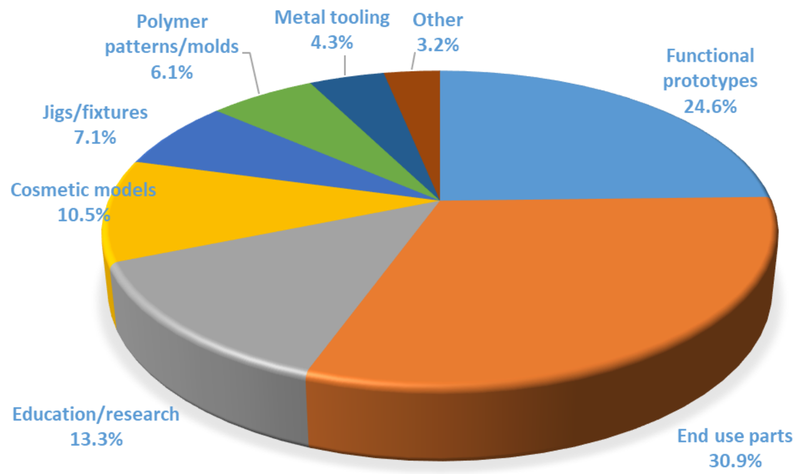

Figure 5: Most common AM applications figure recreated from Wohlers 2020 report [6]

The aerospace industry was one of the early adopters of end use parts. As shown in the 2020 Wohlers report, and in Figure 8, this sector now ranks third in application sector with a value of 14.7%. For example, the American aerospace company Boeing have already fitted more than 70,000 AM production parts in their commercial and defence programs [42]. Similarly, General Electric (GE) has also been using AM to produce thousands of fuel nozzles, as part of their LEAP engineering project [43]. Examples of Boeing AM parts can be seen in Figure 6.

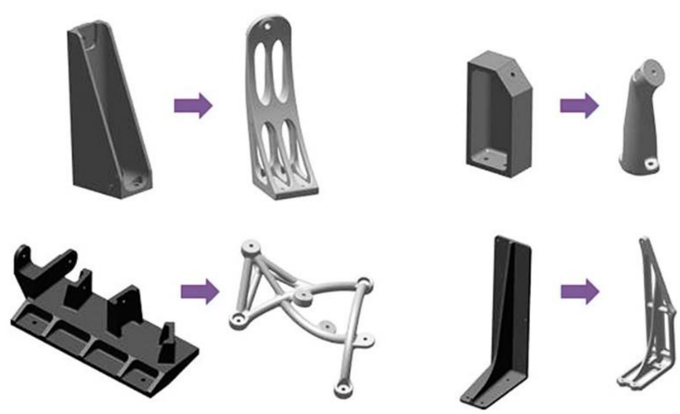

Figure 6: Boeing examples of design freedom and increase of functionality when using AM [44].

The automotive industry comes first in AM applications [6] as seen in Figure 8. For instance, BMW opened an AM centre of production with an investment of €15 million and had produced in 2019 more than 300,000 parts [45]. The recent i8 Roadster from BMW includes multiple AM parts like rails and aluminium made fixtures that can be 44% lighter and ten times stiffer than its injection moulded plastic counterpart [46]. Automotive field is now one of the closest to reach a mass manufacturing scale in AM. Engine components are now also additive manufactured like an additive manufactured cylinder head by BMW in their S58 engine [47] or pistons by Porsche in their high performance 911 GT2 RS model. The additive manufactured pistons by Porsche (Figure 7) are lighter and more efficient as they can withstand 30 PS more power when fitted to their 700 PS biturbo engine [48].

Figure 7: Pistons additive manufactured by Porsche for their 911 GT2 RS model [48].

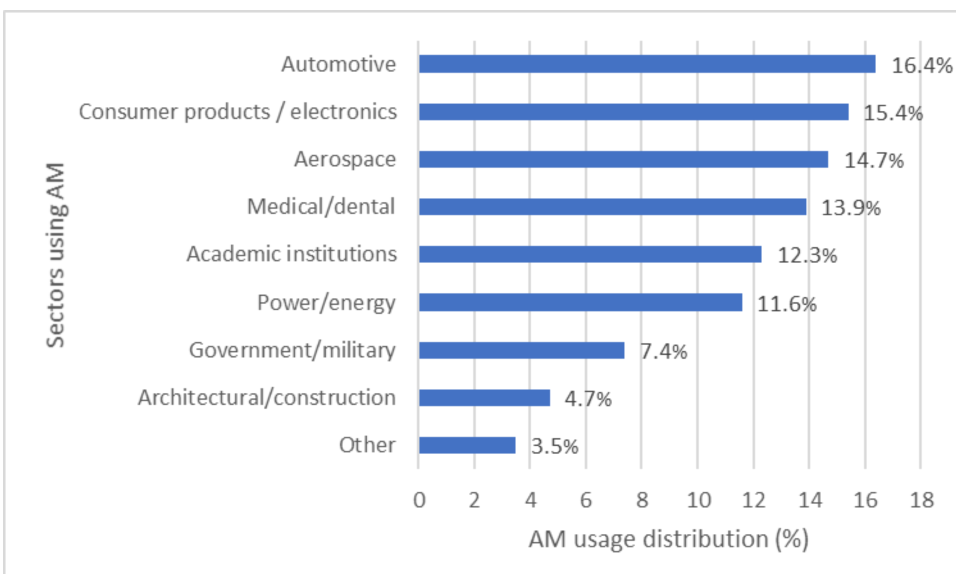

Figure 8: Distribution of AM usage in different sectors recreated from Wohlers report 2020 [6].

Coming fourth in most common application sector is the medical and dental sector with a percentage of 13.9% as seen in Figure 8. AM can most of the time be an ideal choice for medical parts since most of them perform better when they are customised to the patient instead of chosen from standard sizes. Using DfAM principles, design engineers can have increased control over the stiffness and porosity of the produced medical parts or implants [12].

Another example of worldwide AM use has been the recent COVID-19 pandemic which led to multiple supply chains struggling to provide health care consumables [4]. AM enables reduced supply chain times, and on some occasions removal of delivery costs [3]. In this case, AM proved worthy especially in the early days of the pandemic [5]. During this period, it was possible to additive manufacture ventilator valves [6], surgical helmets [8] and wearable respirator [7] sometimes with antibacterial properties [49] as seen in Figure 9. One of the main benefits of using AM was to cover for the shortage period as well as to make patient custom designs or function related materials that are suited for each application. For example, the AM of polymer materials that have copper nanocomposites that acts as an antimicrobial [9]. AM can also allow for the reduction of polluting environmental emissions while allowing the production of parts on demand while being with improved quality [10]. While this section was more focused on general AM applications, more lattice related applications will be mentioned in detail in Chapter 3 section 3.2.1.

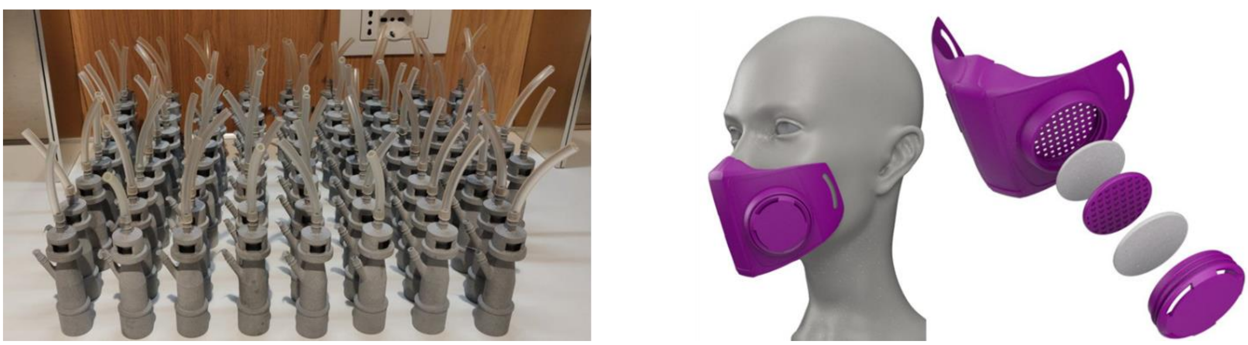

Figure 9: Additive manufactured respirator valves [50] (left) and antibacterial N95 mask [51] (right)

2.4. AM workflow

a) *Design software and 3D modelling*

As mentioned above, the AM timeline starts with different proof of concepts and patents starting with the photopolymerization in the late 1960s [6]. However, another important driver of these research efforts has been in the late 1940s, dating the invention of the computer followed by advances in the computer aided design (CAD) and also computer aided manufacturing (CAM). Although not being directly used for AM, CAD/CAM systems have laid the ground work and were used heavily by the computer numerical control (CNC) machines which were developed in the early 1950s [52].

As seen in Figure 10, the AM process workflow usually starts with a design idea. The design idea can be modelled from scratch using a 2D drawing/sketch as a reference [52]. It is also common to see parts traditionally done in CNC or other processes adapted and re-designed for AM to decrease part count or increase functionality. Currently, The design freedom of AM also allows for part consolidation where part counts can be dramatically reduced alongside the manufacturing cost and assembly time [41].

Another source of obtaining a 3D model can be by using reverse engineering techniques like optical scanners [53] or X-ray computed tomography [54]. XCT can be more critical in cases where the object has unknown internal features like antique parts that might break when disassembled or crime scene evidence that would be tampered if opened. Reverse engineering techniques like photogrammetry [55] can take multiple images from different angles and height steps, find their centre point, and create a digital model.

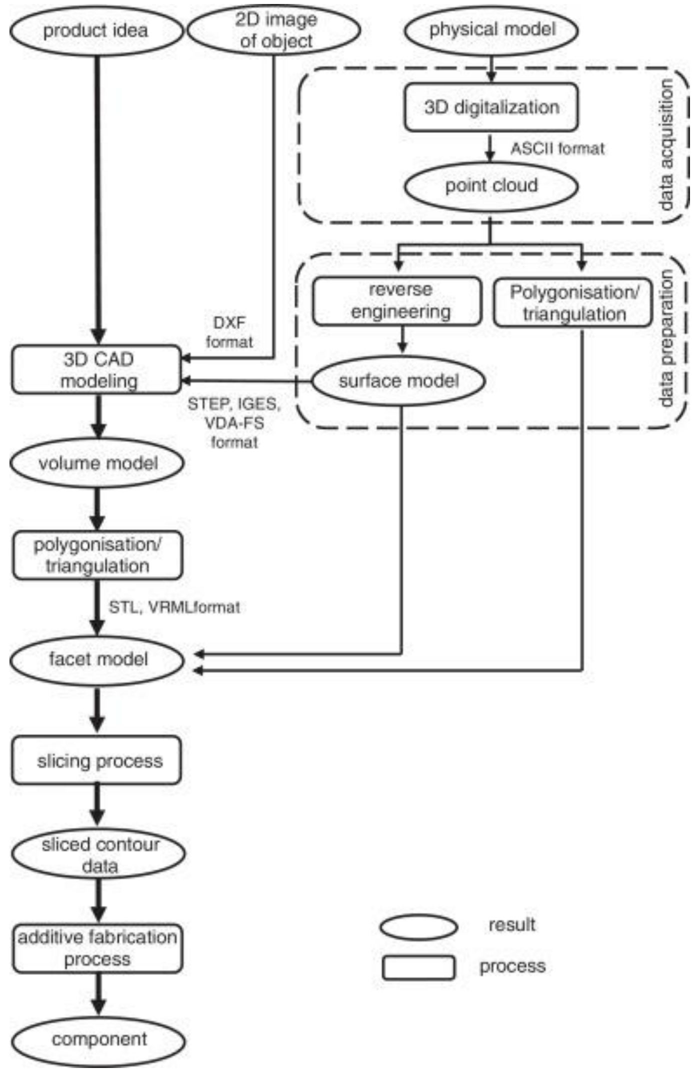

Figure 10: AM process workflow from product idea to manufactured component [52].

b) Slicing of the CAD

Once a 3D model is obtained from either of the techniques mentioned above, it is usually exported to one of the used 3D printing 3D file formats like. STL or the recently highly used .3MF file format or. AMF one. The exported mesh file is double checked for any mesh errors like non-manifold errors [56], flipped normal, holes or gaps between faces, edges, and vertices of the design in AM software like Autodesk Meshmixer or industry used one Netfabb.

The next step involves opening the mesh file exported from the 3D model in what is usually called slicing software [57]. The slicing software translates the 3D volume data to machine instructions and nozzle/laser path. A common exported file format especially the low cost and open-source 3D printers is the G-code [58], which is similar to the traditional one used in CNC machining [59]. Few companies have adapted the G-code and managed to develop their own slicing software that works better for their 3D printer hardware, however, there are many open-source slicers that can work for multiple 3D printers at once like Cura [60]. Instructions that are included in the exported slicing software file include for example the machine heated bed temperature, the nozzle temperature or laser power.

c) Raw material quality control

Raw material used in the AM process plays an important role in the produced quality of the part. This is crucial since it is often possible to recycle the non-used raw material like powder in an LPBF process, however, excessive recycling can lead to increased porosity and reduced mechanical properties [61]. Also, LPBF powder or material extrusion filaments have the risk of absorbing unwanted moisture and should be stored accordingly [62,63]. During the AM process, and before the laser sinters a layer, a coater passes and depose the raw material powder on the print bed. Therefore, the powder particle size and flowability play a crucial role in the success of the powder deposition as well as properties of produced part. The flowability of the used powder can be influenced by the standard deviation of the particle size distribution (PSD) [64]. The powder flowability also improves with coarser powder particles [65] and get decreased with increase in moisture [66].

d) Fabrication from the slicing data

The following step usually involve sending the slicing data (which has different file formats depending on the machine manufacturer) to the AM machine either wirelessly or using a universal serial bus (USB). In the case of FDM process, when the AM machine is started and the file is set to be printed, the machine usually warms up the printer bed and on some occasions perform automatic build platform calibration [67]. Otherwise, the user would have to perform a manual bed levelling or sometimes a semi-automatic one where the machine performs the calculations and instruct the user on for example which screws to tighten to have a calibrated bed [68]. As for the LPBF process, several studies are investigating and testing the possibility for in-situ monitoring of the AM process at different levels, as seen in Figure 11, allowing for increased reliability and earlier detection of manufacturing defects [69].

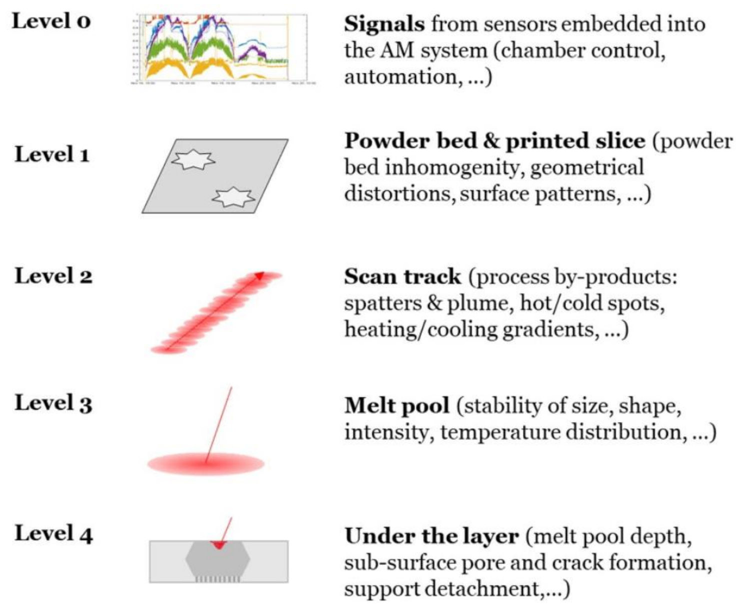

Figure 11: In-situ monitoring of a PBF system at different process levels [69].

e) Stress relieving and support removal

In general, during the manufacturing process of the LPBF method, the part being built experiences fast heating and cooling cycles that usually impact the physical part properties as well as microstructure [70]. These multiple and rapid changes of thermal cycles induce residual thermal stresses on the final produced part. Furthermore, a heat treatment is usually necessary to be performed on the final part to relieve these residual stresses and reach a homogenised microstructure and improved mechanical properties [71]. Most of the times, the part is still attached to the build platform and gets transferred to a furnace following standardised heat treatment procedures. In other occasions, the stress relieving procedure is included in the machine being used without the need to or moving it.

After the stress relieving procedure comes the next step of removing supports and separating the part from the build plate [72]. In the case of material extrusion processes like FDM the part is easily removed after cooling down using a sharp spatula, however in cases like metal AM processes, wire electrical discharge machining (EDM) is used to separate the part from the build plate [73]. Research has been looking at different aspects to ease this post processing step, from automatic support removal [74], using dissolvable metal supports [75] to using advanced lattice designs for optimised supports during the AM process [76]. Examples of different warpage scenarios or cracks on produced AM parts can be seen in Figure 12.

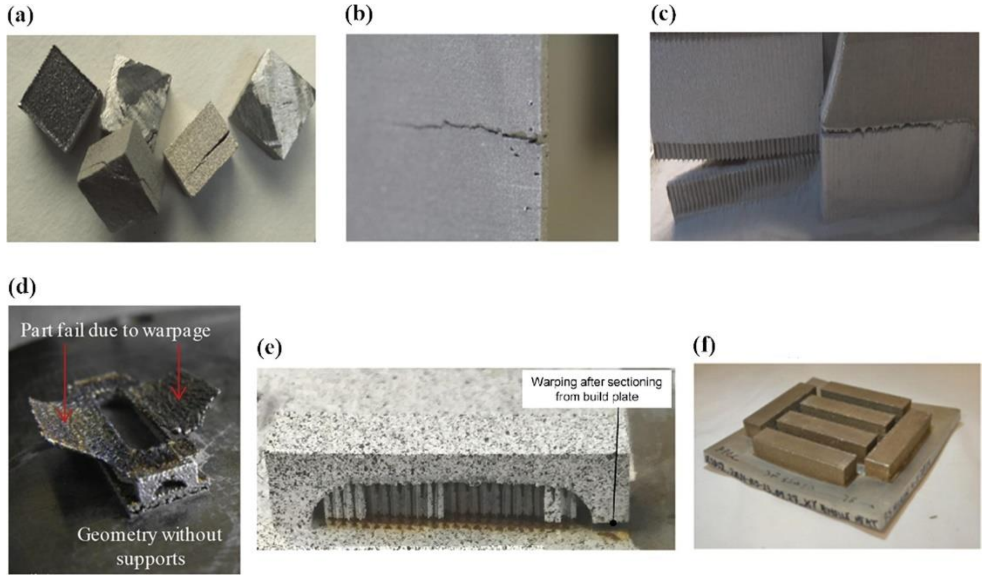

Figure 12: Examples of part failures like part cracking in Inconel-718 (a), part cracking in Titanium Ti-6AL-4V (b), part cracking in build plate interface (c), warpage of non-supported structures, warping from build plate sectioning (e) and of the part base (f) [77].

f) Finishing and advanced heat treatment

The finishing step has post-processes like machining the holes, thin walls and critical features of the part using CNC equipment for increased accuracy and tighter tolerances that cannot be reached using AM process [78]. In other occasions, surface treatment operations are done on the part by either machining the critical features or applying chemical etching for internal features that would not be reachable with machining like the case of lattice structures [79,80]. Further to the support removal, increased part performance and mechanical properties can be obtained by more advanced heat treatments like hot isostatic pressing (HIP) [32]. The HIP process relies on applying high pressure (400 to 2070 bar) and high temperatures up to 2,000°C resulting in parts that are way closer to the theoretical 100% density with far improved ductility and fatigue resistance [81]. Example of an AM part cross section using XCT before and after HIP treatment [82] can be seen in Figure 13.

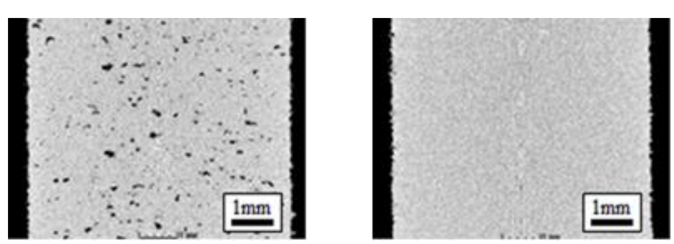

Figure 13: XCT slice image of an aluminium AM produced sample before HIP (left) and after HIP process (right) showing decreased porosity [82].

g) Inspection

Additive manufactured parts follow an inspection and quality control process for example to evaluate any dimensional deviations from the original CAD, making sure that the critical features are within the intended tolerances [83,84]. Beside dimensional measurements, surface roughness can also be measured using either contact, optical and also XCT [85,86]. The surface roughness of LPBF processes has relatively higher amplitudes compared to the conventionally machined surfaces, especially in the overhang areas which can for example affect a fluid flow in cooling channels [87]. Also, instead of using profile surface measurements which are more conventional in the case of CNC machined components, AM parts usually have different surface roughness's across the different faces/sides of the same part depending on the geometry, overhang angle. The use of areal surface parameters is the norm when assessing AM surfaces [88]. Porosity is also usually checked for additive manufactured parts using different methods like Archimedes for a faster general value [89]. Otherwise, for more holistic porosity analysis with pore volume distribution and density, the whole part or a smaller section of it can be XCT scanned and analysed using volume analysis tools [90]. Examples of contact, optical and XCT instruments being used for metrology can be seen in Figure 14.

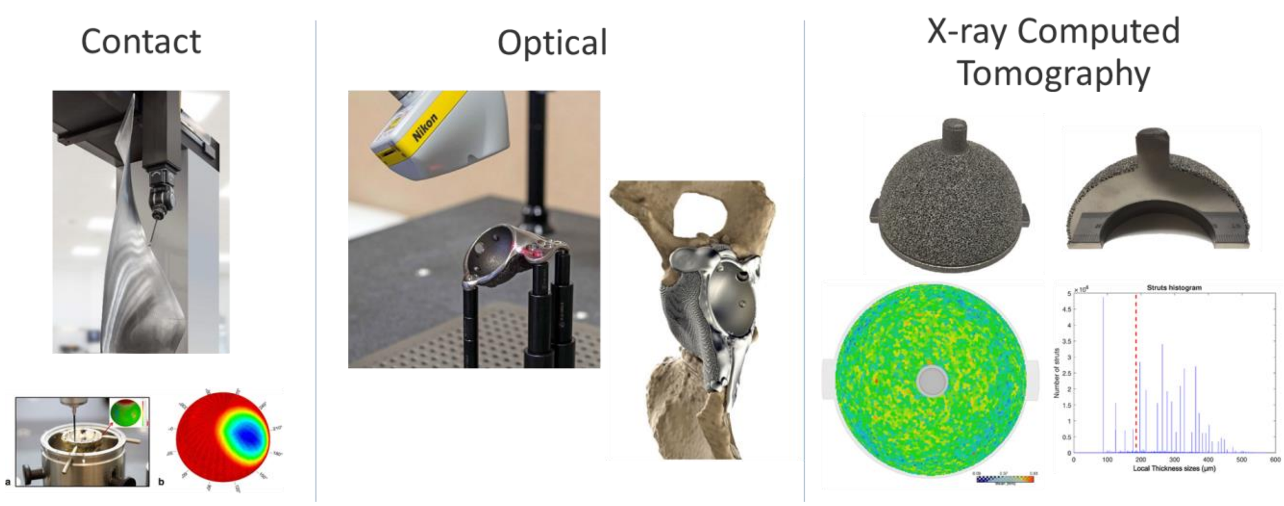

Figure 14: Examples of inspection using contact methods [91,92] , optical methods [93] and XCT methods [94].

2.5. Additive manufacturing standards

a) Start of AM standards

With every new emerging technology, standards play a key role in accelerating global adoption in industry. While few AM standards for materials and processes exist, there is still a lack of AM specific standards and also need for further development of existing ones [95] especially in the case of complex parts like lattice structures. The beginnings of AM standardisation can be considered from 2009 with the American Society for Testing and Materials (ASTM) International establishing the F42 committee and recognising the importance of AM standards.

In 2011, an agreement has been reached between ISO TC 261 and ASTM F42 to avoid competing standards [96] and in 2016, America Makes and American National Standards Institute (ANSI) started the AMSC collaborative [97]. Also in the same year, ASTM and ISO released the AM standard development framework, splitting types of standards to three main categories, general standards, category AM standards, specialised AM standards as seen in Figure 15 [98].

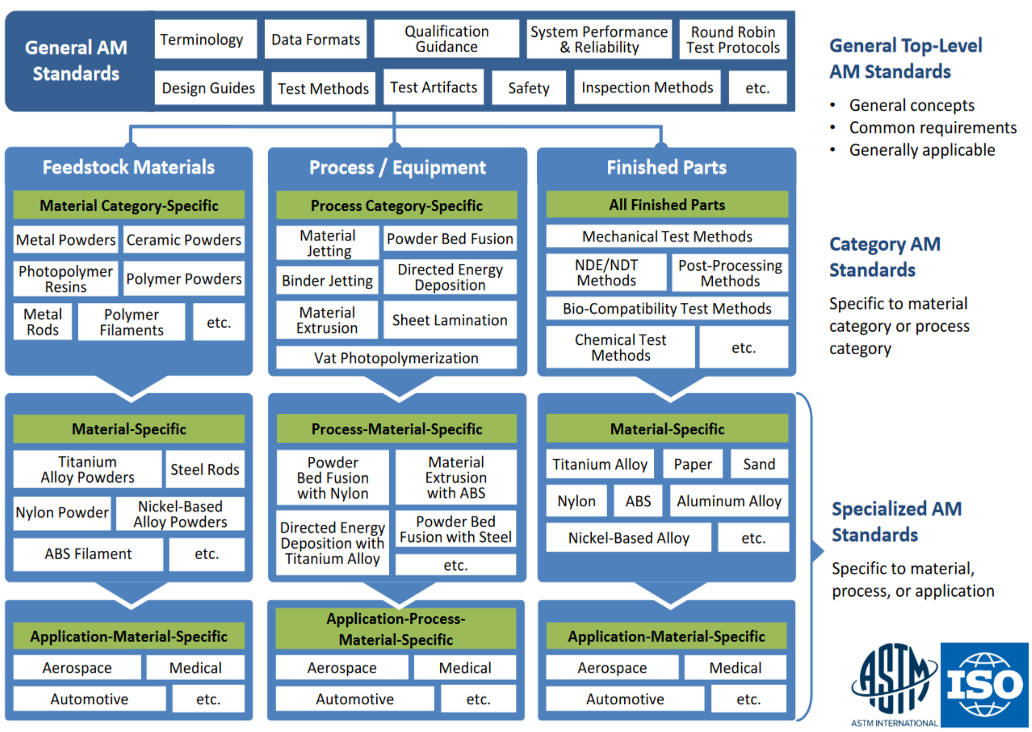

Figure 15: Common AM standards roadmap and organisational structure shared by SO/TC 261 and ASTM F42 showing the three level hierarchy of AM standards [98].

Other government agencies have also released their take on AM guidelines and quality standards like Food and Drug Administration (FDA) [99] for their biomedical AM components or National Aeronautics and Space Administration (NASA) [100] for their spacecraft parts. Agency specific standards can be important in the case of a rapid increase of AM use in a niche field that was untapped before. The best example in this case can be the rapid rise of community responders who rushed into additive manufacturing millions of medical personal protective equipment (PPE) like masks or face shields. Although slightly delayed, this has caused the FDA to share in November 2020 guidelines on 3D printing PPE [101] to tackle the covid pandemic. The shared guidelines were insightful and helped address multiple frequently asked questions regarding the AM parts viability and necessary risk assessment.

The increase of AM adoption in aviation meant that the federal aviation administration (FAA) released different guidelines for manufacturing inspection district offices (MIDOs) and also to regional aircraft certification offices (ACOs) to better assess and evaluate and certify additive manufactured parts [95]. The unique custom aspect of AM means that while few process standards from different fields (biomedical, aerospace...) can be similar, most AM part certification processes and part requirements are different, depending on the part criticality level and its type of application.

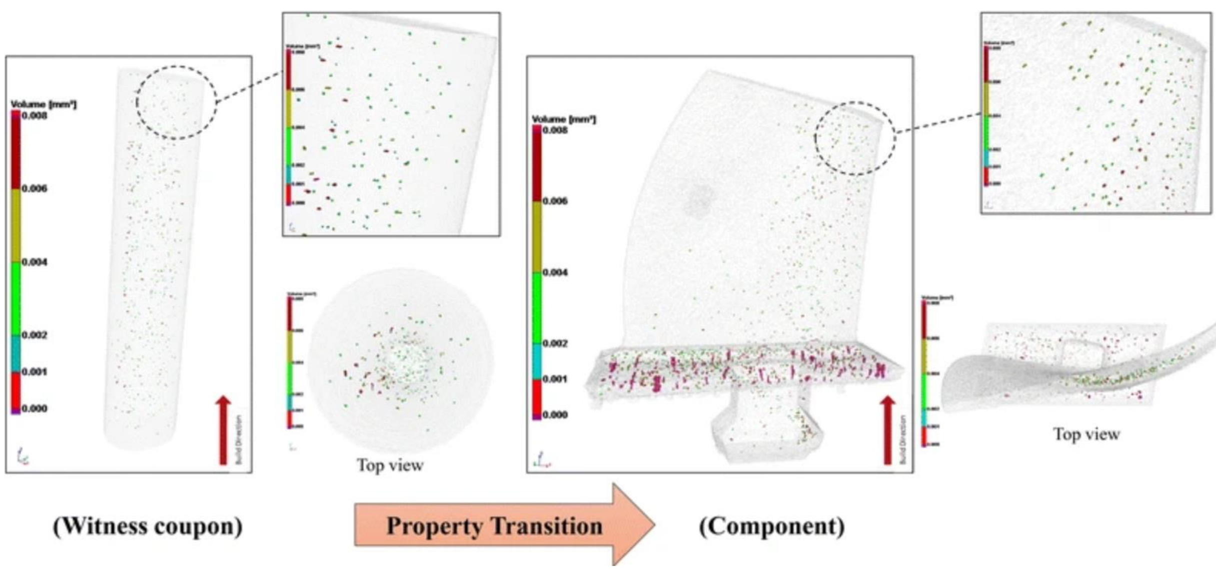

Figure 16: XCT porosity analysis results showing how a witness coupon (left) and turbine blade (right) made at the same time, do not necessarily have transferrable and similar properties/characteristics [95].

Industry accepted standards are crucial when developing an innovative and emerging manufacturing method as they remove any ambiguity during each procedure and also level out the playing field for new AM start-ups by showing the minimum accepted requirements for each AM process. AM standards are also becoming important since it is often challenging to correlate AM machine settings and raw material properties to the produced part defects/microstructure and eventually, the produced mechanical properties especially the fatigue behaviour.

Unfortunately, using standards previously developed for other manufacturing methods might not be necessarily transferrable since the specimen size, geometry or homogeneity assumptions that are not always practical for AM [95]. For example, when developing a fatigue standard for AM, it is common to test a manufacturing process by using a specific standardised coupon. However, when it comes to AM, having multiple coupons in the same build does not necessarily mean similar properties, especially when placed at different orientations. Most importantly, the AM coupon defects will not necessarily be similar to the defects detected in the actual engineering part [95], as seen in Figure 16. This means that applying quality inspection methods only on witness coupons printed alongside the AM products is not a definitive method, and further research is required.

b) Current state and gaps in AM standards

As of April 2021, ISO/TC 261 committee which consists of 25 organisations and seven working groups has 19 published standards, of which 16 are jointly made with ASTM F42 committee. Also, 33 standards are currently under development, which are all jointly being developed with ASTM [102]. Relevant standards from the officially 19 published ones can be seen in Table 1. Most AM standards are either general or oriented for metal AM and more specifically LPBF process. Most important standards at the moment can be considered to initially be the terminology one [103], ISO/ASTM 52901:2017 regarding the requirements for purchased AM parts and ISO/ASTM 52910:2018 guidelines for design can also be significantly important when developing a validation process to either sell, purchase or design AM parts [104].

Table 1: Relevant AM standards from the 19 officially published as of April 2021 by ISO/TC 261 of which 16 are jointly made with ASTM F42 committee.

Standard	AM process	Material	Category	Title
ISO/ASTM 52900:2015	-	-	General principles	Additive manufacturing — General principles — Terminology
ISO/ASTM 52902:2019	-	-	Test artifacts	Additive manufacturing — Test artifacts — Geometric capability assessment of additive manufacturing systems
ISO/ASTM 52904:2019	PBF	Metal	Metal AM process characteristics	Additive manufacturing — Process characteristics and performance — Practice for metal powder bed fusion process to meet critical applications
ISO/ASTM 52910:2018	-	-	Design	Additive manufacturing — Design — Requirements, guidelines, and recommendations
ISO/ASTM 52911-1:2019	LPBF	Metal	Design	Additive manufacturing — Design — Part 1: Laser-based powder bed fusion of metals
ISO/ASTM 52942:2020	LPBF	Metal	Metal AM qualification principles	Additive manufacturing — Qualification principles — Qualifying machine operators of laser metal powder bed fusion machines and equipment used in aerospace applications
ISO/ASTM 52950:2021	-	-	General Principles	Additive manufacturing — General principles — Overview of data processing

The number of AM standards currently in development, which is 33, clearly shows how full AM standardisation still has a long way to go before being relatively normalised compared to conventional manufacturing methods. For a clearer idea of the necessary AM roadmap and possible standard gaps needed to be filled, AMSC has developed a study highlighting 93 standard gaps of which 18 are high priority [97]. Each one of these gaps have no published standard and doing so will help deliver a specific AM industry need. Furthermore, AMSC has developed an online tracker where each one of these gaps are being updated depending on the standards released about it, its progress status and level of priority, delivering a concise holistic location useful for standard organisation, academics wanting to choose AM research topics and AM newcomers wanting to adopt and implement a solid AM process [105].

One of the main gaps mentioned by AMSC and related to this study is firstly, Gap D18 and Gap D26 which highlights “new dimensioning and tolerancing requirements” and “design for measurement of AM features/verifying the designs of features such as lattices” respectively [20]. The unprecedented design freedom and challenging features means that current verification and validation (V&V) and geometric dimensioning and tolerancing (GD&T) compatibility when applied to AM must be evaluated. A portion of the measurement challenges especially for lattices and internal features will have to be addressed by using non-destructive evaluation. This need has also been highlighted by AMSC in a range of non-destructive evaluation named Gap NDE 1-8. Relevant to this study is Gap NDE3, which is a gap related to a “standard guide for the application of NDE to objects produced by AM processes [20] and most importantly Gap NDE4 related to dimensional metrology of internal features and complex geometries like lattice structures. Another relevant gap to this study is Gap P4 which highlights the need for developing surface metrology tools related to complex geometries like lattice structures, of which literature has been limited to profile measurements on lattice struts [79,106]. In terms of standards, the one related to this topic and is still being under development and currently in the proposal stage is ISO/ASTM AWI TR 52905 [107] which is related to NDE of metal AM parts. The lack of standards in the field of metrology of AM lattices and XCT further highlights the importance of gaps specified by the AMSC, which published an April 2021 report highlighting the latest development in each gap [20]. The research presented in Chapter 5, 6 and 7 come as a direct response to Gap NDE4, Gap P4 and Gap D26. The presented studies focus on not only improving the design and measurement techniques for AM lattices but also the used NDE process, which in this case was the XCT one.

2.6. Additive manufacturing benchmark artefacts

AM has enabled the production of parts previously impossible to produce using common subtractive manufacturing processes. Optimised AM parts with topology optimisation or lattice structures are usually challenging to manufacture and inspect. One of the ways to tackle this challenge is to use AM benchmark artefacts like the ones seen in Figure 17.

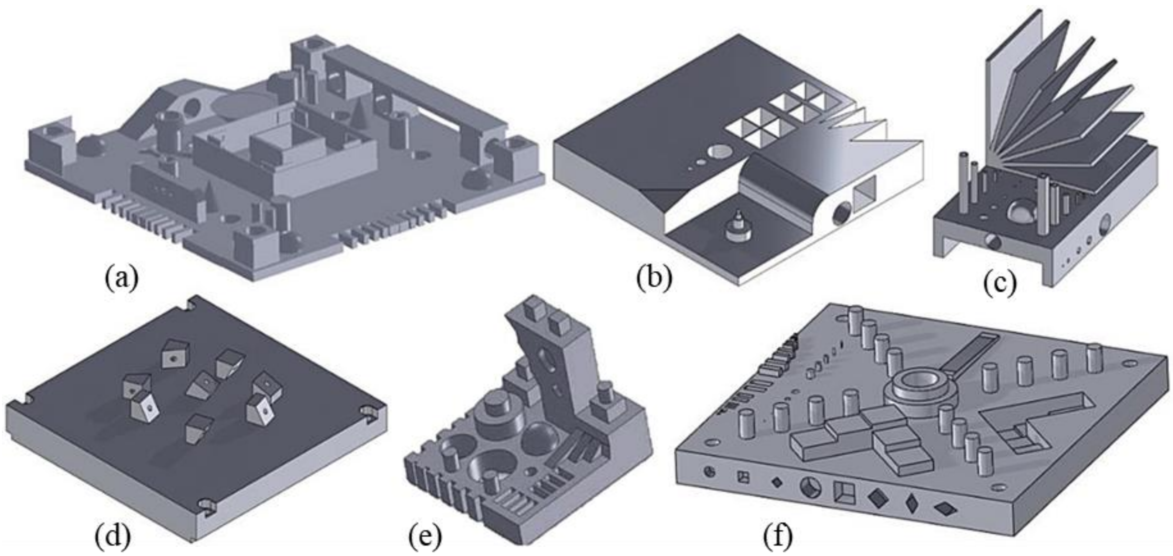

Figure 17: Example of AM benchmark artefacts [108]showing Mahesh (a) [109], Kruth (b) [110], Castillo (c) [111], Delgado (d) [112] , Johnson (e) [113], Moylan (f) [114] (not on scale).

Due to the increasingly high number of AM technologies and processes, different methods and tools are needed to compare them and assess their capabilities and limitations. AM benchmark artefacts can be used as a comparison method or also as a calibration tool. They can be split into three categories [115]: (i) geometric benchmark artefacts to evaluate the AM system accuracy and design requirements, (ii) mechanical benchmark artefacts to evaluate the properties of the additive manufactured parts, (iii) process benchmark artefact used to further improve and optimise different stages of AM process from print orientations and layer thickness to post processing stages.

There is currently no standardised benchmark artefact that can be used for all AM processes or systems, which has led many researchers to publish different AM benchmark artefacts usually more adapted to a specific AM process and with a clear goal and measurement strategy [116]. The timeline of AM benchmark artefacts starts with the one published by Kruth in 1992 [117,118]. Another well-known benchmark artefact in AM community is Moylan's NIST artefact which allows for evaluating the AM system spatial repeatability. Another one is Mahesh's artefact [109,115,119] which is composed of multiple features that can assist in evaluating the AM system resolution as well as its spatial repeatability while considering geometrical product specifications ISO standards like flatness [120]. The first instances published AM benchmark artefacts had relatively simple geometries adapted for GD&T. These benchmark artefacts did not however assess the unique capability of additive manufacturing complex and free form geometries, opening the door to more proposed designs. An example can include Yang et al. published AM benchmark artefact done as a redesign of NIST artefact with multiple free-form features. Detailed comparison between general AM benchmark artefacts has been performed and published by Rebaioli et al.

Comparisons between the different literature AM benchmark lattice artefacts have been previously performed by Rebaioli et al. [118]. Another review in this field is the one published by De Pastre et al. [116] and focused on comparing different AM artefacts although this time, from a design methodology point of view.

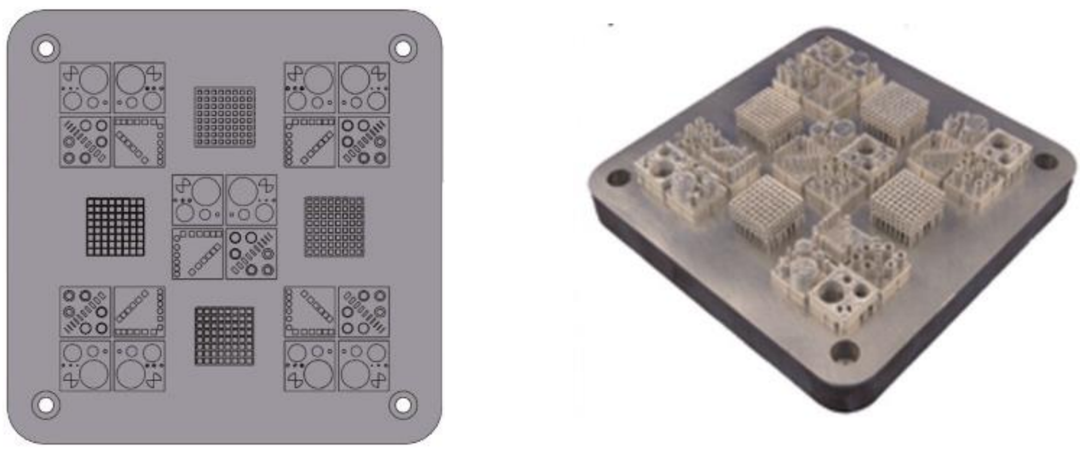

Figure 18: AM benchmark artefact with four lattices Top view of rendering (left) and manufactured one (right) [121].

However, from more than 65 AM benchmark artefacts already published in literature since early 1990s [122], only two designs included a lattice structure. Lattice structures represent the non-stochastic or controlled type of cellular solids and can be classified by type of unit cell used and its geometry variables like thickness and cell size. Two common categories of lattice structures are strut based ones, like the simple cubic [123] Figure 19 (a) or body centred cubic (BCC) [123] seen in Figure 19 (b), and triply periodic minimal surface (TPMS) ones like gyroid [124], seen in Figure 19 (c). While strut based lattices are composed of usually cylindrical connected beams, TPMS ones are composed of surfaces with zero mean curvature [124]. More information about lattice structures can be found in Chapter 3. The first AM benchmark artefact design to include a lattice structure is in a study published by Teeter et al. in 2014 [121]. The AM benchmark had different features like holes or cylinders, and also included four lattices, each with a different strut thickness (0.3mm, 0.4 mm, 0.6 mm, 0.8mm). As seen in Figure 18, the four different lattices were placed symmetrically across the build platform and had a “simple cubic” type of unit cell. In terms of measurement strategy, the lattices were dimensionally measured using STM6 Olympus microscope, micro-CT, in conjunction with other measurement tools like callipers and gauges. Upon analysis, the author reported that the 0.3 mm strut thickness value was an ideal minimum for the used LPBF process.

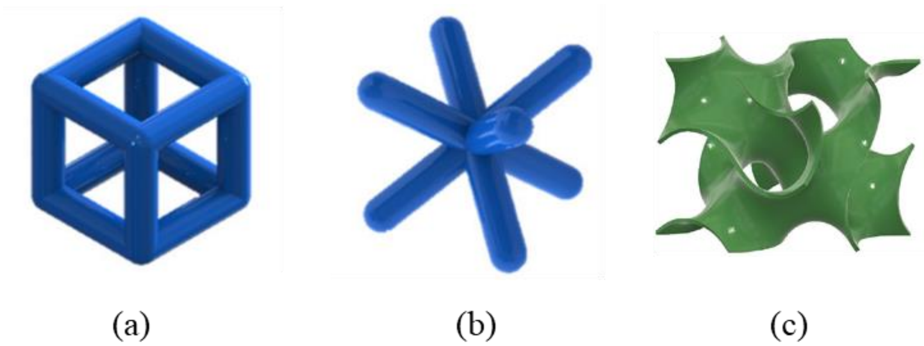

Figure 19: Unit cell of simple cubic (a) [123], BCC (b) [123] and gyroid TPMS (c) [124] lattice structures.

The second study that included a lattice design is the AM benchmark artefact published by Taylor et al. in 2021 [122]. The lattice included in the design was composed of a gyroid Triply Periodic Minimal Surface (TPMS) unit cell as well as a strut-based BCC unit cell. The author mentioned that these two lattice unit cells were chosen due to being the most common ones reported in literature [122]. The objective of this design was to avoid common AM test cubes have a compact (40x39x40 mm) general LPBF design that can be used for multiple purposes due to the multiple features included in the design as seen in Figure 20. For example, the AM benchmark artefact can be used to evaluate the dimensional accuracy and resolution using thin features like holes and walls but also to assess the microstructure, residual stress and more. Measurements applied on the added lattice structures included surface integrity, microstructure assessment as well as easiness of the trapped powder particles left from the LPBF process.

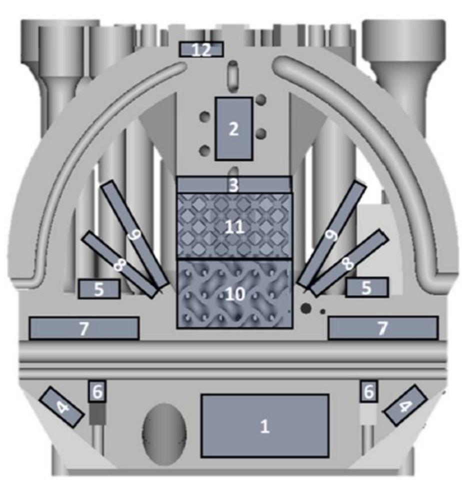

ZONE	Description
1	Lower Bulk Infill
2	Upper Bulk Infill
3	Over Lattice Poor Thermal Conductivity
4	40° Bulk Overhang
5	Shrinking Vector Triangle
6	Unsupported Overhang
7	Over Thru-hole
8	1mm Thick 40° Overhang
9	1mm Thick 60° Overhang
10	TPMS Gyroid Block
11	BCC Lattice Block
12	Upskin/Top Surface
13	All Areas Within 500µm Of Edge

Figure 20: Taylor et al. [122] *AM benchmark artefact and its different zones.*

Nevertheless, the internal features of these lattice from the two mentioned benchmark artefact were not assessed. More measurements that are important for evaluating lattices like dimensional deviation, surface roughness and porosity were not measured. This highlights a crucial gap in terms of AM benchmark artefacts since there has been no artefact solely focused on lattices. Furthermore, more development must also be done in developing an adequate measurement strategy that is optimised for lattices. Research focused on developing a lattice benchmark artefact and adequate measurement strategy would directly meet the previously mentioned research gaps highlighted by AMSC, specifically Gap D26 related to design and measuring lattices [105]. A comparison can be seen below between the two published AM benchmark artefact that added lattices to their designs.

Table 2: Comparison between lattices included in Teeter's benchmark artefact and Taylor's one

Artefact	Teeter	Taylor
Size	Box size of each lattice was:16x16x7mm	Box size of whole artefact was: 40x39x40mm “Lattice box size not mentioned”
Lattice unit cell	Simple cubic	Body centred cubic, gyroid
Cell size	2mm	“Not mentioned”
Strut thickness	0.3mm, 0.4mm, 0.6mm, 0.8mm	0.5mm
Performed measurement and instrument	Dimensional measurement: STM6 Olympus microscope, micro-CT Gauges, callipers	Surface integrity, microstructure, and easiness of powder removal

3. Chapter: Design for Additive Manufacturing and Lattice Structures

3.1. Design for additive manufacturing

When trying to additive manufacture CAD designs that were made for CNC machining or injection moulding, the cost is usually higher and harder to justify beside few benefits like the removal of stock and print on demand or reducing material waste. To justify the usual high cost of AM, design engineers often take full advantage of the AM offered shape complexity, material and mass customisation and decentralized manufacturing as seen in Figure 21. Needless to say, some parts will always stay optimised for non-AM processes like large and thin making it easier for stamping or some small assembly parts with no special functionality like standardised screws, bearings or gears. This section will focus on multiple ways DfAM can be applied with more emphasis on the use of lattice structures, their characteristics and also challenges in inspecting them.

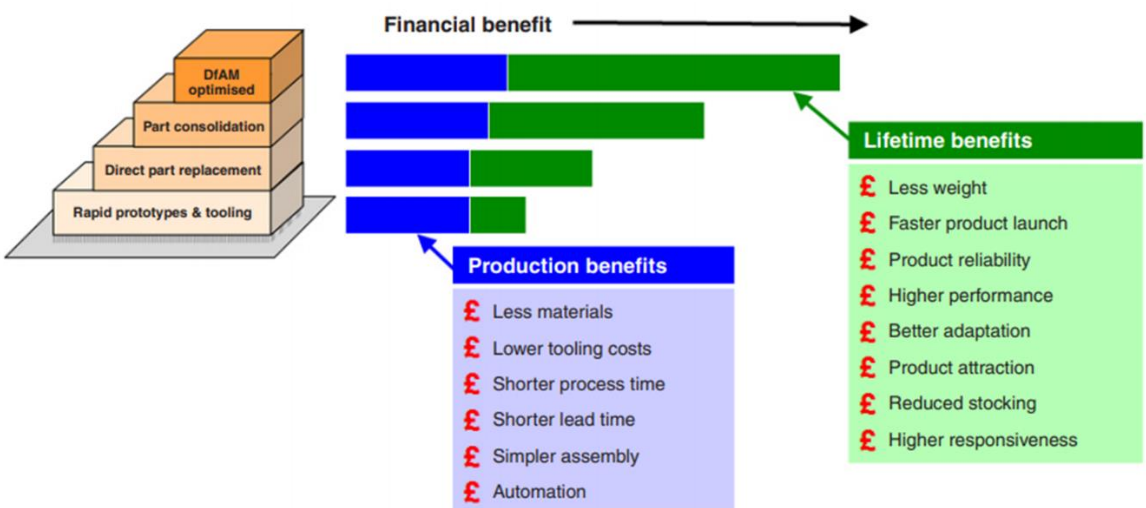

Figure 21: DfAM benefits compared to rapid prototyping, direct part replacement and part consolidation [125].

a) *Cellular and lattice structures*

Cellular structures are the parent category of lattices. They are common in nature and range from Coral, sea sponge, insect nests and more [126], as seen in Figure 22. They have been used in a broad range of applications, for example 5000 years ago with wooden artefacts in the pyramids, or cork as bung for wine bottles in roman times [127]. Examples of man-made cellular materials can be polymeric foams or foam metals, ceramics or glass which can be used for insulation or cushioning [127]. While cellular structures have attractive properties, they are often less researched, documented or understood [127].

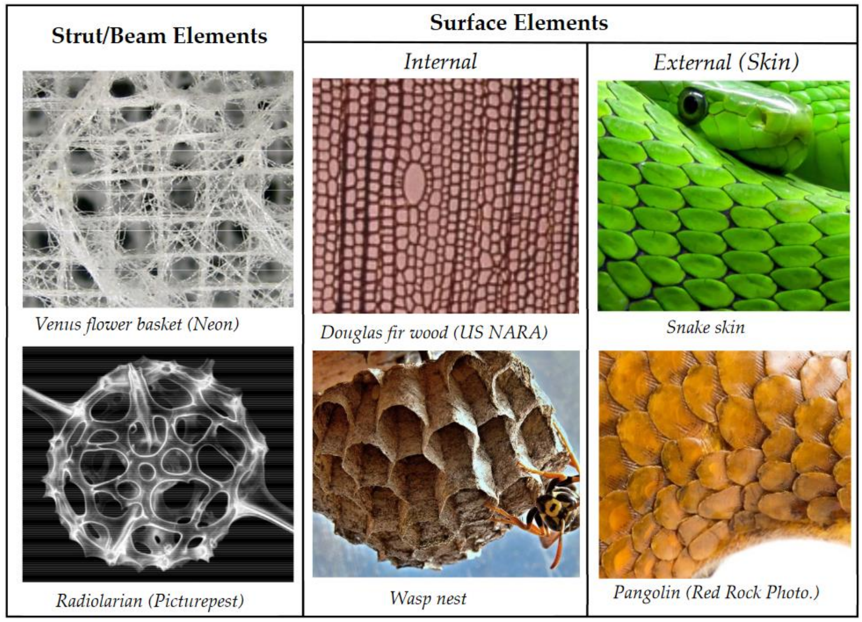

Figure 22: Examples of strut based or surface cellular structures from nature [126].

Lattice structures are one type of cellular solids. Cellular materials include either honeycomb structures (2D) or foam structures (3D). Foam structures are then differentiated between open cell foams and closed cell foams where not only the vertices and edges are full but also the faces [127]. When foams are not produced by a stochastic process but with a rather controlled one, they are referred to as lattice structures. This explains the dominant use of the lattice structures term in the AM field instead of cellular structures.

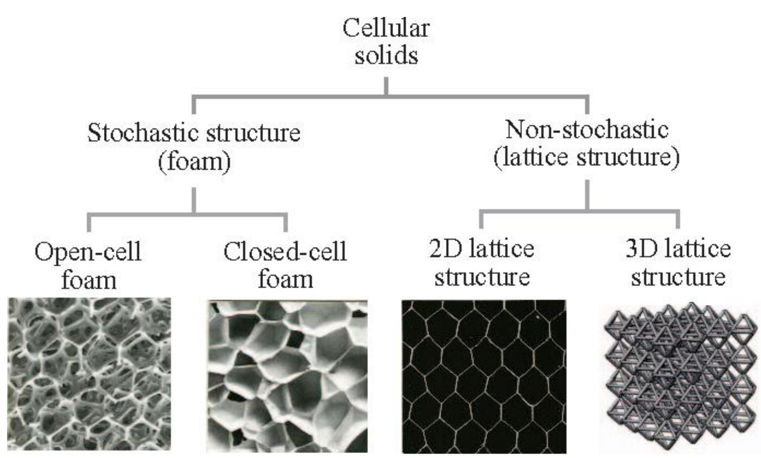

Figure 23: Cellular structures classification to stochastic (foam) and non-stochastic structures (lattice structures) [128]

Ashby et al. defines a lattice as a "connected network of struts". Due to their millimetre or micrometre scale, they can be viewed as both *structures* and *materials* [129]. While being previously (sometimes currently) considered just as a different version of its monolithic material, lattice structures should be viewed as a *material* on their own allowing a direct comparison with their fully dense monolithic material [129]. Historically, it was also thought that lattice properties were linearly relative to their density, which is not the case for most of their properties [129].

Lattice structures classification can be done using different parameters like overall lattice structure and distribution, the type of unit cell used and the unit cell geometry like its strut diameter and strut size [129]. Indirect parameters can include the material, manufacturing process and post processing method used. Unit cell classification can be done to categorise lattices to strut based, with triply periodic minimal surface or topology optimised unit cell as seen in Figure 24.

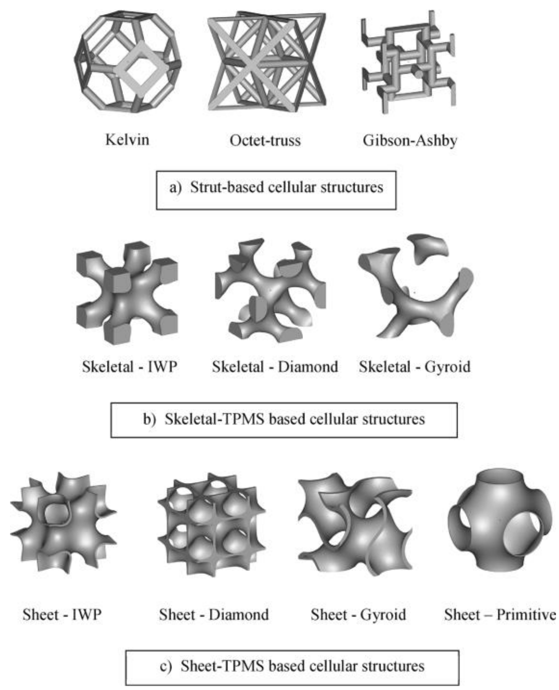

Figure 24: Different cell unit examples like strut based (a), TPMS based (b) or sheet-TPMS unit cells (c)[130].

Lattice structures can be very beneficial and used in different applications like heat dissipation, energy absorption and tissue engineering scaffolds[131]. Other applications can include acoustic ones [132] or damping [133]. One of the trending current applications is implementation of cellular solids in medical implants. The unprecedented possibility to control the medical implant porosity leads to implants with closer bone properties to the human bone surrounding it, reducing common implant problems like stress shielding [14,134].

Different strut-based cell unit geometries can have different applications. For example, in applications where high stiffness and strength is required, the octet-truss unit cell lattice (see Figure 24) can be used [135] while in bending dominated applications the BCC unit type lattice can be used since they have a longer compression stress plateau [136]. Triply periodic minimal surfaces (TPMS) type of cellular solids like gyroids, suffer less from issues like stress concentrations compared to its strut based equivalent, leading to higher fatigue resistance making them ideal for applications like medical implants [137].

The usual multiple parameters possible to choose from when designing a lattice within a part like cell type, cell size, strut thickness and more, makes the design process challenging for most DfAM engineers [138]. This challenge has led to multiple research studies in the field that address the connection and linking of geometry parameters and the expected/resulting mechanical performance [139–142]. More information on applications of lattice structures as well as their AM workflow from design to manufacture can be found in section 3.2.

b) Part consolidation (PC)

Another way to apply DfAM is part consolidation (PC). Changing the manufacturing process from for example CNC machining different parts of an assembly to the AM process is not always cost-efficient. Instead, a design engineer can take advantage of the complexity and design freedom to use part PC which consists of consolidating different parts of an assembly into a single 3D printable part.

Figure 25:Example of consolidating multiple moving parts into one printable part [143].

This method can increase the part functionality and its strength since a stress concentration could have been existing in the assembly features [144]. PC can also dramatically decrease assembly time and reduce the number of parts in the company design database and physical inventory cost. Another iteration that can be done on conventional parts is to embed electronic components like sensors or conductive tracks during the AM process, requiring methods that have the multi material capability [145].

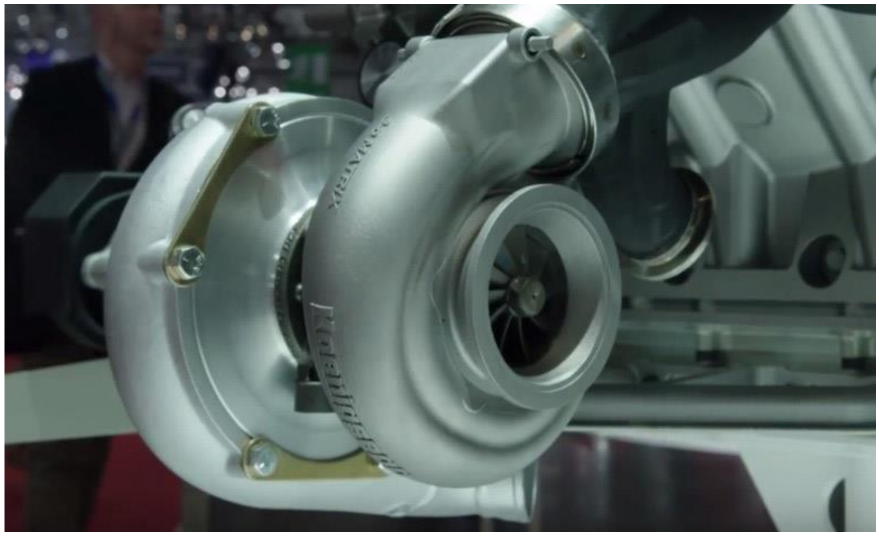

Figure 26: Additive manufactured and patented variable turbo consolidated and with enclosed moving parts [146]

Part consolidation can also be optimised for AM to not only reduce the part count but also produce assemblies as one object with moving parts straight after the AM process as seen in Figure 25 and Figure 26. This usually requires advanced understanding of the machine limitations regarding the achievable tolerances and minimum size features. AM assemblies with movable parts means that the clearances between the parts will be filled for example by powder, resin, or filament, depending on the chosen AM process. This means that the positions of these clearances need to be accessible so that it can be removed during post processing. For material extrusion and in cases where supports are necessary during the printing process in the clearances, materials like polyvinyl alcohol (PVA) can be used since they are soluble in water and don't have to be manually accessed by the user [147].

c) Overhangs, supports and part orientation.

During the AM process, features that have a horizontal angle or under 45 degrees features have more chances of distortion, rougher surface or even failure during the printing process. These parts of the design are usually called overhangs and are fixed by adding supports below them. The supports also assist in holding the part during the printing process as well as diffusing the heat, reducing the chances of warping and part distortion [148]. Supports are usually generated during the slicing process presented before and performed by the slicing software taking different shapes [149] decided by the user as seen in Figure 1.

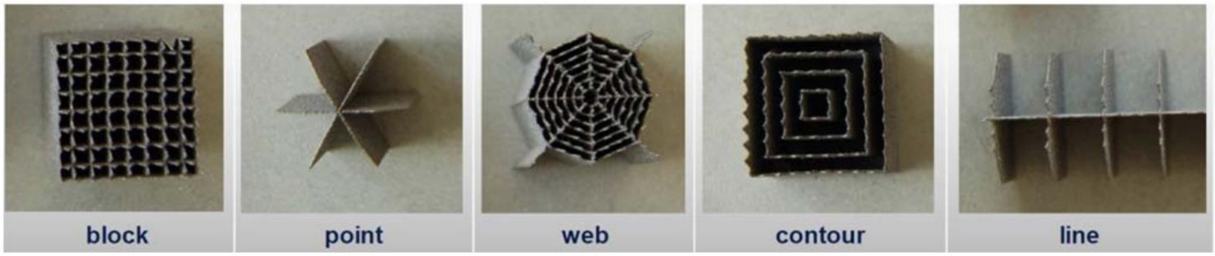

Figure 27: Different support geometries for metal AM [149]

In some cases, and in the LPBF process, the part would not have overhangs, however, since it has a large surface area touching the build plate, the part will have to be oriented (most of the times diagonally) and supports are added to assist in the heat diffusion during the printing process. Failure to do so would lead to higher temperature gradients exerted on the part leading to warpage and ultimately failure of the print.

The shape of the supports can differ and since one of their functions is to hold the print during AM process, previous research has looked into applying finite element methods to find ideal shape for a certain design as seen in Figure 28 [149].

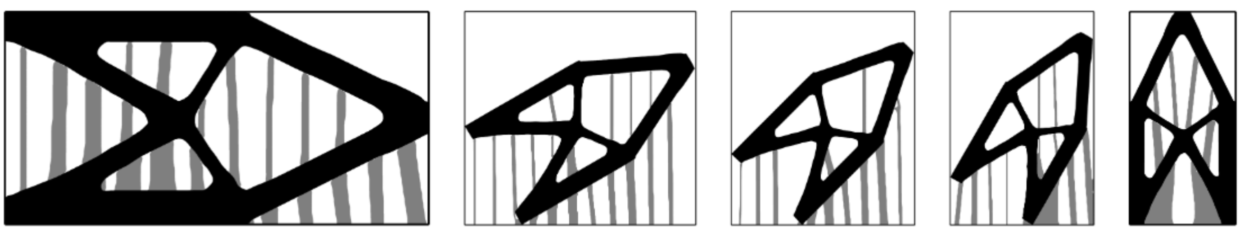

Figure 28:Optimal support generation for different build angles [149].

Different AM software is being developed to simulate what happens during the AM process using numerical modelling methods. The simulation process can also assist in finding the ideal orientation and supports that can minimise residual stresses, simulate the part removal process and ultimately reduce energy and production costs [150]. Ultimately, further research in this field will allow detailed simulation and prediction of the final AM product microstructure and increase the precision at which a factor is cornered to be the one responsible for a certain failure.

d) Hollowing the part and infill

One of the main characteristics of AM is the ability of adding material only where is needed. This design freedom is not only used on the outer shell and design of the part but also in the infill of the part. The infill term in AM usually means if the part will be additive manufactured as a 100% full dense part or with a less density percentage. In the case where the part is hollow, and depending on the chosen AM process, a shell of chosen thickness is set for the part and a hole is usually left at the bottom of the design to be used as an escape route for the raw material (powder, resin or else).

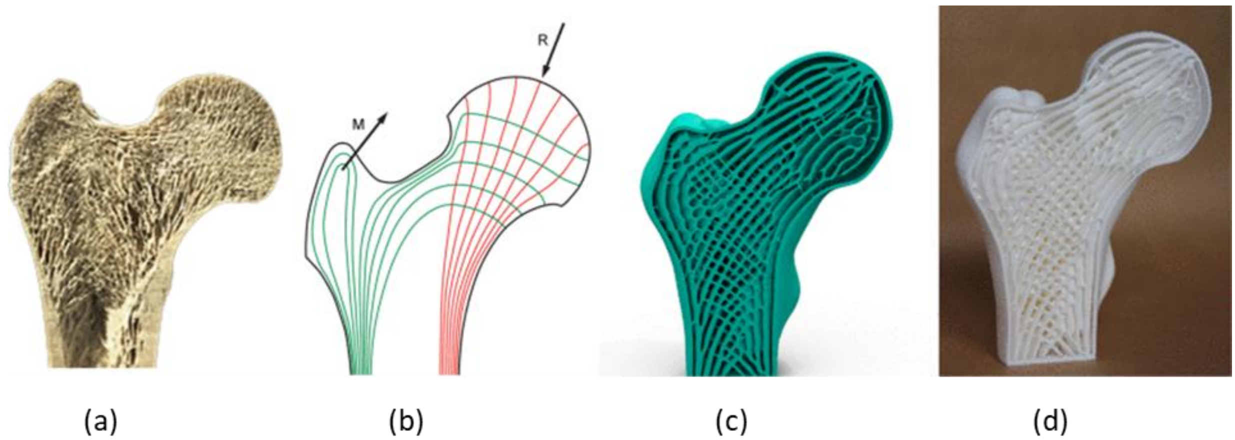

Figure 29: From the left to the right, human femur, principal stresses, rendering of optimised porous infill, additive manufactured model [151]

The shape of the infill can also play a functional role. Usually, the infill is a form of a lattice structure like BCC or gyroid. Trending research in this topic is looking at further optimisation techniques of the infill shape, direction, and density. The optimisation and infill characteristics can be based on the part load values and direction as seen in Figure 29. The amount of infill can also influence the duration of the AM process as well as the cost since its increase means more raw material being used leading to increased cost.

3.2. Lattice structures

3.2.1. Applications of lattice structures

a) Additive manufactured lattice filters

An ideal example of a local company that is a leading filter manufactured for over 30 years and located in Northwest England is Croft filters. The applications of filters range from the Food & Beverage field to the Pharmaceutical one or Oil & Gas. Traditionally, the company has been producing filters using subtractive manufacturing methods like perforation, machining, and welding for assembly of final part as seen in Figure 30. The approach taken by Croft Filters in applying AM is a hybrid one. Instead of drastically changing the manufacturing process and forcing the use of AM across all company's product portfolio, Croft Filters team has been meticulously considering added value per part, from the part size, improvement of functionality, decrease of tooling costs, ease of supply chain and more [152].

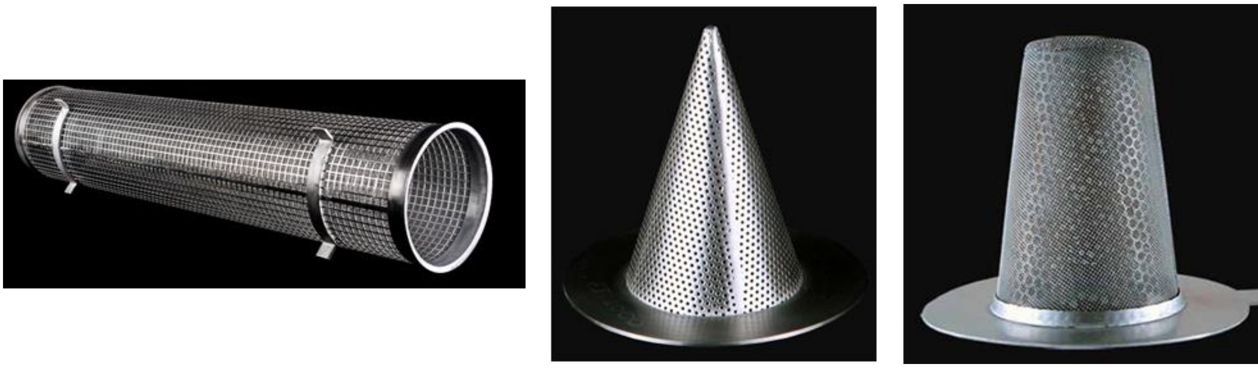

Figure 30: Example of filters like custom filter cylinder (left) witch hat filter (middle) and cone filters (right), all produced by Croft filters using subtractive manufacturing methods [152].

By using AM, Croft filters managed on many occasions to apply part consolidation to reduce total number of parts while increasing their design freedom. Therefore, a significant increase in filter's functionality has been noted with critical light weighting of the produced part. However, producing parts like filters with internal channels leads to AM challenges which the dominant one in this case being the surface roughness [153] of the as built parts. The significant surface roughness can be especially critical in the functional features, lowering the chances of meeting the set design tolerances, as well as making the powder removal process and final inspection more challenging.

When adding a filter in the passage of a running fluid, the latter would add turbulence and added resistance quantified as a pressure drop between the incoming flow and outcoming one before and after passing through the filter. Usually, the optimisation goal when designing a filter consists of minimising this resistance and pressure drop which ultimately leads to less pumping energy, making the filter more efficient [154]. For example, a usual solution is to put the orientation of the filter's perforations or holes in the direction of the passing fluid.

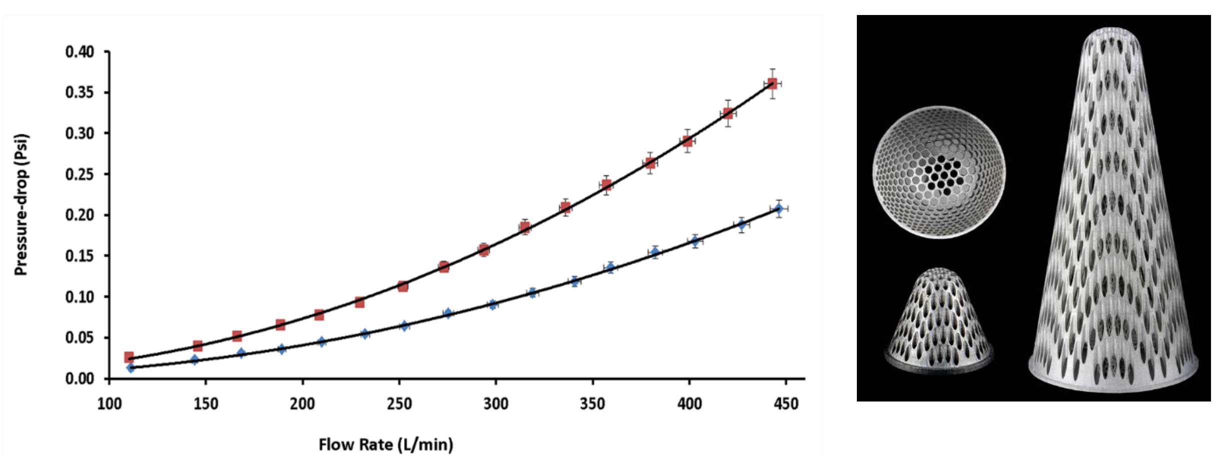

Figure 31: Comparison between conventional and AM made filter part [155].

Croft filters is using AM for its design freedom capabilities to control the filter's aperture/strut dimensions and orientation. For example, and as mentioned above, by aligning the aperture holes in the direction of the fluid, the additive manufactured filter, seen in Figure 31, allowed for a significantly lower pressure drop, which allowed a reduction in the needed pumping energy by as much as 20% from all trialled flow rates [155]. This functionally advanced design, named by Croft the "Straightliner™ Filter", was not possible to produce by using subtractive manufacturing or conventional machining due to the required accuracy especially in designs with long thin aperture walls.

Beside decreased pressure drops and pumping energy, following a DfAM approach, the company managed to have side walls and internal features that are self-supportive and more efficient, leading to a decrease in operation costs for the end user as well as the carbon footprint along the lifespan of the part. Building lattice structures using AM has also allowed the company to lightweight the final part as well as reducing their waste levels when compared to conventional subtractive operations from a bulk part. This achievement has allowed a significant gain in the buy to fly ratio, which is a common measure, especially in the aerospace industry, of the ratio between the raw material weight used and the final produced part weight [156]. Using DfAM in this field can allow the designer to add material only where necessary while being self-supportive and with good structural integrity. Complex filter designs however raise another challenge in terms of quality inspection which at the moment has limited published research.

b) Additive manufactured lattices for light weighting applications

Another company that has successfully implemented lattices is Cobra Aero [157]. The company is specialised in the aerospace market and has been producing 2000 engines for drones or unmanned aerial vehicles (UAV). The company switched from using castings to AM process, mainly due to the increased design freedom. Using the LPBF process with a Renishaw AM500 machine and in Aluminium (AlSi10MG), the company could replace conventional fins with lattice structures that delivered increased heat transfer results. This change also meant that the company reduced wasted material by 50% and also consolidated six parts into one final component as seen in Figure 32 [158].

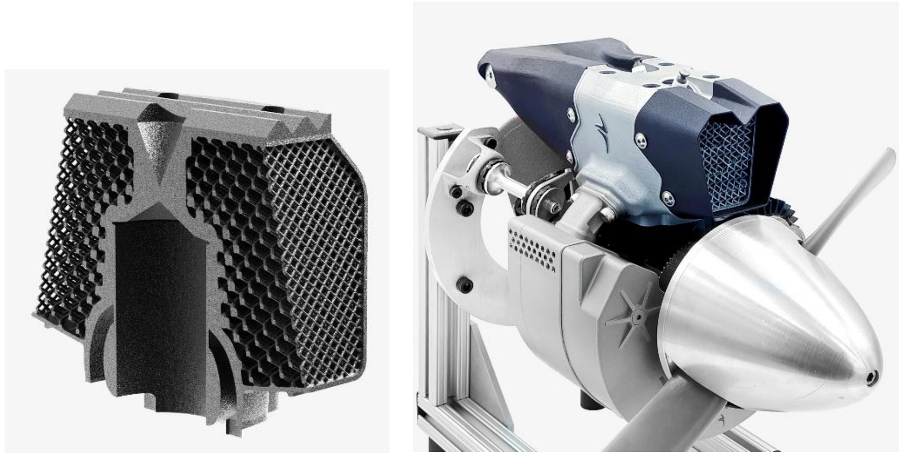

Figure 32: Cross section of the additive manufactured lattice used for heat transfer (left) and an assembled view (right) [158].

Another application in this field has been done by the United States U.S Air Force Institute of Technology (AFIT) which also used AM lattice structures and where this time, Gyroid TPMS was used for light weighting and increased functionality [15]. The redesigned part was a CubeSat, which is a small or miniaturized satellite version, often used for space research. Using the design freedom of AM and using a Concept Laser M2 machine, it was possible to consolidate 125 parts and manufacture complex shapes in Inconel 718 [15]. The use of the Gyroid TPMS lattice structure led to 50% weight reduction accompanied by a 20% increase in stiffness [15]. The final produced part can be seen below in Figure 33.

Figure 33: Conventional CubeSat on the left [159] and on the right a CubeSat developed by Airforce institute with an internal TPMS lattice structure [15].

c) *Additive manufactured lattices for medical implant applications*

An innovative use of AM lattices during the shortages caused by the recent global pandemic was the AM of nasal swabs as seen in Figure 28. The lattice design and material properties meant that it was possible to meet the targeted absorption rates seen in conventional design, it was also possible to additive manufacture more than a million swab per week using Carbon’s printers [160]. In other occasions, it was possible to surpass the conventional design with 63% viral gene transfer rate of the AM lattice swabs compared to 36% of the conventional flocked fibre ones and 14% of the polyester ones [161].

Figure 34: Design of lattice nasal swabs [51] (left) and one’s additive manufactured by Massachusetts startup OPT [161] (right).

Another common use of AM lattice structures is the medical orthopaedic implant field. The first advantage from using AM is the design freedom allowing the manufacturing of structures that are more similar to the trabecular and porous structure of bones leading to increase chances of bone ingrowth and osseointegration between the implant surface and the bone of the patient [162]. The capability of manipulating the pore thickness and distribution can also lead to controlled Elastic modulus of the implant, matching the patient needs and placement as well as having mechanical properties closer to the cortical bone, further decreasing chancers of stress shielding [13,163]. Stress shielding is usually caused by conventional hip implants when they absorb most of the load, leaving the lower bones with little to no load which results in bone shrinkage and resorbing due to Wolff’s law [164]. This effect unfortunately leads to failures like periprosthetic fracture and often requires a revision surgery for the patient [165].

To produce medical components using improved manufacturing techniques, Betatype [166] company is capable of producing 100 spinal cage implants in an impressive time of 7 hours which is two times faster than when following conventional AM workflows [162].

Figure 35: Different types of implants Ti6Al4V implants (left) and SEM of AM porous surface of an acetabular cup (right) [162].

Previously developed by the author, and as seen in Figure 36, conventional hip implant designs can be redesigned to benefit from AM advantages and have a trabecular lattice structure that is relatively closer to human bone trabecular bone design compared to conventional one. The design incorporated an average pore size of 1.1mm which is associated with an increased chance of osseointegration, usually happening at pore dimensions between 0.64 mm and 1.4 mm [167]. The design also led to a 23% reduction of maximum Von Mises stress, 15% reduction in maximum displacement as well as 30% reduction of total volume when compared to full conventional implant design [168]. The produced design had a variable trabecular strut thickness and density distribution linked to the finite element simulation resulting in only having material where necessary and reducing it in low stress areas. The design was submitted to the international 2020 Additive World DfAM student category competition and won first place prize [169].

Figure 36: Hip implant design with optimised lattice structures and winner of 2020 Additive World DfAM challenge [168].

3.2.2. Design of lattice structures

a) *File formats used for design and AM process*

Designs for engineering purposes are usually done using CAD software and exported to .STL file format when it comes to AM. STL file format has been initially released in 1987 [170] and developed by 3D systems to be for stereolithography AM machines but has become de-facto standard file format for over three decades [171,172]. However, the universal nature of the STL file format comes at a cost. For example, one of the downsides of the STL file format is the fact that it does not carry information about the unit, scale, colour or material to be used [173,174]. Since STL file format relies on tessellating a model with multiple triangles to represent the surface geometry, it usually suffers from a design fidelity issue [173], that is more prone to happen for lattice structures. The mesh representation issue also happens when building FEA models as seen in Figure 37, leading to increased computing power when using a fine mesh density.

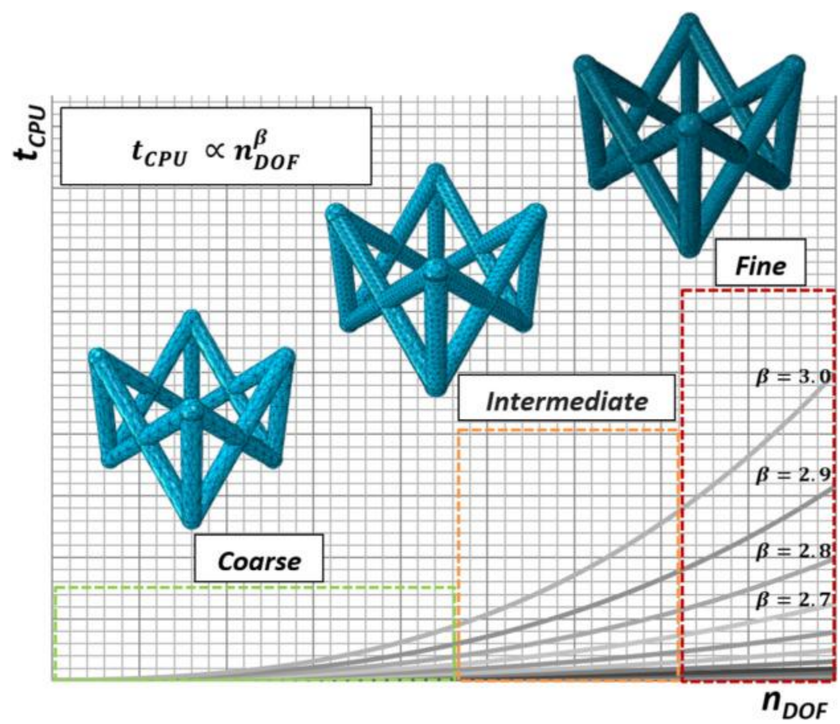

Figure 37: Comparison between coarse, intermediate, and fine mesh representation of lattices in relation to CPU time (t_{cpu}) [175].

Lattice structures are not always efficiently representable with STL file format for different reasons. In the case of a design with multiple stochastic lattices struts like trabecular AM hip cup seen in Figure 35, a compromise has to usually be reached between the maximum accuracy of the geometry that can be reached and the file size of STL file [172] and needed computing power [175]. Another challenge when designing lattices is how the conventional software is not always optimised to handle large amount of lattice strut representations and geometry break ups would usually happen in boundary representations (B-rep) and in mesh representations. Along the lines of this challenge, many innovative workflows or file formats are being suggested by companies in the AM field and academic researchers like. AMF and .3MF file formats. 3MF has been developed and shared by the 3MF consortium which include 3D Systems, EOS, Siemens and more [176]. Opposite to STL, This new file format carries way more data regarding the design like the full colour and texture, support structures, efficient storage of lattice that can reach one third the file size of STL lattices [177] and can also be currently opened by most AM design software or slicer software.

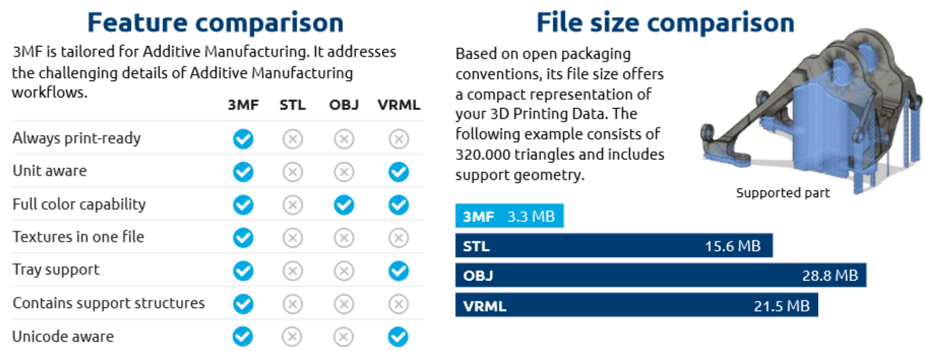

Figure 38: Comparison between mesh based file formats and 3MF file format for AM [176].

Another solution is the universal Common layer interface (CLI) file format that is simple, unambiguous and represents the multiple cross sections representing the 3D volume part where the space between the cross sections is the layer thickness [2]. While the conventional method start by designing a model in a CAD software, exporting it to STL file format and then slicing it in AM machine software to a CLI format, it is possible to currently generate a CLI directly from the original design without going through the STL file format [178]. This workflow can assist greatly in reducing the different issues of file size and usual mesh problems like inverted normal and manifold ones, which are easily detected and fixed by pre-processing software like Netfabb [179] or Magics [180] but nevertheless increase the processing time of the AM process.

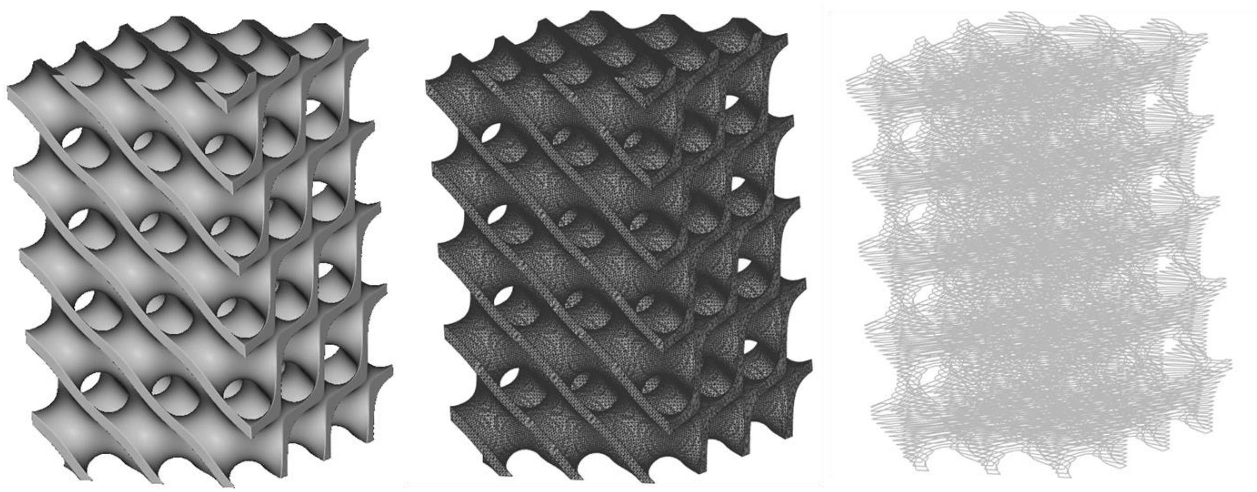

Figure 39: Example of a gyroid designed by author showing from left to right the rendering, mesh view and CLI view.

b) Boundary representation versus signed distance function

A recent innovation in the field of AM design and especially AM lattice design is the rise of "implicit modelling" instead of boundary representation or mesh modelling. For example, conventional CAD software like Solidworks usually represents geometry in a boundary representation (B-rep) form. A B-rep geometry is usually a topology made of a list of vertices, edges, faces and a boundary separating the inside and outside of the part [181]. This representation works fine for low and medium complexity designs but struggles when dealing heavy complex designs [182,183]. Implicit modelling is based on signed distance functions. Since the goal of a design is to specify the boundary of a model, signed distance functions are capable of modelling a boundary and are capable of determining whether any point x in space is inside, outside or touching the boundary Ω [181]. For example, and as seen in Figure 40, a circle in two dimensions can be either represented in a B-rep format where only information about the circle's curve is mentioned which works well for simple shapes but might break when for example the starting point does not match the ending one. Instead, the two-dimensional circle can be represented in a signed distance field (SDF) format where the inside of the design is represented by the distance from the centre minus the radius. Negative values in this case will represent the inside of the part, values equal to zero will represent the boundary and positive values represent the outside of the boundary. Representations in this format can handle better complex geometries since the B-rep will have multiple building blocks prone to failure while implicit method can handle complex Boolean operations, containment and offset operations [183].

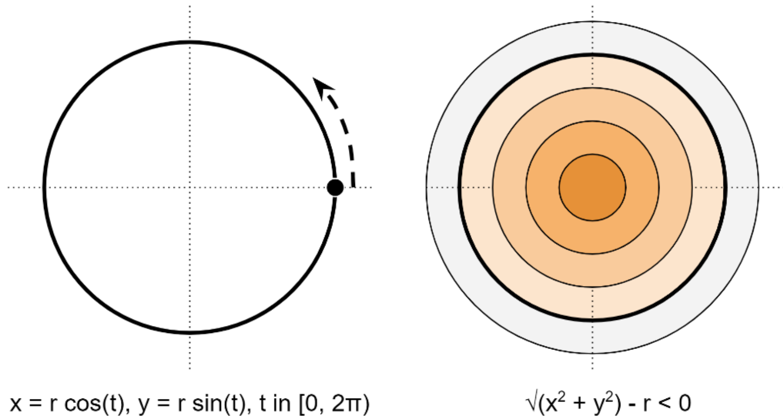

Figure 40: One the left is a B-rep circle representation and on the right a signed distance representation [181].

Using an implicit way of modelling using signed distance functions has another advantage which is the use of data fields [158]. Data fields can carry structural stress data, thermal distribution data, fluid dynamic data or electromagnetic one. When combined with the concept of signed distance representations, the strut thickness for example of a lattice can be easily driven by simulation results based on different load cases as seen in Figure 41. Also from the same figure, two different fields can be combined to drive different design parameters. While on the Figure 41 (a) all fields were structural ones, the combined fields [184] can be of different type like thermal one with pressure results of a simulation and more as seen in Figure 41 (b) . This means that when a part has different functions and constraints, lattice structures can be used in combination of these field data to add material exactly where needed to ultimately create perfect fit parts that are lightweight, with increased efficiency and improved function [158].

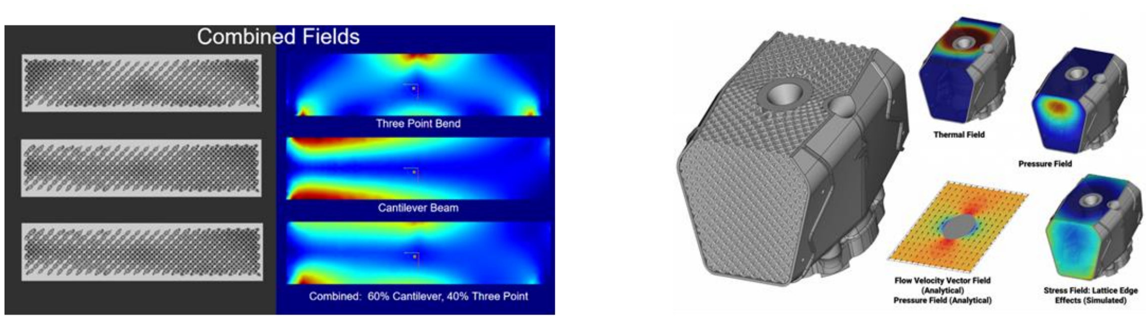

(a) (b)

Figure 41: Different loading compositions used as fields and superimposed on signed distance field data to drive the strut thickness distribution in both (a)[184]and (b)[158].

c) Generative design

Choosing the right lattice can often be a challenging task. Initially, the type of unit cell can be chosen depending on the wanted part optimisation wanted result like maximising stiffness or thermal efficiency.

However, when multiple constraints are combined, choosing the right unit cell as well as its parameters like strut thickness and density can be a demanding task that requires large amounts of data analysis from both experimental and simulation data [185]. A common solution in literature is to choose unit cell depending on if it is a stretch dominated or bending dominated one [186], leaving nevertheless a wide range of options [185].

To tackle this challenge, a recent trend in this field has been the use of generative design to automate the selection process. Generative design is an iterative design method that assists in generating multiple outputs meeting a multi-criteria design problem where each variable has defined input limits [187]. The method is heavily used by leading architecture practices and taught in most Master level architecture programs [187].

Practically, and in the case of lattices, an initial generative design of experiment can first be done to choose the right lattice structure and a second one to choose the ideal lattice parameters [188]. Generative design allows for a deeper understanding of the part constraints since advanced correlations can be drawn from the input variables and measured outputs. Instead of designing one CAD model, the design engineer ends up with an adaptative workflow of which the constraints can be tuned again to obtain a new custom part, a feature that is very suitable for AM mass customisation especially in cases like the medical field.

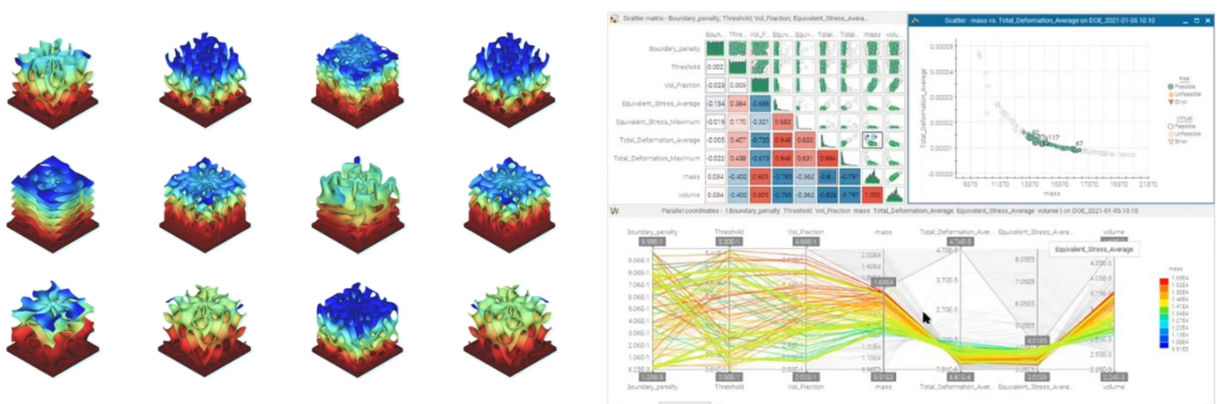

Figure 42: Example of generative design process where multiple designs are generated (left) and correlations as well as ranking of obtained designs is performed (right) [188].

3.2.3. Evaluation of lattice structures

a) *Mechanical properties of lattice structures*

One of the most used references in mechanical properties of lattice structures is the work performed by Gibson and Ashby in 1997 [127]. The elastic moduli or Young's modulus of a lattice is proportional to its density as seen in equation (1) below where $E_{lattice}$ represents the lattice elastic moduli and E_{solid} the elastic moduli of the material making the lattice. Density of the lattice is represented as $\rho_{lattice}$ while the density of the material making the lattice is ρ_{solid}. The prefactor C_1 can span from 0.1 to 4.0 while the n value depends on the type of lattice deformation from being bending dominated to being stretching dominated [138].

$$\frac{E_{lattice}}{E_{solid}} = C_1 (\frac{\rho_{lattice}}{\rho_{solid}})^n \tag{1}$$

Another developed by Gibson and Ashby [127], equation (2) seen below relates the compressive strength of the measured lattice $\sigma_{lattice}$ and yield strength of the material making the lattice σ_{ysolid} to again the density of the lattice $\rho_{lattice}$ and density of the material making the lattice ρ_{solid}. The C_5 prefactor ranges from 0.1 to 1.0 and the m also depends on the lattice type deformation. For example, for bending dominated lattices, the m and n value are ~ 2 and $\sim \frac{3}{2}$ respectively [127,142].

$$\frac{\sigma_{lattice}}{\sigma_{ysolid}} = C_5 (\frac{\rho_{lattice}}{\rho_{solid}})^m \tag{2}$$

For further analysis, manufactured lattice structures can be evaluated using experimental methods which are most of the times destructive. Currently, only few standards are released specifically for lattices experimental testing like ISO 17340:2020 "Metallic materials. Ductility testing. High speed compression test for porous and cellular metals" [189] and ISO 13314:2011 [190] "Mechanical testing of metals. Ductility testing. Both ISO standards are for ductility testing and one of them (ISO 17340:2020) uses high speed compression. To perform the ISO 13314:2011 standard, number of specimens should be no less than three while a minimum of five is recommended. Great care must be taken when cutting the lattices from the printer bed using processes like EDM to remove any supports and performing any necessary deburring. The surfaces touching the test machine plates needs to be parallel, which can be performed by adding a skin in both sides of the lattice. It is also recommended by the standard to have cylindrical test pieces; the diameter of the test piece needs to be at least 10 times the average pore size of the lattice with a minimum size of 10 mm [190]. In the case of a rectangular test piece, the width needs to also be at least 10 times the average pore size. The ratio of the height of the test specimen to its width or diameter needs to be between one and two as also seen in Figure 43. These lattice compression testing standards are not always followed in literature, making the comparison between them increasingly challenging.

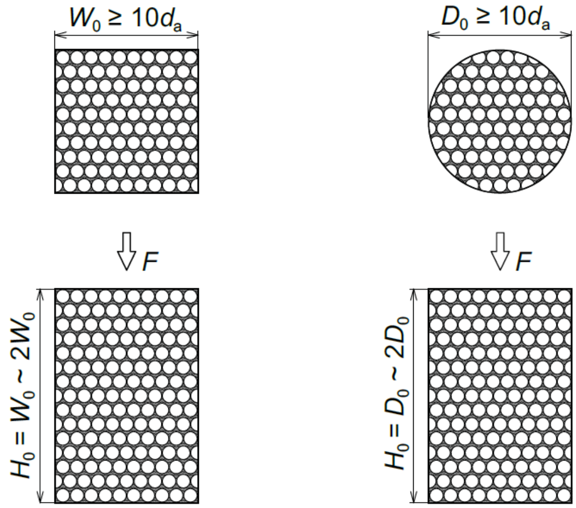

Figure 43: Design rules of ISO 13314:2011 for compression test of lattice structures. Rectangular cross section on the left and cylindrical one on the right [190].

The mechanical properties of lattice structures can be classified to bending dominated ones and stretch dominated ones. Strength dominated lattices have high strengths and low compliance and vice versa for bending dominated lattices [191].

The multiple parameters involved in design of lattices and AM means that experimental testing is often necessary for definite validation. For example, Al-Ketan et al. [130] used compressive testing to evaluate multiple additive manufactured lattices done using the PBF process at different densities. As seen in Figure 44, the results showed that the sheet-based diamond TPMS lattice had the highest stiffness behaviour that was almost independent from the variable relative density set in the experiment. Also, results showed how in general, sheet based TPMS structures performed better under compression when compared to strut-based lattices and skeleton based TPMS structures, especially at low densities. This shows how the importance of the cell unit design becomes more important at low densities and tends to converge at higher ones.

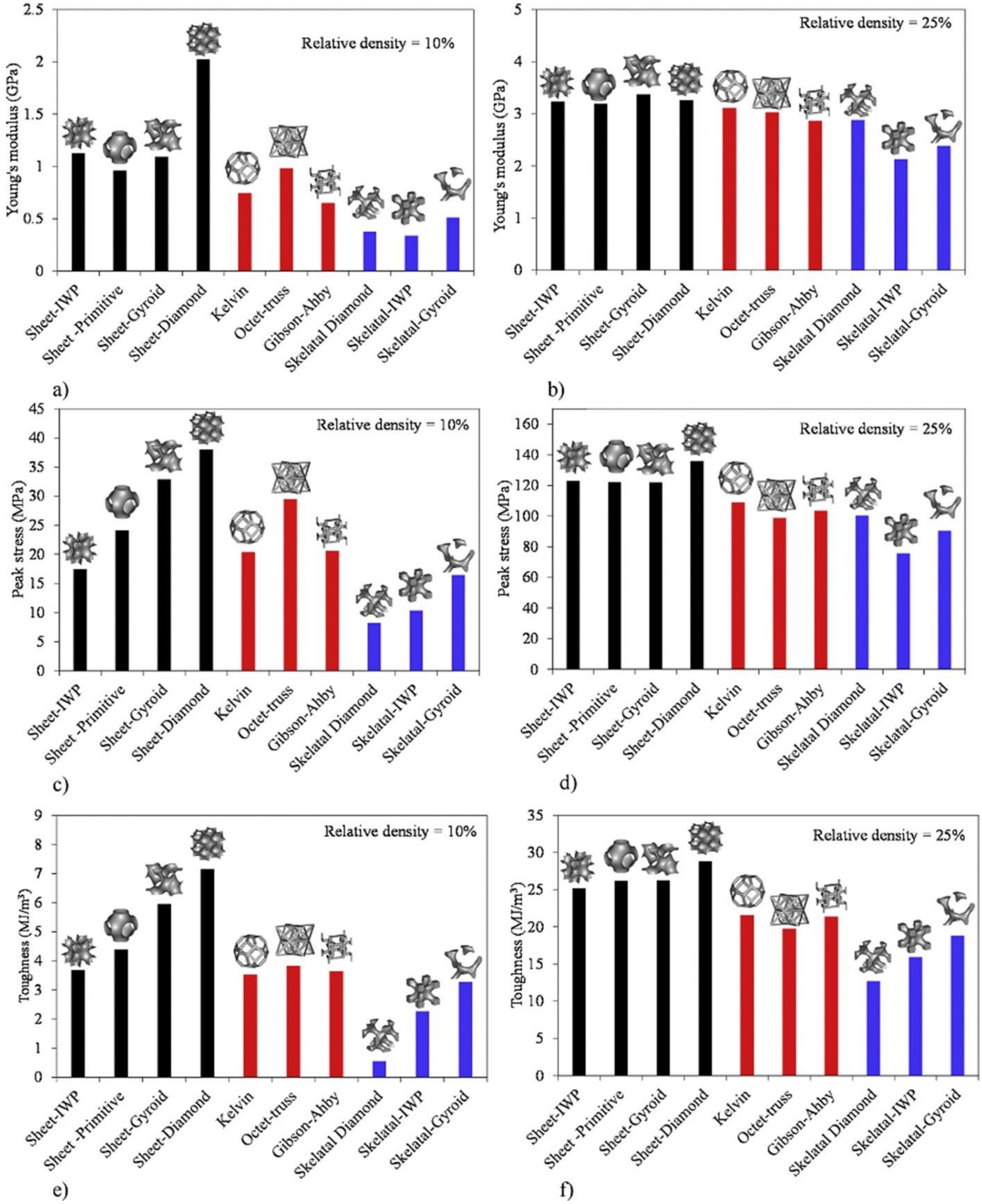

Figure 44 : Young's Modulus (a) peak stress (c) and toughness at 10% relative density compared to Young's modulus (b) peak stress (d) and toughness (f) at 25% density [130].

b) Finite element methods for lattice structures.

In cases where experimental testing is not possible due to complex geometry or cost, finite element analysis methods can be used. To do so, the CAD is usually used to generate a simulation ready model that can be based on 3D elements like tetrahedrons or beam elements. The usual complex shape of lattices and increased mesh size makes beam elements an attractive choice in this case [191]. Beam elements can be more cost effective and efficient computationally. Another route for simulating lattices is the homogenisation method. Homogenisation method relies on applying a macro mechanical behaviour on the general units used to represent the part further reducing the simulation complexity [192]. In the case of lattices, and when facing a large design with lattices, the mechanical behaviour of one unit cell can first be extracted, the large design is then taken as a full volume and given the extracted mechanical properties of the one-unit cell as seen in Figure 45. This process can significantly speed up the finite element simulation process [193].

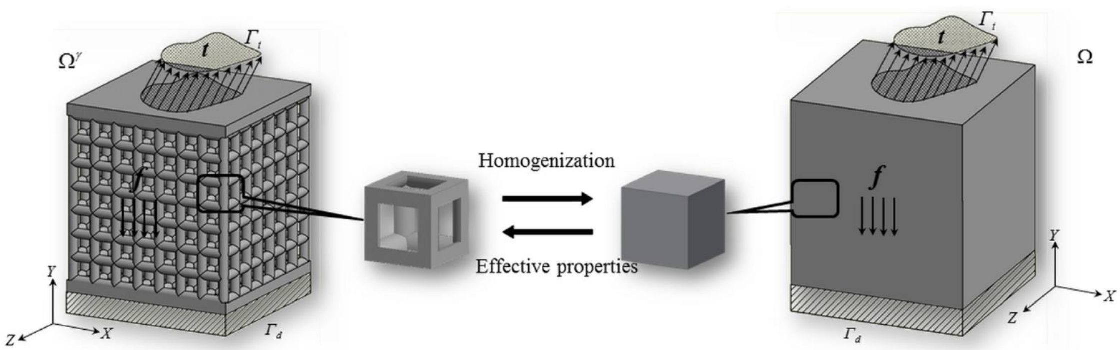

Figure 45: Example of homogenization where properties of a unit cell are used on the whole part model [192]

However, all methods mentioned above assumes that the additive manufactured lattice resembles the original CAD, which is not always the case. The next section will discuss methods developed to tackle this challenge.

c) Lattice structure defects incorporation in design validation phase.

The AM process of lattice structures using LPBF process can be prone to many challenges in variations of the manufactured compared to original CAD of the lattice due to different reasons [194]. For the LPBF technology, up to 130 variables can be responsible and have a an impact on the quality of the additive manufactured part [195]. Additive manufactured geometry of a product can be divided to the core part, up skin and downskin areas [196]. The areas with no further upper layers are named up skin and areas with no underlying layers are named downskin. Both upper and down skin surfaces suffer from the staircase effect which is caused by the layer per layer process, which leaves visible marks and surface topography as seen in Figure 46. Moreover, the down skin has a more significant surface roughness further caused by the dross formation process. The dross formation process is an unwanted “coat” composed of an accumulation of irregularly solidified melt pools (Figure 47). This formation is also caused by local heat accumulation from the melt pool, and dross formed in the overhang area exposed to the unsupported loose powder, seen in Figure 46, causing the partial melting and attachment of the loose powder to the down skin surface of the lattice strut.

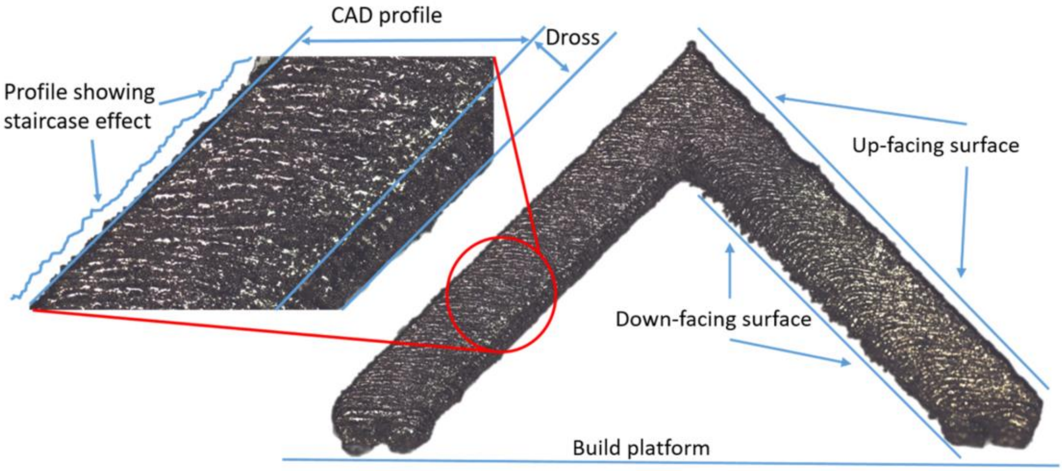

Figure 46: Staircase effect affecting up and down skin surfaces as well as dross formation, mainly present in the down skin surface [197].

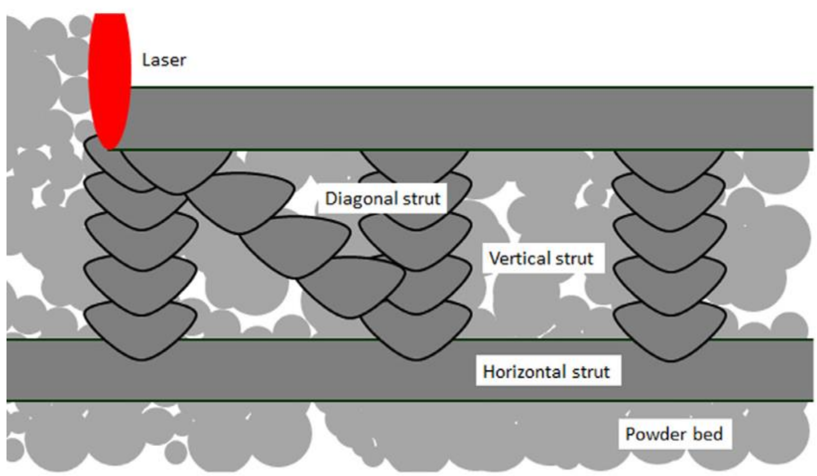

Figure 47: Forming mechanism of lattice struts in the YZ plane showing the irregular melt pools [198].

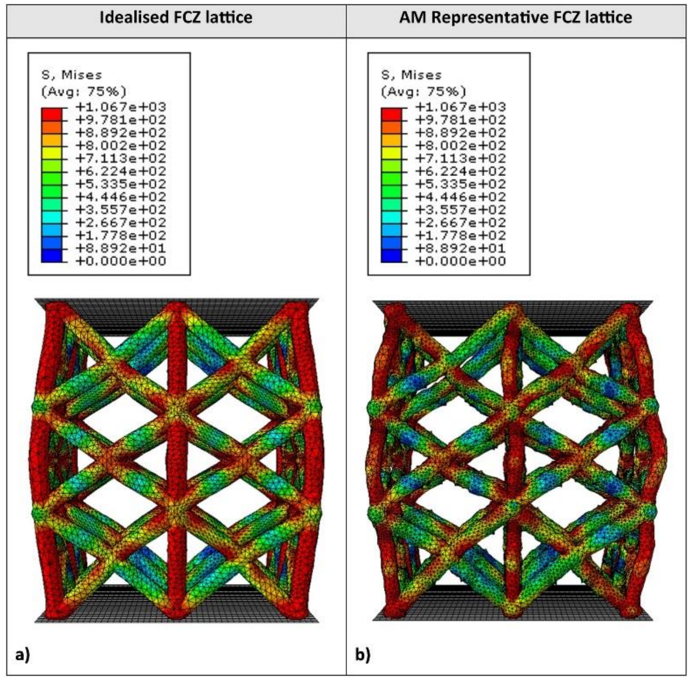

Figure 48: Finite element analysis on ideal CAD (a) versus lattice design with dimensional deviations (b) [175].

When additive manufacturing lattice structures using the LPBF process lattice, it is not uncommon to end up with parts that are dimensionally different than the CAD or have significant rough surfaces undesired and not designed in the original CAD [195]. This is usually due to an oversizing that happens to horizontal struts and under sizing of the vertical ones [199].

The discrepancy between original CAD of the lattice and the additive manufactured one let to many attempts in literature to try and include these disparities in the design phase of the lattice as seen in Figure 48. One side of solutions have focused on offering compensation methods to the CAD before the AM process. These methods can be split to three categories: in the design phase by parametrically changing the strut diameter in relation to the overhang angle to adjust for the planned discrepancy[200], in the manufacturing phase by adjusting optimising AM machine settings[201,202] or in the post-processing stage by chemically etching the produced lattice while carefully controlling the etching solution concentration and bathing time[79,203,204]. Compensation approaches allow AM engineers to have more reliable and predictable AM lattices that have less deviation from their CAD. However, obtaining a lattice with little dimensional deviation usually requires settings that lead to slower builds, while smoother surface require chemical etching, leading to piled up costs when manufacturing AM lattices. On some occasions, lattice structures are mainly used as a way to reduce the weight of the part with no need to have them perfectly accurate or with the smoothest surface. In other occasions, avoiding dimensional deviations and smoother surfaces when producing AM lattices is simply challenging especially when working with constant innovations happening in the AM field.

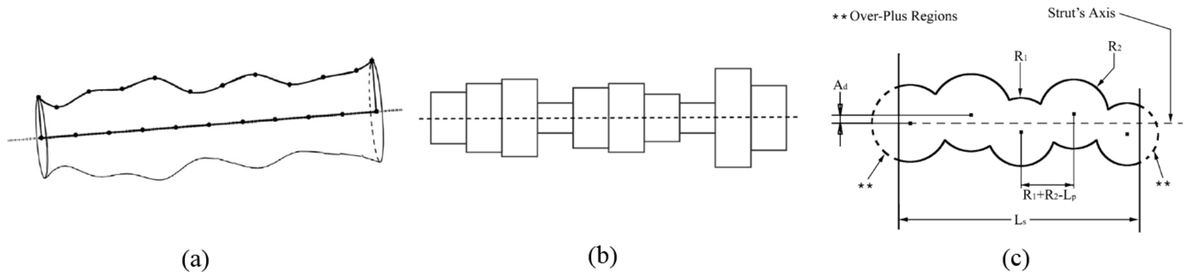

Figure 49: Different methods from literature to include as manufactured AM lattice deviations in the design phase

With these factors in mind, the other approach that can be considered is to understand the impact of these deviations and rough surface on the lattice either after production or by including them on the design phase of the AM process. The next paragraphs will summarise the advances done in literature to include AM lattice production deviations from the CAD in the design phase.

Multiple methods have been developed to try and include the expected deviation of the as manufactured AM lattice in the design phase. For example, and as seen in Figure 49 (a), a revolution on the strut axis can be done from multiple n points made by a spline [205]. Another method from literature (Figure 49 (b) include the design of a strut from primitive beam elements with different sizes of their cross section [206]. Also from literature, and as can be seen in Figure 49 (c), a method has been developed to design strut shape by using a Boolean operation to combine N number of spheres of which the centroid is not always touching the strut axis [207]. Modelling using stochastic methods can also lead to having a range of strut diameters in the same CAD of a lattice leading to better finite element analysis results [175,206,208].

However, the suggested methods from literature do not change the main shape of the cross section and only changes the strut dimension and sometimes the centroid of the strut as seen in Figure 49 (c). To tackle this challenge, another method has been suggested in literature that extracts surface of produced AM lattice from its XCT scan and apply it on the CAD resulting in both strut diameter and cross sectional variation [175]. This method however relies on always using an XCT as a source to get the intended surface on CAD instead of designing it from scratch and only use XCT as an initial guide. Another limitation of literature is how none of the studies from literature previously compared the produced CAD of AM lattices using surface metrology. Most of the analysis has only been done dimensionally or using finite element analysis, ignoring how the surface roughness compare between the manufactured AM lattice and the CAD with designed deviation.

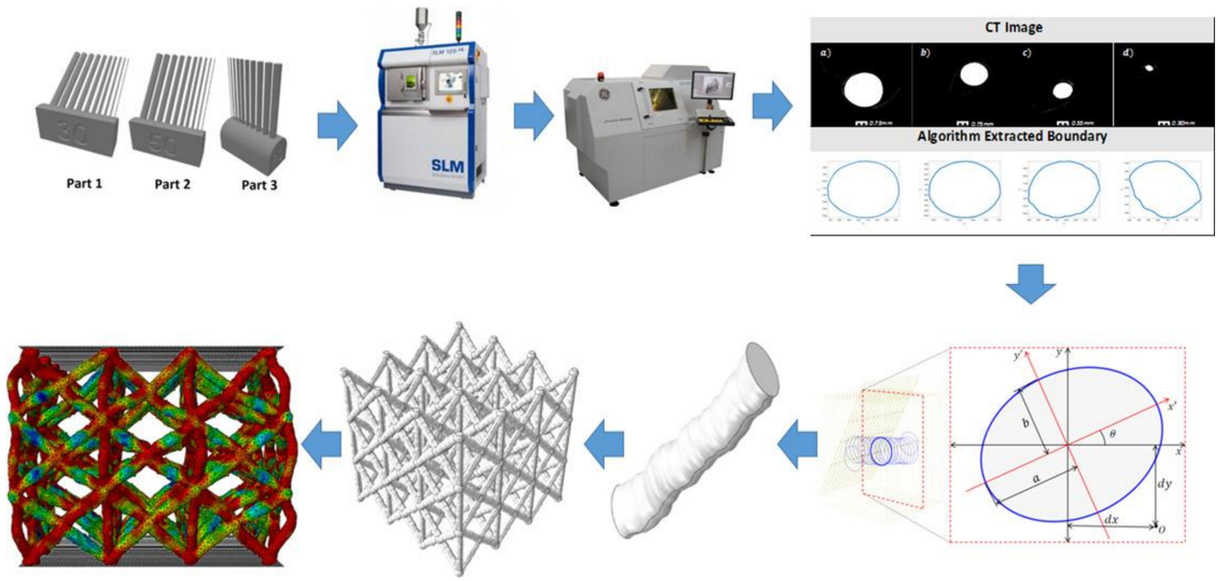

Figure 50: Method suggested in literature to incorporate dimensional deviations on the AM lattice part back to the original CAD using XCT data [175].

3.2.4. Manufacturing of AM lattices

After finalising an AM lattice CAD design, the model is usually taken to the AM machine manufacturer's slicer like QuantAM [209] for Renishaw AM machines or a general-purpose slicer that works for many types of AM machines like Magics by Materialise [180]. Common parameters to set prior to manufacturing an AM part in the LPBF process include the laser energy and scan strategy. When it comes to lattice structures, scanning strategies can include a contour strategy [210], point strategy [211] or pulsing strategy [212]. On the other hand, laser energy (E) usually include laser power (P) and exposure time (t) as well as layer thickness (l), hatch spacing (h) and scanning speed (u) [213] and seen in equation below. These parameters can be used to define the laser energy projected to the melt pool as seen in the equation (3) below as mentioned by Ghouse et al. [213].

$$E = P \times t \;\; or \; E = \frac{P}{u \times h \times l} \tag{3}$$

When optimising the AM manufacturing parameters, the goal is to have a high geometrical accuracy which can for example mean a smaller mean strut thickness deviation to the CAD, a high material density that can be measured by porosity and reach the desired surface roughness and microstructure.

A deeper understanding of the ideal scanning strategy means that the user can directly output the ideal laser path without going through the meshing step which is computationally expensive as mentioned in the examples above using formats like .CLI file format. In-line monitoring of AM process using thermal, infrared, or structural light scanning can also be used for increased part quality for lattice [214] or AM parts in general [215]. A photodiode can for example be added to the AM system to monitor the laser input as well as high speed cameras to monitor the melt-pool quality and produced surfaces [216].

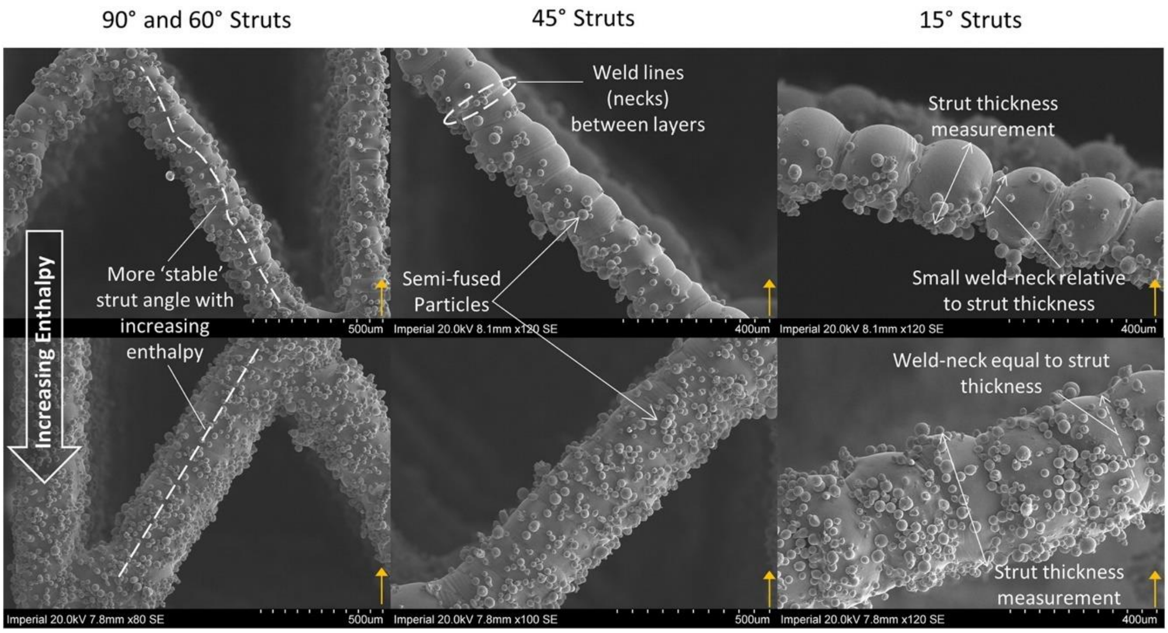

Figure 51: Different strut thicknesses achieved by controlling specific enthalpy. From right to left are different strut angles including 15°, 45°, 60° and 90°. Right image with small 15° angle shows undesirable weld necks [213].

While contour hatch scanning strategies are common for most AM parts, it is challenging to use them on lattices. The small strut diameter usually means that the laser path becomes highly sensible to .STL format strut resolution creating many laser vectors and high-speed jumps as well as being computationally expensive to run. On the other hand, point scanning strategy is often considered more suitable especially for small thickness and stochastic lattices [213]. Instead of creating a contour, the point strategy relies on exposing the laser at a specific location, time and energy, creating a strut thickness equal to the width and shape of resulting melt pool. This method leads to less laser vector jumps, reduced build time as well as computational cost. Pulsing strategy is similar to the point scanning strategy with the only difference of repeatedly firing the laser at different time intervals, creating a new duty cycle parameter and also number of exposures per location [213]. In a pulsing strategy, a heartbeat like motion is created due to the periodic heat input. The turning off of the laser beam leads to a shorted melt pool and eventually a periodical change in the melt pool length that is also rounder when compared to a continuous laser method [212]. This shorter and rounder melt pool resulting from pulsing strategy can lead to a smaller achievable strut thickness [213].

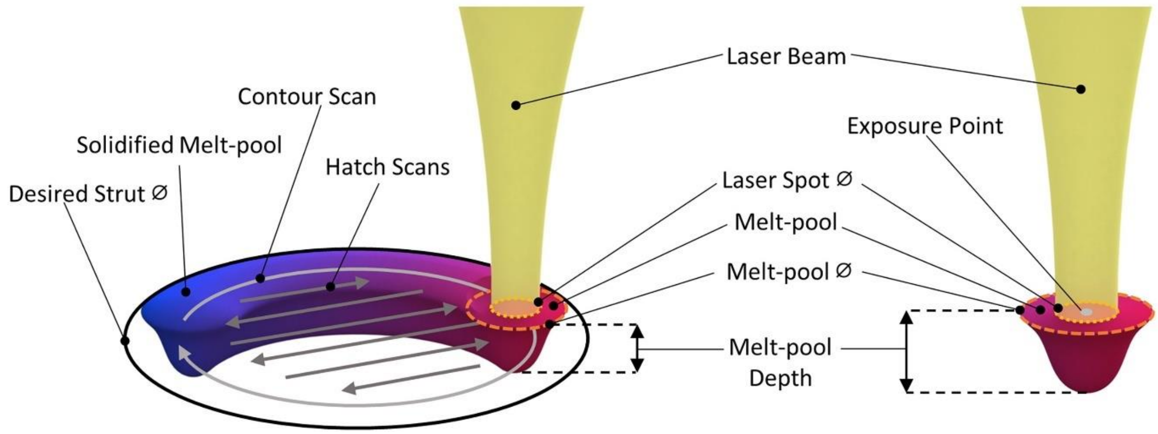

Figure 52: Contour hatch scanning strategy in (left) and single exposure scanning strategy (right) [213].

Study published by Ghouse et al. [213] shows a linear relationship between a laser's specific enthalpy delivered to the melt pool and the strut thickness. Enthalpy accounts for changes in thermal properties of a material or in a thermodynamic system and is usually used in AM as one of the methods to quantify the melt pool [217]. Specific enthalpy (ΔH) can be described as a function of absorptivity (A), density (ρ) and thermal diffusivity (D) of the powder as well as laser power (P) and other laser parameters like laser spot diameter (Ø) and scan speed (u) as seen in the equation (4) below.

$$\Delta H = \frac{A \cdot P}{\rho \sqrt{\pi \cdot D \cdot u \cdot \emptyset^3}} \tag{4}$$

By controlling the specific enthalpy, the melt pool size can be controlled and therefore the strut thickness size. Results also showed that the relationship is more accurate when using the in-process monitoring laser parameters not the slicing software requested ones. It was also observed that at small lattice strut angles like in 15 degrees angle, the strut develops weld necks between the laser melt pools as seen in Figure 51, making the structure more fragile and prone to premature failure [213].

3.2.5. Common lattice structure defects.

Lattice structures can suffer from multiple type of defects caused by different sources. The thickness of a lattice strut can be linked to the melt pool size as mentioned above, but also to the strut angle, powder quality, as well as material shrinking after cooling process [218]. Along these lines, the prediction of the as built geometry of AM lattices is very challenging which means that a deep understanding of the potential defects and their impact on the product structural integrity is very important. With better understanding of the impact of defects on lattices, better design constraints and tolerancing will be possible to implement during the AM process of lattices.

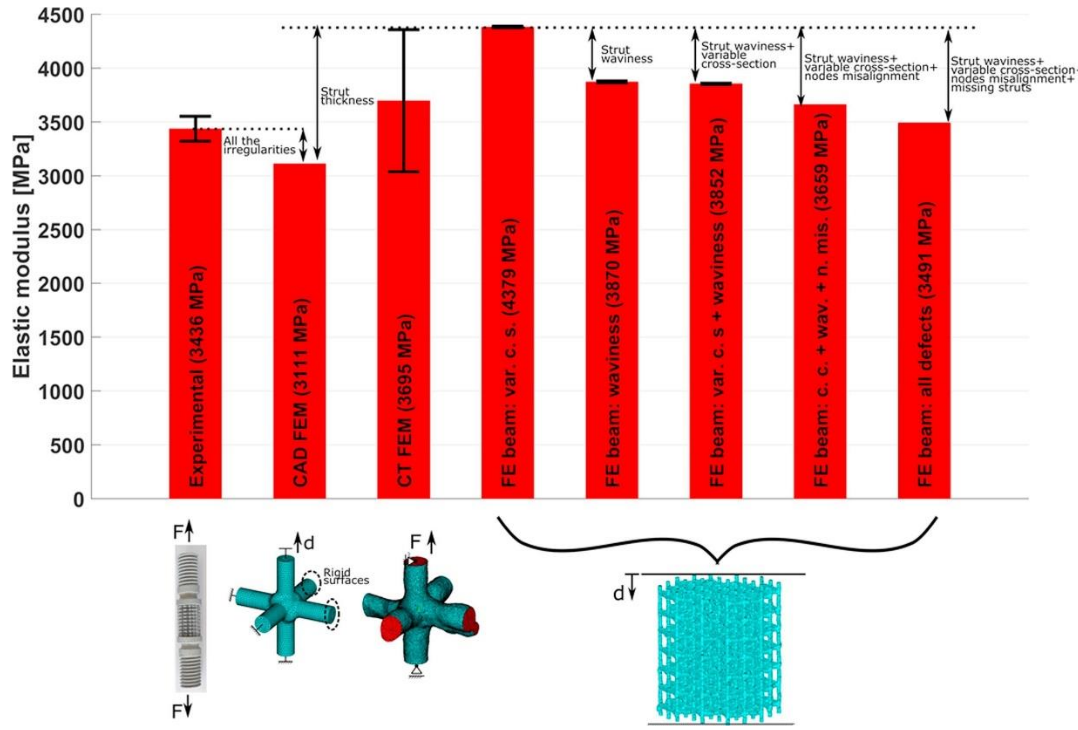

Figure 53: Comparison between elastic moduli obtained from experimental measurements and FE simulations [219].

Since it is unlikely that a produced lattice has only one type of defect, Dallago et al. [219] generated multiple lattice design defects in order to assess their individual impact and influence on the elastic modulus. Study results, as seen in Figure 53, initially showed that FE simulations on the original CAD are not representative of the additive manufactured lattice. The study also showed that higher strut thickness is linked to a higher elastic modulus, however, defects like strut waviness or junction/node centre displacement from its centre lowers the elastic modulus as they introduce bending actions on the lattice [219].

Also, irregularities that are close to the surface like sharp notches had more detrimental impact on the fatigue that internal pores. This means that heat treatments like HIPing will not have a direct impact on the fatigue since the latter mainly assists in reducing internal porosity [220].

Beside geometrical deviations, lattice structures also suffer from surface defects. Using profile surface texture parameters, the Ra value of down skin surfaces of lattice strut was found to be double the Ra value of the up skin surface [203]. Also, lattice structures unit cell can have a crucial impact on the surface roughness value. For example, a lattice produced with a BCC unit cell had a down skin Ra that is three times larger than the Ra found in down skin of a face centred cubic (FCC) lattice due to a BCC lattice overhang angle being around 35° degrees while an FCC° has a 45 degrees overhang angle [221]. Furthermore, TPMS structures would usually have better surface roughness due to their lower influence from the stair stepping effect [130]. Stair stepping effect is the effect produced by the increasing change in the strut angle caused by the overhang angle. Other defects like varying cross section, strut waviness, bonded powder particles and surface porosity can be seen in Figure 54 from study performed by El Elmi et al. [222].

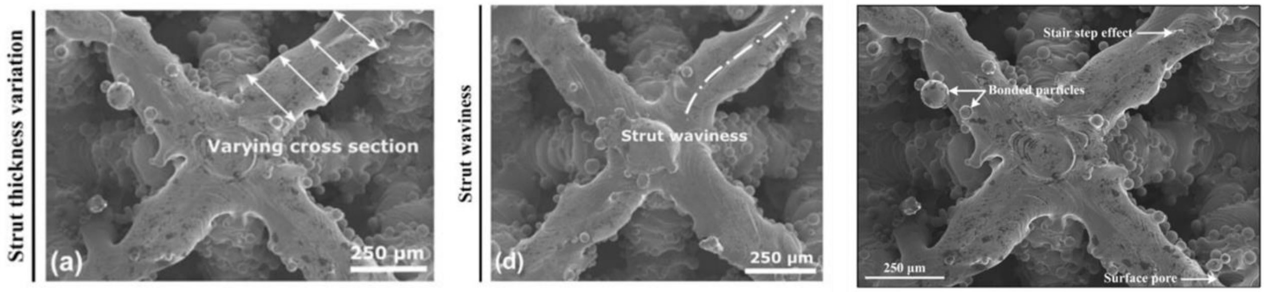

Figure 54: SEM micrograph of an additive manufactured lattice strut showing from left to right a varying cross section strut, strut waviness, stair step effect, bonded particles and surface porosity [222].

Internal porosity in additive manufactured parts can negatively impact the fatigue strength of a lattice since it decreases the cross section area of the produced part, which increases the location's stress concentration [223]. For example, stochastic Ti64 lattice samples built at 50 W showed a higher fatigue increased by 7% at 10^6 cycles when compared to samples built at 200W [224]. For lattices, scanning strategy can also have a significant impact on the internal porosity of the part [224].

As mentioned above for geometrical deviations and surface roughness, a deeper understanding of the impact of unwanted internal porosity can also assist in better quality control and cost efficient tolerancing. For example, Tammas-Williams et al. study shows how in AM parts, both the size and location matters when classifying internal pores with higher influence on the fatigue crack initiation [225]. Porosity has also been shown to be dependent on the lattice strut angle or orientation where higher porosity was observed at lower overhang angles [226]. To reduce the cost of experimental and destructive testing, simulation models can be developed that take into account the pore distribution types and their impact on the mechanical behaviour on the produced lattice [227].

4. Chapter: X-ray Computed Tomography (XCT)

4.1. Introduction to X-ray computed tomography

a) Introduction and main differences between medical and industrial XCT

Introducing industrial X-ray computed tomography can hardly be done without mentioning the medical field of it since the latter played and still does play a big role in both its start and current innovation. The Nobel prized invention of which the first patent was granted in 1972 was done by Allan Cormack who was head of physics institution at Tufts University located in Medford, USA and Godfrey Hounsfield who was chief of medical division in Electric and Musical Industries located in Middlesex in England [228]. Allan Cormack started his invention with publications done in 1963 and 1964 [229] who soon realised that the challenge to use X-ray was a mathematical one and a question of finding an equation that defines the attenuation of each material in regard to X-ray intensity [228].

Figure 55: Early X-ray imaging without radiation protection [230].

In 1969, the first scanner was made by Godfrey Hounsfield and the first medical brain scan was achieved in 1971 [231]. An example of early X-ray imaging that lacked proper radiation protection [230] can be seen in Figure 55 compared to an early CT scan used in 1980 seen in Figure 56. The first X-ray machine made solely for industry and specifically dimensional metrology was in 2005 [231,232]. It is possible to see from these two dates how the medical field XCT has been existing far longer than the industrial one which means as one might expect that industrial use is not as mature as in the medical XCT field which has more standards. Since 2005, XCT has been growing steadily and more manufacturers have started introducing larger and better XCT machines capable of not only scanning small section taken from large parts but host large workpieces without sectioning them [231], opening a new door for non-destructive measurement techniques.

One of the two main differences between the medical and industrial use is the architecture of the machine in which for example it is the machine that rotates around the patient in the medical field whereas it is the sample that rotates in the industrial one. The other difference is the usual far lower radiation doses that are lower to protect the health of the patient X-ray use on human body is carcinogenic and that a controlled exposure is necessary as mentioned by World Health Organisation (WHO) [233].

Figure 56: Early CT scanner in use in 1980 [234].

Another difference with the medical field is how the industrial XCT is usually far demanding in resolution and accuracy [231]. This means that the industrial XCT would occasionally require when possible uncertainty measurements [235] and traceability to SI units [231] which is not generally achievable. The mentioned above differences meant that the transition from medical to industrial use has not been the smoothest and many bottlenecks and breakthrough had to and still must be achieved to reach a headache free stage or a “plug and play” XCT machine that does not require extensive experience. Along these lines, the following sections will discuss the basic principles of industrial XCT machines, their general use, and how they are specifically being used in metrology and more specifically metrology of AM lattice structures.

b) XCT applications

XCT can allow for holistic non-destructive measurement of non-accessible internal features [236] which is a typical thing in design for AM in the case of reducing part count in an assembly. As AM is the next generation leap in the manufacturing field that is slowly and steadily growing, XCT can certainly be considered as the metrology next gen tool since the CMM appearance in the seventies and optical scanners in eighties [236].

XCT is a non-destructive testing (NDT) method and is usually used in detection of defects like cracks, pores and voids and in different research fields as seen in Figure 57. When compared to other NDT processes, XCT can reach a large range of spatial resolutions with the capability of assessing features at the surface, near surface and inside the volume as seen in Figure 58. However, to reach the small range of resolutions, specific XCT systems must be used like micro or nano CT which also means that the object size will be limited, as seen in Figure 58.

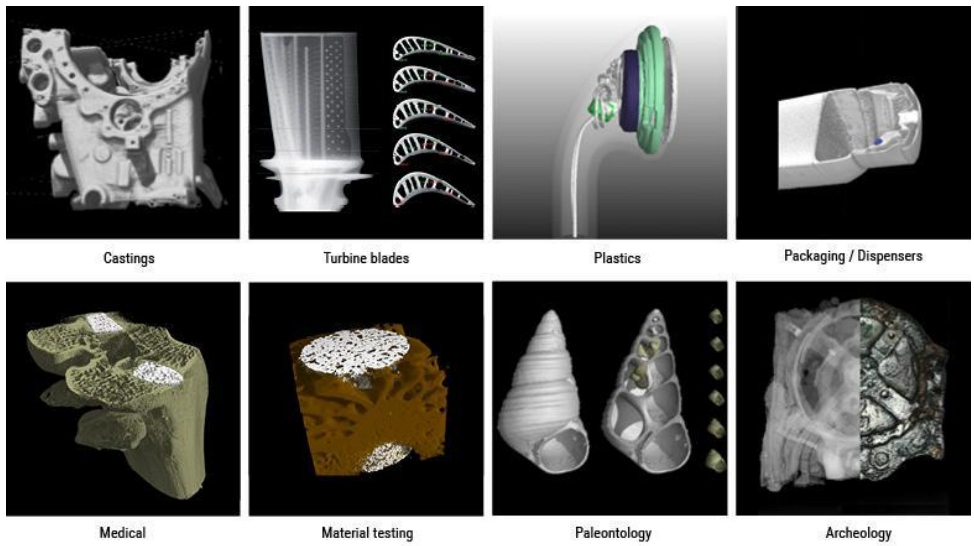

Figure 57: Growing applications of XCT in different research fields [237].

XCT comes as a great replacement to optical and tactile CMMs when features are inaccessible, however, being mainly developed for industrial uses in the recent decades, XCT still need further research when it comes to guidelines and standards of use [238]. This is also due to the inexistence of the standards that currently details uncertainty estimation making traceability a very challenging task when using XCT. While this challenge can be overcome in the CMM by modelling interaction between the surface to be measured and the CMM probe, the XCT x-rays interaction with the part to be measured is furthermore challenging to model and simulate.

Along these lines, XCT research studies that are looking for increased accuracy in measurements usually use the substitution method where a calibrated item is measured before or alongside the part of interest, which is a similar method developed for CMMs in the ISO 15530-3:2011 [239]. The calibrated workpiece or masterpiece is usually of the same material as the part of interest to be measured and have closer shape and dimensions. Most importantly, measurement strategy and form or texture features to be measured on the part of interest should be possible to be done on the calibrated workpiece. This method has been published and used for dimensional XCT measurements [240], XCT surface measurements [86] and XCT porosity measurements [241].

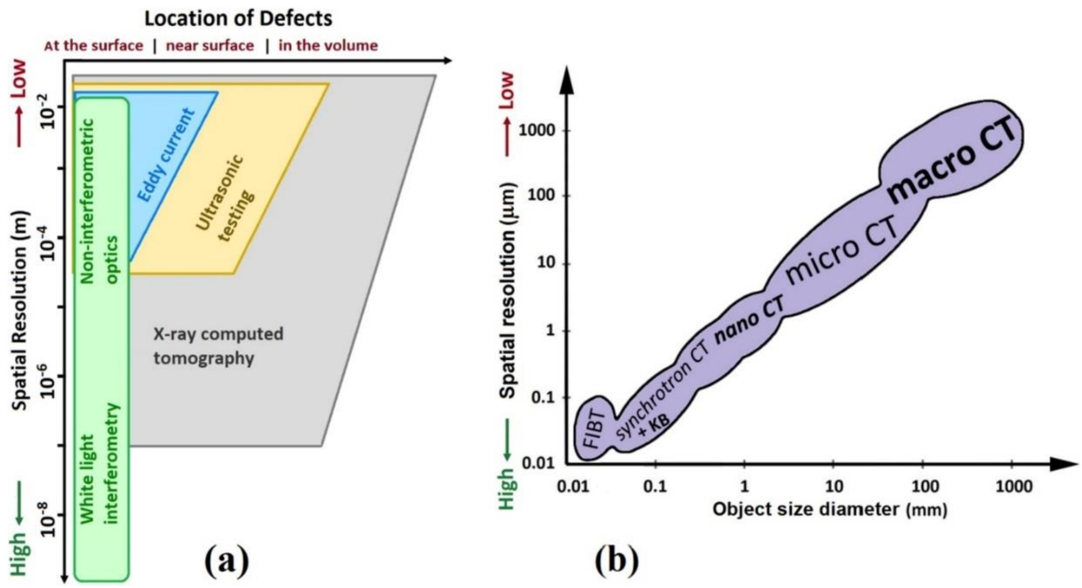

Figure 58: Comparison of NDT techniques (a) and typical spatial resolution and object size of each type of CT (b) [238].

4.2. XCT working principles.

a) Theory

X-ray emission is composed of radiations that belong to the category of electromagnetic rays. This means that the rays can be considered as both waves or photons which eventually means that they can be expressed by two different equations and can be found in [242]. Along these lines, X-rays are characterised and can be compared in a larger spectrum with other rays like visible light or microwaves. The component allowing X-ray emission in an XCT machine is called the X-ray tube, the latter, is composed of a cathode that emits electrons which are accelerated due to the electric field between the cathode and anode [243]. The accelerated rays are then focused using a magnetic lens and hit the target (usually in Tungsten) where 99.3% of energy gets converted to heat (hence the need of a cooler component in the X-ray tube) and 0.7 % to X-rays [244]. The main generated radiation is called Bremsstrahlung which means in German “braking radiation” or “deceleration radiation” [245] caused by the sudden slowing down of electrons hitting the target atoms. The second interaction is called characteristic radiation, which happens when the incoming electron collides with another electron from the outer shell leading to an electron vacancy. The filling process of this vacancy from an outer shell lead to the emission of a discrete X-ray spectrum named characteristic radiation, which highly depends on the anode target [246].

The special characteristic of X-rays is their interactivity with matter that allows them to penetrate it with a relationship that depends on the energy of X-rays and the scanned part material composition and density [231].

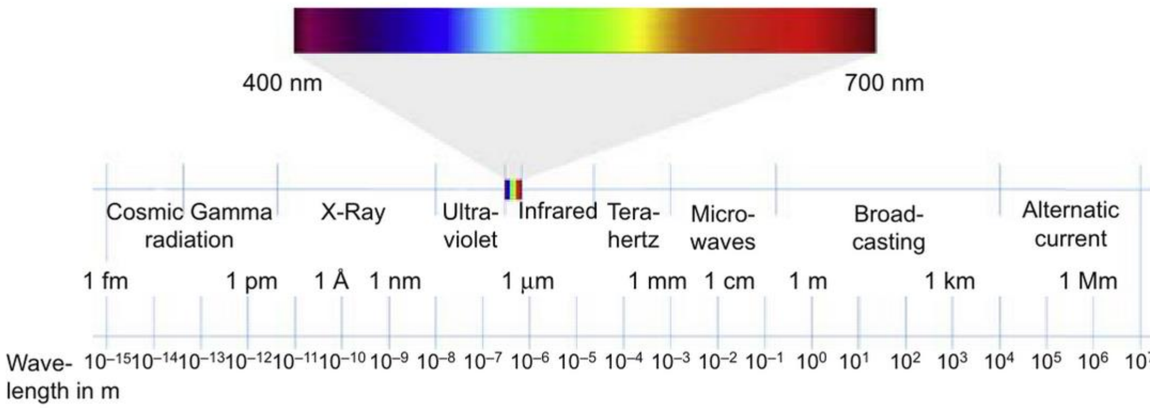

Figure 59: Spectrum of electromagnetic waves showing where for example visible light and microwaves are located in relation to this study's X-rays [247].

X-rays that managed to penetrate the part are captured on the other end of the machine using a detector, resulting in a 2D image with grey scale values. After capturing multiple 2D images from different rotation angles, a mathematical reconstruction can be performed to generate a 3D voxel-based model. Using the right thresholding technique can then lead to isolating the scanned part for further processing. Analyses of the reconstructed 3D volumes can include dimensional metrology, surface metrology and more as seen in Figure 60.

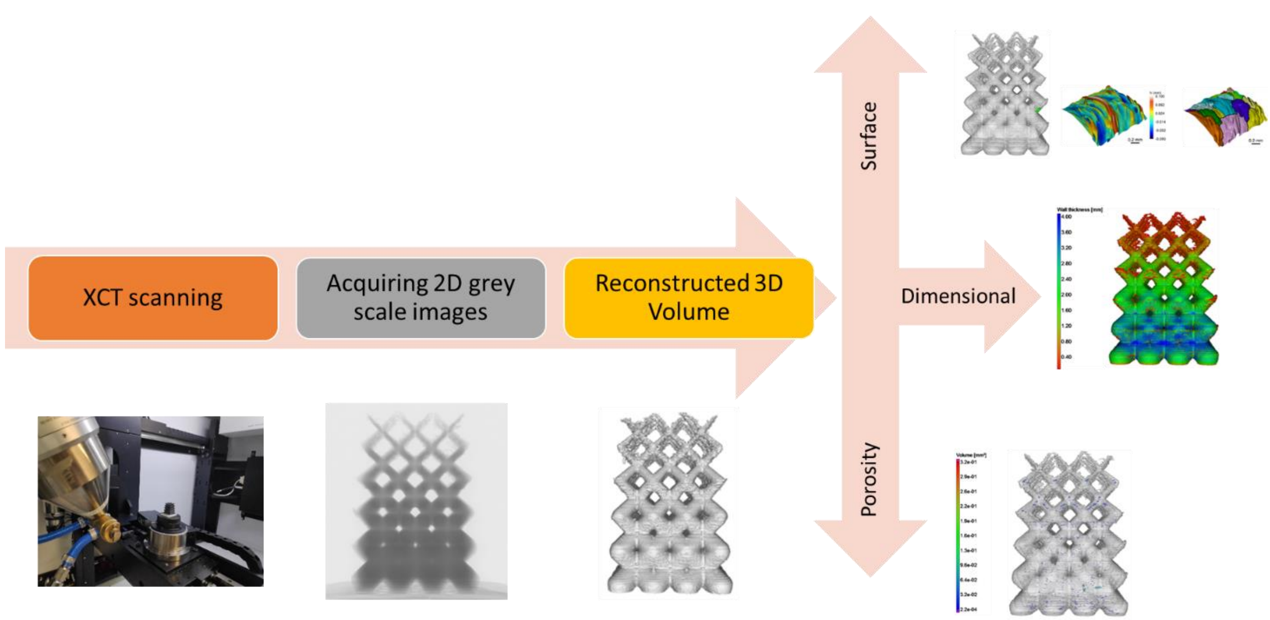

Figure 60: Conventional workflow for XCT and metrology of additive manufactured lattice structures.

b) *XCT hardware and interaction with matter*

As mentioned above, the X-rays are emitted from the X-ray source in a cone beam method followed by a 2D detector behind the part or fan beam emission followed by a 1D line detector behind the part of interest depending on the chosen setup as seen in Figure 61.

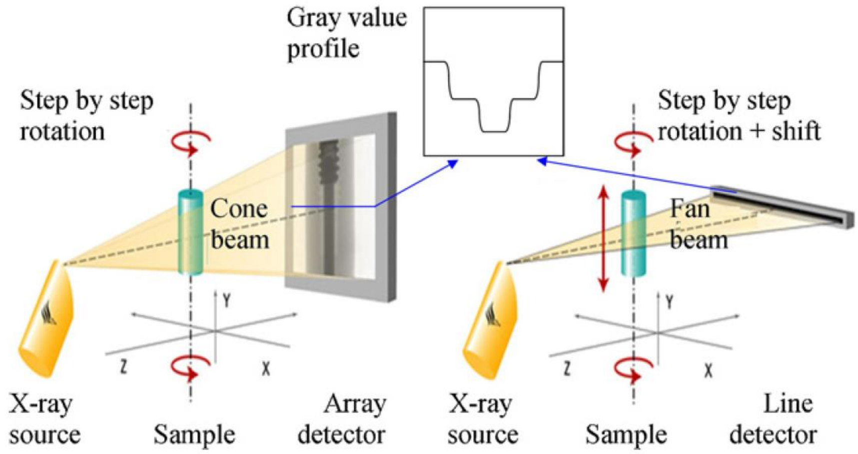

Figure 61: On the left of the image the cone beam and on the right the 1D line detector [231]

The interaction of X-ray with an object leads to the decrease of X-ray intensity due to the attenuation mechanism. The attenuation is caused by four main parameters that govern the X-ray and matter interaction which include the photoelectric effect, Compton scattering, Rayleigh/Thomson scattering and pair production [248]. The photoelectric effect, discovered by Albert Einstein in 1905 [249], is when the incident photon is absorbed with a relationship that is proportional to the atomic number Z of the irradiated material and the photon energy. During this phenomenon, the photon of an X-ray would collide and get absorbed by the inner shell electron. The incident photon energy would be equal or greater than the biding energy of the electron in the shell resulting to removing it from its shell. The electron that escaped from the orbit gets replaced by an electron from the outer shell which creates a new photon going in a different direction as seen in Figure 62 (a).

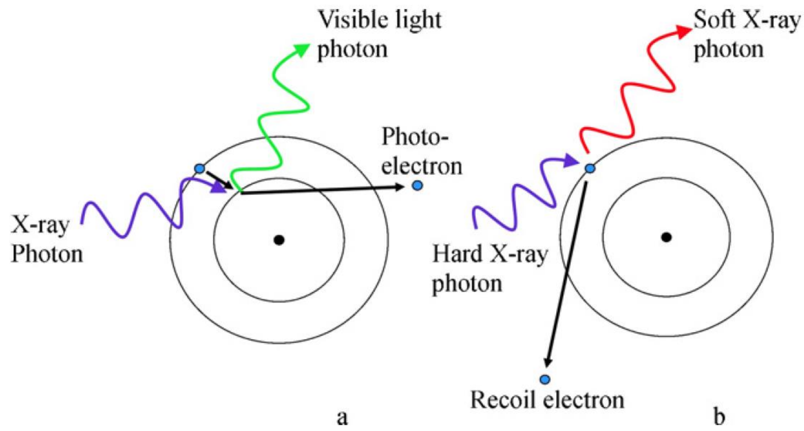

Figure 62:Photoelectric absorption (a) and Compton scattering (b) [231].

In addition to the photoelectric absorption, the other effect happening in power range of 20-450 kV (usual range of industrial XCT) is the Compton scattering seen in Figure 62 (b). In this case, the incoming photon would interact with an outer or free electron leading to its ejection. This results in the X-ray photon to be deflected to another direction with an energy loss gained by the electron [231]. If scatter miss the workpiece, photons are eventually deviated by the environment leading to a high background signal in the projections and in general loss of contrast [249]. An example of ideal situation versus real situation can be seen in Figure 63.

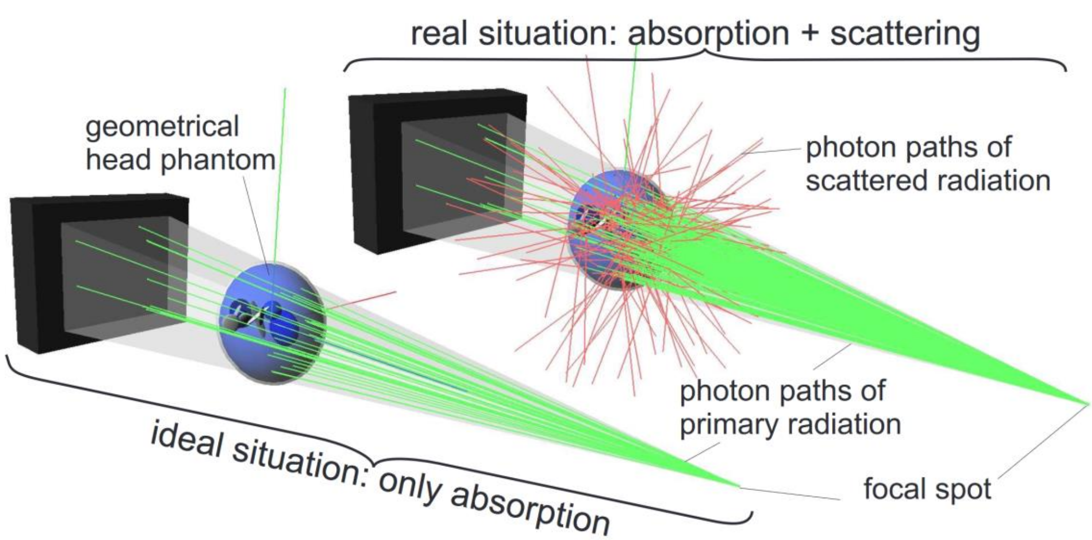

Figure 63: Ideal situation where photons are either absorbed or passing the sample (left), real situation with large amount of scattering affecting the attenuation results (right) [250].

However, scattering is not always onward. A higher probability of backscattering or ghosting on the detector happens in the case of low energy photons. The Compton effect is named after Professor Arthur Holly Compton (1892-1962) who won the Nobel prize award for is Compton effect discovery in 1927 [251].

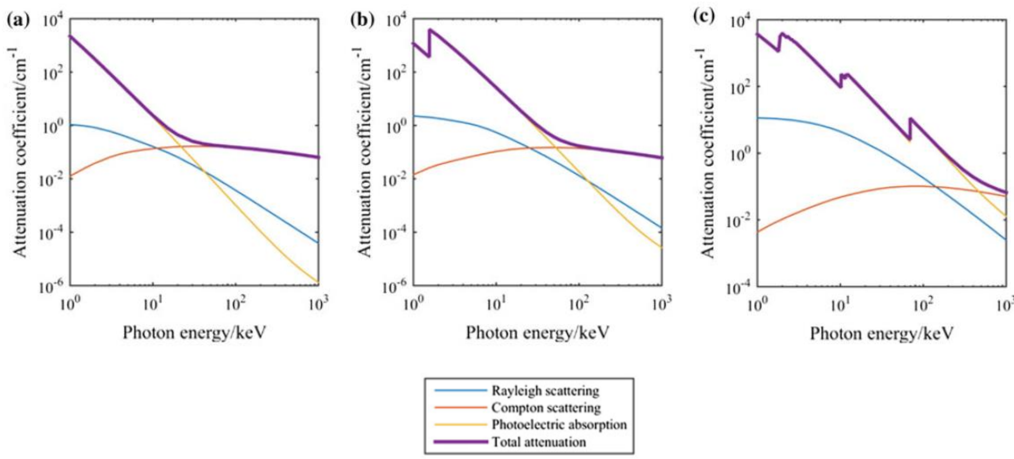

Figure 64: Three main types of attenuation and their total value for (a) carbon, (b) aluminium and (c) tungsten in relation to photon energy based [245]

Rayleigh scattering or Thompson scattering happens in cases of lower incident photon energy. The incident photon energy is not enough to liberate the electron from its bound. The low energy needed for this type of scattering means there are less chances of it happening in a typical XCT operation. The last form of attenuation is pair production (PP). This phenomenon is like the photoelectric in the sense that the incident photon is fully absorbed and attenuated [252]. However, the incident photon colludes with the strong nucleus energy field, called the Coulomb field, leading to a change of state. This change of state leads a transformation into two particles, one electron and one positron hence the pair production name. The emerged positron and electron would annihilate each other and two gamma photons get created and either scattered or absorbed by nucleus [249,253].

By adding up the four types of attenuations described above, the total attenuation μ parameter of the X-rays passing through the part of interest as seen in the equation (5) below where μ_{pe} refers to the photoelectric effect attenuation, μ_{compt} to the Compton effect attenuation, μ_{ray} to the Rayleigh effect attenuation and μ_{pp} pair production attenuation.

$$\mu = \mu_{pe} + \mu_{compt} + \mu_{ray} + \mu_{pp} \tag{5}$$

The challenging aspect in the XCT attenuation is how the latter is composed of multiple nonlinear attenuation effects. This is because the determination of the type of attenuation with the highest impact depends on the X-rays energy and the irradiated material's properties. As mentioned by Hermanek et al. in the principles of "X-ray Computed Tomography" chapter [245], and when comparing for example carbon, aluminium and tungsten, as seen in Figure 64, carbon has an atomic number of Z = 6 and its Compton scattering becomes dominant after 25 keV while aluminium which has a an atomic number of Z = 13 had its Compton scattering dominant from 50 keV. However, for tungsten, which has an atomic number Z = 74 has its photoelectric attenuation dominant for a wider range of energies compared to the other two materials. The pair production type of attenuation mentioned above is not usually included since most industrial application are below 1 meV so its contribution is usually considered negligible [245].

After calculating the total approximative attenuation of a material and knowing the material thickness to be penetrated by X-rays, Beer-lambert law equations (6) and (7) seen below before and after differentiation, can be used. Beer-lambert law governs exponential relationship between the X-ray intensity I, and the total attenuation coefficient μ obtained by the sum of different attenuations shown above and the distance travelled or thickness of the material x. Another challenge from using this equation is the usual assumption of the homogeneity of the material to be XCT scanned. Another assumption is considering the X-ray beam to be monochromatic, which is not the case in industrial XCT machines. Adequate additions can be done on the equation to take in consideration the material variability and polychromatic nature of X-rays shown in [245].

$$\frac{dI}{I(x)} = -\mu dx \tag{6}$$

$$I(x) = I_0 e^{-\mu x} \tag{7}$$

c) 2D projections and reconstruction.

As seen in Figure 61, X-ray photons would pass from the material, get attenuated following the description mentioned above and gets captured by the detector. The flat panel detectors manage to convert x-rays to measurable photons of light proportional to the sent X-ray energy using scintillation, which are then converted to electrical signals using a photon detector like a photomultiplier tube [231]. Multiple parameters can affect the detector data quality like its energy resolution, which is the capability of the detector to resolve the incoming radiation energy or afterglow, which is how persistent the image would stay after turning off the X-ray radiation potentially causing motion blur [254]. An example can be seen in Figure 30 where increased scan time resulted in improved scan quality [255]. The collected data from the detector get processed and result in a 2D image representation in a spatial location domain compared to MRI which would process data into spatial frequency domain [256]. The spatial location domain in this case is a representation where columns and rows represent different pixels with different bit value depending on the X-ray energy reached.

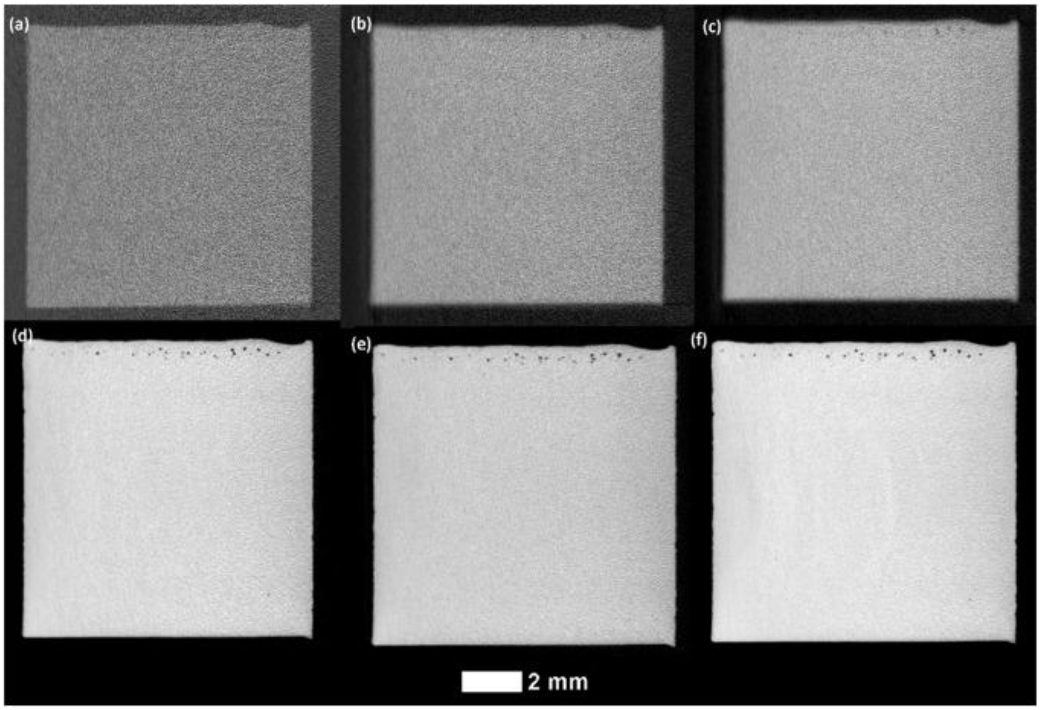

Figure 65: Example of increasing scan quality by increasing scan time where (a) is 3min, (b) 20min, (c) 45min, (d) 2h, (e) 3 hr and (f) 4hs [255].

Usually, the smaller the pixel size, the smaller and better spatial resolution. Also, the bit depth of the pixel plays a role in data accuracy. Bit depth is the range or number of grey levels that can be assigned to each pixel as an exponent of 2. For example, the values of the detector pixels used in this PhD experiments were ranging from 0, which is tending to low intensity X-rays meaning higher attenuation to a value of 65536 which refers to higher X-ray intensity meaning low attenuation before reaching the detector. The range was from 0 to 65536 since the pixel bit depth was 2^{16}. Higher bit depth means that the pixel values have a higher range making it possible to have higher contrast images.

After obtaining a set of 2D projections after performing an XCT operation, different filtering or image correction techniques can be used like denoising or edge enhancement [257]. These operations however have to be done carefully as it risks masking important data or creating new artefacts non-existent in the original part. Once the 2D projections are ready, a reconstruction algorithm is applied in order to obtain the 3D volume which consists of voxels [258], which are a volumetric 3D equivalent of 2D pixels. Many image reconstruction algorithms exist however the usual and most commonly used reconstruction algorithm is the filtered back projection (FBP) [259].

d) *Volume thresholding and analysis*

After obtaining a 3D volume following a reconstruction algorithm on the 2D obtained XCT images, a thresholding or segmentation of the 3D volume is needed. Segmentation has a crucial influence and can be affected by the quality of the input data where an example of this operation can be seen in Figure 66.

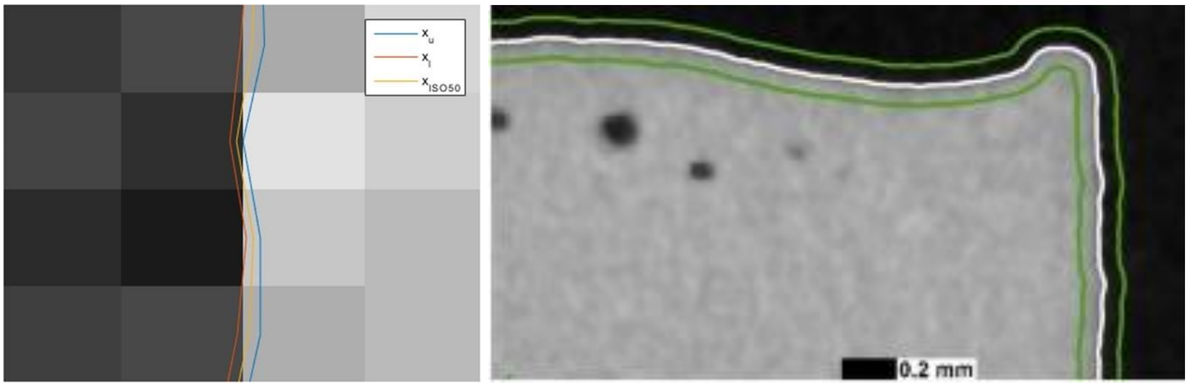

Figure 66: Comparison between ISO50 and two other reconstruction algorithms (left)[260] and example of near surface ROI that can be used for increased measurement accuracy (right) [255].

Different segmentation techniques are available and are usually facing the main challenge of either over or under segmentation leading to less or extra material at the edges of the XCT scanned part. The two main segmentation methods can be split to either a global one or a local one. In a global segmentation technique, an algorithm like Otsu method or ISO50 can be used to determine the single threshold value that will segment the part using the two peaks of the histogram. While both methods are based on selecting a single threshold value from the histogram, the Otsu method tries to maximise the separability of grey value classes [261] while the ISO 50 method algorithm calculates the exact middle between the two histogram peaks [108].

The second type of segmentation is the local method where instead of choosing one threshold value for the whole image or volume from the histogram, the threshold value is optimised for each voxel depending on the surrounding voxel values and starting from an ISO 50 [86] or user defined contour. This method is extremely important in cases where the material of the scanned part is not dense or homogeneous especially when it comes to surface roughness analysis [262]. Example of comparison between standard ISO 50 surface determination and local iterative surface determination can be seen in Figure 67. Local iterative surface determination starts from an initial baseline contour that can be defined from an ISO 50 surface. The algorithm places hair lines that have a default spacing of 4 voxels and are perpendicular to the baseline isovalue surface. Along those hairlines, the algorithm searches for the location of the largest gradient between the individual gray values. This results in a subvoxel precise surface line as the position of the largest gradient is interpolated between the individual positions along the surface. This also means that the same grey value can be interpreted differently depending on the surrounding voxels [263].

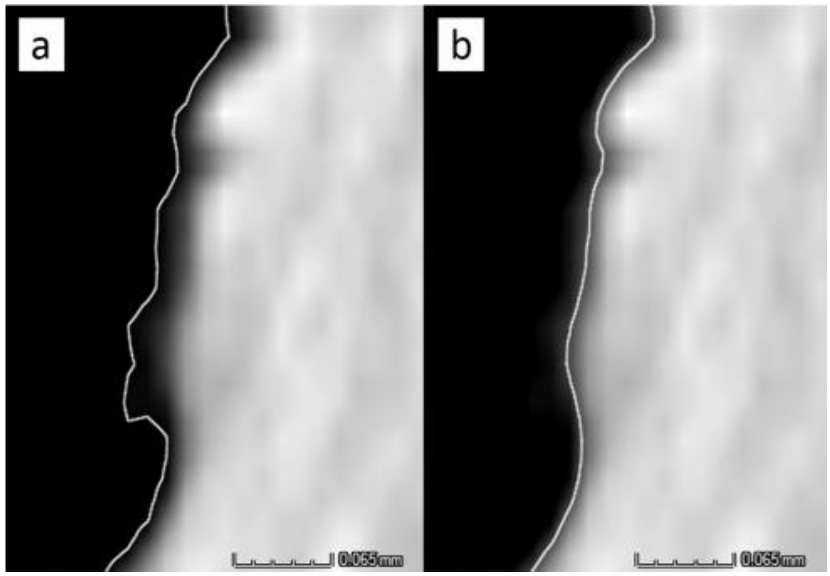

Figure 67: Comparison of standard surface determination (a) and local iterative surface determination (b) [264].

e) XCT scanning process artefacts

Different scanning parameters, scanning strategies or part orientation/geometry can affect the results and sometimes result in artefacts which are discrepancies in the obtained data that do not exist in the original part. A common example of XCT artefacts are beam hardening artefacts [265]. As mentioned above, most industrial XCT machines have a broad energy spectrum and are unfortunately polychromatic [266]. This means that when choosing an unfiltered X-ray energy, the low energy levels (soft) are easily attenuated by matter compared to high energy (hard) ones. As the soft rays do not contribute to the detected signal, the X-ray beam mean energy that passes through the matter is increased (hardened). This can lead to what is referred to as cupping artefact, causing brighter edges than the centre [249]. This artefact can affect the results of for example dimensional analysis done on the volume since a significant proportion of it can affect the grey values of the part edges and therefore the surface determination operation.

Another type of artefact is the scatter artefact [267]. Scatter can be caused by the part, for example from the Compton scattering phenomenon mentioned above or even from the environment inside the machine. The latter can be due to cone beam generated photons not directly touching part and getting deviated by other parts in the machine environment. Scatter usually leads to increased signal captured by the detector leading to unwanted artefacts that can significantly affect the contrast of the obtained results [268]. Ring artefacts can also appear and can be due to detector defects or miscalibration. Ring artefacts [269] usually get more significant toward the centre of the part. Other sources of error include noise [270] or in most cases XCT user experience as discussed more below.

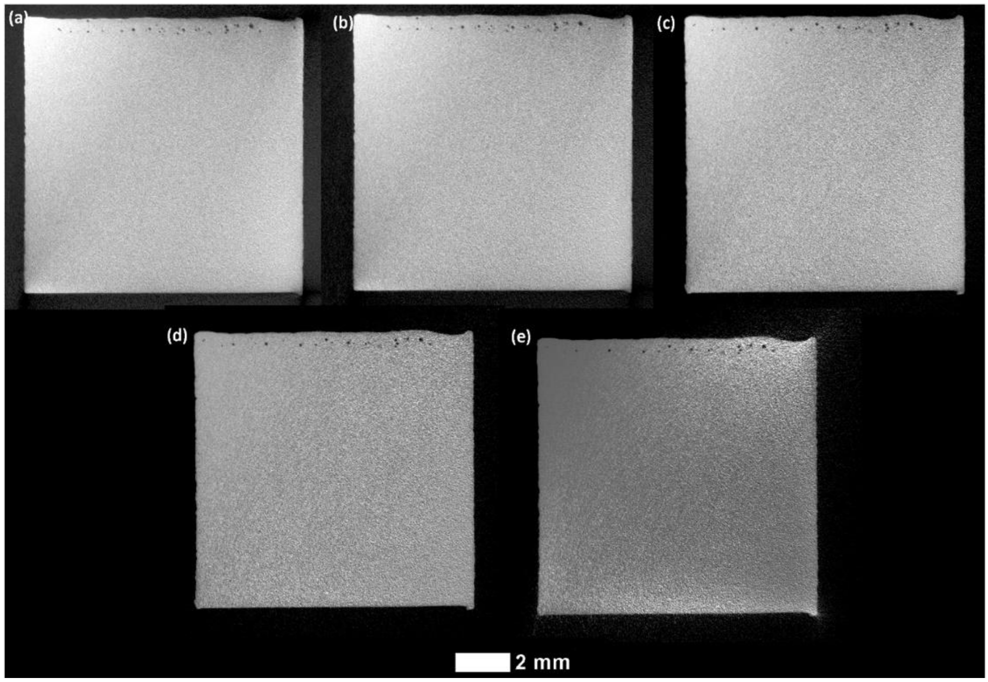

Figure 68: XCT cross section slices showing the impact of varying beam hardening correction factors on the resulting image where (a) is 0, (b) 5, (c) 8, (d) 9.0 and (e) 9.5 [255].

f) Challenge of choosing XCT settings

XCT settings are usually chosen by the user, leading to possible discrepancies [271]. Also, current users cannot usually provide an uncertainty statement [272] due to the lack of holistic models correlating the effects of different parameters on measurement uncertainty [231]. Different XCT scan settings can lead to different scan results like the blurring on the scanned lattice struts seen in Figure 69 due to different voxel sizes [273].

For example, expert users of XCT can usually limit the range of settings to be used on a part with unknown internal features. This is usually done from experience and the usual guidelines provided by the machine manufacturer manual. However, it is usually not possible to decide on the exact setting from the drawn range made by the user since it is difficult to decipher the small subtle changes between them manually.

The main initial solution is to train users for XCT as expert users have been shown to provide better results compared to non-trained ones [271]. The usual solution to tackle this challenge is to use quantitative tools like image analysis ideally before the scanning process. A semiempirical method suggested in literature is the knowledge-based system (KBS). The method relies on using previous knowledge on previously scanned parts to optimise the settings for new parts that have similar features. The study showed better result in comparison to relying only on user experience [271].

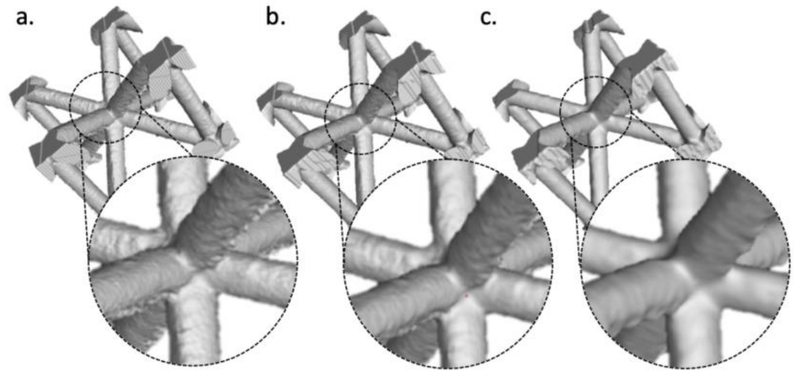

Figure 69: Blurring or smoothening effect of lattice structures when measured using XCT at different voxel sizes, 38 µm (a) 58 µm (b) and 101 µm (c)[273].

Another technique is to use XCT simulation software like aRTist. The software is based on primary attenuation law and Monte Carlo model for scatted radiation[274] and simulates different XCT settings and part orientations to optimise and choose setting that delivers the minimum artefacts like ring artefacts or beam hardening, all leading to a better scan quality[275–277].

Image analysis can also be used in multiple ways to compare different XCT scans and optimise towards ideal settings. Contrast to noise ratio (CNR) is one of the most common equations in this discipline [255,274,275]. The CNR equation (8) shown below is composed of two parameters, the mean grey value μ_{1-2} and the standard deviation value σ_{1-2}, for number one meaning the foreground and two meaning the background. This equation is also employed when using a scanning electron microscope (SEM) [278] or in the medical field [279]. This equation can be used on a pre-scan image or post scan reconstructed image.

This can be considered a semi-automatic operation since it can be applied on multiple images all at once with detailed exported automated reports, the user however is still needed to choose the initial region of interest from which the parameters will be extracted unless extracted automatically from histogram peaks as suggested Reiter.M et al. in literature[277]. Equations like CNR and signal to noise ratio (SNR) have been used in literature to quantitively compare different XCT settings before scanning to rank different XCT settings. Another method is used by focus measurement in focus variation (FV) microscopy using standard deviation affected in this case also affected by image contrast [280].

$$CNR = \frac{Contrast}{Noise} = \frac{|\mu_1 - \mu_2|}{\sqrt{\sigma_1^2 + \sigma_2^2}} \tag{8}$$

4.3. Design for XCT metrology

As mentioned above, X-rays emitted from the X-ray source are attenuated by the scanned part allowing the detector to capture different absorption values. Along these lines it can be clear how one of the initial limitations of using XCT is the combination of the material and thickness of the part to be measured [231]. XCT can easily penetrate polymers and relatively good aluminium material, however, denser materials like ceramic, steel, titanium, tungsten, or zinc become very challenging as can be seen in Table 3. Using higher voltage is not always an option since the latter can create broader X-ray spectrum leading to beam hardening artefacts or in another scenario the pixel detector can be saturated and create unwanted measurement artifacts [281].

This challenge should be considered when designing for AM and can be introduced in the DfAM workflow where design engineers decide beforehand on the method of the measurement and optimise the part shape for it. The AM design freedom can allow for such adaptation where specific features can for example be added to the AM part with the main objective as being used as a guide during XCT measurements as previously researched and published in literature [282].

Table 3: Typical values of thicknesses that can be penetrated for a certain voltage and material [221,267].

X-ray voltage	130 kV	150 kV	190 kV	225 kV	450 kV
Steel/ceramic	5 mm	<8 mm	<25 mm	<40 mm	<70 mm
Aluminum	<30 mm	<50 mm	<90 mm	<150 mm	<250 mm
Plastic	<90 mm	<130 mm	<200 mm	<250 mm	<450 mm

On some occasions, the part to be XCT scanned can have a steep variable thickness gradient which create an additional challenge even if all thicknesses in the part are penetrable. One of the reasons of this challenge is the polychromatic nature of XCT that makes the absorption non-linear [281]. This means that while “hard” X-rays are attenuated by all features in the part to be scanned, thinner features of the part will absorb additional “soft” X-rays making the results looks as if the thin features are less dense creating severe beam hardening issues. Since usually only one XCT setting is chosen prior to the scanning process, scanning a thin layer of a material will mean that in some specific angles of the part rotation in the XCT machine thick features will be non-penetrable. Design engineers developing parts to be XCT scanned will have to try and have a smooth thickness transition alongside the whole part, avoiding scenarios and shapes like shown in Figure 70.

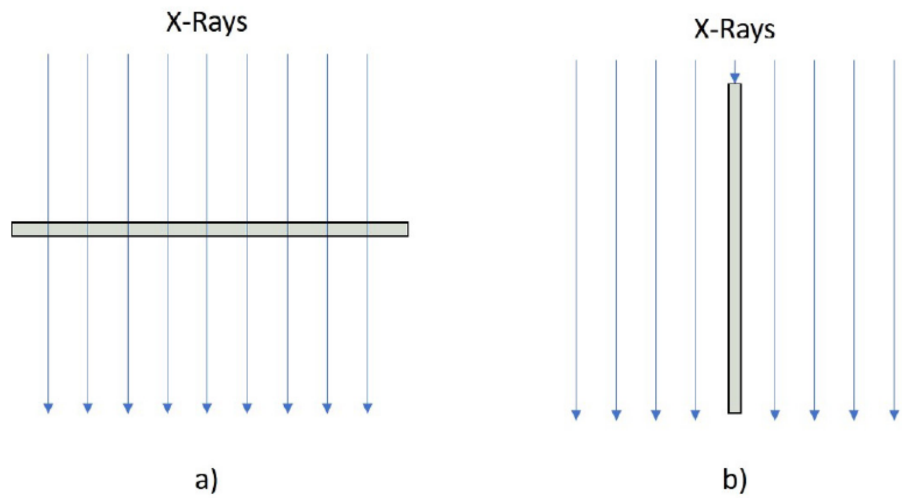

Figure 70:a) X-rays pass through the whole part while in b) only few X-rays have managed to pass due to the thick part [281].

4.4. XCT dimensional metrology

In dimensional metrology, XCT has been the go-to tool when facing internal features that could not be accessed any other way. The CMM can only measure outer features and sometimes distort them due to the stresses exerted by its probe [283,284]. The XCT on the other hand, is non-contact and can measure multiple external and internal dimensions in a time that is independent on the number of features to be measured [285,286].

Applications include in the automotive where the internal features of a car oil manifold can be dimensionally evaluated, measurement can include not only feature measurement but also constraints like position and straightness [231]. In other occasions, XCT generated model from the manufactured part can be aligned and evaluated against the original CAD using a deviation analysis[287] showing exactly where excess or less material is in the part.

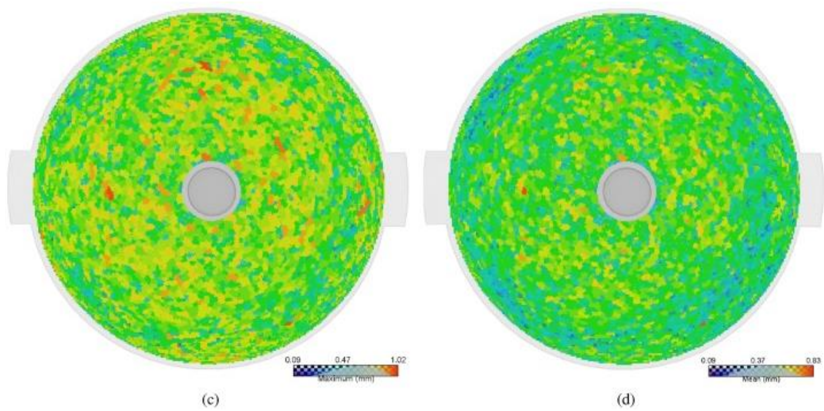

Figure 71: Image processing from XCT data showing local thickness distribution (a) and (b) as well as maximum and mean value of local thickness at each point of the pore analysis [94]

For lattices and in the medical field, XCT has been used to examine dimensionally a hip prosthesis cup as seen in Figure 71. The pore and strut thickness distribution has been evaluated against author set tolerance limits [94]. The analysis in this case has been done using image analysis implemented by software like ImageJ [288]. The analysis relied on local thickness algorithm [289] which uses binarised images and fits the largest sphere that can fit inside the object as seen in Figure 72. Other methods using the same principal have also been developed, fitting multiple circles on a lattice strut geometry [200]. Alternatively, the area and volume of a produced AM lattice structure can be compared with the original CAD[290,291] allowing for drawing correlations between the different measured instances and produced defects.

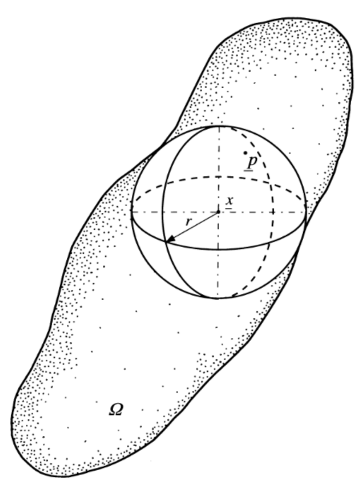

Figure 72: Local thickness determined by maximum sphere diameter fitting[289]

The mentioned techniques can be extremely beneficial and provide more details compared to using traditional contact measurement. Vernier callipers or optical microscopes can be used to dimensionally evaluate a produced lattice[198], the results however are local and from external struts and henceforth cannot be compared to the more holistic results produced using an XCT. For example, the relation between thickness distribution to orientation can be analysed using XCT data as seen in Figure 73, assisting in future lattice designs or production settings [200].

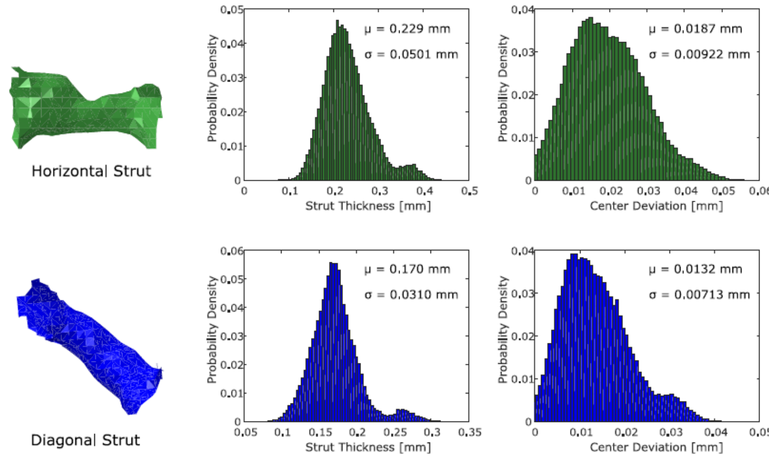

Figure 73: Distribution of strut thickness to orientation of an XCT measured lattice structure [200].

The methods mentioned above do quantify the produced lattice either using image analysis or XCT to know the distribution of many parameters like strut diameter. However, with these methods, it is not always clear where exactly the produced part does not match the original design. To tackle this challenge, it is common practice to do a deviation analysis [292–294].

In order to complete, an XCT of the produced AM lattice, align it with the design of the original AM lattice and then perform a deviation analysis. An example can be seen from literature in Figure 74. The results from this study performed by Yan et al. showed an average deviation of +0.1702/-0.1491 mm for the lattice shown in Figure 74 (a) and an average deviation of +0.1588/-0.1655 m in the lattice shown in Figure 74 (b). Both lattices had the same Gyroid TPMS and volume fraction of 7.5% with however a different unit cell size of 4mm and 7mm. The results showed good AM process printing fidelity and the deviation differences were attributed to corrugations and roughness of the surface of the lattice struts [292].

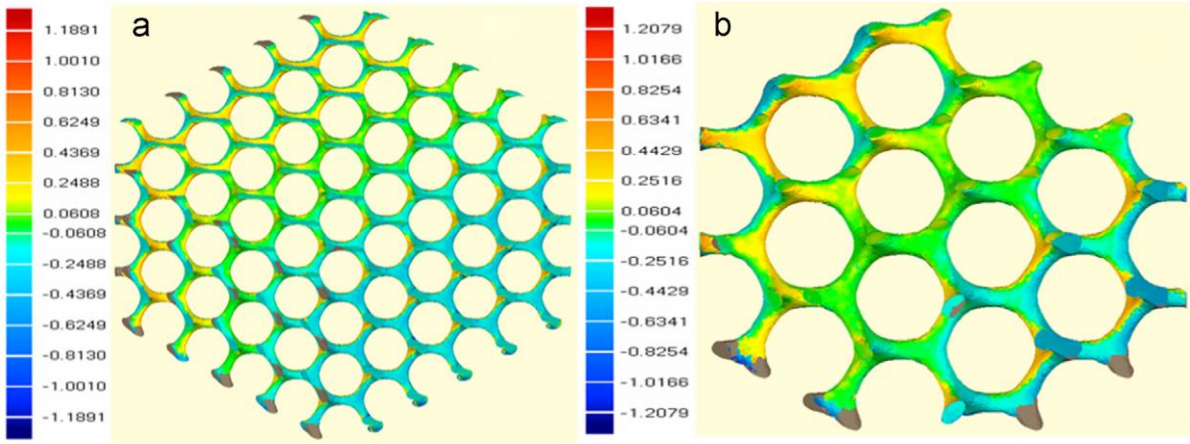

Figure 74:Deviation analysis of a Gyroid TPMS with a fixed volume fraction of 7.5% and unit size of 4mm in (a) and 7mm in (b) [292].

The deviations of lattices, as seen in Figure 75 are usually angle dependent (angle between the strut and AM machine build plate). For example, it is documented how horizontal struts usually have higher deviation where struts are more elliptical than circular, due to their higher overhang that makes them more exposed to surrounding powder and local heat accumulating from the melt pool, causing the loose powder in contact to partially melt and get attached to the lattice strut (Figure 46), causing a dross formation and oversizing [131,290,295–298].

When a significant increase of this sorts happens during the AM process to a strut diameter, it usually increases the chances of a possible decrease in porosity [295]. This correlation has led other researchers like Zhang et al. observing how the deviation of the produced AM lattice to the original CAD is dependent to which type of strut is dominant, if there are more vertical struts, the produced AM lattice is usually undersized with a lower volume fraction percentage and vice versa if the horizontal struts are dominant [299]. While most of the above studies are related to strut based lattice structures, angle dependant deviations have also been observed in TPMS type lattices [131].

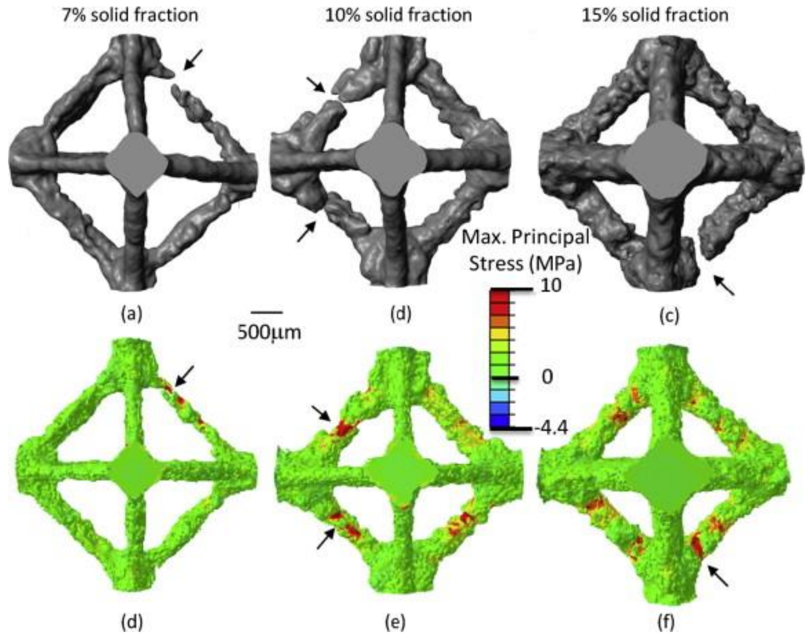

Figure 75: Comparison between the real failure sites (a,d,c) and FEA predicted failure sites (d,e,f) at different solid fractions (7%, 10% and 15%) [300].

The angle of shell structures that were vertical were undersized compared to shell structures that were horizontal to the AM process build plate, shell structures that were at a 45° degrees angle had closer average thickness values to the original CAD design [131]. Also, and along the lines of the literature above, TPMS lattices with larger shells and higher surface of overhangs ultimately have more oversizing [131] due to overhangs being exposed to the heat transfer and build plate powder. Another reason is how most lattices do not need supports, which has good advantages like saving printing times and post processing cost of removing them but these supports could have been the one exposed to heat transfer and print bed powder instead of the overhangs[131].

These differences usually mean that applying finite element simulations on the original perfect CAD will not deliver accurate results since the printed AM lattices has local or global deviations. A solution from literature can be to apply FEA or CFD on the volume design obtained from the XCT of the produced AM lattice. As performed by Sercombe et al., it was possible to predict using FEA on the XCT of the produced AM lattice the location of the failure location [300]. While the mentioned changes were mostly about the strut deviations dimensional deviation in lattices also happen in the node location or the connection point of the lattice where struts meet

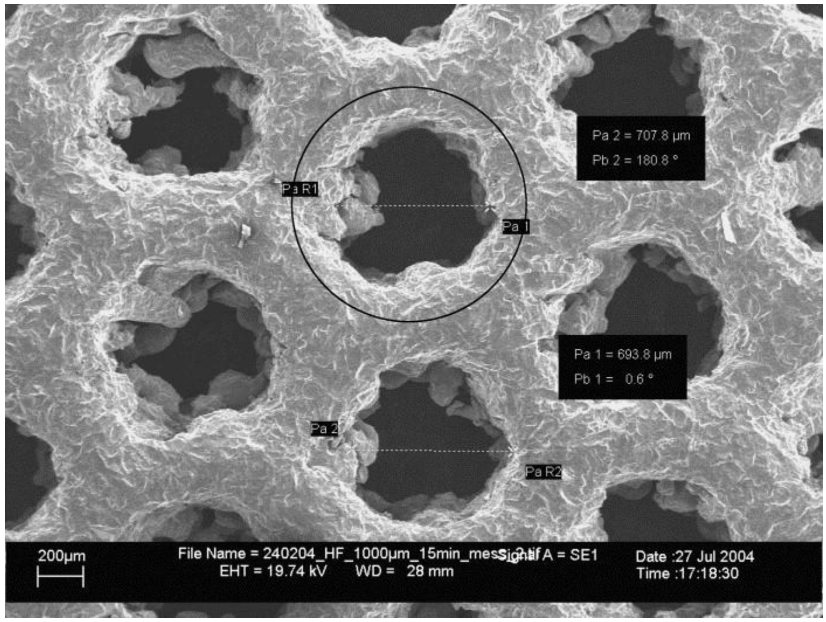

Figure 76: SEM of the additive manufactured lattice using LPBF process called Direct laser forming (DLF). The original CAD had designed pore of 1000 μm but the SEM show manufactured pore of around 700 μm [301].

Along these lines and from literature, TPMS lattices usually have smoother nodes with less deviations compared to strut based lattices [130] creating less stress concentration points. Finally, another parameter where dimensional deviation is present is in the designed porosity, which means the gaps or pores that are present in the original CAD of the lattices compared to unwanted porosity which is usually present inside the lattice and will not be covered thoroughly in this thesis, more information about it can be found in Echeta et al. review of usual AM defects [199]. The designed pores of AM lattices produced using LPBF process usually suffer from dimensional deviation making them smaller than designed. For example, in Hollander et al. study [301], a lattice was designed with pore of 1000 µm but when produced, had pores of approximately 700 µm as seen in Figure 76. While SEM was used in the previous study, it is only possible to use when the feature to be measured, designed pores in this case, are in direct line of sight or otherwise a sectioning will be required. To have a holistic measurement of all designed pores an XCT can be used as done by Lin et al. who also observed smaller designed pores when additive manufactured compared to the original CAD pore [302] due to excessive sintering of the used Ti-6Al-4V powder during the LPBF process of the lattices. This difference between designed and printed pore can be detrimental to the function of the part especially for example implants of which pores are important to reduce the stress shielding effect and also increase chances of osseointegration [167].

4.5. XCT surface metrology

The surface roughness of additive manufactured components is often considered challenging to measure when compared to conventional manufacturing surfaces like machined ones. This challenge is due to the usual increased AM surface irregularity and complex surface features like re-entrant ones [303] as seen in Figure 77. Surface characteristics unique to AM process can include Unmelted powder, spatter, balling formation and more [85]. The challenging surfaces meant an increase usage in literature of areal surface measurement compared to profile ones for evaluating AM surfaces in literature [85]. The increased use of areal surface roughness measurement is necessary for a holistic understanding of an AM surface since a profile measurement could be missing valuable information on the homogeneity of the surface and repeatability across the part.

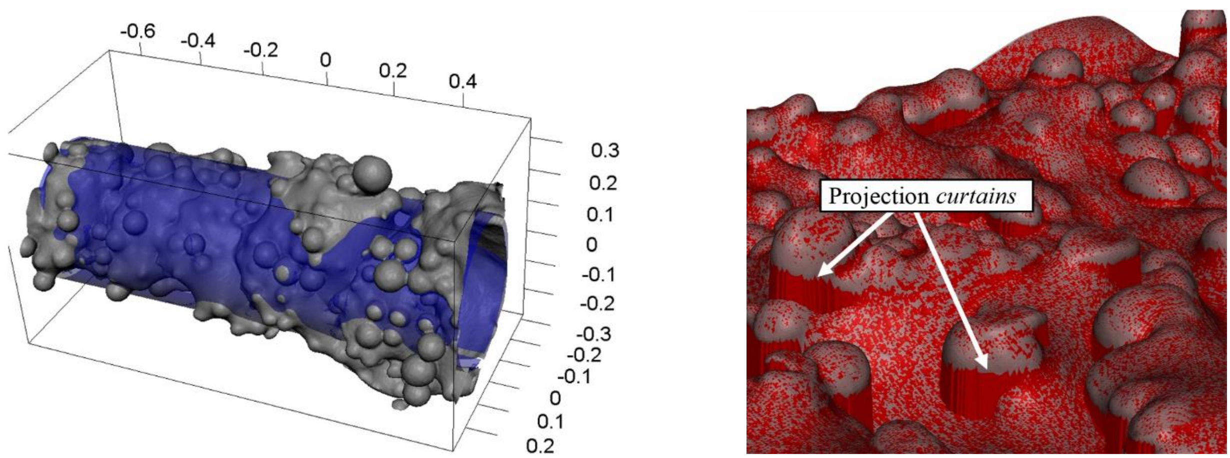

Figure 77: Isolated lattice strut used for surface analysis (left), Unwrapped lattice which shows the curtains caused by projecting the features on the grid plane [303].

While areal surface roughness of AM parts is usually measured using focus variation or confocal microscopy, the increasingly challenging designs produced in AM means that these instruments are not always possible to use. In the recent years, XCT use in measuring surface roughness has been heavily explored in literature. The use of XCT in the process of analysing surface roughness is highly applicable for AM lattices since conventional line of sigh instruments are simply impossible to use, especially in cases of inaccessible internal features. In fact, the first research related to using XCT to extract surface data was applied on AM lattice structures as shown in the following paragraphs.

The timeline of analysing surface roughness of lattices starts by the use of conventional methods to analyse lattice structures surface roughness by Pyka et al. study published in 2012 [79]. The method started by embedding the porous structure in epoxy resin to be later grinded and polished, resulting in a cross section that is along the longitudinal axis of the lattice strut as seen in Figure 78. The grinded and polished lattice strut was then imaged using a digital camera coupled to an optical microscope. Image analysis tools developed by the author were later used to extract the profile surface roughness measurements.

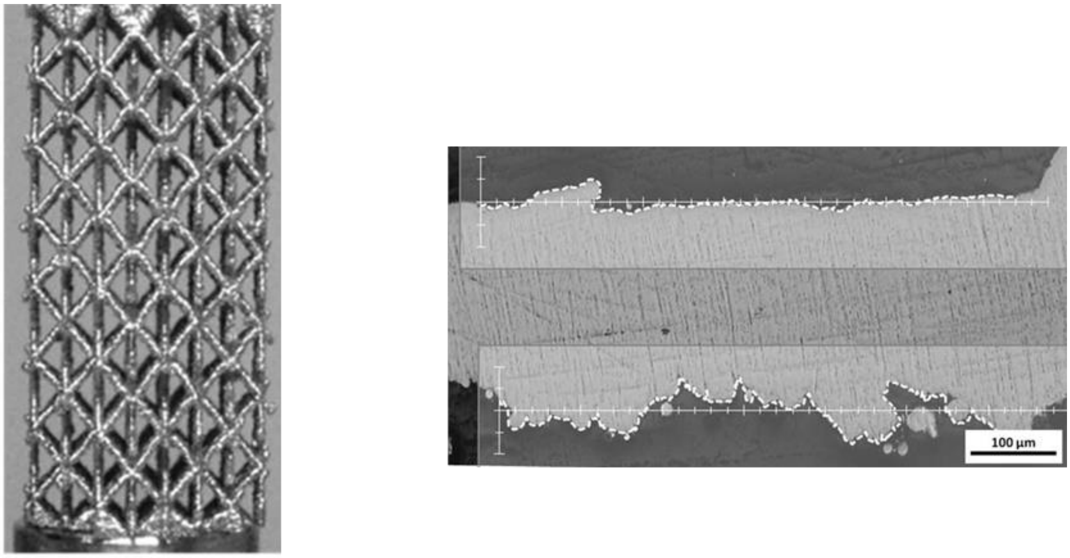

Figure 78: Porous AM lattice structure (left), grinded and polished lattice strut (right) [79].

To analyse the surface roughness of lattice structures non-destructively, the author Pyka et al. in 2010 [304] and Kerckhofs et al. published a study in 2013 where micro x-ray computed tomography (micro-CT) was used to analyse both outer and internal struts [106]. The obtained and thresholded volume data of the scanned lattice was used to extract a 2D cross sectional image passing through the lattice strut. The lattice strut 2D image would be binarized and ideal profile thickness drawn, followed by an image analysis tool that extracts the strut profile, as seen in Figure 79. The extracted profile lines were then used to calculate the arithmetic mean deviation from the mean profile resulting in a profile surface roughness measurement. While the method was limited to profile measurement, it delivered a better non-destructive method than its predecessor and was the first to use XCT for a profile surface measurement, highlighting the challenges associated with the process like voxel size and more. Findings of the paper also included that un-melted surface powder and homogeneity affecting the surface and needing post processing methods like chemical etching (CH). For example, the lattice can be immersed for 10 min in hydrofluoric solution to remove stuck un-melted powder [106]. The post process can be followed by electro-chemical polishing (EP) to obtain a homogenous surface roughness from top to bottom as seen in Figure 79.

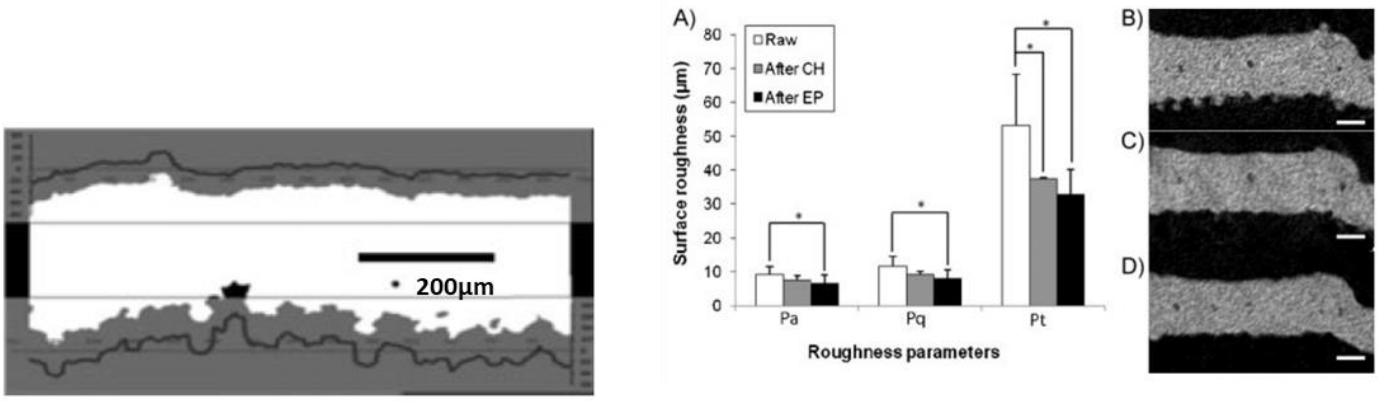

Figure 79: The use of micro-CT to extract and analyse profile surface measurement of a lattice strut [106].

Moving from surface profile measurement using XCT, the first study to extract areal surface measurement using XCT data was published by Townsend et al. in 2017 [264]. The extracted areal parameters were per ISO 25178-2:2012 and applied on an additive manufactured cube sample. The method started by performing an XCT scan on both the AM cube and a machined dimensional artefact of the same material. A CNC machined dimensional artefact was used for surface determination [305] compensation as well as scaling error correction. The resulting data from the novel areal surface roughness extraction method using XCT volume data was remarkably similar to results obtained using conventional focus variation microscope instrument [305]. For example, the Sa value obtained from XCT volume data was 29.6 µm (sample standard deviation less than 0.013 µm) while the focus variation measurement done using Alicona G4 of the same surface was 30.8 µm (sample standard deviation of 0.006), a small difference of less than 2.5% between the two methods. For additional result validation, a round robin experiment was also performed using four different XCT systems which showed similar results of less than 0.5% from all XCT systems, further validating the developed method [86]. Also, and from the round robin experiment, differences between Sa obtained from XCT system (specifically one labelled MCTC) compared to focus variation measurement were again less than 0.5% [86] and can be seen side to side in Figure 80.

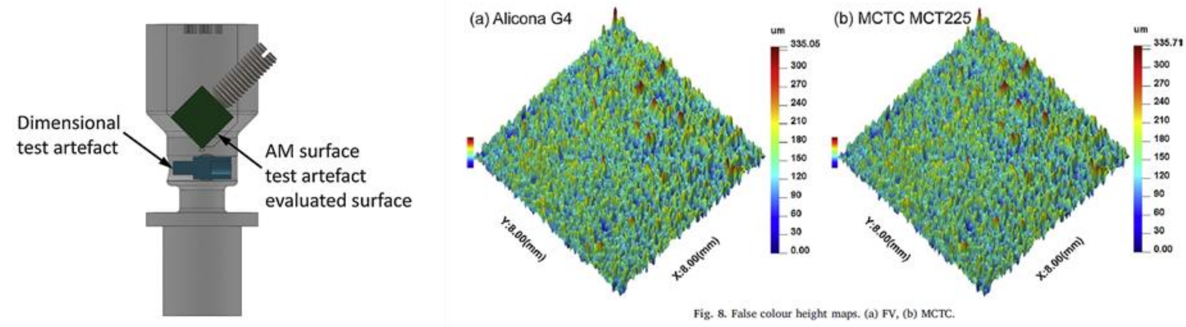

Figure 80: Measurement setup of AM surface and dimensional artefact (left) and comparison of XCT extracted surface data versus Alicona extracted surface data (right) [86] .

It is not always possible to use XCT for surface roughness measurements due to sample size limitation and other factors. Another limiting factor is the voxel size where for example, and from the round robin experiment mentioned above, the sample was progressively positioned further from the X-ray source with measurements taken at different voxel sizes to assess the influence of the latter. Initial results from the study showed for example that the voxel size to be used when extracting surface roughness using XCT should be less than one half of the Sa value to be measured [86]. Another factor affecting surface data extracted using XCT was the type of surface determination applied on the obtained volume. Comparison between multiple types of surface determination showed that the local iterative surface determination method was the most accurate when used to generate surface texture parameters [262].

Advances in the field of extracting surface texture data using XCT has prompted extensive literature in this field especially for AM surfaces. This is because AM surfaces are significant and easier to scan compared to smoother surfaces from CNC machining. A prominent one has been the comparison of XCT extracted areal surface texture and analysed parameters to other methods like confocal microscopy (CM), coherence scanning interferometry (CSI) and focus variation (FV) where confidence intervals were drawn providing further insight when choosing the ideal instrument [306]. Unfortunately, advances in areal surface data extraction and analysis using XCT has been limited to developing areal parameter for re-entrant features [303] as seen in Figure 77, however, all literature on surface roughness analysis for lattices has been done using profile measurements [37,106,199,203,221,307–311].

4.6. XCT Porosity

When it comes to lattice structures, pores can fall in two different categories, designed pores which are spacings between unit cells, or non-designed/unwanted pores (as seen in Figure 81) which are existing inside the solidified struts of the lattice and can negatively impact their fatigue life and other mechanical properties [312]. The designed porosity characteristic is unique to lattice structures and gives users the freedom to control the function of the lattice while non designed porosity is an undesirable result present in most AM parts where they become stress concentrations [313].

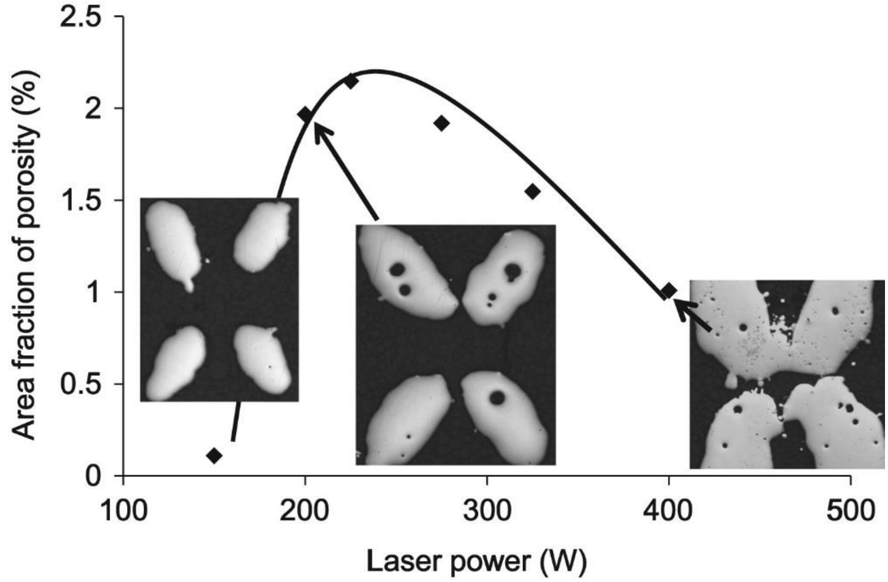

Figure 81: Variation of internal porosity within lattice struts as a function of laser power [210].

Conventional methods to assess porosity in produced AM parts include density based methods like Archimedes method, ultrasonic method [314], or microscopic analysis on part cross sections obtained after manual cutting of the part [315,316]. Archimedes method uses the principle of a part's buoyancy, which is the difference of a sample's weight in the air versus when submerged in water. The density of the sample ρ_{sample} can be first calculated using equation (9) where the mass of the sample in the air is M_a, the mass of the sample in the air is M_w and the density of water is ρ_{water} [89]. Upon calculation of the sample density ρ_{sample}, the latter can be used to calculate the sample porosity using the bulk material density using equation (10) [317].

$$\rho_{sample} = (\frac{M_a}{M_a - M_w})\rho_{water} \tag{9}$$

$$P = \left(1 - \frac{\rho_{sample}}{\rho_{bulk}}\right) \cdot 100\% \tag{10}$$

These methods have different drawbacks, for example when using the density based methods, only the overall pore percentage can be obtained without a detailed knowledge about the position and distribution of defects which has been proven to have a greater impact on an AM part fatigue life compared to only knowing the percentage or size of biggest pore [225]. Ultrasonic method can be relatively slow and also challenging to use when the goal is a 3D data extraction of the porosity especially in the case of inhomogeneous pore distribution making the obtained porosity inaccurate [318,319]. Furthermore, when using the microscopic analysis method, the cross-sectioning step increases chances and risk of affecting pores before measurement while also making the process time consuming and only providing information on one slice at a time.

Eventually, XCT has been a popular option used in literature for non-destructive measurement of porosity of AM parts [226,227,293,320]. Using XCT result in a holistic evaluation of the pore size, shape and distribution across the part as seen in Figure 82. These results can be used for a better understanding of the effect of different build parameters, as well as to develop a model that is simulating and predicting the fracture location of different kind of AM process pore defects as seen in [227].

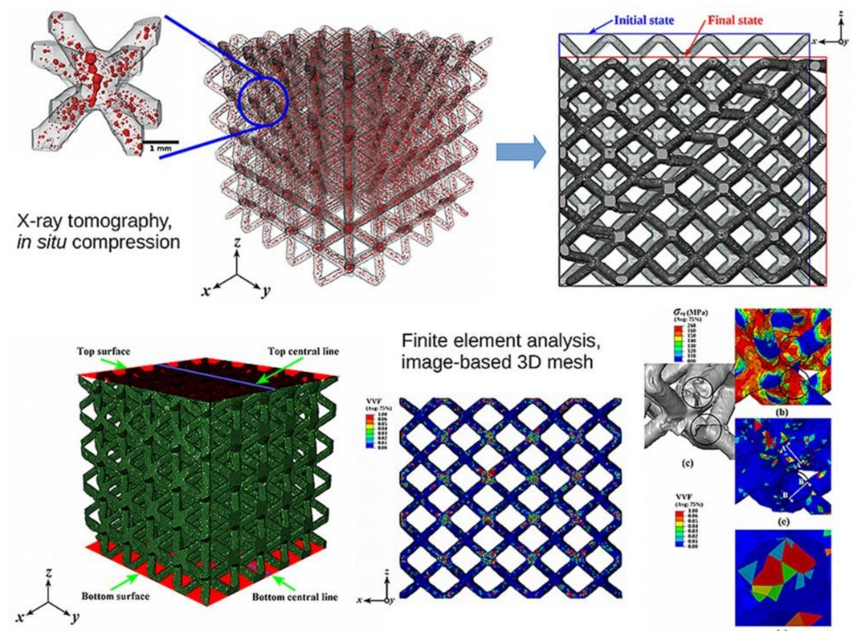

Figure 82: XCT used for porosity analysis and development of prediction fracture location model [227].

As mentioned above for surface data analysis using XCT, porosity analysis performed using XCT can also be prone to limitations and has its own set of challenges. A major influence in this case can be surface determination which can have a direct influence on the size of the pore. A method suggested in the literature is to take the XCT scan of the AM part alongside a calibrated reference part to evaluate measurement uncertainty following the ISO 15530-3:2011 standard [239]. The reference part is usually of the same material to have a closer attenuation value of the AM part to be scanned. The reference part is also usually measured prior to the XCT scan in a conventional measurement method like CMM [241].

5. Chapter: XCT dimensional metrology optimisation for AM lattice structures

5.1. Introduction

This chapter summarises three linked work elements. The first explores and draws comparisons between different instruments and processes to dimensionally assess AM lattice structures. This included using of focus variation microscope and image analysis tools on 2D reconstructed XCT images, done by author. The sample used in section 5.2 and 5.3 was supplied by 3M Buckley Innovation Centre (3MBIC) and Ahmed Tawfik respectively. The second element focuses on testing an author developed equation to rank ideal XCT settings from 2D projections before reconstruction to assist the user in choosing the right XCT setting combination from a set range. The experiment in section 5.3.2 was initially completed on a titanium machined part designed and measured using a CMM by Andrew Townsend before experimenting with more complicated lattice geometries. The third work element focuses on applying the developed method for AM lattice structures and assisting in reducing dimensional error when using XCT. In this third element (section 5.4), a more conventional and standardised equation was used for image analysis alongside a dimensional artefact designed by the author, manufactured in the University of Huddersfield under author guidance and measured in CMM by Dr. Radu Racasan. A holder for XCT fixturing was designed and manufactured by the author. The lattice structure used was designed by the author and additive manufactured by Alexander Liu. The developed method proved to be highly efficient compared to using conventional XCT methods when choosing optimal XCT settings whilst being semi-automatic, user friendly and cost effective. All XCT data acquisitions, image analysis, CMM data analysis and volume analysis was performed by the author. The second element work in section 5.3.2 was presented in DXCT 2019 conference and third element work in section 5.4 was published in ASTM (STP1631) [321] and can be seen in Appendix 12.2.

5.2. Comparison between dimensional evaluation of AM lattices using conventional methods, 2D image analysis and volume methods using XCT

a) *Experiment highlighting challenges of using non XCT methods for dimensional measurement of AM lattice structures.*

An initial experiment was carried out to test first-hand, conventional measurement methods that can work for AM lattice structures and record their strengths as well as their limitations. To do so, two lattice structures supplied from 3MBIC and made of Titanium and LPBF processes were assessed as shown in Figure 20. For the purposes of this section exact manufacturing condition are not relevant.

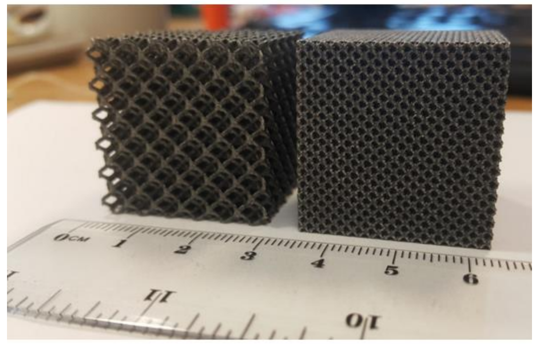

Figure 83: Additive manufactured lattice structures in titanium done using LPBF process, produced on a Renishaw AM 400 supplied by 3MBIC.

The conventional measurement instrument used in this study was the Alicona G4, a focus variation optical microscope that is mainly used for relatively fast but highly accurate surface roughness and surface form measurement. Alicona claim the instrument has a slope detection capability of more than 90º [322]. While Alicona is mainly used for surface analysis, which was also valid in this case, it can also be used for dimensional and full form measurements. After being fixed on the stage, a region of interest was defined, and measurement was performed. Initial captured data can be seen in Figure 84. The Alicona G4 was calibrated according to manufacturer recommendations.

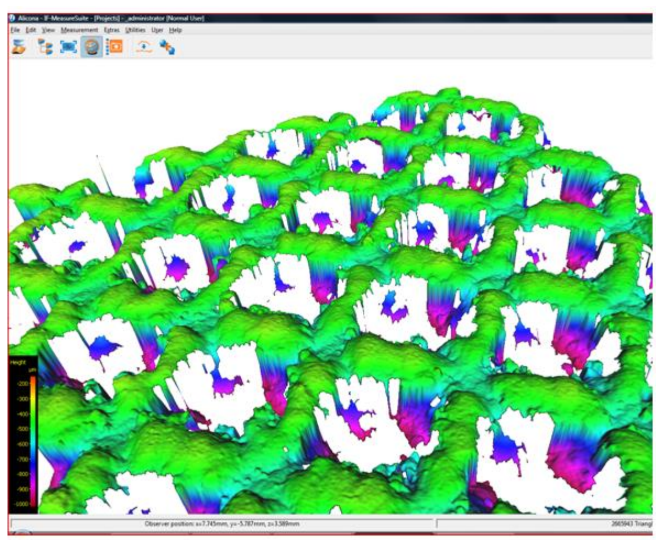

Figure 84: Initial data acquired using Alicona G4.

As mentioned above, the captured data can be analysed by different methods. When it comes to lattices, an important parameter to measure is the lattice strut length and thickness. This can give an insight into the AM machine repeatability and stability when making multiple struts forming a lattice. To do so, the profile form measurement module was used as shown in Figure 85. The distance between two points is manually chosen to represent the strut limits, the same method can be used to calculate the strut thickness as well as cell size. Although the multi-step measurement protocol can be scripted, optimal measurement however can only be obtained manually, below are the main challenges:

- **Alignment:** The top face of the lattice to be measured must be perfectly parallel to the base and fixed, fine lattices could be damaged by fixturing pressures.
- **Incomplete diameter:** while it is possible to get the diameter of the strut, only few were totally complete from both sides and deemed suitable for data extraction. (Measurement slope limitations).
- **Manual procedure:** While it was possible to measure the length, the centre of each junction has to be manually chosen as well as at the end of the length.
- **Slow procedure:** While the data acquisition stage was relatively quick, the analysis of the data had to be completed manually making the process inefficient and time consuming.
- **Incomplete data:** The AM surface has very high contrast data points with the surface occasionally having bright and reflective surfaces and high slope or re-entrant features leading to missing points.

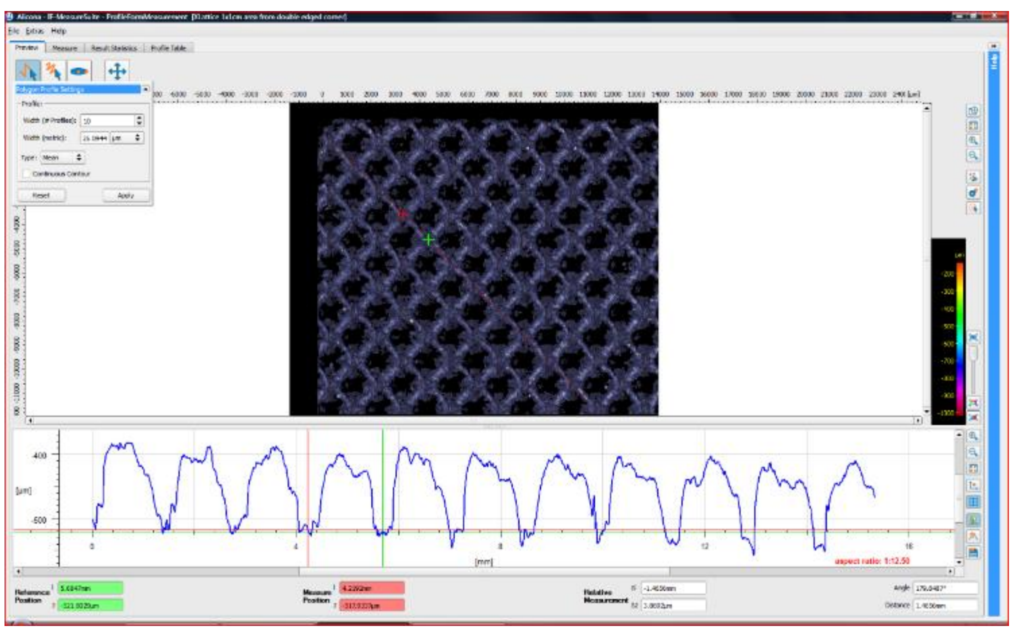

Figure 85: Strut length measurement done on the data captured using Alicona

Nevertheless, focus variation instruments remain a good reference for outer surfaces and can be used as a reliable reference to be compared with XCT measurements as used in previous studies [86,264]. Some considerations will however be taken when using focus variation microscopy on AM surfaces such as the smoothness of the surface, surface repeatability or Z height variation, and data analysis automation. Smoothness of surface can be a problem for Focus Variation technologies due to lack of pixel-to-pixel contrast however this is not a significant problem for AM surfaces. A repeatable surface in this case means that the average surface height after alignment needs to be approximately similar across the region of interest to be measured, otherwise, the minimum and maximum Z axis height used for stitched measurements for example will be very high. A high Z height value can significantly increase the measurement time making it less cost effective and reducing resolution. Finally, data analysis automation tools can be considered when using Alicona focus variation instrument as scripts can be developed to both clean and filter the regions of interest to be measured and analysed.

b) Dimensional analysis of lattices using 2D image analysis

Before using volume analysis of XCT data of AM lattice structures, a study was done to assess the usually cheaper, less computer intensive and sometimes faster methods of evaluation using 2D image analysis was carried out. In this study, the same sample shown in Figure 83 was used and XCT scanned using a Nikon XT H 225. The XCT scanning parameters were an acceleration voltage of 85 kV, filament current of 74 µA, exposure of 2000 ms, projection number of 1583 and 0.049 mm voxel size. The detector of the XCT was 1008x1008 pixel size and no filter was used. The XCT scan was then reconstructed and thresholded using local iterative surface determination.

An initial and much quicker method to get information on the lattice struts, such as strut thickness is to use a manual point overlay method on a reconstructed 2D image slice as seen in Figure 86 (b). While this measurement was completed using expensive VGSTUDIO MAX 3.1 software, it can also be accomplished using free and open-source software like ImageJ, which will be used later. To avoid analysing a 2D slice that might be incomplete due to it not being parallel, the 3D truss can be measured by fitting point methods as seen in Figure 86 (c). Lattices with rough surfaces would be more challenging to measure using these two methods since the strut limits are set manually, making the process far from repeatable and stable.

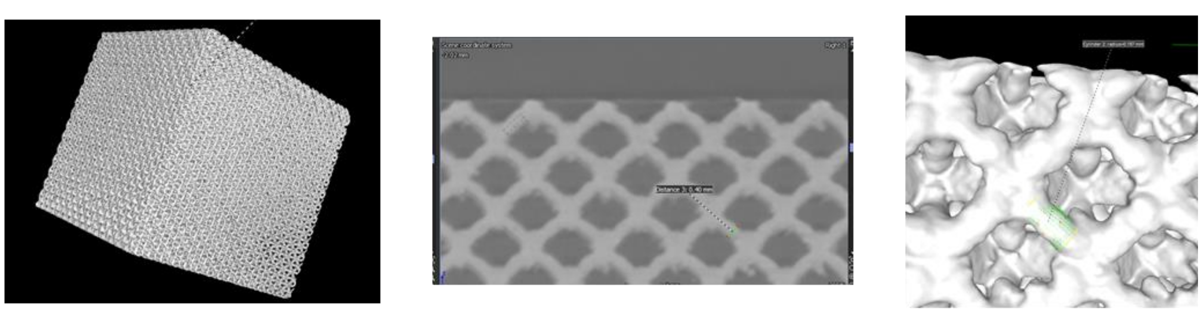

(a) (b) (c)

Figure 86: Manual measurement from the 2D reconstructed image using VGSTUDIO MAX 3.1

Instead of analysing CT data in VGSTUDIOMAX 3.1, a cheaper alternative was tested. In this case, it was free, using the image analysis software FIJI. FIJI software is an open source project based on ImageJ software [323]. FIJI software is composed of a multitude of plugins. The plugin used to analyse the trusses thicknesses is the local thickness plugin [323]. The algorithm works by trying to fit the biggest enclosed sphere inside of the reconstructed and thresholded image stack as seen in Figure 87.

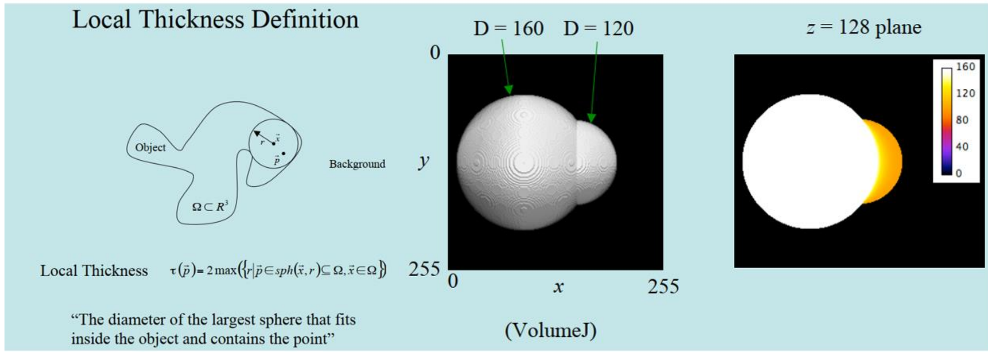

Figure 87: Local thickness algorithm used in FIJI to get the truss diameter distribution [323].

The lattice used in this case was a Diamond unit cell TPMS also XCT scanned using Nikon XT H 225. The scanning parameters were an acceleration voltage of 193 kV, filament current of 75 µA, exposure of 4000 ms, projection number of 1583 and 0.032 mm voxel size. The detector of the XCT was 1008x1008 pixel size and a 0.2 mm copper filter. Before using FIJI software, 2D Projections acquired from the CT had to be reconstructed, aligned, and then exported as tagged image file format (TIFF) Images. The exported TIFF images are then imported in FIJI software and an image stack was made. TIFF file format was used for its support of lossless compression and compatibility with FIJI software [5]. The XCT scans were performed with a detector with maximum resolution of 16 bit, which led to the use of 16 bit for the TIFF images as well.

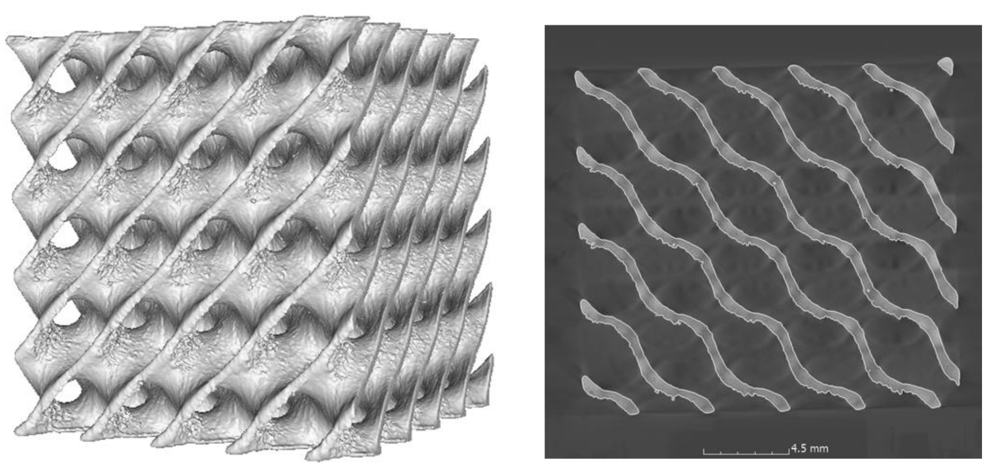

Figure 88: Volume rendering of the XCT scanned Diamond unit cell TPMS.

The exported stack of images is then thresholded using binarization method. Multiple algorithms like Otsu, MaxEntropy, Percentile and others can be used in this case each delivering a different result as can be seen in Figure 89 (b) when inputting a reconstructed cross section 2D image seen in Figure 89 (a). This visualisation gives a quick and good comparison method before choosing the optimal thresholding method to be applied on the whole image stack.

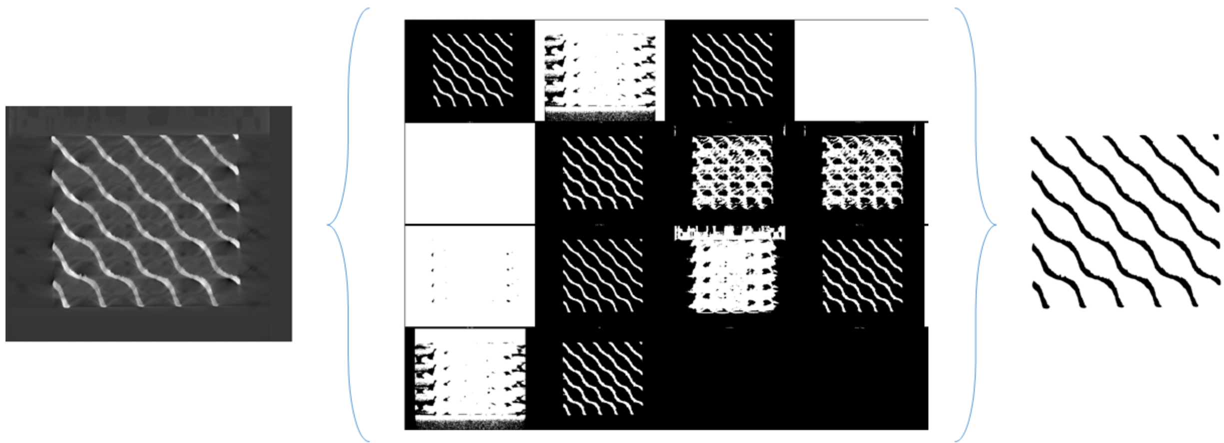

(a) (b) (c)

Figure 89: Thresholded image slice (a) and resulting threshold solutions using different algorithms like Otsu method. Mean method, MaxEntropy method and more seen in (b) and Otsu thresholding (c).

The thresholding method chosen in this case was the class separation based Otsu method [324], for visually delivering relatively better results than other methods as seen in Figure 89 (c) and also for being widely implemented in literature [94,325,326]. After applying the thresholding on a stack of images, the latter is then analysed using the local thickness module seen in Figure 90 (b) and strut length analysis seen in Figure 90 (c). The obtained analysis result is displayed as a colour map that can be scale calibrated as shown in Figure 91 and applied on the previously shown strut-based lattice. Also from the same figure, a histogram can be constructed on all of the slices showing a better representation of the diameter distribution of the lattice.

This method was relatively fast and required less computing power compared to analysing volume model. The scale calibration is however usually done manually, limiting the results accuracy. Also, while strut length analysis showed good results for the diamond TPMS lattice, it would be more challenging to use in the case of other lattices of which the struts are connected, making one chain of lengths instead of separated ones. Clearly two elements contribute to poor measurement i) methods like this one requires a good quality of XCT scan data and ii)the manual elements involved increase uncertainty and reduce repeatability.

Unfortunately, protocols and clear guidelines to achieve repeatable XCT scans are still not fully standardised making user experience and user manual involvement necessary in most stages, increasing uncertainty and reducing repeatability. The next section will highlight a study performed to assist in evaluation and optimisation of XCT setting combinations.

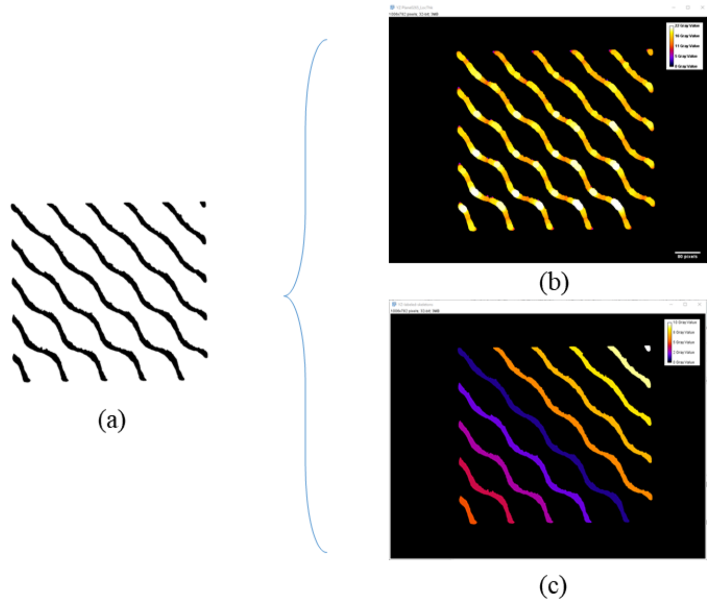

Figure 90: Otsu thresholded 2D image (a), local thickness analysis (b) and strut length analysis (c).

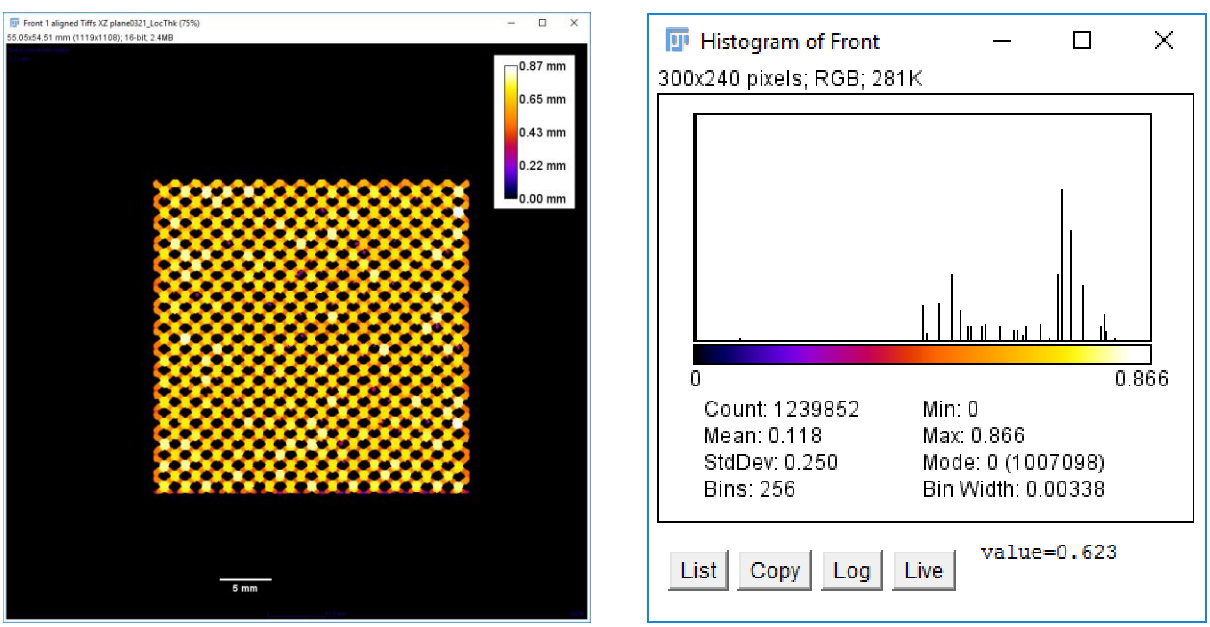

Figure 91: Local thickness analysis (left) and histogram showing the diameter distribution of the lattice (right).

5.3. Optimizing XCT settings for dimensional metrology using 2D image analysis for machined parts

5.3.1. Initial study and proof of concept

As previously outlined in the literature review, choosing XCT settings is usually a manual process prone to user error and requiring user experience. The goal of this study was to assess different methods to semi-automate the process of choosing XCT settings, mainly in this case, the voltage and current. When choosing XCT settings for a new part, the user would usually gauge its choice by analysing the displayed 2D image on the XCT machine monitor viewer. As used in some photography methods and in measurement instruments like focus variation, the aim was to compare the image quality of different 2D projections prior to CT scanning. This idea stemmed from the way Alicona focus variation works. The latter, has a minimum and maximum Z axis height set by the user prior to measurement. As seen in Figure 92 below, the microscope goes through all of the Z axis heights and picks the image at the height with the best focus [327]. The image with the best focus is defined in this case with the image with the highest standard deviation/intensity contrast between its pixels.

Scan position	Surface image	Standard deviation
Out of focus	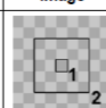	10
Almost in focus	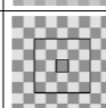	20
In focus		50
Almost in focus	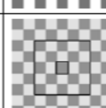	20
Out of focus	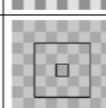	10

Figure 92: Focus value of an image using standard deviation [327].

One of the first experiments that was completed was on a small cylindrical specimen (approximate diameter of 10 mm and height of 18 mm) made in Aluminium, supplied by Ahmed Tawfik. Eight different X-Ray CT settings combinations were chosen and a 2D projection was taken using each one of them. Based on FV method explained above and shown in Figure 92, the standard deviation was also used in this case and calculated using the whole 2D image pixels grey values taken prior to reconstruction. The results were ranked from the highest value to the lowest, which by following FV method shown above should lead to the setting with highest contrast. To verify the results, two experienced users of X-CT within the research team were asked to choose the ideal setting based on histogram and image quality as shown in Figure 93. Using user experience was subjective and will be discussed below.

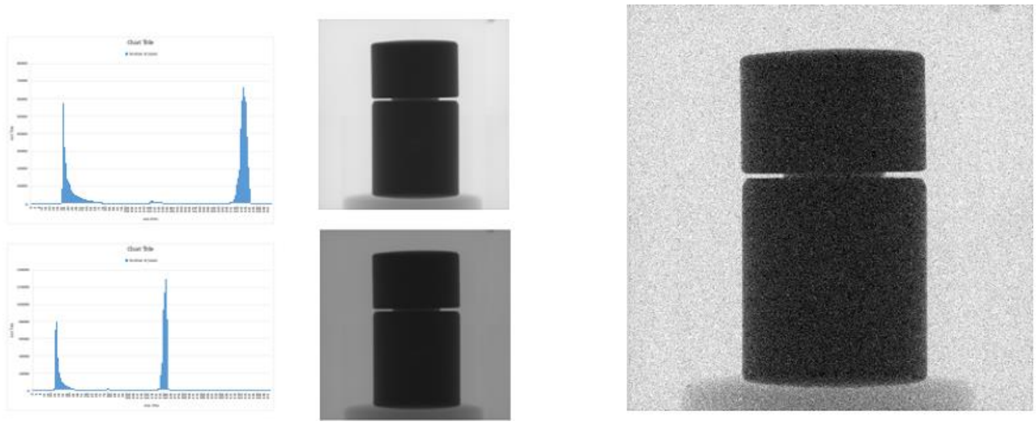

Figure 93: Example of two different 2D X-ray scans and their histogram (left), synthetic noise added to 2D X-ray image scan (right) [329].

From Table 4, it can be seen that the setting combination ‘'one’ from the eight performed ones had the highest standard deviation which makes it the ideal setting with the highest contrast. Furthermore, the setting combination ‘one’ was also the one chosen by the two experienced users from the author’s research group.

However, due to the occasional presence of noise in radiographs, the approach can be compromised in terms of standard deviation and mislead the optimisation process. To visualise this challenge, synthetic noise was added to the ideal 2D scan setting as seen in Figure 93, this led to a standard deviation of 85.2, close to the chosen ideal CT setting value which was 86.3.

To tackle this challenge, further studies were performed to not only rank settings using a standard deviation on the whole image but using contrast equations that consider background noise as well as a dimensional artefact that can be used as a validation process when ranking ideal XCT settings as further explained in following section. Another challenge in this initial study was to verify 2D image analysis results using subjective user experience. To solve this challenge, following studies have relied on using a clear dimensional workpiece previously measured on CMM of which the outer diameter was used as a benchmark.

Table 4: Different 2D projections standard deviation.

Setting combination	1	2	3	4	5	6	7	8
Full image standard deviation (Grey Value)	86.33	52.99	58.59	36.05	56.49	54.22	35.74	50.42

5.3.2. Optimisation of XCT settings using 2D image analysis and 3D volume validation for machined parts

This section summarises study presented in 4th Dimensional X-ray Computed Tomography Conference which was hosted by the University of Huddersfield [329]. The aim of the study was to improve the 2D image analysis method to account for background noise and include a 3D volume validation method using a dimensional artefact. The method was initially tested on machined parts as they could be easily measured using conventional traceable methods such as CMM. The developed method was further improved as seen in section 5.4 to work for AM lattice structures.

a) Methodology

The part used in this study, as seen in Figure 94, is composed of three features: a 3 mm outer diameter, a 3 mm inner diameter and a 4.5 mm step-length defined as the perpendicular distance between two planes referred to as the ‘length’. The dimensional workpiece, previously developed and measured in CMM by Townsend et al., 2018 in a prior study [86], was machined from Ti6Al4V ELI bar stock to produce a consistent grey value and have less chances of porosity. This design allows the separation of the two errors encountered when CT scanning, the voxel scaling error and the surface determination error [86]. This is done by measuring the ‘length’ shown in Figure 94 between two parallel surfaces which has a negligible effect from surface determination, since both planes would move in the same direction depending on the determined surface. This means that the offset between CMM and XCT measurement of the ‘length’ can be attributed to voxel scaling error and used to correct the latter [86].

The same dimensional workpiece was held using an additive manufactured polymer during the XCT scans, minimising the movement of the part, while not being in direct contact with the measured features. The CMM used was a Zeiss Prismo Access, which has a maximum permissible error (MPE) of ± (1.9 + L / 300) µm (L in mm). More details on the used measurement protocol can be found in [264] and more information on the dimensional workpiece can be found in [86].

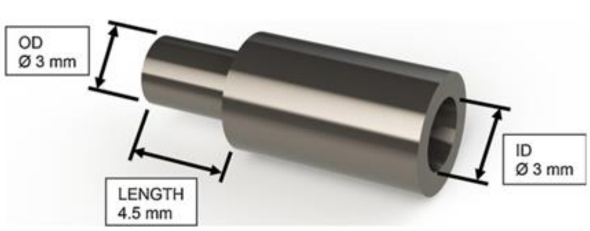

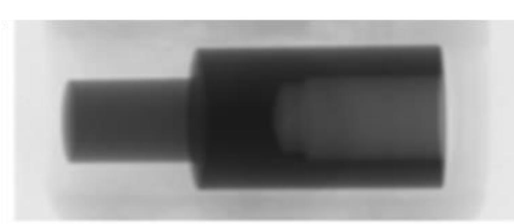

Figure 94: Rendering of dimensional artefact previously measured in CMM and used in XCT setting optimisation study (left), example of radiograph of the dimensional artefact (b) [329].

Six X-CT scans using different settings combinations (Table 5), each done five times, were completed on the dimensional workpiece. The CMM measured outer diameter (OD) dimension was measured in Volume Graphics VGSTUDIO MAX3.1 [330] and the scanning parameters were ranked from the one with the least mean difference to the one with the greatest mean difference to CMM values.

The six XCT Nikon XT H 225 [331] combinations used for XCT scanning of the dimensional artefact can be seen in Table 5. The voxel size, exposure time and number of projections were fixed to 0.018 mm, 2829 ms and 1583 projections, respectively. The magnification was fixed in order to avoid the need to scale the measurement ROIs further explained below. While more settings combinations were first considered, due to the associated time, a compromise was made, limiting the number of setting combinations used in favour of repeating the same scan 5 times, to assess repeatability. The result was the use of six different settings combinations, each scanned five times. This decision was also considered valid, since the goal of the study was not to correlate the effect of different parameters on the CT scan accuracy, which was previously addressed in literature [332], but to rank a range of CT settings combinations, from the one providing the least dimensional error using image analysis on non-reconstructed radiographs.

Table 5: Six XCT scanning combinations used for the study.

Setting	Voltage (Kv)	Power (W)	Copper Filter (mm)
A (5 meas.)	80	5	0.25
B (5 meas.)	100	5	0.25
C (5 meas.)	120	9.8	0.5
D (5 meas.)	120	20	1
E (5 meas.)	160	9.8	0.5
F (5 meas.)	180	20	1

The 2D projections measurements were analysed using FIJI software [323] accompanied with the ROI Manager Tools plugin developed by Ferreira.T [333]. The projection images used were 16-bit TIFF images with a size of 1008x1008 pixels. The grey value of each pixel ranged from 0 to 65,536. Three different ROIs as seen in Figure 95 were defined in order to analyse the 2D image quality using the author proposed SFN equation (11) where $\sigma_{part+background}$ is standard deviation of the both part and background, $\sigma_{background}$ is standard deviation of a local area in the background and σ_{part} is the standard deviation of a local area in the part, all named ROI_1, ROI_2 and ROI_3 respectively as shown in Figure 95 and further explained below.

$$SFN = Sharpness + \frac{Focus}{Noise} = \sigma_{part} + \frac{\sigma_{part+background}}{\sigma_{background}} \tag{11}$$

- **ROI_1**: Describes the Focus of the image and include the part of interest and its background, in this case the bottom cylinder and its background ($\mathbf{1008 \times 384px}$).
- **ROI_2**: A $\mathbf{25 \times 25px}$ square comprised of only the background quantifying the noise of the latter.
- **ROI_3**: A $\mathbf{25 \times 25px}$ square compromised of the part only, quantifying the sharpness of the latter.

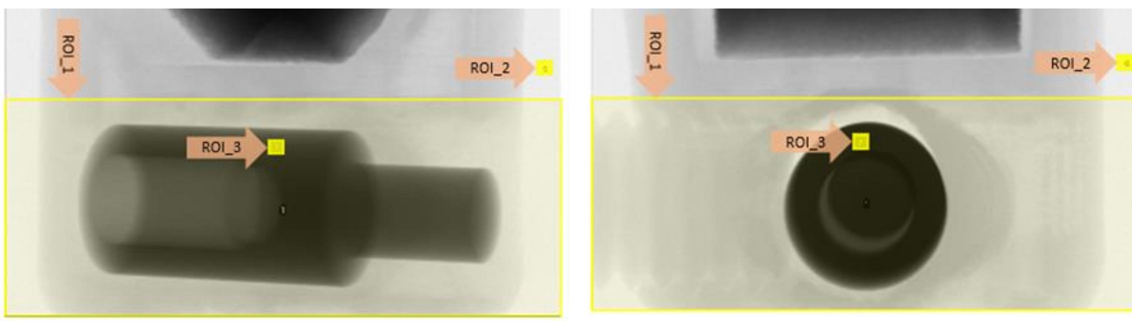

Figure 95: Three Regions of interest used in SFN formula [329].

Before ranking 2D projections of each CT scan setting, FIJI was again used to first run a convergence test to find the minimum number of projections needed to be analysed as seen in the following results section. A ranking was then performed by analysing SFN of each of the six setting combinations while averaging their value since each scan was performed five times.

To assess the image analysis ranking method, each of the 30 performed XCT scans was reconstructed and used to rank the six different XCT settings combinations by evaluating the 3D volume scan error. This error was quantified by calculating the variance between the part CMM measured Outer Diameter (OD) and the Voxel Scaled Outer Diameter measured in VGSTUDIO MAX 3.1. When using a CT for dimensional metrology, the voxel size can be calibrated [231]. The calibration or scaling value in this experiment was determined by the variance between the CMM measured ‘length’ and CT scanned one, as previously done in literature [86]. The ‘length’ design of this part, allows it to not be affected by surface determination error and provides a good choice for voxel scaling calibration. The reason for not being affected by surface determination is that if the latter is adding air voxels to the part or reducing part voxels, the two planes used for the ‘length’ measurement would both move in the same direction, keeping the distance intact. The local iterative surface determination can play an important role in this case to minimise errors that could be due to grey values being different at different parts of the volume, since the method works by locally analysing the surrounding voxels.

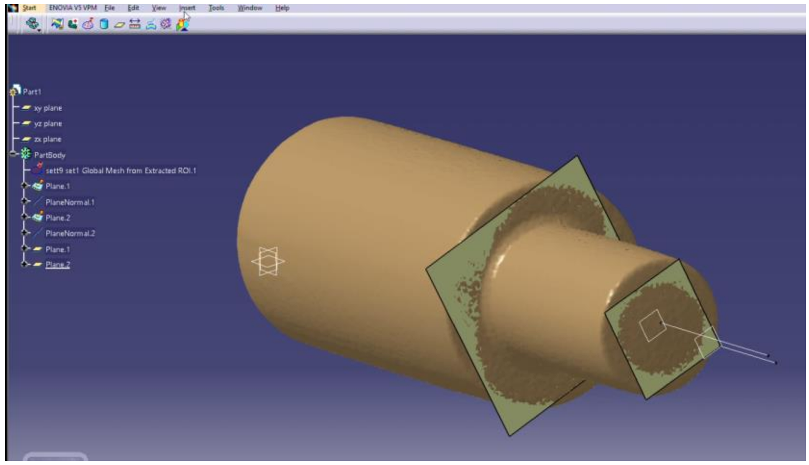

Figure 96: Measurement method for the "length" where two points were created by intersecting the centreline of the OD feature with each of the two fitted planes [329].

Reconstruction was performed using Nikon CT Pro 3D [334] and no beam hardening or noise reduction algorithm was applied during the reconstruction. The reconstructed XCT scans were thresholded using a local iterative surface determination method using VGSTUDIO MAX3.1. This type of surface determination delivers the most accurate results during reconstruction [262]. Both the 'length' and the OD were extracted to be compared with the CMM measurements. The 'length' is described as the perpendicular distance between two planes. Since the two generated planes might not be perfectly parallel and to avoid measuring the minimum distance between the two, two points were created by intersecting the centreline of the OD cylinder axis feature with each of the two fitted planes. The 'length' was then extracted as the distance between the two generated intersection points. The software used for the feature extraction and measurement was CATIAV5 as seen in Figure 96.

a) Results and discussion

Using all 1583 projections can be time consuming during both the scanning and analysis steps, which is why a convergence analysis was completed to establish the minimum number of projections needed to compare CT settings' 2D images quality and rank the settings. It can be seen from Figure 97 that the projections' average SFN starts stabilizing at 75 projections. This number of projections was therefore averaged for each setting instead of 1583 allowing less time and computing power consumption. While the convergence study was done on all settings to check for robustness of the method, it only needs to be completed for one setting when faced with a new part.

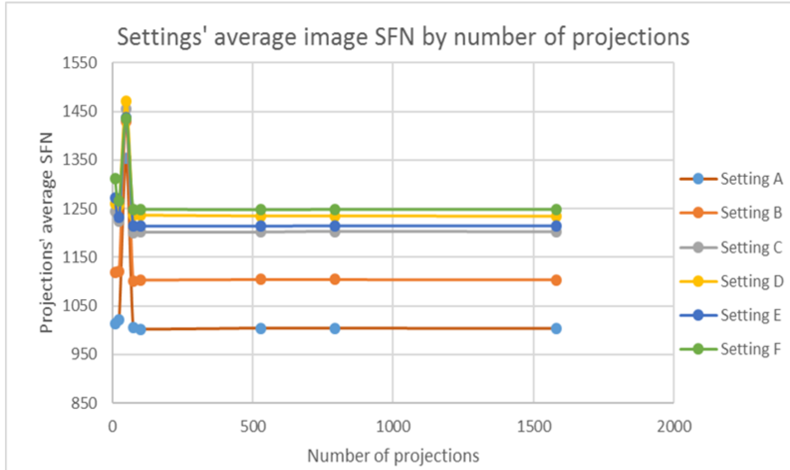

Figure 97: SFN Average value per number of projections [329].

Table 6: Ranking of X-CT settings combinations using image analysis and SFN equation [329].

CT Settings' ranking	**Average SFNs ranking of 75 projections per setting and sample std. dev (grey value)**
F (5 meas.)	1241.30 [3.95]
D (5 meas.)	1232.35 [2.19]
E (5 meas.)	1206.91 [4.10]
C (5 meas.)	1200.10 [0.64]
B (5 meas.)	1103.19 [1.23]
A (5 meas.)	999.68 [3.80]

Using SFN equation (11) shown above, 75 projections were averaged per CT setting. The 75 projections were chosen from the performed 1583 projections and were equally spaced not continuous. This was done using image sequence tool in FIJI where an increment can be set to choose equally spaced images from a stack of images. Since five scans were performed per setting, the averaged SFN values were computed alongside their sample standard deviation value as seen in Table 6 where setting F had highest SFN value.

After the 2D image analysis using SFN equation, volume analysis was done using local and global surface determination as seen in Figure 98, where the dimensions of the OD extracted from both the CMM and CT scans using different parameters can be seen. Each of the six CT scan settings analysed and compared was run five times, making 30, the total number of CT scans performed. Sample standard deviation from five measurements each was calculated. It can also be seen in this case how the setting F had closer results to CMM mean OD value making it the ideal setting as previously calculated using image analysis (Table 6).

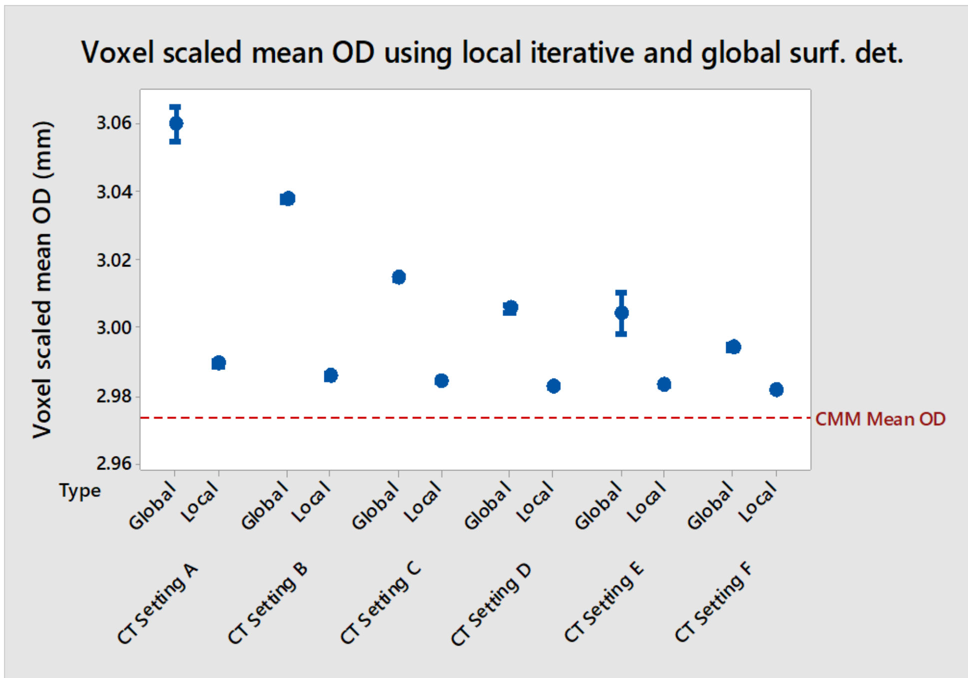

Figure 98: Ranking of X-CT settings from the one with the least difference from the X-CT measurement [329].

From the results above, the ranking of the CT settings combinations from 3D Volume analysis using both surface determinations (Figure 98) matches the ranking of the ideal CT scanning setting from 2D projections analysis (Table 6). This proves a high correlation, allowing the production of an accurate ranking of the 3D volume quality (for dimensional metrology) using 2D projections' image quality (before reconstruction).

Again, from Figure 98, it can be seen that the local iterative surface determination had a smaller variance from the CMM than the global method. In fact, the first ranked setting combination F, had +21.6 µm (+0.72%) difference from the CMM using global surface determination in comparison to only +7.6 µm (+0.26%) when using local surface determination. Townsend et al. [86] also compared the same OD variance to the CMM of the part using local surface determination. The result was +8.0 µm (+0.27%), which is only 0.4 µm different from this study's result. Also, before voxel scaling and as seen in both Table 7 and

Table 8, the values of the variance of the mean OD from the CMM have a different ranking favouring the setting combination D instead of F. The concluded 3D volume and 2D image quality ranking correlation can be due but not limited to the noise level, calculated using ROI_2. Noise can be caused by the quantization of X-ray photons [231], or a low X-ray flux [331]. As seen in Table 9, the setting combination A and B have the highest background noise and also rank the lowest in 3D volume quality ranking (Figure 98). The setting combination F however have the lowest background noise (Table 9) making it the highest in 3D volume quality ranking (Figure 98).

To minimize noise. One of the user guidelines from ISO 15708-2:2017, is to have a minimal X-ray transmission of 10%. Minimal X-ray transmission is calculated by comparing the screen grey value when X-ray is off and the scanned part lowest grey value.

Due to the CT repeatability error when scanning after long intervals [231] (impacted by filament life and other factors), it is expected, when using this method, that the CT scan is performed shortly after performing the suggested protocol. This study suggests and validates a new protocol and equation that allows the ranking of CT settings combinations (prior to reconstruction). The method can greatly assist in choosing the optimum setting combination before fully CT scanning a part, leading to a massive gain of time and increase of accuracy.

While a high-fidelity standard deviation was produced when analysing five samples of each scan (in both 3D volume and 2D analysis), the validation method relied solely on the variance between the CMM measured OD and the CT volume measured OD. This means that the SFN method produces accurate results when the goal is to have CT scans with the least dimensional measurement. The suggested method needs to be assessed for when the goal is different, for example when the objective is to have minimal error when calculating porosity or extracting areal surface roughness. Having different protocols for different objectives will allow a closer step to an automated or semi-automated CT scanning process limited in terms of user input and error with a high fidelity and accuracy. This method was also developed using a machined part, the next study will assess its use for AM lattice structures.

In retrospect, and using the workpiece above as an example, the CT scanning and 3D volume comparison of six scans took around 9.50 hours. Alternatively, the convergence analysis and 2D projection analysis of six CT scans took 2.56 hours. If the minimum number of images needed is known and the convergence analysis is not needed (for example if a similar part was previously analysed and a convergence test was already run), taking 75 projections per setting and comparing them using FIJI and the SFN equation would take only 1.06 hours, making the time needed when comparing 6 CT settings combinations to be a ninth of the time needed using the classical 3D volumes comparison.

This study compared settings combinations in which only significant few parameters were changed (voltage, current, filter thickness). More parameters need to be studied in the future alongside their impact on the SFN equation. It is expected, for example, that if the magnification is a changed, the ROI need to be scaled accordingly as well.

Table 7: CMM and CT scan mean values and sample standard deviation using local iterative surface determination [329].

Measurement method	Mean length (mm) [% dif. Wrt CMM]	Sample Std. Dev	Mean OD (mm)	Mean OD variance from CMM	Voxel scaled Mean OD (mm)	Voxel scaled mean OD variance from CMM (mm)	Sample Std. Dev
CMM (10 meas.)	4.6240	<0.00005	2.9735	_	2.9735	_	_
CT scan setting A (5 meas.)	4.6223 [-0.04%]	0.0002	2.9880	0.0145	2.9890	0.0155	0.0006
CT scan setting B (5 meas.)	4.6227 [-0.03%]	0.0002	2.9848	0.0113	2.9857	0.0122	0.0007
CT scan setting C (5 meas.)	4.6208 [-0.07%]	0.0002	2.9817	0.0082	2.9838	0.0103	0.0002
CT scan setting D (5 meas.)	4.6187 [-0.11%]	0.0004	2.9790	0.0055	2.9823	0.0088	0.0003
CT scan setting E (5 meas.)	4.6240 [+0.00%]	0.0004	2.9828	0.0093	2.9828	0.0093	0.0002
CT scan setting F (5 meas.)	4.6234 [-0.01%]	0.0004	2.9807	0.0072	2.9811	0.0076	0.0002

Table 8: CMM and CT scan mean values and sample standard deviation using global surface determination [329].

Measurement method	Mean length (mm) [% dif. Wrt CMM]	Sample Std. Dev	Mean OD (mm)	Mean OD variance from CMM	Voxel scaled Mean OD (mm)	Voxel scaled mean OD variance from CMM	Sample Std. Dev
CMM (10 meas.)	4.6240	<0.00005	2.9735	_	2.9735	_	_
CT scan setting A (5 meas.)	4.6121 [-0.26%]	0.0006	3.0071	0.0336	3.0148	0.0413	0.0014
CT scan setting B (5 meas.)	4.6138 [-0.22%]	0.0020	3.0067	0.0332	3.0133	0.0398	0.0016
CT scan setting C (5 meas.)	4.6131 [-0.24%]	0.0020	3.0009	0.0274	3.0079	0.0344	0.0013
CT scan setting D (5 meas.)	4.6097 [-0.31%]	0.0020	2.9914	0.0179	3.0006	0.0271	0.0015
CT scan setting E (5 meas.)	4.6175 [-0.14%]	0.0007	3.0006	0.0271	3.0049	0.0314	0.0007
CT scan setting F (5 meas.)	4.6191 [-0.11%]	0.0015	2.9919	0.0184	2.9951	0.0216	0.0009

Table 9: CT scan mean values and sample standard deviation using FIJI image analysis software for different ROIs [329].

Setting	ROI 1 average (grey value)	Sample Std. Dev	ROI2 average (grey value)	Sample Std. Dev	ROI3 average (grey value)	Sample Std. Dev	Average SFN of 75 projections (grey value)	Sample Std. Dev
CT scan setting A (5 meas.)	18319.48	16.27	963.62	3.73	532.96	4.00	997.99	3.80
CT scan setting B (5 meas.)	16823.95	22.86	1064.53	1.54	421.61	3.01	1104.43	1.23
CT scan setting C (5 meas.)	14823.08	9.98	1154.89	0.61	335.67	1.15	1199.05	0.64
CT scan setting D (5 meas.)	13534.70	13.02	1190.84	2.01	340.72	2.29	1230.57	2.19
CT scan setting E (5 meas.)	13733.97	18.14	1153.91	3.96	272.05	1.11	1204.39	4.10
CT scan setting F (5 meas.)	12245.34	10.16	1190.18	3.83	243.41	0.71	1240.49	3.95

5.4. Study to optimise XCT settings for AM lattice structures for dimensional metrology

5.4.1. Introduction

This section summarises work published by author in ASTM (STP1631) [321] “Structural Integrity of Additive Manufactured Materials and Parts”, which can be seen in Appendix 12.2. The study presents a semi-automatic method developed to assist in choosing XCT settings for lattice structures. Four XCT settings were compared, and a correlation has been found between the CNR value and the quality of the XCT 3D volume scan quality. A summary of the developed workflow compared to the conventional one can be seen below in Figure 99. While the previous study was applied on a machined part, this study is a follow up that is adapted to work for lattice structures and uses standardised contrast equation from ISO 15708-3:2019.

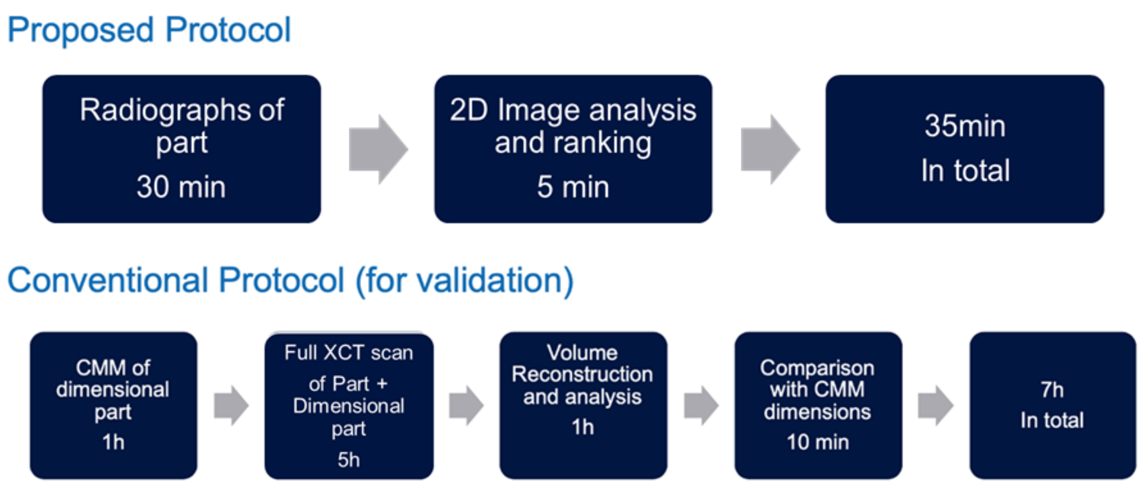

Figure 99: Proposed and conventional protocols with time needed to complete each one if four XCT settings were to be compared.

5.4.2. Methodology

a) Design and manufacturing of additive manufactured lattice structures

Ntopology software Element Pro was chosen to design a range of lattices where most started with a box like shape of dimensions of 15x15x25mm and strut diameter of 1.5 mm. The box was designed in Blender software [335] and then exported to an STL file. After opening the STL box shape in Ntopology Element Pro, the chosen type of unit cell design was BCC, Cubic Diamond and Hex prism edge. To validate the design mesh quality, a mesh analysis can be completed in AM specialised software. For this experiment, Autodesk Meshmixer was used (Figure 101). No errors were detected, and the designs were taken to the next step. A rendering of the designs can be seen in Figure 100

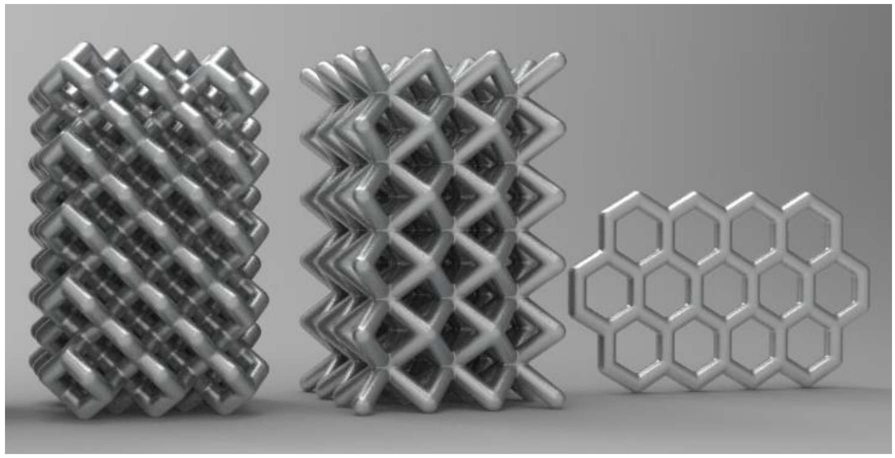

Figure 100: Updated and optimised designs.

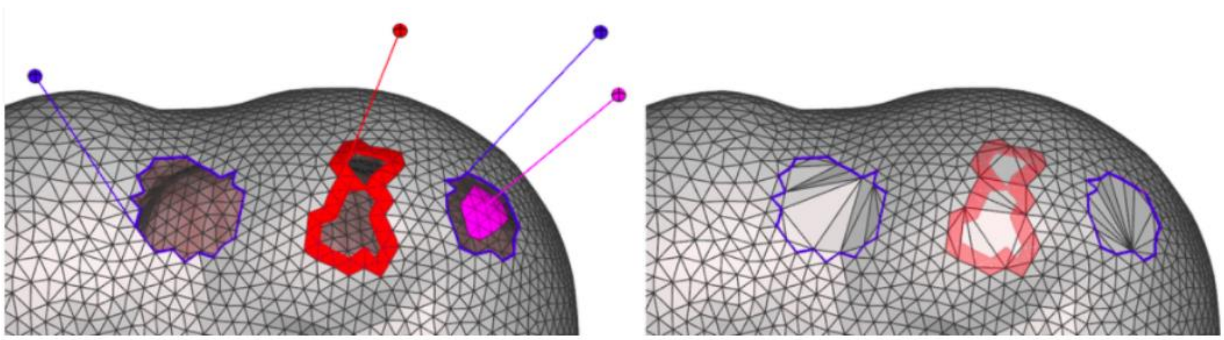

Figure 101: Example of mesh analysis and repair where blue, red and magenta highlights holes in the mesh, non-manifold regions and small component areas, respectively [336].

In the manufacturing optimisation step, supports can be generated for the lattices, orientation can be changed, and other manufacturing settings parameters can be chosen and simulated to optimise the quality of the print. As seen in Figure 102, a small overhang area has been highlighted in red, which was clearly the size of few vertices and does not fall in the bridge distance that needs a support. The 2D hex prism design was oriented to be flat on the print bed and not needing any supports. This has meant that the designs were printed supports free.

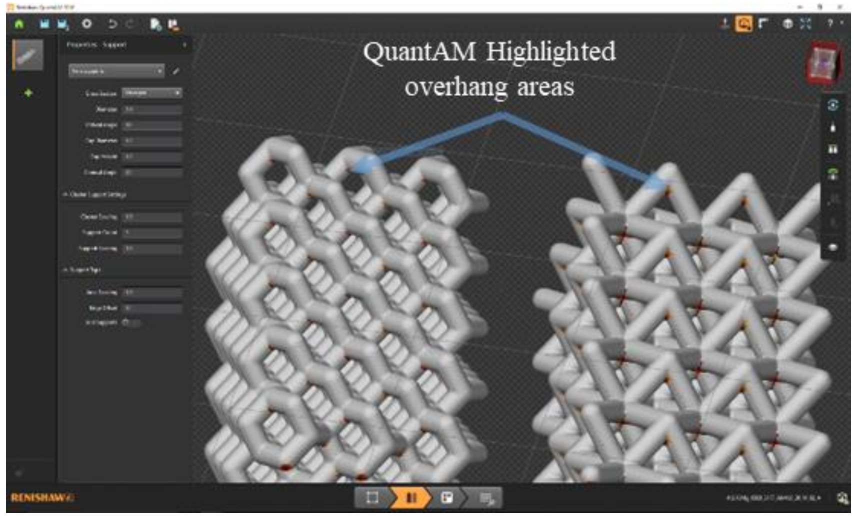

Figure 102: QuantAM software showing overhang area needing supports.

After validation of the designs in QuantAM, the manufacturing process was done by Alexander Liu who was a co-author in the related publication [321]. The lattices were made using an EOS M290 machine. The DSLM process, developed by EOS is one of the oldest and most reliable process in the metal AM field. The chosen material was AlSi10Mg. This material is both inexpensive (compared to Titanium or Inconel), widely used and easier to penetrate with an X-ray CT. An example of machine used, and manufactured lattices can be seen below:

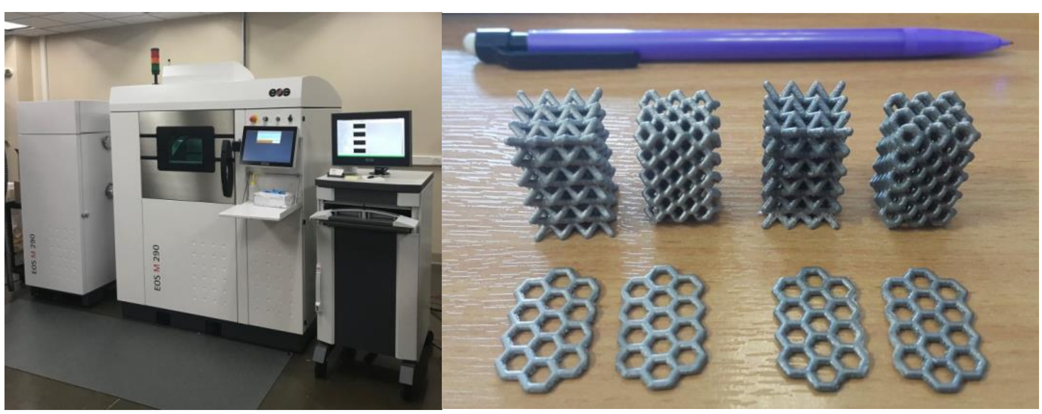

Figure 103: On the left, an example of the EOS machine [337]. On the right, the manufactured lattice structures.

The post processing stage plays a big role in metal AM, especially for lattice structures. Mesoscale features (0.1mm to 10mm) are the building block for lattices and are sensible to dimension, surface and porosity values alterations caused by post processing [338]. As seen in Figure 103, eight lattices in total were produced. Half of them were not post processed and the other half had a sand blasting process which made the surface roughness smoother. In this study, the BCC lattice that is post processed was the one used in the following study of which a rendering and manufactured view can be seen in Figure 104. The lattice structure used in this study was as printed, with no applied heat treatment.

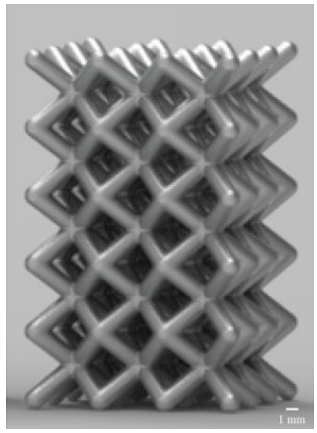

(a)

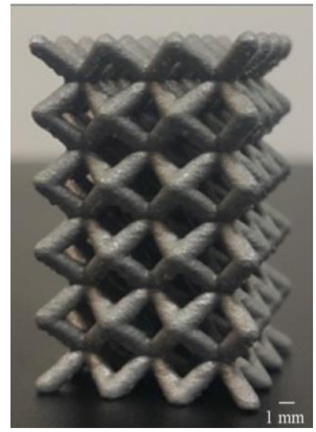

(b)

Figure 104: The lattice design rendering (a) and the AM manufactured lattice (b) [321].

b) Design and manufacturing of dimensional artefact and part holder

As discussed, XCT lattice measurements can hardly be validated by re-measuring the lattice using a CMM since the latter cannot reach all features of the lattice like internal ones. This leads to the use of alternative methods like substitution measurements as shown in literature [86]. In this study, a dimensional workpiece has been CNC machined from Aluminium bar stock to preserve a consistent grey value. The diameter of the dimensional workpiece is 1.5mm, which is similar to the lattice strut diameter. This was done to allow an edge detection that is similar and has nearly similar X-ray attenuation properties between the dimensional workpiece and the lattice. A Zeiss Prismo Access CMM was used to measure the dimensional workpiece; outer diameter using four circles, each was measured five times, allowing the extraction of the cylinder they form.

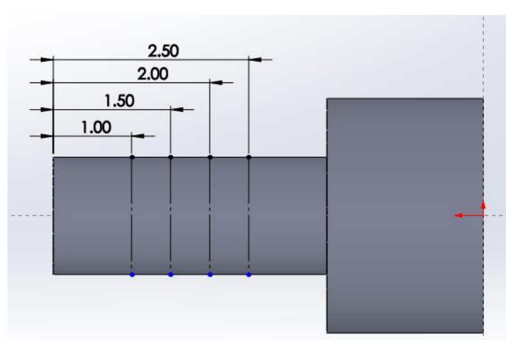

Figure 105: CMM strategy of the dimensional workpiece showing the four circles used to extract the cylinder[321].

(a) (b)

Figure 106: Dimensions of the dimensional workpiece (a) and the CNC manufactured one next to a pencil tip (b)[321].

To hold both the lattice and the dimensional workpiece during the XCT process, a holder was designed, and 3D printed using fused deposition modelling (FDM) process in the PLA material. The main role of the holder was to minimise the movement of the lattice and dimensional workpiece during the multiple XCT scans. The holder was not in direct contact with the main features and had a low attenuation due to its material allowing clear edge detection and separation from the parts of interest.

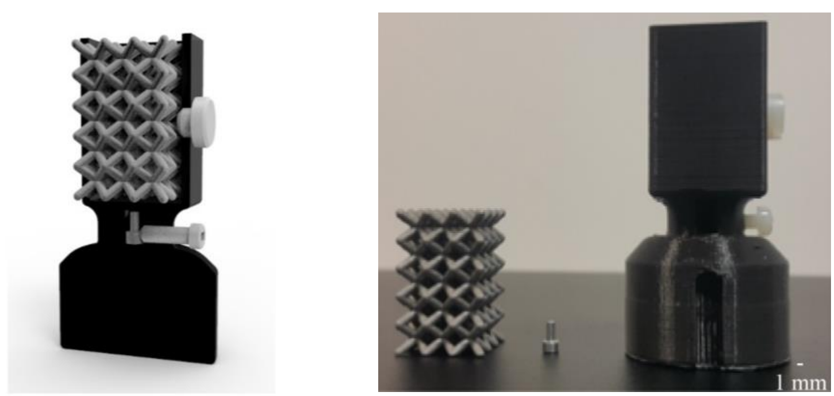

(a) (b)

Figure 107: Section view rendering (a). The lattice, dimensional workpiece and holder (b) [321].

c) XCT scanning and image analysis setup

The XCT measurement was carried out on the Nikon XT H 225 machine. Four XCT measurements were completed, each one performed three times resulting in a total of 12 scans, all performed in random order. The XCT scanning settings were 0.023mm voxel size, 2829ms projection time, 1583 projections and no filter. The magnification was also fixed to avoid scaling the ROIs used in the measurements. Future research will need to vary more settings like number of projections and exposure time which is usually crucial in both quality of XCT scan and duration. The varied voltage and power value can be seen below in Table 10.

Table 10: Different settings used in the XCT process [321].

Settings Combinations	Voltage (kV)	Power (W)
100_6 (3 meas.)	100	6
120_7 (3 meas.)	120	7
140_8 (3 meas.)	140	8
160_9 (3 meas.)	160	9

To quantify the quality of each XCT scan before starting the full volume scans, three radiographs were saved after shading correction. Image analysis was done with FIJI software using the CNR equation from ISO 15708-3:2019 [339]. The XCT sensor panel is made of 1008 by 1008 pixels. Since the projections format is a 16-bit TIFF image, each grey value ranged from 0 to 65,536. When analysing the projections, a high CNR value means a better-quality scan since the goal is to increase the grey value difference between the foreground and background with minimum noise as seen below in equation (12):

$$CNR = \frac{|\mu_f - \mu_b|}{\sigma_b} \quad (12)$$

In order to extract the equation values mentioned above, three regions of interest were created. As seen in , ROI_1 and ROI_3 are used to extract the local mean grey value of the foregrounds (μ_f) of both the dimensional workpiece and lattice respectively. While ROI_2 and ROI_4 are used to extract the local mean grey value of the background (μ_b) and background noise as standard deviation (σ_b) of both the dimensional workpiece and lattice respectively. The projection angle used for the dimensional workpiece is the one where the part is not overlapping with the PLA holder as seen in Figure 108 (a) as opposite to Figure 108 (b) below. Also, the projection used for lattice is the one where the struts are not overlapping as seen in Figure 108 (b), which was done to avoid creating a darker grey value not representative of the individual strut as seen in Figure 108 (a). Choosing the right projection for each part meant that they had closer grey values, which was the goal at the beginning of the study. The complicated lattice geometry meant that only one 2D image was used for CNR measurement compared to more images as done in the previous study. Also, the small scale of the dimensional workpiece compared to the one from the previous study meant that it was not possible to extract the two planar faces used for voxel scaling.

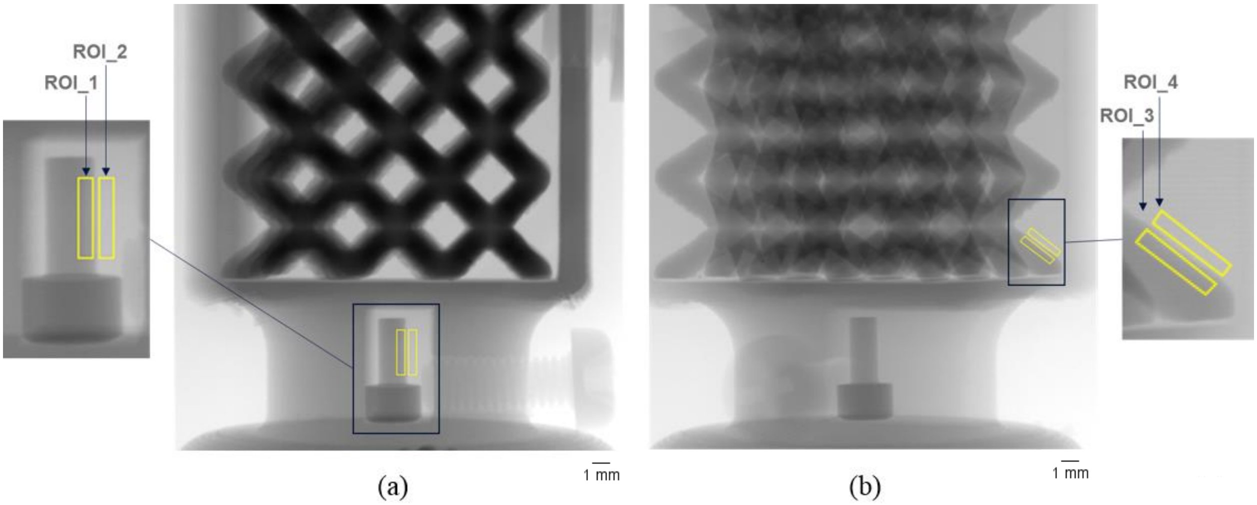

Figure 108: Regions of interest used in the CNR equation [321].

The setup of the part in the XCT machine can be seen in Figure 109. The XCT 3D volume reconstruction process was carried out using Nikon XCT Pro 3D without using any noise reduction or beam hardening algorithm. Surface determination was completed using the local iterative surface determination algorithm which is usually better than the global methods [262]. Global surface determination was also performed and later compared to the local method. The PLA holder allowed the limitation of potential errors due to moving the part between scans, which is why all 12 scans were done as a batch and at a random order.

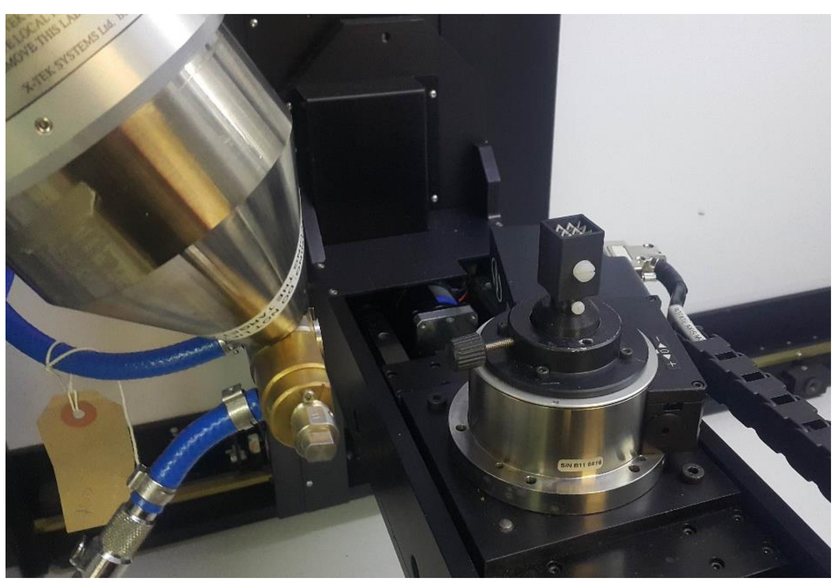

Figure 109: XCT setup showing the target and fixture with the lattice and dimensional workpiece.

5.4.3. Results

The analysis on the radiographs with image analysis using the CNR equation showed that the setting with 160 kV and 9W had the highest CNR for both the lattice and dimensional workpiece. Since three XCT scans were performed per setting combination, three 2D projections were used and the calculated CNR is shown as an average of the three projections alongside a standard deviation as seen in Table 11.

Table 11: CNR of the dimensional workpiece and lattice in different XCT settings [321].

XCT settings	**Dimensional workpiece CNR [std. dev.] (grey value)**	**Lattice CNR [std. dev.] (grey value)**
100_6 (3 meas.)	16.3 [0.3]	19.3 [0.5]
120_7 (3 meas.)	16.3 [0.6]	18.4 [0.6]
140_8 (3 meas.)	20.2 [0.9]	19.5 [1.2]
160_9 (3 meas.)	21.6 [0.2]	20.1 [0.2]

To verify the results, the conventional method shown in Figure 99 was completed by reconstructing and analysing 3D volumes of each setting and extraction of the outer diameter to be compared with the CMM output. The XCT setting that had the closest outer diameter to the CMM was considered to be more accurate. As pointed out above, surface determination was done using both local iterative and global method. As seen in Figure 110, both surface determination methods showed the same ideal XCT setting, the one with 160 KV and 9W, validating the analysis on radiographs above. Also, as seen in previous study, the global surface determination had further values from the true measured CMM value compared to the local iterative one. All settings had a standard deviation of less than 0.1 µm beside the setting 100_6 and 120_7 which had a standard deviation of 0.3 µm and 0.5 µm respectively.

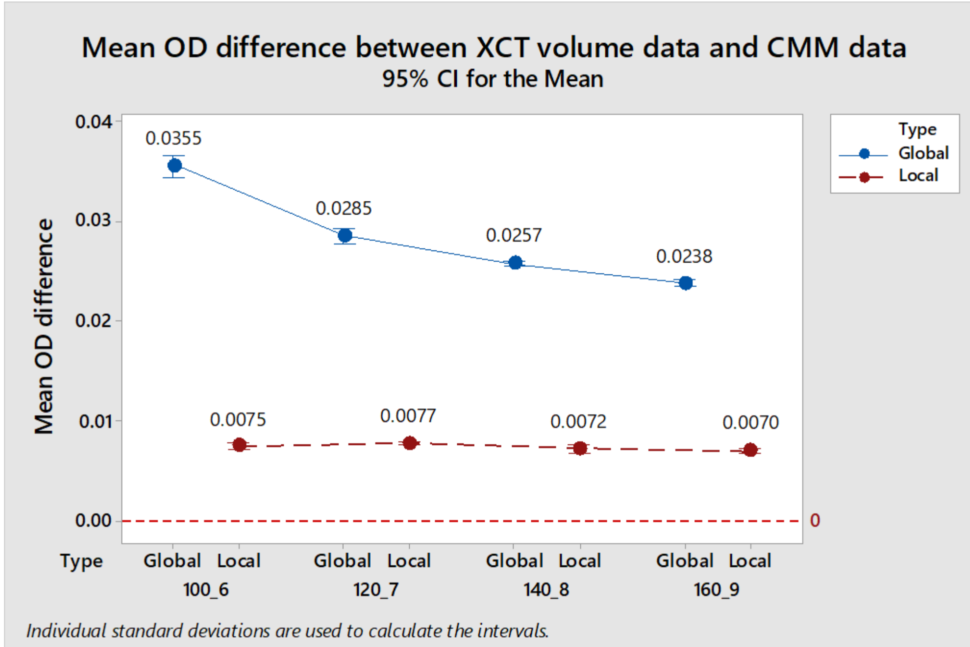

Figure 110: Mean difference of OD between the CMM data represented as the 0 line and the XCT data [321].

Finally, both the proposed method and the conventional one showed similar results. The study can significantly reduce time needed to choose the right XCT settings before taking a full 3D volume scan. If four XCT settings were to be compared as seen in Figure 99, the conventional method would have taken more than seven hours while the proposed one would take only 35 minutes.

5.5. Chapter summary

In this chapter, initial study was performed to assess the limitations of conventional measurement methods like FV as well as cheaper and faster image analysis methods when it comes to the metrology of AM lattice structures. The second segment focused on method to optimise XCT settings for machined parts [329]. As for the third segment, a follow up study was performed and adapted for optimisation of XCT settings for dimensional metrology of lattice structures [321]. In this study, a convenient dimensional artefact and fixture were designed and manufactured, and a faster semi-automatic cost-effective protocol was developed and verified using dimensional workpiece previously measured using CMM.

Previous studies in literature like Kraemer et al. 2015 pointed to the possibility of using image analysis equations prior to XCT scanning in order to assist in choosing the right XCT setting, but the results were not conclusive and the used image analysis method was deemed not sufficient to assist in determining XCT scan parameters [340]. However, in this study, the results of the 2D image analysis correlated not only with the 3D volume analysis one but also showed that the setting with the highest CNR in both 2D and 3D was the one that showed closer results to the CMM measurement, used in this study as the benchmark result.

This result shows how there is a strong possibility that with further research, choosing XCT settings can potentially be chosen after analysing radiographs before the XCT volume scan which usually takes a long time making the process less cost effective.

Nevertheless, the presented methodology introduces a novel method of isolating regions of interest and semi automating the process using image analysis software like FIJI and its advanced batch measurement scripts and plugins like "ROI manager". The presented method also presents a novel way to validate the results with a dimensional artefact previously CMM measured and accompanying the XCT scan process. This means that this study sets a backbone for future research that can introduce even more image analysis equations like signal to noise ratio (SNR) and more XCT scanning parameter variables such as magnification or filters while having a strong framework of batch processing and results validation.

The XCT setting combination that had the least difference to the CMM measurement was the with the highest Power (W) setting. Higher power values during an XCT scan usually leads to broader values between the material peak and background peak in the general histogram. This peak broadening is usually captured using a contrast equation (mean background value subtracted from mean material grey value). However, noisy pixels can create artefacts in the 2D projections, misleading the measurements by resulting in a greater difference between the peaks. For this particular reason, the noise variable has to be accounted for, hence the use of the contrast to noise ratio (CNR) equations which gets not only has a higher value when the material to background peak is further but also gets lower when the noise value is higher minimising the chances of noise affecting the image analysis process. One of the main tools of XCT engineers when choosing XCT settings is to rely on the histogram peaks, however, subtle changes in noise value between XCT settings might be challenging to visualise manually in a computer monitor increasing chances of user error.

As previously mentioned, noise can be reduced by following ISO 15708-2:2017 recommendation which aims for a minimum X-ray transmission value of 10% [339]. This is because transmission values lower than 10% will mean less photons traversing and reaching the panel, giving space, and allowing for a rise of noisy pixels. It is vice versa, if the transmission value is very high, histogram peaks will be too close leading to low contrast and difficulty in thresholding the part from the background.

The reason the suggested method is semi-automatic instead of being fully automated is the fact that XCT users will still have to rely on experience to choose the XCT settings to be compared and ranked from ideal to least ideal. This means that when getting a new part of which the internal features are not known, the user will select the XCT setting combination candidates to be compared and also select the regions of interest, following the proposed method guidelines mentioned above. It is expected that the number of XCT settings to be compared is dependent on the function of the part and how critical the measurement tolerances are, the experience of the user to set a small range of XCT settings to be compared and also the maximum time allowed for the experiment which directly affects the known high costs of using an XCT.

Similar to the process followed in this study, and of the previous study, it is recommended that all XCT settings to be compared are scanned at very close intervals if not ideally, and when possible, as a continuously uninterrupted batch scan. This is due to the potential repeatability obstacle that might occur when XCT scanning after extended intervals, either due to filament life or other factors [231].

Initial further work regarding the Chapter 5 study can include an interlaboratory study using multiple XCT systems and different users with different experience levels, first to clearly assess the repeatability of the study and second to test the developed measurement protocols for users with different experience levels. The aim would again be to reduce chances of user error when choosing XCT settings and potentially assisting users with less experience to confidently take reliable XCT scans with repeatable quality and thus increased user confidence, especially for AM lattice structures. Also, only two main factors were used as variables in the study. Further research can look at more input parameters that can be altered in a structured DOE while monitoring their impact on the CNR equation values. For example, it is anticipated that when choosing the magnification parameter as a variable and changing the voxel size, the region of interest dimensions cannot stay the same as performed in the study above. In the mentioned scenario, the ROIs will have to scale according to the voxel size or with a specific factor to be found after a thorough DOE study.

In the case of a generic part, user experience will be highly needed in choosing a representative region of interest in case the geometry is not uniform across different scan angles. Another scenario can be a variable thickness which can be present in parts like turbine blades. The challenge in this case would be to find an XCT setting that works for most of the part instead of a section of it. The developed method was tested on a conventional part with no sharp change in thickness which means that further studies need to investigate the application of the method on gradient thickness parts with possibility of using multiple regions of interests, or dimensional workpiece with variable thickness. Due to this current limitation, the method developed in this chapter was not applied in Chapter 7 study, which has a gradient lattice strut.

Also, the verification used in this study was the CMM measurement on a dimensional artefact. This means that this method works when the goal of the XCT scan is to minimise the dimensional error. Along these lines, different verification methods might need to be used if the goal of the XCT scan was for another objective like minimising areal surface roughness error or characterising porosity, which explains why the developed method was not used in Chapter 6 and 7. In these last two scenarios, a surface workpiece or designed porous part can accompany the test part to be measured and be tested again with the CNR equation. An alternative would be to design a dimensional artefact which also has a variable surface roughness and machined pores of which both can be measured prior to XCT process and accompany the lattice measurement. This can significantly increase measurement reliability by verification against the measurement of the dimensional artefact prior measurement by CMM or focus variation microscope.

Further work can also include further automation of the suggested process. While the suggested protocol saves significant amounts of time when comparing XCT scanning settings, the method still relies on the user input. This input at the moment includes completing the setup and taking radiographs of multiple scan settings, setting the ROI regions of the material and background, and carrying out the 2D image analysis using the CNR method. The outlined further automation can be achieved by using application programming interface (API) between XCT machine interface and image analysis software. In this case, the interface that can be used is called by Nikon the Inter Process Communication (IPC) and allows users to control their XCT from a custom built interface that suits the user application [341]. This IPC feature comes in all Inspect-X that are 3.0 or newer, which would be helpful compared to that used on the XCT machine that has an older Inspect-X version which uses Visual Basic a language not supported anymore by Microsoft [342].

Finally, the main steps of the suggested protocol are completed on 2D projections that are performed before reconstruction. This opens the door for potential scenarios when a 2D projection is deemed as ideal when analysed before reconstruction but the chosen XCT scanning angle, material or filter will cause artefacts that are only clear after reconstruction like beam hardening or ring artefacts. This is one of the reasons experienced XCT users will still be extremely valuable until further research can greatly assist in predicting 3D volume artefacts before XCT scanning. Carrying out further work aimed at predicting 3D volume artefacts and combining its findings with the developed study can greatly decrease set up times and significantly increase XCT scanning accuracy. To tackle this challenge, parameters like orientation and geometry as well as image analysis equations like SNR, Just Noticeable Blur (JNB) or Sum of Modified Laplacians (SML), previously used in literature [340], can possibly be tested. Machine learning models adapted from the medical field to correct for reconstruction artefacts [343]. Further discussion can be seen in Chapter 8 section 8.2b), and related future work in Chapter 10 section 10.1.

6. Chapter: XCT surface metrology optimisation for AM lattice structures

6.1. Introduction

This chapter summarises two main sections of work of the overall project. The first element of research was an initial exploration of ways to include AM lattice defects, mainly dimensional and surface ones, in the designs stage. The second element is focused on novel method developed to extract up and down skin areal surface data of AM lattices using XCT as well as development of a script to design surface topography on CAD, for improved design validation phase. The lattice structures used in this chapter are designed by the author and additive manufactured by Alexander Liu. Form removal and areal surface parameter extraction was done by Luca Pagani. The design of parametric surface models, Alicona data acquisition and analysis, XCT data acquisition, volume analysis, isolating surface ROIs, and extracted surface data analysis was done by the author. The second element of this work been published by author in the AM Journal in paper titled "Parametrically Designed Surface Topography on CAD Models of Additively Manufactured Lattice Structures for Improved Design Validation" [344], which can be seen in Appendix 12.3.

6.2. Initial study to compare; experimental compression test with FEA simulations

a) Methodology

As discussed in literature review, additive manufactured lattice structures are often far from being perfectly similar to their initial CAD design and have both dimensional deviations and significant rough surface topography especially on the down skin of the strut overhangs. The intended aim of this study was to investigate the differences between the experimental compression tests on additive manufactured lattices with (i) (FEA) compression on ideal CAD and (ii) XCT volume scan of the as manufactured AM lattice and (iii) FEA on CAD with designed surface (CADwDS), which will be explained below. Understanding these differences will allow for better understanding of dimensional and surface defects in order to greatly optimise the design phase of AM lattices instead of using simulations on ideal perfect CAD.

The test lattice was designed using Ntopology software called Ntop. Starting from a box size of 15x15x25mm. A BCC unit cell with a size of 5mm and a 1.5mm strut diameter was chosen to fill the region of interest. For the AM process, the design made in Ntopology software was exported to STL format and additively manufactured without any added compensation algorithms. The additive manufacturing was done by Alexander Liu on an EOS M290 and the material used was AlSi10Mg. The lattice structure was as printed, with no applied heat treatment. Aluminium was chosen for its lower attenuation and ease of XCT scanning compared to its counterparts like Stainless Steel, Titanium or Inconel.

Initially, a compression test was carried out on the as manufactured lattice according to ISO 13314:2011 design rules and using an Instron Tensile/Compressive test machine, with a displacement rate of 1.2mm/min. The specimen was an aluminium additive manufactured BCC lattice structure it was non-post processed and consequently retained its as manufactured rough surface roughness, Figure 111.

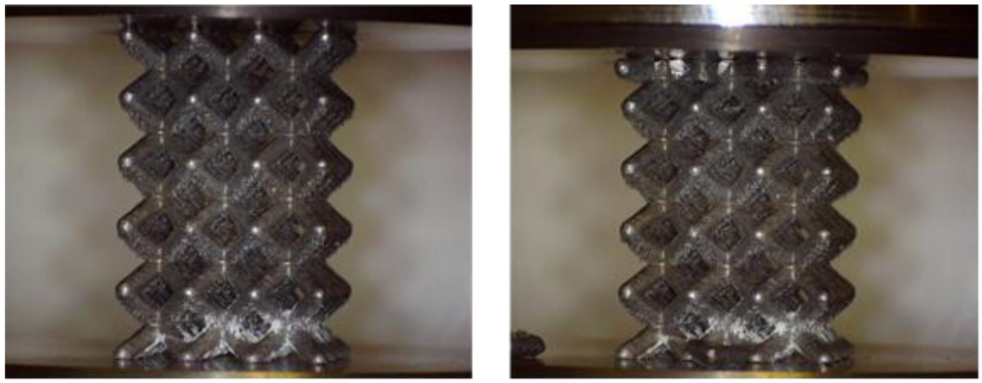

(a) (b)

Figure 111: Compression test applied on as built BCC AM lattice.

The XCT scanning of the AM lattice was carried out using a Nikon XT H 225 with acceleration voltage of 100 kV, filament current of 90 μA, exposure of 1415 ms, projection number of 1583 and 0.030 mm voxel size. The detector of the XCT machine used was 1008x1008 pixel size and no filter was used. After reconstruction, surface determination was accomplished using a local iterative fit algorithm. The XCT model can be seen in Figure 114 (c), the original CAD in Figure 114 (a) and the CAD with designed surface (CADwDS) in Figure 114 (b). The CADwDS was obtained using Ntop software, which allows the use of a simplex noise algorithm to “add” a surface topography to any CAD surface. The parameters used in the simplex algorithm are amplitude and frequency. At this stage of the research, the amplitude and frequency were manually chosen to have a visually closer surface topography to the XCT roughness. The visual comparison was done by aligning the CADwDS with the XCT and looking at the 2D cross section outline of the surface.

Keeping a balance between accurate modelling of LPBF lattice structures while minimising the computing power needed to run a finite element simulation is still an open field of research [345]. This complexity is even further in this case due to the intricate surface topography of the XCT volume seen in Figure 114 (c), which can be extremely challenging and computationally expensive to run using a conventional boundary conform mesh. It is reported for example in literature that the discretization of a complex geometry can take 80% of the analysis time with only 20% of time spent on the finite element analysis [346]. The alternative used in this preliminary experiment falls in the category of meshless simulations named immersed-boundary methods, also known as finite cell method [346]. While this method deals better with complex geometries, it is still limited in the used VGSTUDIO MAX 3.1 software module to linear elastic simulations, which does not provide the full picture on the failure mode, which can be more relevant in many practical cases [347]. The meshless immersed-boundary method used in this study has been used in literature and showed correlation between predicted and experimental measured tensile strengths [347]. The core idea relies on evaluating in a linear-response material model using the Young's modulus and Poisson's ratio. The simulation itself is a mesh-free finite-element analysis for which the voxel grid is used as the basis for the simulation. The model is discretized into an approximated simplified structured grid, as seen in Figure 112, which can assist in reducing computational cost and avoid errors related to generating conforming boundary meshes [346]. A review on the used finite cell method has been performed by Schilliger et al. [346] and a comparison with the used VGSTUDIO structural mechanics module with experimental data has been performed by Fieres et al. [347].

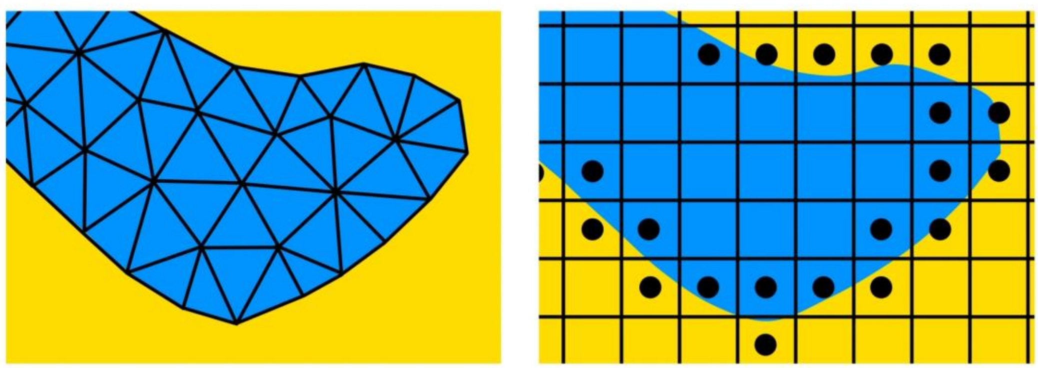

Figure 112: Example of conventional finite element method (FEM) discretized following a boundary conform mesh (left) and immersed-boundary FEM discretized following a simplified structured grid (right)[330] .

While the used method significantly reduced the needed computing power and extensive time related to the conventional boundary meshing, it was still challenging to use a small simulation size that captures the detailed geometry of the XCT volume data. In this preliminary study, the finite element analysis had to be set with a simulation size of 4 voxels (limited by available computing power) in order to be run on the XCT volume model, as well as on the CAD and CADwDS for comparable results. The effect of using a larger simulation size in this case leads to smoothening of the original surface, leading to a subsampled version of the model, certainly affecting the simulation results and can be considered a limitation of this preliminary study. An example of the original and simulated surface with larger voxel size can be seen in Figure 113. Due to this limitation, a future study can be performed using more computing power in order to run a convergence analysis, assessing the effect of surface smoothening due to using a larger voxel size and also to run the finite element simulation on a voxel size that is more representative of the complex lattice surface geometry.

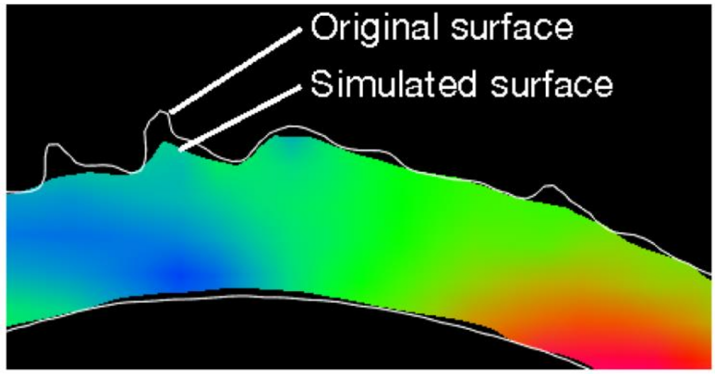

Figure 113: Example showing the original surface and simulated surface with a simulation cell size of four times the original voxel size [330].

The static FEA process of all designs was completed in VGStudio software where the Young's modulus was chosen to be 4.6 x10^8Pa and Poisson's ratio to be 0.3, similar to additive manufactured Aluminium properties published by EOS [348]. A user chosen load of 8500 N with direction uniaxial in the Z axis as seen in green arrow in Figure 114 (d). The load ROI as well as fixture ROI had a height of 1 mm as seen in green and red respectively in Figure 114 (d).

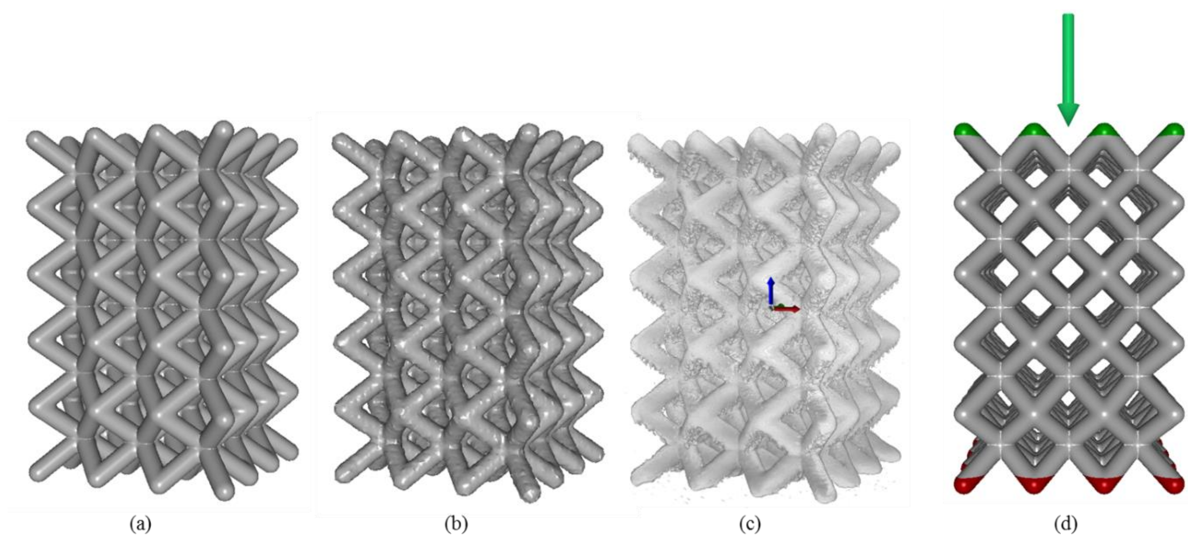

Figure 114: Rendering of CAD (a), CADwDS (b), and XCT volume (c) as well as boundary conditions (d)

b) Results and discussion

The compression test results can be seen in Figure 115 where the test started with the force gradually increasing to compress the part (elastic region). After 3 mm displacement, the top layer of struts broke, leading to a drop in the required compression force. Nevertheless, and as usually seen in lattice compression tests, the force further increased when the machine top plate reached the next lattice node. However, from around the 3.6 mm displacement mark, the lattice started tilting/twisting and sliding meaning the plate load was no longer perpendicular to the lattice Z axis, this led to breakage of some of the bottom lattice struts. This tilting also led to a decrease in force needed to compress the lattice since until it failure occurred as seen in the timeline images in Figure 115.

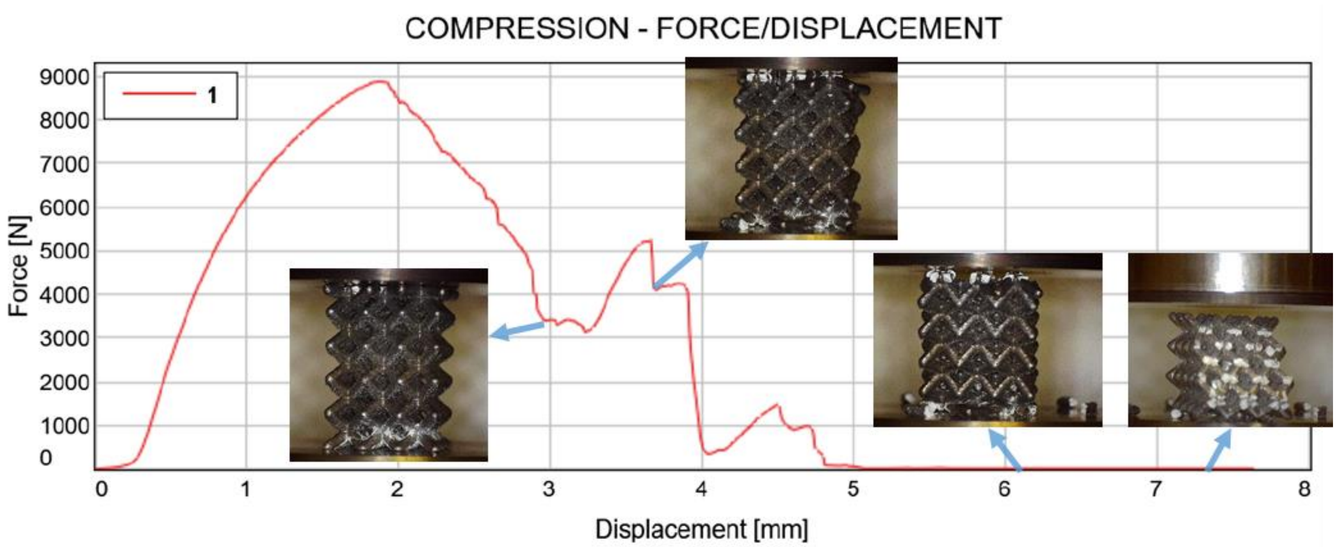

Figure 115: Compression test with displacement rate of 1.2mm/min

Unfortunately the tilting and consequent incomplete test results as well as limited numbers of samples instead of the recommended five as outlined in ISO 13314:2011 [190] meant that the intended comparison could not include results from the compression test. It is considered that in future tests, including skin plates at both sides of the lattice to avoid this sliding effect. The results of the three FEA models however can be seen in Figure 116. While the XCT model showed a maximum Von Mises stress of $4.0\text{x}10^9$ Pa, the CAD showed a maximum Von Mises stress value of $5.4\text{x}10^9$ Pa and CADwDS showed a maximum Von Mises stress value of $4.6\text{x}10^9$Pa. This was due to the XCT part being slightly oversized compared to CAD which was approximately the case for the CADwDS. The original CAD mesh also had sharp angled edges leading to increased stress concentration. This result clearly highlighted how the CADwDS had a closer simulation property to the actual AM part than the CAD with its ideal geometry.

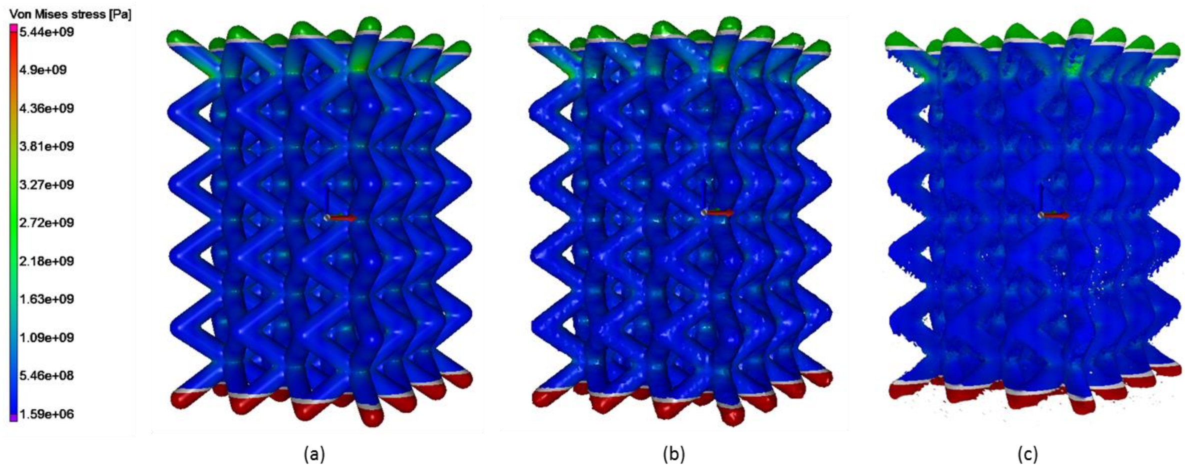

Figure 116: Von mises stress distribution for CAD (a), CADwDS (b) and XCT volume analysis (c).

Nevertheless, and while the CADwDS had closer results to XCT FEA than the original CAD, the amplitude and frequency values used to design the CADwDS in Ntop software were tweaked manually to have a closer geometry to the XCT model. While this manual method proved a proof of concept and was considered reasonable for this initial test, the study shown below focused on investigating correlation between the amplitude and frequency parameters of Ntop software and the commonly used areal surface roughness parameters. Correlating the Ntop parameters to realistic areal surface roughness parameters should allow a repeatable and automatic process to add roughness to models that is reliable and cost effective during the design phase of AM lattice structures.

6.3. Parametrically Designed Surface Topography on CAD Models of Additively Manufactured Lattice Structures for Improved Design Validation

a) DOE to evaluate correlation between Ntop variables and areal surface variables

As seen discussed above in section c) and clearly shown in Figure 49, the different methods in literature to virtually "include" additive manufactured lattice deviations in the original CAD focused mainly on dimensional deviations with no mention of surface topography or ways to design or measure for it. After the initial proof of concept shown above, the goal of this experiment was to evaluate the correlation between Ntop surface roughness module variables (amplitude, frequency, shape and seed) against areal surface parameters such as Sa and more (ISO 25178-2:2012). While Ntop software company released this surface roughness module with the intention of designing and additively manufacturing custom surface topographies, LPBF AM machines are not capable of reaching the resolution of most designed surfaces carried out using the module. Consequently, the goal of this study was to use the module to "design in" the anticipated surface topography on CAD of lattice structures using areal surface parameter as input values prior to manufacturing, allowing for improved design validation.

In this study, the Ntop module feature called "Surface Roughness" which is based on the Simplex Noise [349] uses three main inputs; the amplitude, frequency and seed parameters. These parameters are usually manually attributed and has not been linked before to the common areal surface roughness parameters. In this regard, a Design of Experiment (DOE) [38] was performed to try and establish correlation between Ntop parameters and areal surface parameters.

Ntop parameter defined as the frequency, is a unitless scalar that affects how coarse the surface is in the sense that higher values will have greater spacing between topography elements and may appear smoother. Amplitude (mm) is defined by Ntop as a scalar field. of which higher values leads to taller peaks and deeper valleys. Seed is defined by Ntop as a unitless integer used to generate randomness using algorithm based on Simplex Noise [349]. Figure 117 and Figure 118 show how changing the Ntop surface roughness affects the surface height values in relation to their nominal form for both a planar and cylindrical shape respectively.

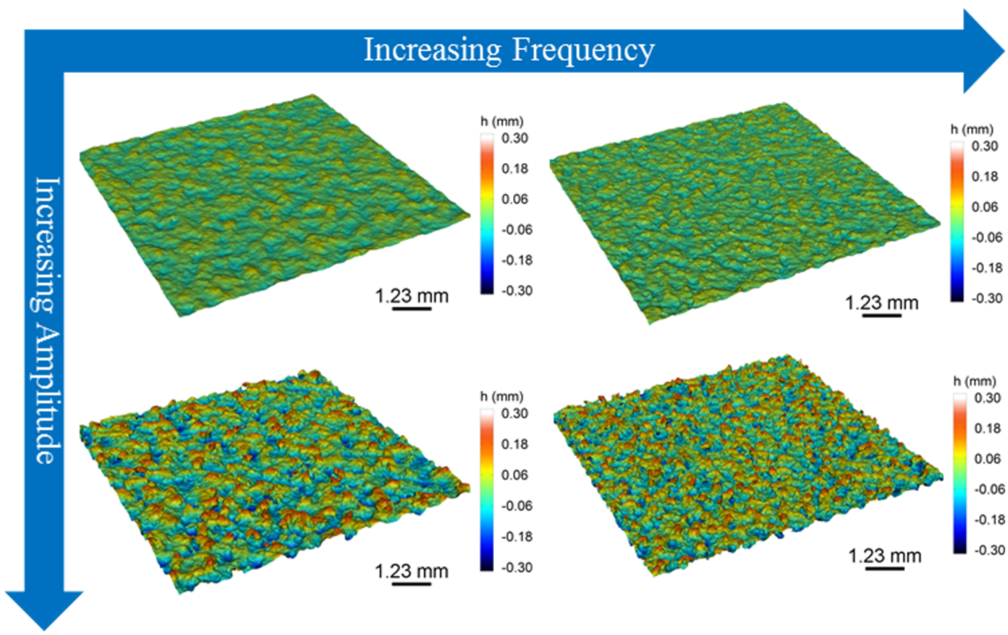

Figure 117: Changing the frequency and amplitude on a 10x10 mm planar surface [344].

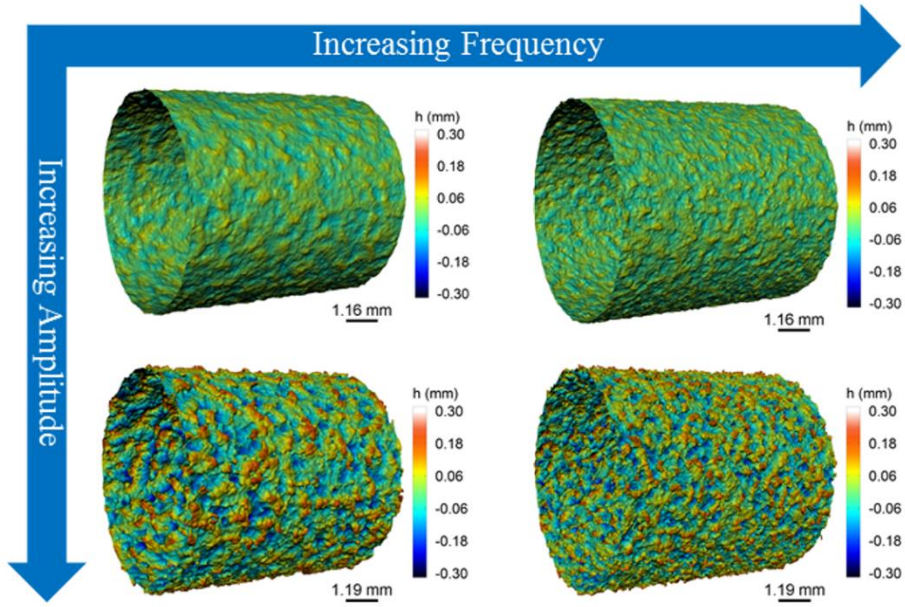

Figure 118: Changing the frequency and amplitude on a cylindrical surface with diameter of 8 mm and height of 10 mm [344].

As outlined previously, a DOE was performed to evaluate correlations between Ntop parameters and areal surface parameters. To achieve this, a full factorial DOE was performed using a total of four factors. Frequency factor had the following values: 1250, 1500 and 1750. Amplitude factor had 0.1 mm, 0.2 mm and 0.3 mm and seed factor was one, two and three. A shape factor was also added and was either a plane or cylinder as seen in Figure 117 and Figure 118. Using these factors and their values, 54 DOE samples were generated and the areal surface parameters Sa, Sq, Spd and $\hat{a}$ was extracted for each one of them. The planar surface seen from Figure 117 had dimensions of 10 x 10 mm while the cylindrical shape seen in Figure 118 had a diameter of 8 mm and height of 10 mm. The dimensions of the chosen plane and cylinder were chosen to be approximately closer to the dimensions of the lattice used in this study, which has a box size of around 15x15x25 mm. The size of the mesh feature was 0.03mm. Having more than one shape (planar and cylindrical) was used to investigate if the shape factor affected the extracted areal surface parameters. The frequency and amplitude DOE range values were chosen from the author experience and previously shown initial study. Future research can include more values as will be later explained.

$$\hat{a} = max\{Sp, Sv\} \tag{13}$$

$$Spd = \frac{\#peaks}{A} \tag{14}$$

After generating 54 samples using a developed Ntop script to automate the operation, areal surface roughness parameters were extracted by Luca Pagani, and main effect plots were produced to investigate if any correlation existed as seen below in Figure 120. The main two parameters used are, as will be explained more in the following section, $\hat{a}$ and *Spd* of which the equations can be seen in equation (13) and equation (14) seen above. The parameter $\hat{a}$ is defined as the highest value of either Sv, which is the maximum pit value or Sp, which is the maximum peak value. *Spd* on the other hand, is the density of the peaks in a certain area. The A area in the formula of Spd is from the surface area of the surface plane or cylindrical form of the cylinder, while the number of peaks ($\#peaks$) is obtained after applying the watershed segmentation using Wolf pruning [350,351]. Watershed segmentation is used as a method to apply feature-based surface analysis by partitioning the surface into different features. The method can be compared to water being poured on the surface, filling the different pits, and creating ridge lines using contact points between different filled pits [352]. However, using this method alone can negatively lead to multiple peaks and pits since a mere difference in height can create a separate partition. Wolf pruning comes at this stage to remove regions at a certain height/depth threshold and suppress the over-segmentation challenge [351,352]. Form removal and areal surface data extraction in this Chapter was done by Luca Pagani.

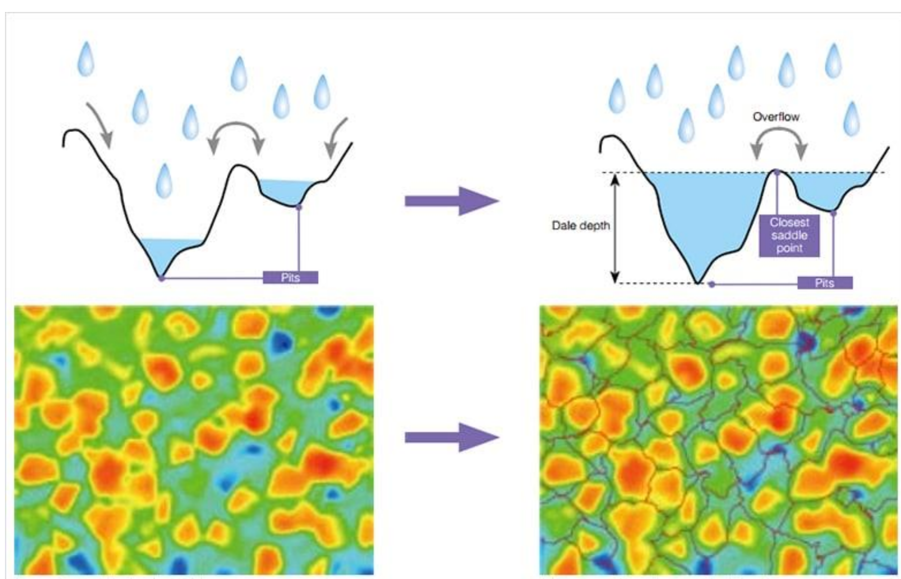

Figure 119: Watershed and Wolf pruning applied on a surface [352].

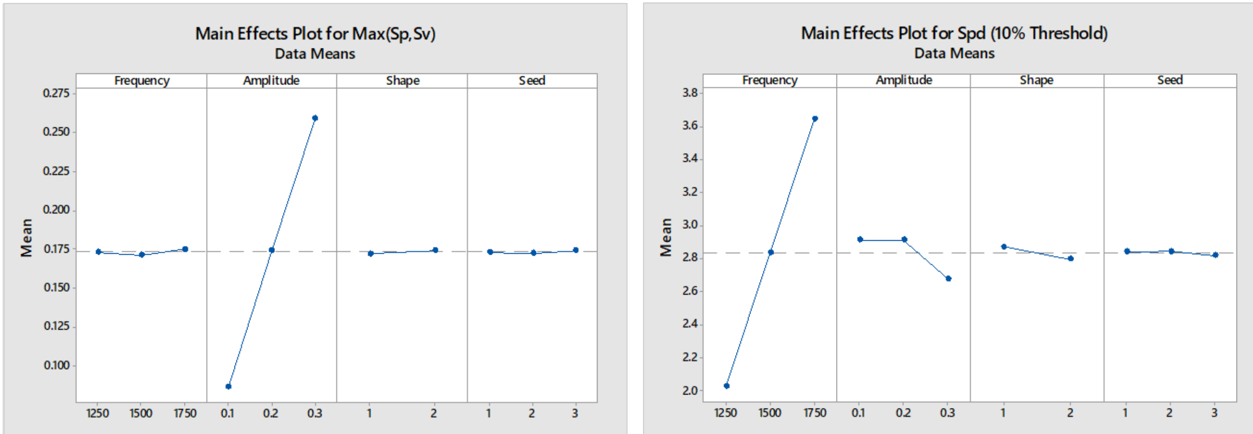

Figure 120: Main effects plot between Ntop parameters and areal surface parameters Spd and Max(Sp,Sv) [344].

From the main effects plot shown above in Figure 120, it can be seen that the Max(Sp,Sv) or $\hat{a}$ parameter has a clear correlation with the Ntop amplitude parameter. The obtained Max(Sp,Sv) is slightly lower than each chosen amplitude, but the correlation is clear and a trendline can be used for prediction. As for Spd, and as expected, a clear connection can be seen in regard Ntop frequency parameter.

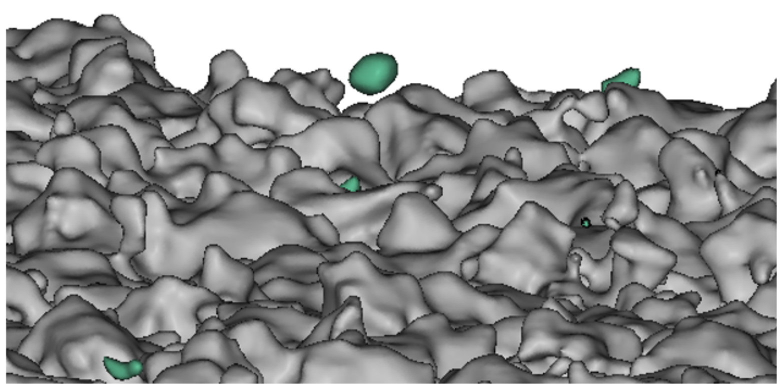

Figure 121: Unwanted particles coloured in green when using high amplitude (0.3 mm) [344].

It can also be seen in Figure 120 that at high amplitude (0.3mm) the Spd value was lower. After investigating the source of this issue and as seen in Figure 121, it was clear that at high amplitudes, the peaks sometimes do not “stick” to the surface, creating physically meaningless particles that are eventually removed by isolating the manifolds, this leads to lower Spd. Since this issue mainly appears at high amplitudes with no great significance on the study, future research will try to investigate it further. As for Ntop shape parameter, whether the shape was planar or cylindrical, no significant impact can be seen on the extracted Spd and $\hat{a}$ as clearly seen in Figure 120. Lastly, the seed number, responsible for generating different stochastic surface did not have any significant impact on the surface extracted parameters as also seen in Figure 120. Henceforth, to design a custom surface with a specific Spd and $\hat{a}$, the frequency and amplitude parameters can be used respectively without worry on the impact of the seed number and shape. The DOE had a limited range of amplitude and frequency values meaning that future studies have to be performed with broader limits.

While *Spd* and $\hat{a}$ parameters were linked to frequency and amplitude, other areal surface parameters were also extracted and found to be correlated with amplitude like Sa and Sq as seen main effects plot below in Figure 122. The surface height-based Sa and Sq parameters are highly correlated to each other, so similar effects plots are expected.

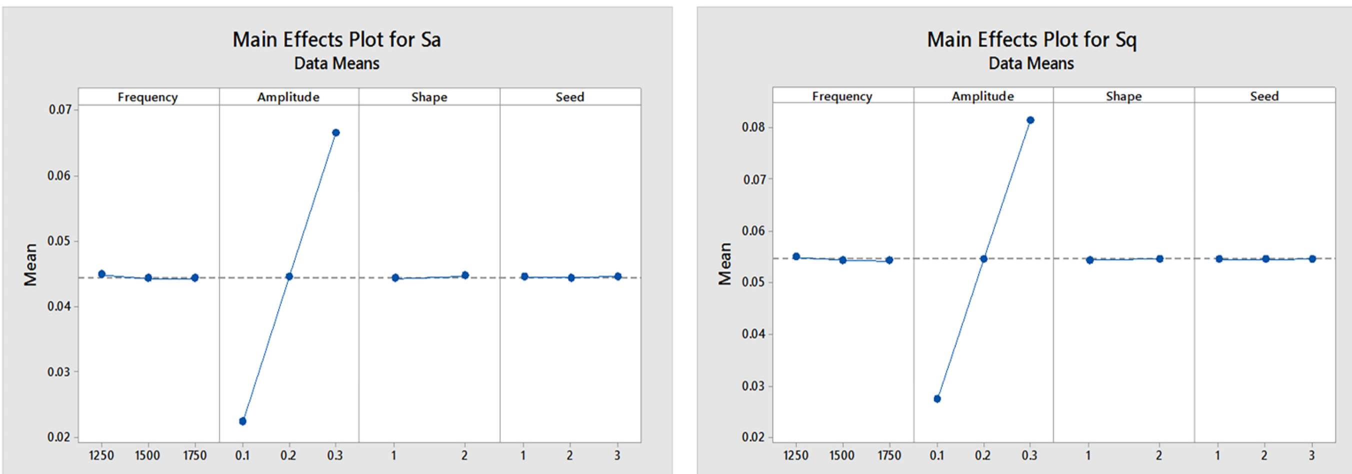

Figure 122: Main effects plot showing Sa and Sq correlation to amplitude [344].

As outlined correlations above, trendlines can now be used to design a specific *Spd* or $\hat{a}$ from frequency and amplitude, respectively. To do so, the equations shown below were modelled from the link of *Spd* to frequency as seen in equation (15) and $\hat{a}$ to amplitude as seen in equation (16). The R-square of equation (15) was 96.1 % while the R-square value of equation (16) is 99.6 %. These equations were used to develop a script to design custom surface roughness to have a specific Spd and $\hat{a}$ on a CAD, which will be the mainly used parameters as seen in following sections.

$$Spd = 0.0032\, f - 2.013 \tag{15}$$

$$\hat{a} = max\{Sp, Sv\} = 861.6\, a + 0.9 \tag{16}$$

$$Sa = 221.4\, a + 0.2 \tag{17}$$

$$Sq = 271.2\, a + 0.3 \tag{18}$$

b) Extracting surface roughness data from AM lattice using XCT

As seen from the section above, it was possible to find strong correlation between Ntop software surface module parameters and areal surface parameters. This allows for the design of surface topography on to CAD using areal surface parameters as inputs. Before designing surface topography on a lattice CAD, it was important to know variation of the surface roughness data of the additive manufactured lattice, in both its up skin and down skin of the struts [199].

The lattice used in this study is the same one used in the initial experiment above in section 6.2 and can be seen side to side with its XCT volume rendering equivalent in Figure 123 (b). Since no surface post-processing operation was performed and as discussed in the literature above, an overhang angle usually leaves unwanted surface on the downward surface, which was also the case for this part [203].

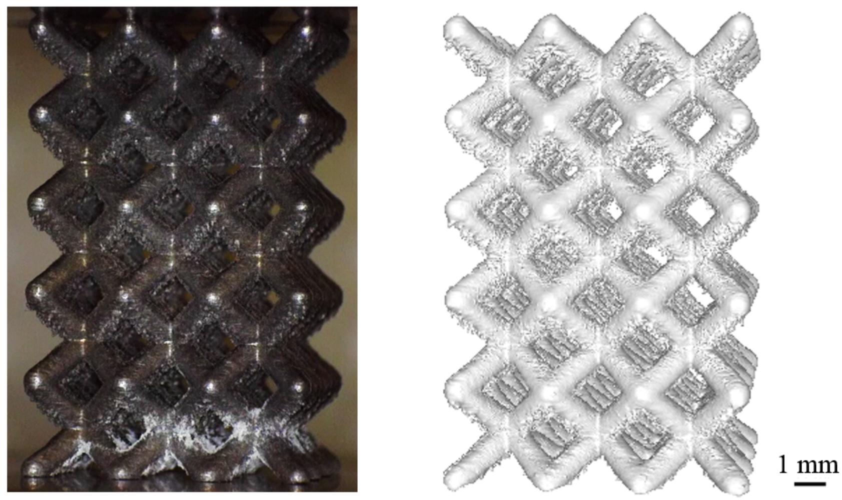

(a) (b)

Figure 123: Additive manufactured BCC lattice (a) and X-ray CT volume rendering (b) [344].

Extraction of surface from AM parts can usually be achieved using multiple methods and instruments ranging from confocal microscopy, focus variation and more. However, XCT was used for the present study as this method is optimal to cases where the lattice is internal, inaccessible with line-of-sight tools and can also not be sliced or cut destructively, thus this suggests non-destructive method like XCT as the ideal candidate, if not the only one, that can provide holistic analysis of all inaccessible struts of the lattice. Nevertheless, before XCT scanning, it is important to make sure that the voxel size is small enough to capture the details of the surface to be measured. While not a conclusive method, the study published by Townsend et al. [86] mentions that the voxel size needs to be at least half or lower than the expected *Sa* of the surface to be measured. To assess the *Sa* of the lattice, an external strut that has direct line of sight has been measured using a focus variation instrument, Alicona G4, such systems are commonly used in industry to asses AM surfaces.

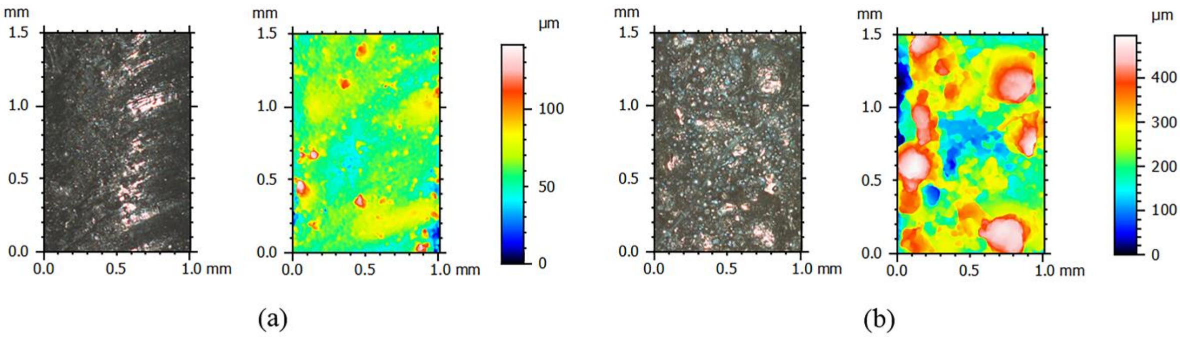

Figure 124: Up and down skin surface of the lattice strut measured using focus variation machine Alicona G4 [344].

Both the up skin and down skin have been captured using lateral spacing of 1.75 µm and no cut off filter, a local region of interest (ROI) of the size 1.5mm x 1mm has been analysed as seen in Figure 124. After removing the form of the extracted surface using an approximated nominal cylinder, the *Sa* of the down skin was found to be 81 µm while the *Sa* of the up skin was found to be 13 µm. While the *Sa* of the down skin is more than double the voxel size used, which is more than ideal, the Sa of the up skin was lower than the voxel size. Nevertheless, the down skin of the lattice has an Sa that is multiple times higher than the Sa of the up skin, which contributes to more discrepancy between the original CAD and printed part making it more significant than the up skin. In this regard, the voxel size was considered sufficient if not ideal. The up skin of the lattice will nevertheless be studied while acknowledging the XCT resolution limitations in its regard. Different studies have compared extracted and analysed surface roughness XCT results with focus variation one seen in [86,264].

To extract the surface from the volume XCT scan of the lattice, a Boolean intersect operation was done between the lattice and a cube that has the size of one lattice cell. This operation allowed the thresholding and creation of a region of interest. As seen in Figure 125, four struts from the region of interest were used to extract four up skin surfaces (T1,T2,T3,T4) and four down skin surfaces (B1,B2,B3,B4). The size of each isolated up or down skin was 1.5 mm x 1 mm which was carried out at the centre and restricted by the strut diameter. To make sure that the study focused on the extraction and design of surface roughness, it was assumed that the distribution of the surface roughness was similar all along the lattice and that the measured isolated regions of interest shown in Figure 125 represented the surface roughness of the whole lattice. This was reflected on the approximate similarity between the extracted surfaces, although, future research can solely focus on repeatability of surface roughness across the lattice and factors affecting it.

To remove form from the isolated surface skins, a cylinder was used as the nominal form. The coefficients of the reference cylinder were computed, minimizing the orthogonal distance between the measured points and its orthogonal projection of the reference surface. The method has been developed by Luca Pagani and detailed explanation can be seen in [353].

Using generalised parameters of ISO 25178-2:2012, the manifold parameters were directly computed on the mesh [354]. The result can be seen in Figure 126 where the distance between the mesh and the estimated nominal form can be seen for both the down skin (B1) and up skin (T1) of the lattice strut.

The removal of the form allowed for the analysis of the surfaces and areal surface parameters were calculated. Common parameters like *Sa*, which is the average areal surface roughness or *Sq*, the root mean square surface height were extracted. The segmented regions using 10% Wolf pruning can be seen in Figure 127 of both the down skin (B1) and up skin (T1). Formal definitions can be seen in study of Pagani et al. [354]. The extracted surface parameters *Sa*, *Sq*, *Spd* and $\hat{a}$ of the region of interest lattice struts show in Figure 125 can be seen in Table 12 where results obtained after isolating regions of interest from the XCT scan of the AM lattice and extracting the common areal surface parameters are summarised. It can be seen how different struts had similar values for up skin or down skin.

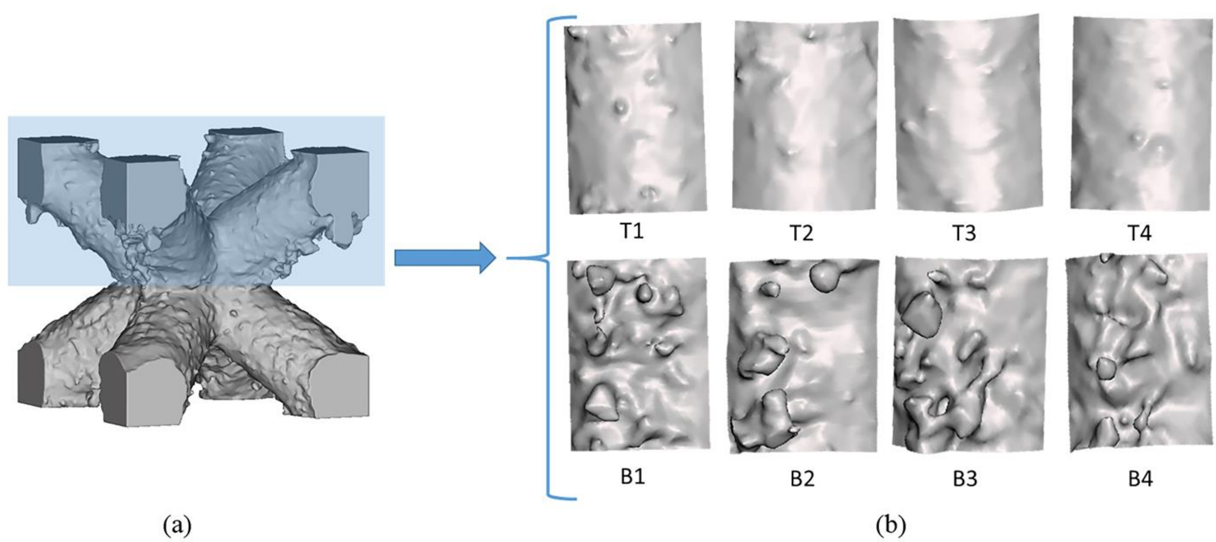

Figure 125: Isolated lattice cell used to extract four up skin surfaces (T1,T2,T3,T4) and four down skin surfaces (B1,B2,B3,B4) to estimate the surface roughness of the lattice [344].

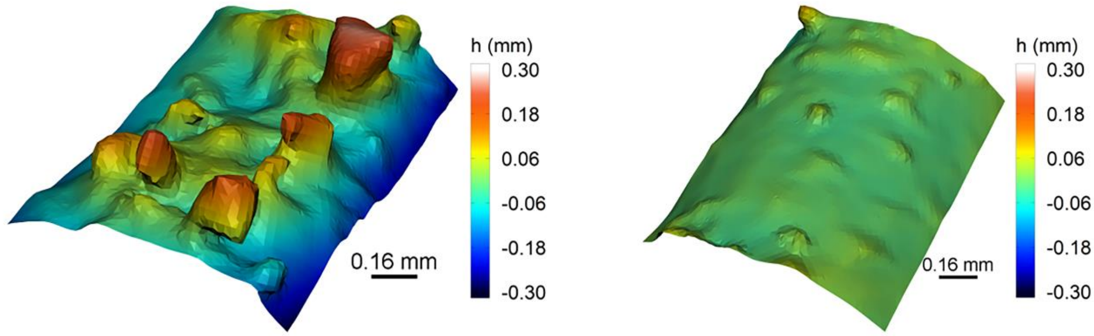

(B1) (T1)

Figure 126: Height map showing distance between the points of the mesh and the estimated nominal form for a down skin (B1) and up skin (T1) of the lattice strut [344].

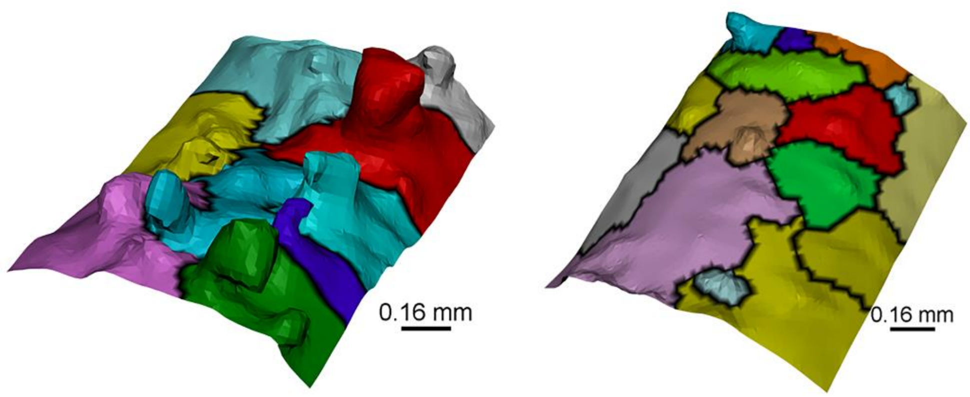

(B1) (T1)

Figure 127: Watershed segmentation using Wolf pruning of both the down skin (B1) and up skin (T1) strut of the lattice [344].

Table 12: Extracted surface parameters of the region of interest struts of the XCT lattice [344].

	XCT lattice surface parameters							
	Up skin (T)				Down skin (B)			
	Sa (μm)	*Sq* (μm)	*Spd* (1/ mm²)	*â* (μm)	*Sa* (μm)	*Sq* (μm)	*Spd* (1/ mm²)	*â* (μm)
Strut 1	9.7	13.4	7.8	107.5	65.4	87.2	5.0	295.3
Strut 2	8.6	10.7	6.7	49.7	69.5	85.2	2.9	299.6
Strut 3	8.7	11.0	8.9	42.4	54.1	69.7	3.6	212.1
Strut 4	9.0	11.2	7.9	50.2	48.9	63.5	4.6	284.8
Standard deviation	0.5	1.2	0.9	30.2	9.6	11.6	1.0	41.0
Average	9.0	11.6	7.8	62.5	59.5	76.4	4.0	272.9

c) Design of CADwDS using DOE results and comparison with AM lattice structure

In section 6.3, a DOE was performed on planar and cylindrical surfaces resulting in possibility to design custom surface topography on a chosen CAD. However, applying the same technique for the CAD of a lattice will result in a lattice with the same surface topography for both the up and down skin, which is not realistic when compared to the produced AM lattice. To solve this challenge, The angle where most down skin surface existed in the XCT scan of the AM lattice was found to be around 60° degrees (a). This was done by manually placing two planes intersecting the centre of the strut and adjusting their angle until the down skin was covered, unveiling the approximated 60° degrees. Therefore, the smaller lattice seen in Figure 128 (b) was dimensioned and its centroid was placed in a way to also cover for 60° degrees of the down skin. This led to a smaller lattice with a diameter of 0.75mm and a centroid touching the surface of the main lattice. This method was developed and tested for this type of lattice at this specific size, the discussed angle might change for lattices of different strut diameter and print settings meaning that further studies will have to be completed for a more conclusive protocol.

To apply the findings and as seen in Figure 129 (a), a general surface was first created representing the up skin, which was then linked using a Boolean union to a smaller lattice that will represent the down skin surface, seen in Figure 129 (b). This will result in a lattice with different up and down skin surface as seen in Figure 129 (c). This method however still lacks the possibility of modelling cavities, which can in future studies be investigated, in order to have a digital twin with closer defect representation to the additive manufactured part.

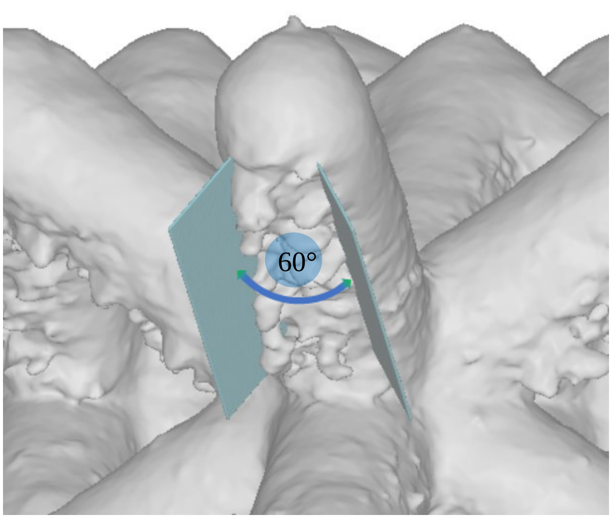

(a)

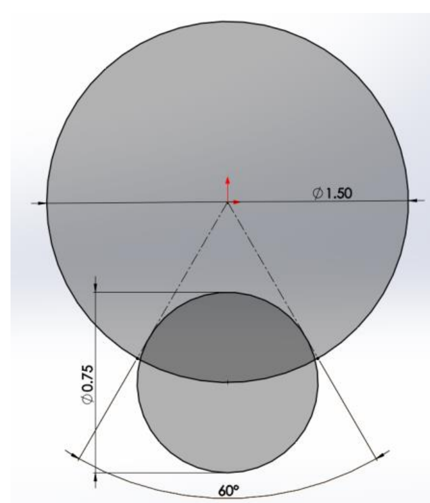

(b)

Figure 128: Down skin surface angle from the XCT in (a) and the cross section showing where the small strut in Figure 129 fits when added to the lattice [344].

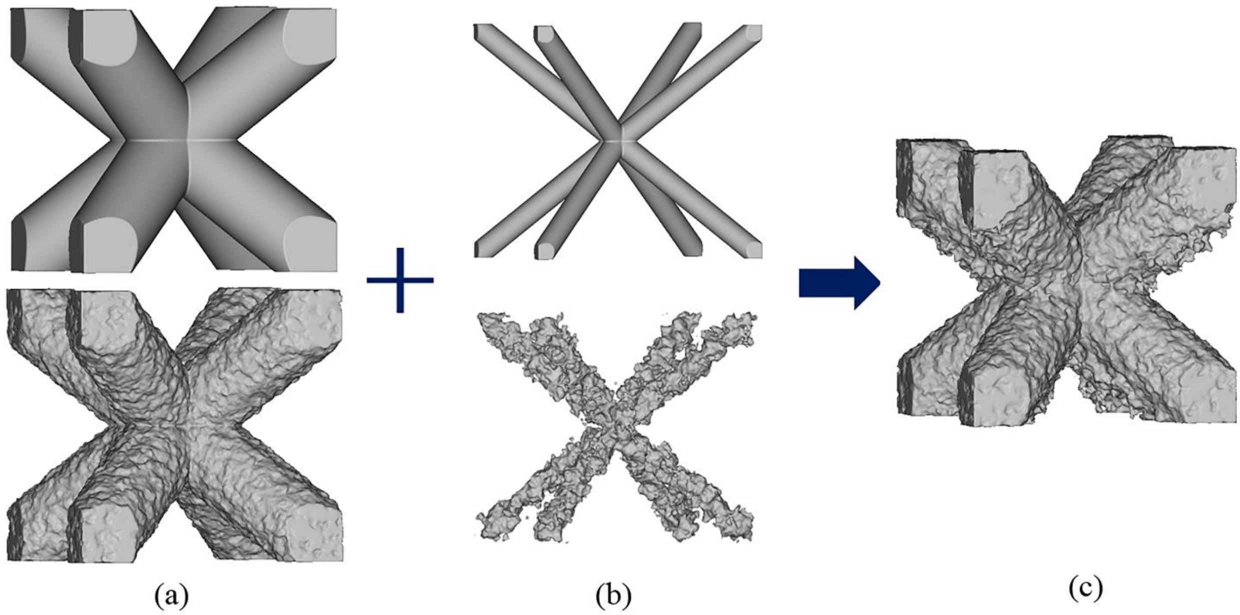

Figure 129: General surface applied on the lattice (a), down skin surface applied on a smaller lattice (b), Boolean union of (a) and (b) resulting in a lattice with up and down skin roughness differences (c) [344].

The modelled equations shown above from the DOE study were used to interpolate and design the same surface roughness measured on the XCT extracted surfaces of the AM lattice. From Table 12, and using the average extracted Spd and $\hat{a}$ of the AM lattice as well as the modelling equations (15) and (16), the interpolated amplitude and frequency to be used in Ntop can be seen in Table 13. Using the interpolated values shown in Table 13 and method explained in Figure 129, CAD with designed surface (CADwDS) was generated as seen in Figure 130. Ultimately, lattice strut skins from the CADwDS were extracted and their surface roughness analysed to be compared with the AM lattice ones as seen in the following section.

Table 13:Interpolated frequency and amplitude used to replicate AM lattice surface.

CAD with designed surface (CADwDS) interpolated frequency and amplitude			
Up skin		Down skin	
Interpolated Frequency	Interpolated Amplitude (µm)	Interpolated Frequency	Interpolated Amplitude (µm)
2964	72.0	1850	315.2

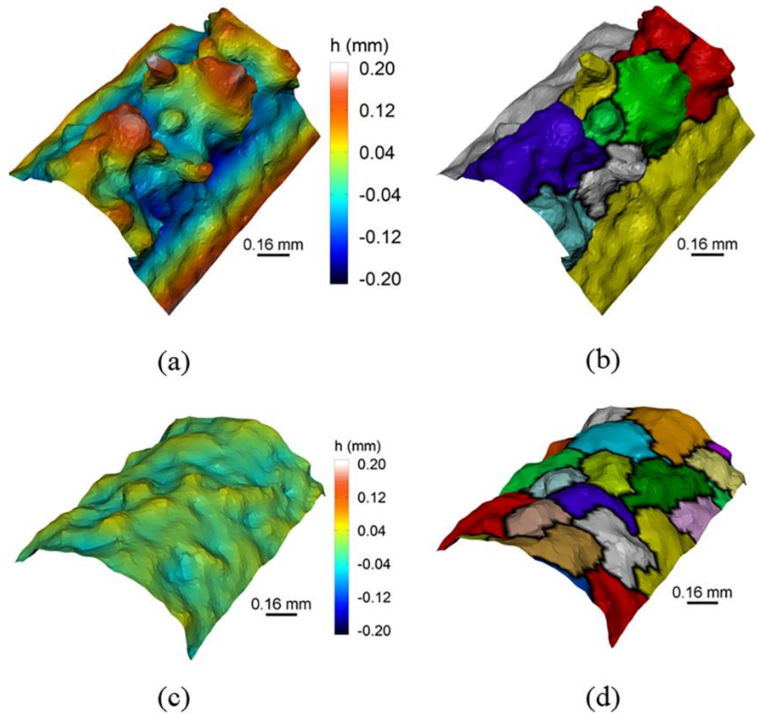

Figure 130: CAD with designed surface (CADwDS) of the lattice showing height map of down skin (a) and up skin (c) and watershed segmentation of down skin (b) and up skin (d) of a strut [344].

After generating the CADwDS, a comparison was performed between the latter surface data and the extracted AM lattice XCT surface data. The comparison which can be seen from Table 14 shows that the biggest difference is in the up skin average Spd of the XCT different to the CADwDS one with a value of 56.7%. This high difference was expected and is due to interpolated up skin value, which is 2964 (Table 13), being outside the studied DOE boundaries which had a maximum value of 1750. This suggested that the relationship between Spd and frequency might not be linear. The up skin however as mentioned in methodology is not of significant importance due to its low amplitude compared to the down skin which usually has far more significant surface and hence potentially more detrimental effects on lattice properties such as compressive strength or fatigue. As for the rest of the comparison in Table 14, the maximum difference was found to be less than 15%. The difference between the $\hat{a}$ of the XCT AM lattice and CADwDS was found to be 15.1% and 9.5% for up skin and down skin, respectively. While the difference between the Spd of the XCT AM lattice and CADwDS was found to be 2.0% showing a good similarity between the two. It can also be seen that in general, the down skin values of the CADwDS were more similar to the XCT AM one compared to the up-skin values.

Table 14: Comparison of extracted areal surface roughness parameters between CADwDS and the XCT ones previously shown in Table 12 [344].

	CAD with designed Surface (CADwDS)	
	Up skin	Down skin
Spd average of four struts (1/ mm²) [standard dev.] Average *Spd* Difference to XCT in (%)	12.3 [2.0] (56.7%)	4.0 [1.1] (2.0%)
$\hat{a}$ average of four struts (μm) [standard dev.] Difference to XCT average $\hat{a}$ in (%)	53.0 [2.8] (15.1%)	247.1 [26.0] (9.5%)

The dimensional comparison between the generated CADwDS and the XCT AM lattice was also performed. To do so, an alignment was first performed using a Gaussian best fit registration. The search distance had a maximum of ± 0.5mm which was based on the diameter of the strut. The resulting deviation analysis can be seen from Figure 131. The design in the figure is of the XCT AM lattice and on the left the comparison with the original designed CAD while on the right the comparison with the CADwDS.

The colour map show in red additional material making a positive deviation and in blue subtracted material making a negative deviation. Qualitatively and from Figure 131 (a), it can be seen how the comparison with the original CAD show a domination of red colours highlighting how the AM lattice had unwanted additional material mainly focused on the down skin of the lattice. Figure 131 (b), it can be seen how there are fewer red colours which are mostly replaced by green and in some occasion blue. The occasional blue colour was expected since the generated CADwDS will not have generated surface on the down skin that is exactly overlayed and touching the AM lattice down skin. The obtained results can also be affected by the complexity of the compared geometry and alignment used. While the same alignment was applied on both XCT versus CAD and XCT versus CADwDS, future research can investigate the possibility to quantify the effect of the alignment on the obtained result.

Quantitively, it can be seen from Table 15 how the mean deviation between XCT and original CAD is 44.6μm while the mean deviation between XCT and CADwDS was found to be 14.4μm, which is three times less. This result shows how in this study, the generated CADwDS using this method not only produces a lattice that has a surface closer to the manufactured AM lattice but one that is also dimensionally closer.

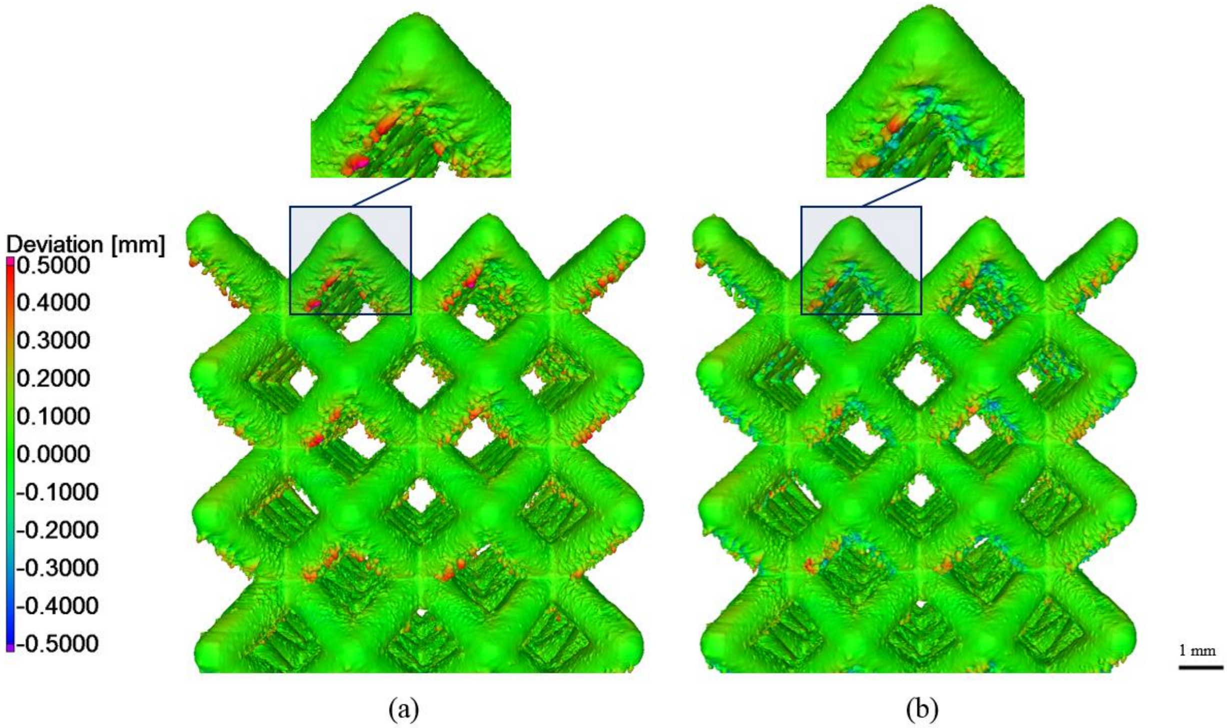

Figure 131: colour map showing the deviation analysis of XCT versus CAD (a) and XCT versus CADwDS (b) [344].

Table 15: Dimensional comparison using deviation analysis of XCT versus CAD and XCT versus CADwDS [344].

	XCT versus CAD	XCT versus CADwDS
Mean Deviation (µm) [standard dev.]	44.6 [67]	14.4 [88.2]

6.4. Chapter summary

In this chapter, a method has been developed to reproduce the lattice surface of LPBF process to avoid using the original perfect CAD and instead use a closer to reality CADwDS. The steps followed to reach this result start by assessing the surface roughness of the produced AM lattice by using XCT to extract the skins and the right regions of interest. Since the design of the surfaces on the CAD is built from scratch and does not rely on directly using XCT data, the initial measurement for a specific lattice and AM machine settings is only expected to be done once. This method, allowed for the first time the correlation between Ntop surface roughness design parameters like frequency and amplitude to areal surface roughness parameters. This allowed for the development of a script that directly inputs areal surface parameters to design a CADwDS. While the study focused on using Spd and $\hat{a}$ as inputs in the developed script, other areal surface parameters like Sa and Sq of which the correlation has been studied in the DOE can also be used instead of the $\hat{a}$ parameter using equation (17) and (18) and respectively. To simplify the use, two lookup tables has also been developed and can be seen in Table 16 and Table 17. The lookup table can be used to directly choose the right input value of frequency and amplitude for a desired Sa, Sq, $\hat{a}$ or Spd value as long as the values are within the DOE intervals. Instead of having a fixed surface on the whole lattice which does not necessarily reflects the reality of the produced AM lattices, the study includes a novel method to design a local surface roughness that is dependent on the location of the surface, whether it is located in the up or down skin of the lattice struts.

Table 16: Lookup table based on DOE results showing Max (Sp,Sv), Sa or Sq when selecting an amplitude between 0.05 mm and 0.3 mm in the surface roughness tool in Ntopology Software [344].

Lookup table for Amplitude			
Amplitude (mm)	*max (Sp, Sv)* (µm)	*Sa* (µm)	*Sq* (µm)
0.05	44.0	11.3	13.8
0.1	87.1	22.4	27.4
0.15	130.1	33.4	40.9
0.2	173.2	44.5	54.5
0.25	216.3	55.6	68.1
0.3	259.4	66.6	81.6

In the scenario where a new lattice is to be additively manufactured. It is expected that user can either find if a similar lattice angle and strut that has been previously printed and might have the same surface or additively manufacture at least one lattice of the new design and analyse its up skin and down skin surface values. These values are expected to be used for any future lattice that shares the same strut size and angle that is to be printed in the same material and AM machine settings as the previously measured strut. This method has allowed for the design of a CADwDS of which areal surface roughness has been compared to the AM produced one, a comparison that has not previously been reported in the literature.

Table 17: Lookup table based on DOE results to give an idea on the obtained Spd when selecting a frequency between 1250 and 1700 in the surface roughness tool in Ntopology Software [344].

Lookup table for Frequency	
Frequency	*Spd* (1/ mm²)
1250	2.0
1300	2.1
1350	2.3
1400	2.5
1450	2.6
1500	2.8
1550	2.9
1600	3.1
1650	3.3
1700	3.4

The comparison has also been carried for dimensional data between all components including the original CAD, XCT of the additive manufactured lattice and the study's generated CADwDS. The comparison was completed using an alignment and deviation analysis that showed how the XCT of AM lattice versus CADwDS was a third of the deviation between the XCT of AM lattice versus original CAD. The resulting CADwDS had a variable strut diameter, centroid and cross section while not being designed using XCT data as a direct input, which has also not been previously reported in the literature. This study is a strong foundation for future research that can focus on improving the design phase of lattice structures and making it more cost effective with realistic surface topography that can with further work be even tied to the chosen AM machine, setting and material used. This is a critical step for the innovation field of lattices of which surface plays a paramount role especially when surface treatments of lattices are usually complex, costly and sometimes not even possible if there are enclosed inside the part.

Consequently, more research in this field will allow further experiment with faster AM printing times that will indeed lead to rougher surfaces but can be tested using FEA, CFD or fracture simulations all during the design phase instead of a perfect CAD making the process more reliable and cost effective. This capability will allow a more realistic digital twin that is resembling the actual part in different AM process stages. Future research can also look at analysing the areal surface data of more struts allowing for evaluation of surface roughness repeatability across the lattice and also further comparison of CADwDS surface data to XCT one. Finally, having accurate designs that better represent the final part dimensions and surface will be more critical in a future where AM is expected to be used for mass customisation [355]. This means that each part to be produced will be different making the cost of testing after manufacturing or XCT will be very high making analysis and testing in the design phase more attractive for this kind of scenario.

Furthermore, LPBF process can often be challenging for reaching extremely precise tolerances compared to other processes like CNC machining. This means that in future research, when designing the CADwDS, instead of having a single input for all or up skins and one for all down skins, both of them can be chosen as a range instead of single value. This addition can possibly better capture the small scale stochastic areal surface differences formed at the surface of AM lattice structures, and also possibly better finite element simulations as proved in [175]. Further research in this field can lead to multiple CADwDS that are designed to be ranging from a least to worst case scenario, capturing the cost effectiveness of the process and design and also leading to a heterogeneous model that is representative of LPBF lattice parts [356].

Finally, the developed script and model in Ntop that assist in designing surface topography on CAD of lattices is based on the results of the DOE experiment. While the results were ideal for this experiment, future research can investigate a broader limit of the factors used in the DOE going to smaller amplitudes and higher frequencies. It is expected for example that research along this path can show better correlation between Spd to frequency, one that might not be linear when a broader range of factors is investigated. Future research can also look at using the generated CADwDS mesh and converting it to a tetrahedral mesh for finite element simulations. An alternative can also be to directly use the generated CADwDS mesh for simulations as supported in software like Altair Simsolid [357]. Finally, future research can have multiple lattices of which the FEA simulations can be compared to physical compression tests respecting ISO standards that are specific to lattices like ISO 13314:2011 [190]. Further discussion can be seen in Chapter 8 section 8.21.1b) and further future work in Chapter 10 section 10.2.

7. Chapter: Development of benchmark artifact for AM lattice structures

7.1. Introduction

The last two chapters presented research programs with novel dimensional (Chapter 5) and surface (Chapter 6) related work, developed to aid in the metrology process of AM lattice structures using XCT. While a logical step was to focus on porosity, extensive work reported in the literature has been completed on the topic, such as research by Amani et al. [227], which managed to include virtual pores in to CAD to improve prediction of fracture location during the design validation stage of lattices.

As a way to improve on the developed methods and have a direct impact on new users of AM lattice structures, this final study hinged on developing a benchmark artefact focused on lattice structures, especially strut-based designs, which has not been previously done in literature. As mentioned in literature review, and from 65 benchmark AM artefacts reported, only two included lattice designs, and was only as a complementary addition with no additional engagement on the measurement procedure, leaving a research gap when it comes to lattice focused AM benchmark artefacts. This study also complements work of the author's research group of which has published on a benchmark artefact to compare and evaluate different AM methods [108] and a benchmark artefact to assess the LPBF limitations when building micro internal features. [358]. The lattice benchmark artefact design, manufacturing in FDM, XCT data acquisition and volume analysis was done by the author. The additive manufacturing in Titanium was done by 3MBIC. The form removal and areal surface parameter extraction was done by Luca Pagani. The work below summarises the novel AM lattice benchmark artefact design, AM in both LPBF and FDM process as well as development and application of a lattice adapted measurement strategy, based on ISO/ASTM 52902:2019. This work has been accepted by Advancing Precision in Additive Manufacturing 2021 Euspen Conference with work titled "Design and measurement strategy of additive manufacturing lattice benchmark artefact" and can be seen in Appendix 12.4.

7.2. Methodology

a) *Design of lattice benchmark artefact*

The design of the lattice used in this study was facilitated using Ntopology software and had a BCC type unit cell with a box size of 18.7x18.7x27 mm. As can be seen in Figure 132 the developed lattice benchmark design had a linear gradient strut diameter change, from 4 mm and thinning upwards to 0.3 mm. Ntop software works using a field-driven design approach facilitated in this case by using the ramp tool. The ramp tool is defined by Ntop as a method to assign new values to a field input in relationship to a reference geometry and with defined boundaries [359]. The reference geometry in this case was a plane positioned at the lowest point of the lattice. From this reference geometry, an input field was assigned and given set boundary values ranging from 4 mm to 0.3 mm which represented the gradient field of the lattice strut diameter distribution.

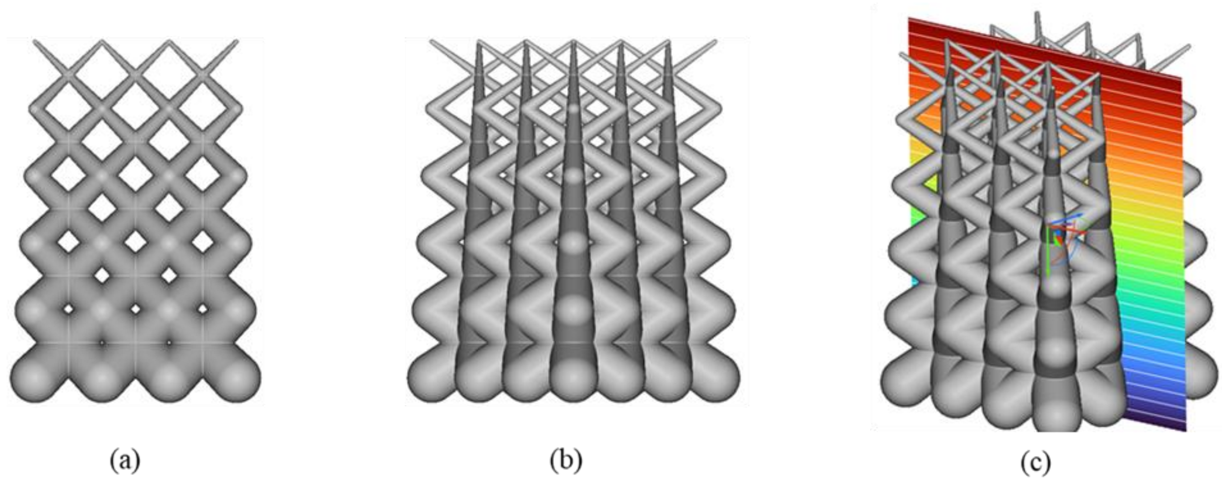

Figure 132: Front (a), 45 degrees side view (b) and perspective view with colour map showing 1 mm spacing gradient lines (c) of the designed AM lattice benchmark artefact rendered in Ntopology.

The generated gradient field can be seen in Figure 132 (c) where the colour map represents the lattice strut diameter thinning (red colour) and where the spacing of contour lines is 0.1 mm. Upon finalising the model, which is called at this stage in Ntop software an implicit design, the model was exported using a mesh size feature of 0.1 mm, preserving the detailed geometry of the part. The file format used was .3mf as it uses far less storage memory without compromising the geometry. For example, in this case, the file size for .STL format was 226 MB compared to only 71 MB in .3MF format. This size difference proves to be crucial in industry where hundreds of parts could be nested to be printed in the same build, necessitating larger computing power if the file size of the parts is significant.

As mentioned in literature in section 3.2.4 related to manufacturing of AM lattices, a lattice model can be exported as a CLI file that can take a contour hatch scanning strategy Figure 133 (b) or single exposure scanning strategy Figure 133 (c). The contour hatch scanning strategy follows the CLI path and usually has fixed laser characteristics while on the single exposure scanning strategy, the enthalpy of the laser is constantly changing to change the melt pool size and henceforth the strut diameter. In cases of very large stochastic lattices, single exposure scanning strategies are usually more suitable.

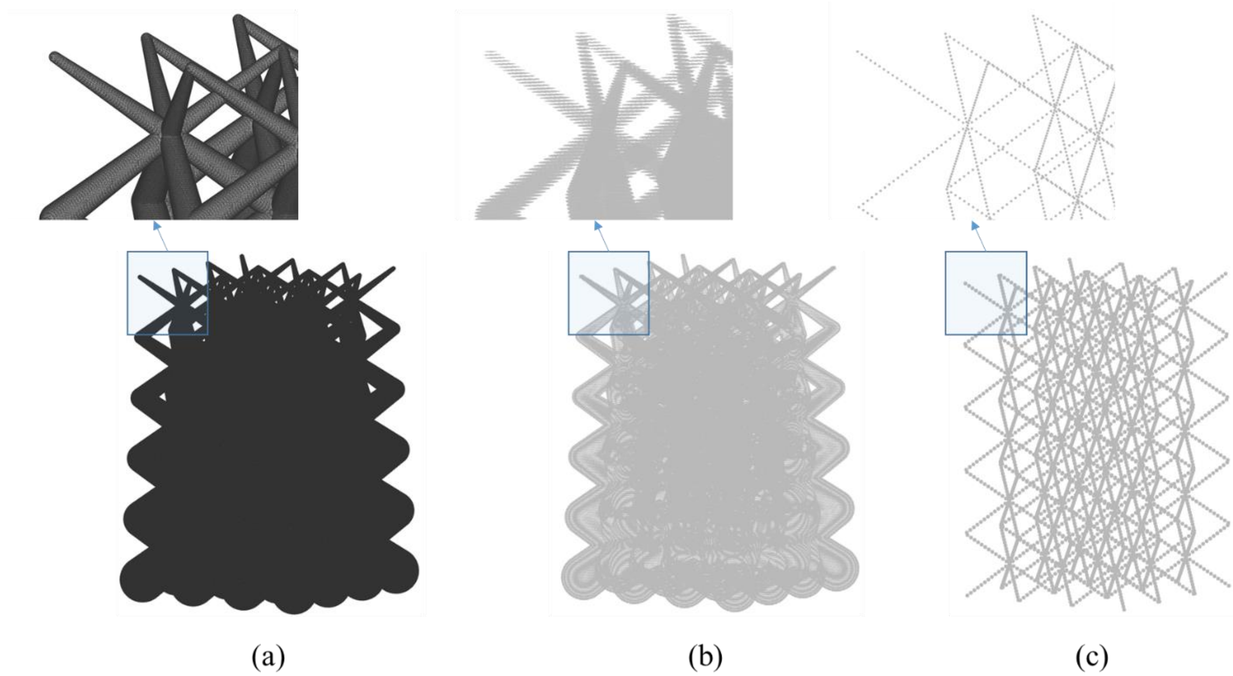

Figure 133: Different lattice export strategies ranging from triangular meshing (a), contour hatch spacing (b) and single point exposure method (c).

b) Measurement strategy using ISO/ASTM 52902:2019 as guideline

While there are many general AM benchmark artefacts in literature, there is still no unique geometric artefact with high consensus that can be used in all scenarios. This is not only due to the different purposes a benchmark artefact can be used for but also due to the measurement strategy that might not always be possible to achieve by the user. When it comes to lattices, it is common practice to carry out a visual inspection and sometimes a calliper or else quick measurement of external features. However, most of these methods are incomplete, and usually have no information on internal lattice features. In other occasions, it is simply impossible to use conventional measurement methods especially for example when the lattice is used as an infill and cannot be reached by line-of-sight instrument.

Using XCT has been a common method in literature to evaluate lattice structures. However, there is still no standardized method to evaluate lattices, a challenge that is highlighted by AMSC and named Gap D26 [105]. To solve this challenge, ISO/ASTM 52902:2019 has been used as a guideline to develop measurement strategies that work for lattice structures, especially strut-based ones. ISO/ASTM 52902:2019 "Test artifacts - Geometric capability assessment of AM systems" has been developed essentially to encompass different test piece geometries that can be used by AM users to evaluate AM system capability as well as calibration. The standard also offers quantitative and qualitative measurement methods that can be applied to the test piece geometries with clear ranking of measurement quality that can be offered by different methods [360].

To interpolate the guidelines in ISO/ASTM 52902:2019 to work for lattices, the pin diameter resolution test piece geometry as seen in Figure 134 can be considered as an equivalent of strut diameter resolution in the case of a lattice structure. This equivalence is seen as ideal since both pin and lattice strut geometry is a cylinder and in both the standard and the suggested design, the cylinder diameter would gradually get smaller. While the standard suggests using optical microscopy or hand measurement tools like micrometres and callipers, the main tool that will be used through this whole study will be XCT. For this specific measurement, the wall thickness analysis module was used which is a protocol that fits the biggest enclosed sphere inside the volume model of which the surface has been determined. Due to the gradient strut diameter, a histogram was chosen as the ideal method to visualise the measured diameter distribution and have it overlayed on the CAD diameter histogram diameter distribution.

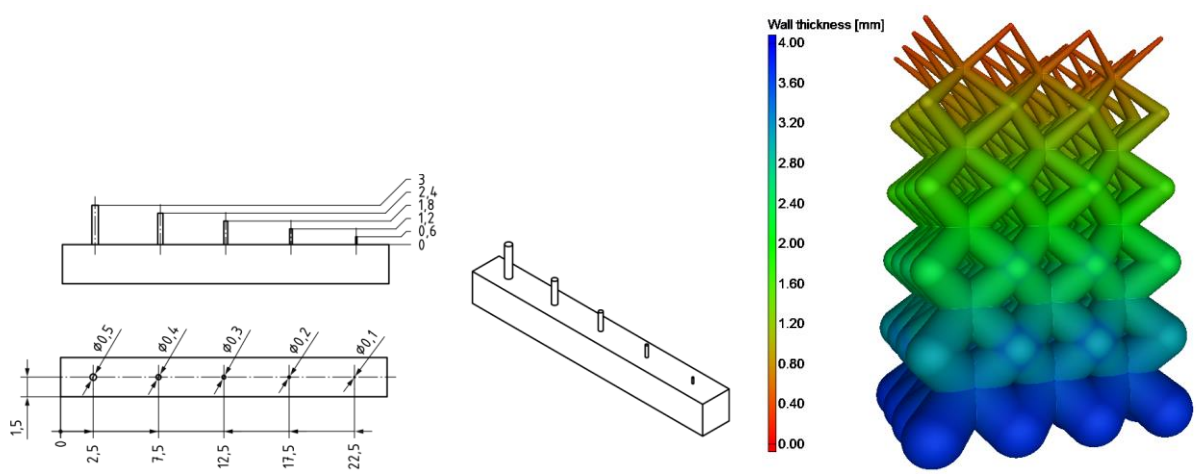

Figure 134:Pin diameter resolution test geometry suggested by ISO/ASTM 52902:2019 [360] *(left) and lattice strut diameter resolution measured using wall thickness analysis on CAD (right).*

Still in dimensional metrology, the positioning accuracy or error alongside each axis can be assessed. To do so, ISO/ASTM 52902:2019 suggests the use of prismatic protrusions a top a rectangular solid base. While the measurement suggestion is to assess the cube position relative to the chosen datum as seen in Figure 136. Also, the spacing between each protrusion can also be measured. It is intended to have multiples of this test geometry, at least three of them each in a specific machine axis direction. To apply this method, an initial idea was to design additional spheres at different corners of the part as done in previously published AM benchmark artefacts [282]. However, instead of designing additional spheres, the new method introduced in VGSTUDIO MAX 3.4.3 named “Create ROI from Wall Thickness Range” [361]was used, which can be seen in Figure 135. The method starts by applying a wall thickness analysis like the one performed in Figure 134, which results in a histogram showing the wall thickness value in the x-axis and the number of voxels in the y-axis. Using the resulting histogram, intervals can be created to isolate the voxels existing between two specific wall thickness values, in order to create an ROI that can be highlighted for better visualisation (Figure 135) or separated for further analysis, as done in this study. Applying this tool can be straightforward on a regular strut based lattice since all of the nodes have an approximately fixed diameter that is different from the lattice struts. However, using this same method on a gradient lattice strut was more challenging and required in some cases isolating a specific lattice strut diameter before extracting the relevant nodes. After isolating a certain height with approximately close strut thickness, the nodes end up being isolated from the interval created in the wall thickness analysis histogram since they have bigger diameter than the struts. The nodes also have a spherical shape since the wall thickness (sphere method) groups different voxels in the largest inscribed sphere located around the model, which ultimately leads to a spherical shape inside the lattice node geometry.

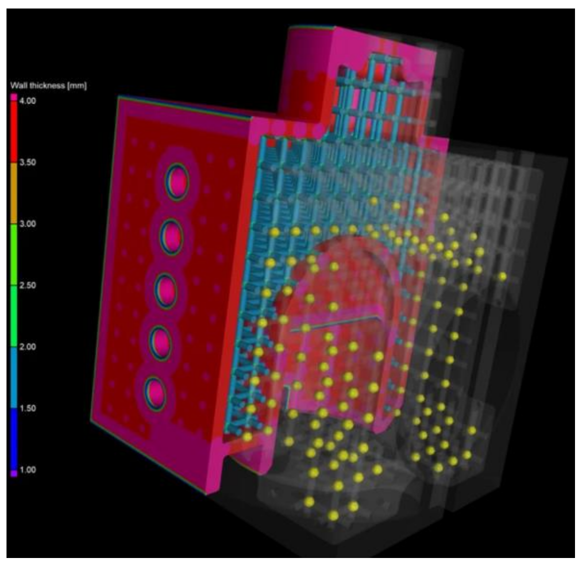

Figure 135: VGSTUDIO MAX 3.4.3 introduced method to isolate and create ROIs from wall thickness analysis [361].

To assess the positioning error alongside each axis, two main measurements were carried out. Initially, the thresholded XCT scan is first aligned with the AM benchmark lattice CAD. The centre to centre distance between the isolated node spheres of the XCT AM lattice and CAD are evaluated. Centre distance between multiple spheres of the produced AM lattice part can also be evaluated in the different X, Y and Z axis. Finally, this type of measurement can assist in identifying the machine capability and its alignment while diagnosing specific motion errors in the AM system and suggesting a basis for its compensation.

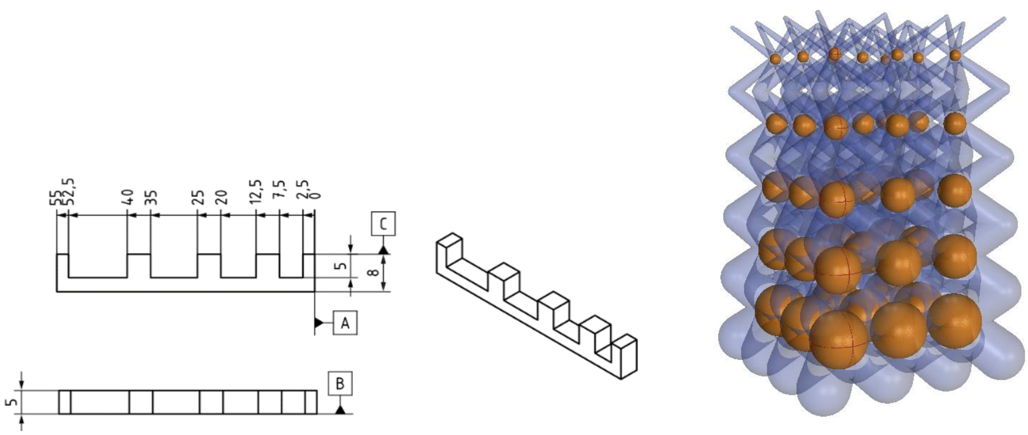

Figure 136: ISO/ASTM 52902:2019 linear positioning accuracy test geometry [360] *(left) and isolated node spheres from the lattice CAD (right).*

Finally, when it comes to dimensional metrology on lattice structures, a usually holistic method is to use deviation analysis tools. Deviation analysis is usually applied after aligning the thresholded XCT volume to the original CAD. To save alignment operation time and reduce chances of error, a “simple registration” was first applied where the user manually orients the part and moves its position until it approximately coincides with the reference CAD position and orientation. Following this, a gaussian best fit registration based on the least square method was applied using VGStudio MAX 3.4.3.

Upon alignment, a deviation analysis was applied with a search distance of 1 mm. To analyse the results, qualitative assessment was performed using a colour map and quantitative assessment was performed by generating a deviation analysis histogram. Also extracted from the deviation analysis is the mean average deviation value and colour map that gives a qualitative comparison on the areas where struts were oversize or undersized. A deviation analysis histogram can also be used for an easier comparison of the print quality and possible oversizing or under sizing.

Porosity is also measured in this study and split into two defined types, external porosity and internal porosity. This was done to avoid any confusion since the word porosity has been often used in literature interchangeably to indicate both internal and external one. External porosity consists of external pores that are desired and are existing in the initial CAD design and found between the lattice unit cells. The equivalent in the ISO/ASTM 52902:2019 of this measurement can be considered to be the hole resolution measurement which can be seen in Figure 137. Since external pores are highly desirable and one of the main reasons of using lattice in application cases like the use of filters, knowing an AM system resolution capability in producing them can be critical, especially in smaller scales. This measurement was also performed using VGSTUDIO MAX 3.4.3 and this time by using the foam analysis module of which the results can be seen in section 1.1c). The results were also split between qualitative visualization using a colour map showing the cell volume distribution, going gradually higher in the upward direction of the Z axis as seen in Figure 137. Quantitative assessment was done by overlaying the CAD external porosity results as a histogram, making the comparison process less challenging.

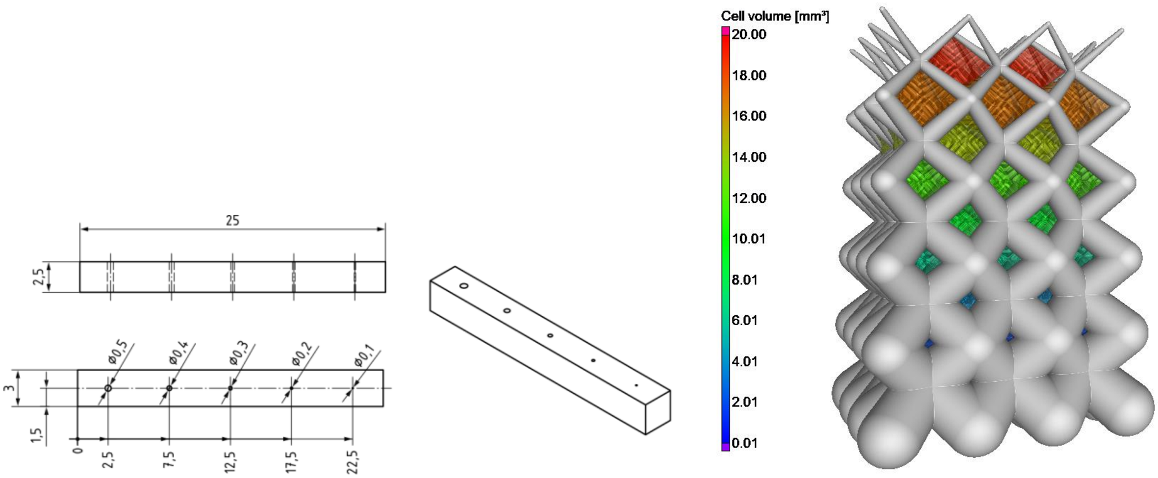

Figure 137*: ISO/ASTM 52902:2019 Hole diameter resolution feature* [360] *(left) translated in this study for lattices with an equivalent named external porosity analysis.*

As mentioned above, porosity is measured as external porosity and internal porosity. Internal pores can be detrimental for the structural integrity of a lattice structure part, especially with thin strut diameters. During the AM process, internal pores can be in the shape of cracks, pores, voids or delamination between layers, usually caused by the temperature gradient [362]. While an AM part can pass visual inspection or external dimensional ones, internal pores can result in significant anisotropic part characteristics that are highly undesirable [363]. The size of the pores that can be measured with an XCT is usually limited by the scan quality, the magnification voxel size, surface determination and more. Due to the lack of standards and challenging ways to validate measurement without destructive processes, the process accuracy is still mostly subjective [364]. To reduce pore volume errors, only pores that had a pore diameter 6 times higher than the voxel size can be considered as recommended in literature [365]. In this study, this recommendation was applied and taken further with only pore diameters that are 10 times bigger than the voxel size being the ones analysed, which in this case means only pores that have a pore diameter equal or higher than 0.3 mm. The pore diameter should not be confused by the pore volume which will be smaller than 0.3 mm^3. Pore diameter in VGStudio MAX 3.4 is described as the "diameter of the circumscribed circle around the pore" where a circumscribed circle is a circle that crosses all surrounding vertices of a polygon. The module used for porosity analysis in VGSTUDIO MAX 3.4.3 is “VGDefX/Only threshold” where the local determined surface was used, the chosen algorithm was “VGDefX”, and analysis mode was “Void”. The analysis parameter includes a noise reduction level set to low and the minimum pore diameter size was chosen to be 0.3 mm as mentioned above. Compactness and sphericity range of the pores were kept per default and ranging from 0 to 1. Compactness in this case indicates the ratio between the volume density of the pore and the volume of its circumscribed sphere. Sphericity however refers to the ratio between the surface of a sphere with same volume of the measured pore volume and the surface of the actual measured pore where a value equal to 1 means a perfect sphere. Both values were kept ranging from 0 to 1 to avoid the filtering of pores. Pores existing in AM parts are far from perfect spheres and using compactness and sphericity filters can assist in categorising them. For example, sphericity between 0 and 0.3 has been previously used in literature to isolate elongated voids and further understand their distribution under different build settings [366]. These filters can be investigated in the future studies for not only creating ROIs of different pore types but also assist in designing digital twin CAD with predicted pore defects.

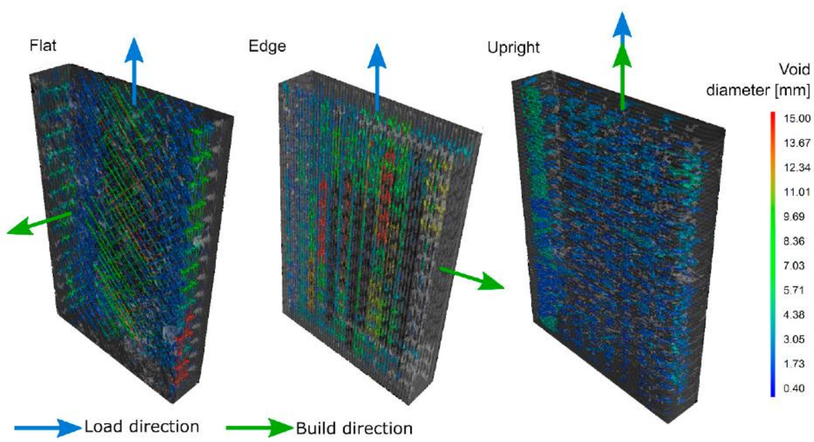

Figure 138: Example of 0 to 0.3 sphericity filter applied on internal pores [366].

The surface roughness has also been included in this study as it is a recommended measurement in ISO/ASTM 52902:2019 where test geometries with different overhangs have been suggested to be added to AM benchmark artefacts. Since including different overhang angles to the lattice would change the type of the unit cell, the overhang angle was kept fixed so that it stays a standardised BCC lattice. This way the surface roughness can be analysed at different strut diameters.

Since the part in this study has a gradient strut diameter, it is expected to have different surface roughness values across the Z height of the part. This means that measuring only one unit cell as performed in the previous study and seen in Figure 125 would lead to incomplete surface analysis of the produced AM lattice benchmark artefact. To tackle this challenge, multiple ROIs can be created at different heights of the

AM benchmark lattice artefact where each represents a strut diameter range. In this study, 24 down skin surfaces were isolated, 12 for each of the two AM lattice print settings. Each of the 12 surfaces were part of the three main regions of interest ROI_1-4, ROI_5-8 and ROI_9-12 as seen further below in Figure 152 depending on their height location. Eventually, the isolated down skin surfaces had their form removed as in the previous experiment, by estimating their cylinder coefficients by applying a total least square fitting [354]. After form removal of each of the 24 isolated down skins, areal surface roughness parameters were extracted e.g., Sa and Spd. Since each four down skin surfaces represented a cluster ROI, surface values were expressed as a mean value and also as a standard deviation giving an idea on the repeatability of the surface roughness across similar strut thickness values. As also mentioned above, the Sa values are the areal surface roughness equivalent value of commonly used Ra, which is a surface profile measurement often used even in case of lattices but not fully descriptive of the surface topography especially in the case of AM surfaces. As outlined in ISO 25178-2:2012, the Sa refers to the "arithmetic mean of the absolute of the ordinate values within a definition area (A)" [350]. The Spd parameter identifies the number or density of peaks per the analysed area after an applied Wolf pruning watershed segmentation as utilized in section 6.3.b) [85,350].

7.3. Additive manufacturing in LPBF process and XCT measurement

The developed AM lattice benchmark artefact was additive manufactured in LPBF process with a Renishaw RenAM500 machine using the manufacturer's recommended settings in Ti6Al4V and followed by a stress relief treatment, both performed by 3MBIC. During the LPBF process, the produced material is introduced to high temperature gradients after the molten material starts to cool down. This effect results in the extraction and contraction of the solidified material, causing thermal stresses that are closer and sometimes higher than the yield strength of the material, leading to possible distortions and fracture of the produced part [367]. The stress relief process was performed by 3MBIC was done using Nabtherm Electric furnace with an argon atmosphere.

The manufacturing settings shared by the manufacturer were a layer thickness of 0.03 mm and powder particle size ranging from 14 μm to 45 μm. To have the as-built surface topography, no other post processing was performed beside removal of supports seen in Figure 139 and the mentioned heat treatment. Subsequent to the AM process, the part was XCT scanned using this time a Nikon MCT 225 which has an MPE of ± (9 + L/50) μm, where the "L" represents the measured feature in mm. The MPE is an approximation of the estimated maximum error depending on the measured feature length. Nikon mentions that to obtain the mentioned MPE, the VDI/VDE 2630 standard [368] was followed, on a single material, and on samples with a maximum diameter of 250 mm and maximum height of 250 mm [369].

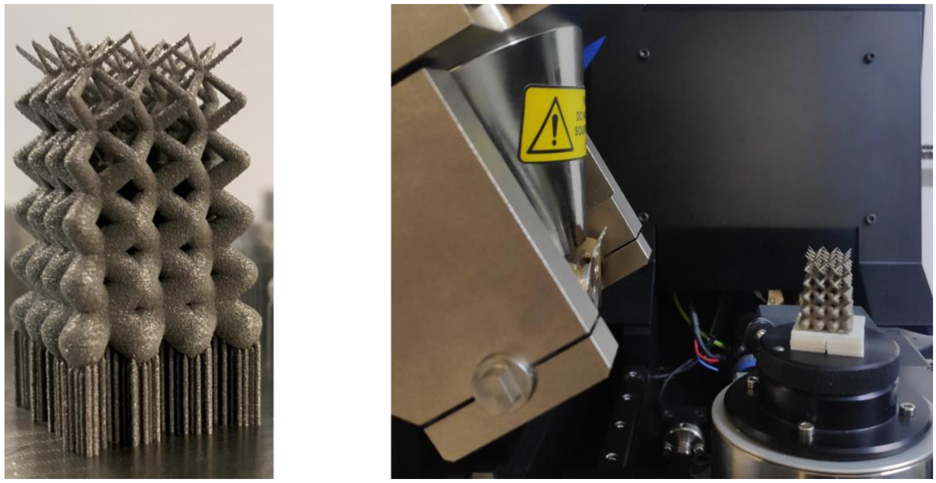

Figure 139: Additive manufactured Titanium lattice benchmark artefact (left) and XCT setup on the MCT225 (right).

The scanning parameters were an acceleration voltage of 161 kV, filament current of 58 µA, exposure of 4000 ms, projection number of 721 and 0.015mm voxel size. The detector of the XCT was 2000x2000 pixel size and a copper filter of 0.25 mm thickness was used. The XCT scan was then reconstructed and thresholded using local iterative surface determination. While the voxel size was approximately two times smaller than the one used in previous two Chapter's XCT scans, the file size was more than three times larger and was challenging to analyse. This has led to needing higher computing power and to longer surface determination as well as analysis time.

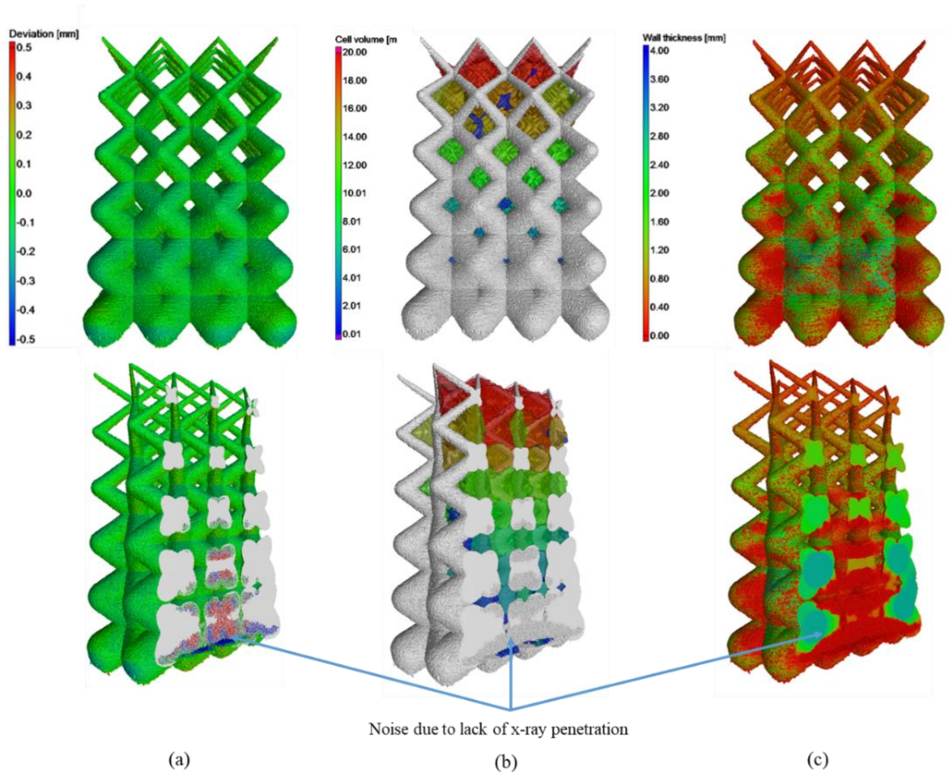

Figure 140: Front and sectioned view of deviation analysis (a), external pore analysis (b) and wall thickness analysis (c). Also Noise due to lack of penetration causing inaccurate analysis results.

Initial results shown in qualitative analysis from Figure 140 (a) can clearly highlight how the fine features were additive manufactured with a high fidelity. This is not only due to the usual higher accuracy of LPBF process but also attributed to the small layer thickness (0.03mm) used in the print setting. Further quantitative analysis could not be performed due to the existence of significant noise in the XCT scan which can be especially seen affecting the analysis in the lower part of Figure 140 (a), (b) and in the whole Figure 140 (c). The reason for the existence of this noise was the lack of penetration caused by a combination of factors. The main issue was due to the material being Titanium, which was only chosen due to joining a build previously ordered from the author's research group, to eventually have lower manufacturing cost. The lack of penetration was more significant in the very bottom of the design, with the longest path being around more than 22mm of solid material. Another XCT scan was attempted at a higher acceleration voltage of 195 kV, but the penetration issue persisted, which led to multiple suggestions that can be used for future research.

The first future work suggestion would be to test this design in Aluminium. As seen in previous studies with lattices of approximately the same size, Aluminium would have been easier to XCT penetrate and measure. Future work suggestions when using this design in metals that are harder to penetrate would be to use XCT system with higher voltage and penetration capabilities. In this case, the two contrasting thicknesses might be challenging to capture using one scan setting, which might require the use of the dual-energy method [370] that is usually used for multi material parts.

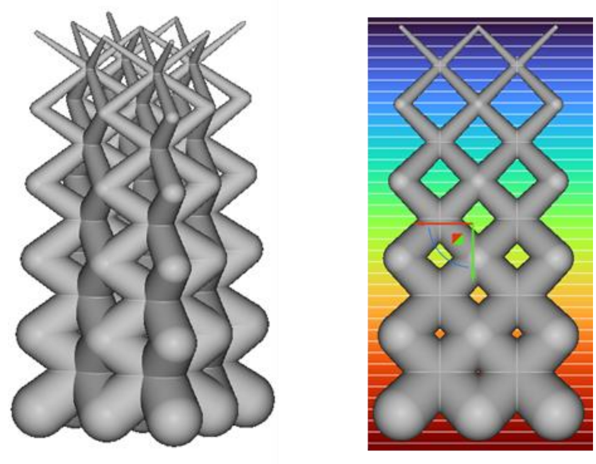

Figure 141: AM lattice benchmark design with fewer unit cells

Another alternative that does not require the use of higher voltage XCT system is to adapt the developed AM lattice benchmark artefact. This can be done by modifying the design in order to only have two-unit cells in each direction, as seen in Figure 141, instead of three as done in this study. While this might reduce the number of struts used to analyse process stability, it will allow for a shorter penetration path, making it easier to XCT scan. The next section will investigate the printing and XCT measurement of the developed design in FDM process.

7.4. Additive manufacturing in FDM process and XCT measurement

The FDM process was chosen due to having lower cost than metal AM process, which allowed for printing in more than one process setting. Using FDM process also allowed for testing the developed design in another AM process which was important since the design is not intended to be process specific but used in different AM systems. The following section will investigate the manufacturing in FDM process and application of the XCT based and lattice adapted measurement strategy.

a) Additive manufacturing of FDM parts and XCT scanning

The machine used to additively manufacture is the AM lattice benchmark artefact is the Ultimaker S3 and the filament material used was polyactide (PLA). Since the machine's slicer Cura does not support CLI file formats, a triangle mesh format was used, in this case the .3mf file format for its low size. The mesh model was analysed using Autodesk Meshmixer software for any meshing errors such as non-manifold errors, holes or tears not existing in original design and flipped normal. The model did not have any mesh errors and was then taken to Cura software for the slicing operation.

The crucial variable that was changed in this study is the layer height or as sometimes referred as layer thickness. In an AM process, after each layer, the user can specify and increase the height of the next layer usually leading to significant surface roughness but decreased print time. However, using a smaller layer height usually leads to less printing deviation to CAD especially in detailed features leading however to higher print times. Geometric benchmark artefacts, like the one developed in this study, are not only used to assess the machine capability in its highest accurate print conditions but also in additional print settings that are not necessarily the most accurate but are cost efficient in scenarios where a tight tolerance is not a priority. To achieve this comparison, the developed design shown above was additively manufactured in two different layer heights which were the 0.06 mm and 0.4 mm ones using a 0.4 mm and 0.8 mm diameter nozzle respectively. It is recommended as a rule of thumb to not exceed a maximum layer height between 75% and 80% of the used nozzle diameter [371–373]. This means for example that a recommended maximum layer height of 0.3 mm is recommended for a nozzle diameter of 0.4 mm. Increasing the layer height to closer or equal values of the nozzle diameter makes the extrusion rounder and with less bonding surface between the layers, increasing the chances of air gaps and void formation, as seen in Figure 142.

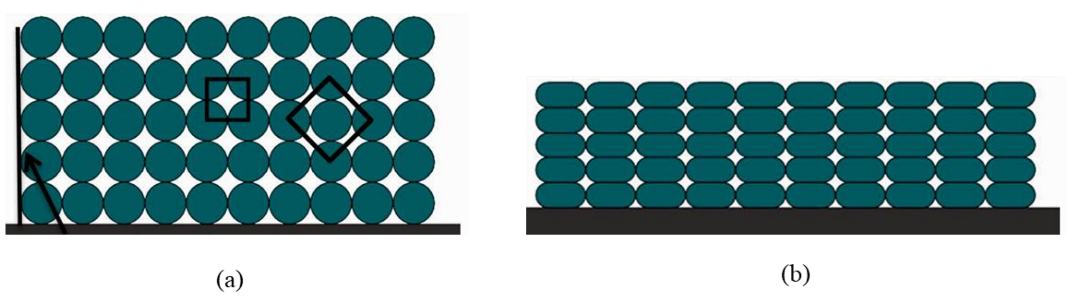

Figure 142: Layer height equal to nozzle diameter (a) showing larger air gaps compared to layer height lower than nozzle diameter (b) [371].

hence the need in this study to use two different nozzle diameters. A preview option can be used in Cura slicer to not only visualise the layer per layer process and nozzle path but also to see any rendering approximation of the finalised part, depending on the chosen print parameters. In this case, and as seen in Figure 143 (A1) and (B1), it was possible to compare the two-layer height settings and visualize an approximate estimation of the features that would or would not be printed in each case. Using the preview option, it was also possible to get an estimation of the print time which was 3.4 hours for the 0.06 mm layer setting compared to 15 minutes using the 0.4 mm layer height setting. This significant time difference of more than 13 fold already gives an idea on how crucial is to understand the machine limitation under different print settings for better matching and optimisation of print conditions depending on part constraints and function.

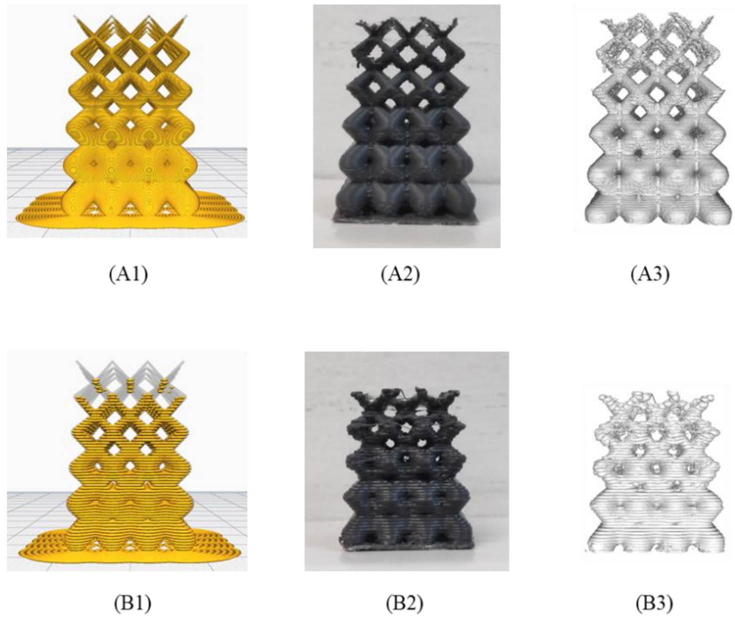

Figure 143: Cura slicer previews (A1, B1), FDM additive manufactured lattices (A2,B2), XCT scans of the FDM produced lattices (A3,B3). A1,A2 and A3 has a layer height of 0.06 mm and B1, B2 and B3 has a layer height of 0.4 mm.

Upon completion of the manufacturing process, the parts were kept as printed, and no post processing was applied after removal from the print bed. The obtained additively manufactured parts using each print setting can be visualized in Figure 143 (A2) and (B2). It can already be seen visually how the 0.4 mm print setting resulted in significantly rougher surface and as expected was not capable to print few fine struts positioned at the top of the lattice. A Nikon XT H 225 was again used to XCT scan the additive manufactured lattices using an acceleration voltage of 60 kV, filament current of 151 μA, an exposure of 2000 ms and a projection number of 1583. The chosen magnification led to a 0.030 mm voxel size and a 1008 by 1008 pixels detector size. As seen in previous experiments, a fixture is usually designed, and additive manufactured to hold the part in position during XCT scan and making sure that the other part is in the same position. This was however not possible to achieve in this study since the parts were already made from PLA, the usual fixture material, which would have meant that the fixture would have the same grey value of the lattice making the surface determination challenging. In this case, a thick double sided adhesive foam tape was used between the turntable and the part, minimising the movement of the latter during the XCT scan. The obtained XCT scan was reconstructed and later analysed using VGStudio Max 3.4.3. Surface determination was performed using local iterative surface threshold method. Renderings of the thresholded

XCT scan volume for both 0.06 mm layer height setting, and 0.4 mm layer height one can be seen respectively in Figure 143 (A3) and (B3).

b) Strut diameter resolution

As illustrated above, the ISO/ASTM 52902:2019 recommended pin diameter resolution test geometry has been translated to strut diameter resolution in the designed AM lattice benchmark artefact. However, in this case, the features to be measured are extensive and need a holistic measurement method. Using XCT and volume analysis tools, initial qualitative results can be seen in Figure 144 as a colour map 3D views representing the CAD, 0.06 mm and 0.4 mm layer height print settings. This qualitative visual evaluation shows clearly how the 0.4 m layer height print setting has more missing struts at the top of the produced lattice as seen in Figure 144 A3. The missing struts can be highly related to their thin and small diameter that was too small to be captured by both the used big nozzle diameter and set layer height. The missing struts were roughly expected as it was shown in the approximate slicing preview shown in Figure 143 B1. As for the 0.06 mm layer height print setting, initial qualitative visualization shows how most struts were additively manufactured with occasional oversizing especially on the down skin of the struts as seen in Figure 144 A2. While the top struts were additive manufactured, they do not look visually accurate with visible strut waviness that will be more visible in the next applied deviation analysis.

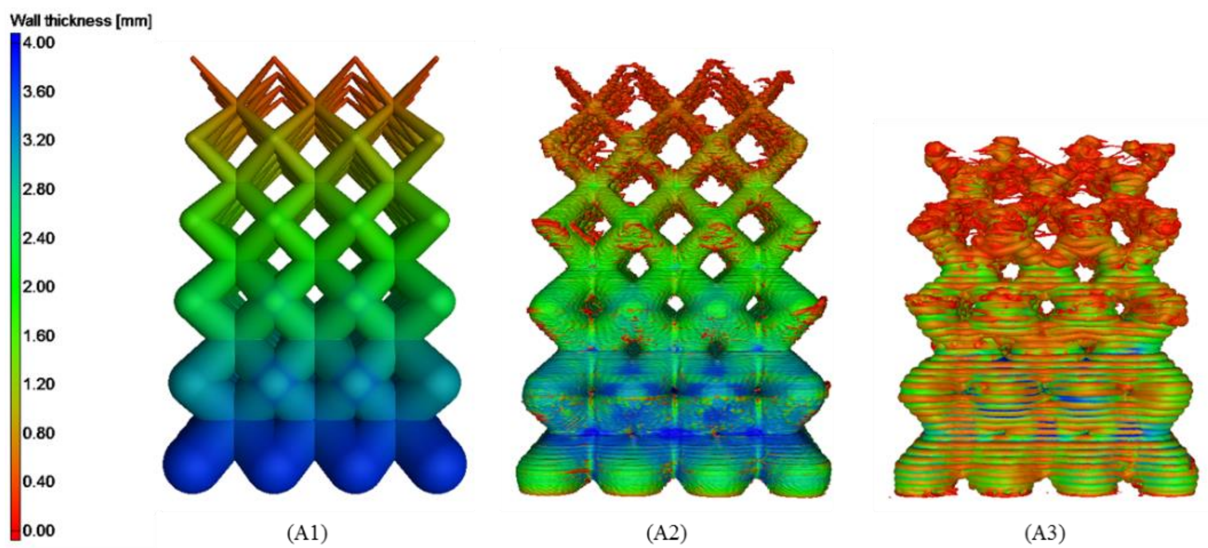

Figure 144: Wall thickness analysis results of the CAD (A1), 0.06 print setting (A2), 0.4 print setting (A3) and their equivalent cross sections as (B1), (B2) and (B3).

As for quantitative analysis in Figure 145, three different histograms were created showing wall thickness analysis of the CAD, 0.4 mm and 0.06 mm layer height print settings. The reason for including the CAD values is that even if the lattice strut diameter value is known and set by user, the node sizes which are a result of the set lattice design parameters can be challenging to compare. This is increasingly challenging with gradient diameter struts since some nodes can have the same diameter as some lattice struts, which makes it easier to compare using back to back histograms and cross sections, as seen in Figure 145. Initial look at the CAD wall thickness histogram in Figure 145 (A1), clearly reflects the CAD design geometry, where less voxels have smaller thickness, with a gradual increase towards thicker diameters, directly represented in Figure 145 (B1) by the cross section showing the lattice nodes. When it comes to the 0.06 mm layer height setting, and from the small voxel percentage on the left of the wall thickness histogram in Figure 145 (A2), the voxel percentage values follow a gradual increase roughly similar to the CAD one. However, the bigger diameters are significantly larger than the CAD ones. As for the 0.4 mm layer height setting histogram in Figure 145 (A3), the small voxel percentage wall thickness values do not seem to follow a similar distribution to the CAD one. Furthermore, the bigger diameters are also larger than the CAD ones, similar to the 0.06 mm layer height setting comparison to CAD. The significantly higher wall thickness value can be attributed to the non-printing of the small external pores existing in the lower half of the part, leading to the merger of the features, resulting in a bigger wall thickness diameter. This result captured in the histogram can be clearly shown in the cross sections of the CAD, 0.06 setting and 0.4 setting seen in Figure 145 B1, B2 and B3 respectively. The cross sections show the wall thickness analysis and clearly highlight the merger of the material at the lower half of the lattice. This analysis gives a clear indication of the expected diameter resolution of the AM system, while also allowing for a back to back comparison of between different print settings. By point fitting and creating a cylinder from the finest struts in each additive manufactured lattice, it was seen that the 0.06 mm layer height setting had allowed a fine diameter of 0.5 mm to be achieved while the equivalent finest diameter that could be additive manufactured with the 0.4 mm layer height setting was 1.2 mm. This analysis gives a clear indication of the expected diameter resolution of the AM system at each layer height setting. To reach the CAD finest strut diameter, which was 0.3 mm, a solution would be in the future to experiment with an even smaller nozzle diameter used with the Ultimaker machine for example a size of 0.25 mm and could potentially manufacture finer features. This is however met with longer print times which might not always be ideal in industrial setups.

Nevertheless, using wall thickness analysis alone when inspecting additive manufactured lattices might not always provide the full picture and assistance to correct the AM system. To tackle this challenge, a deviation analysis can be applied to gain a further understanding of the dimensional quality of the produced part compared to the original CAD.

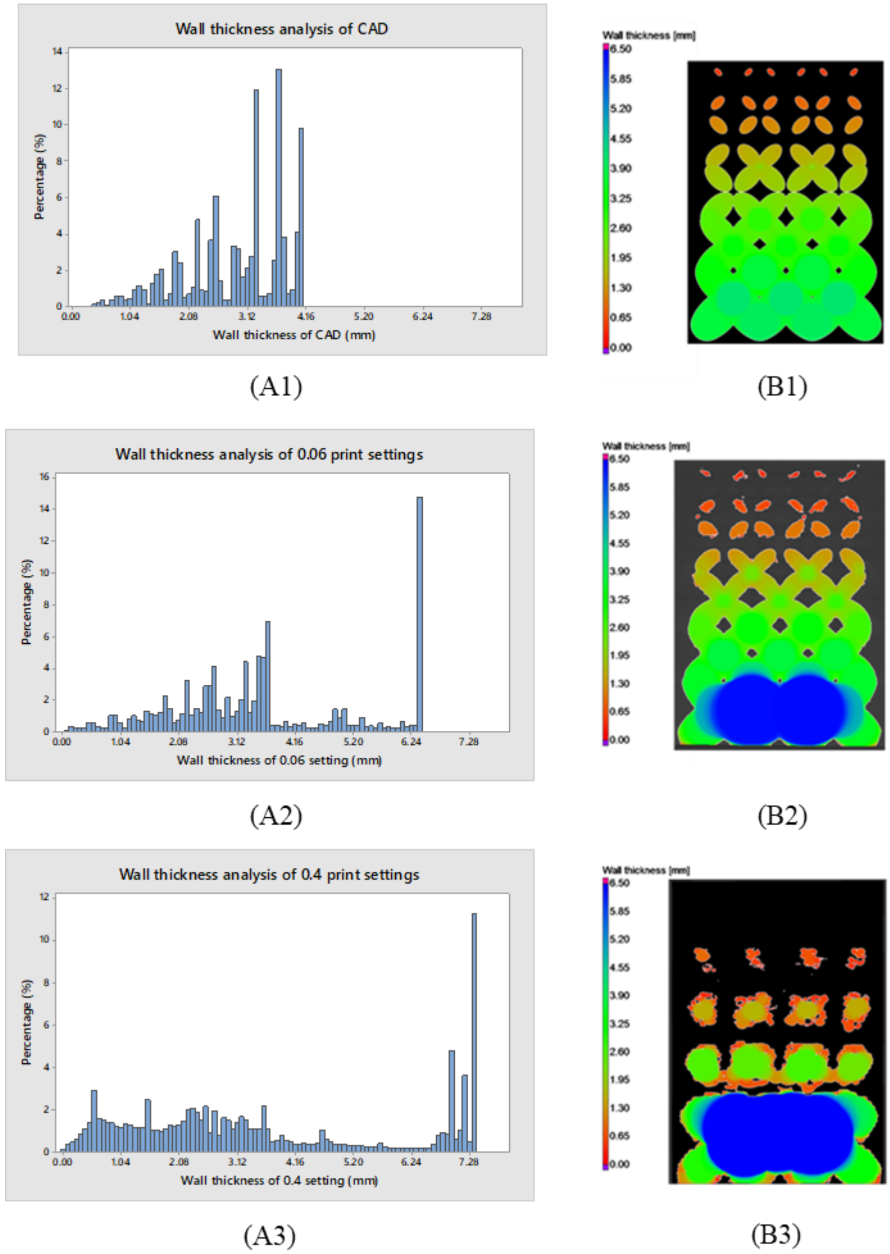

Figure 145: Wall thickness analysis histogram and equivalent 2D cross section of CAD, 0.06 setting and 0.4 setting shown in (A1) (B1), (A2) (B2) and (A3) (B3) respectively.

c) External porosity resolution

The building blocks of a lattice is mainly the cell size and the strut diameter strut size, these two parameters define the dimension of the external pores that are part of the lattice. To assess the quality of the additively manufactured pores and the finest resolution reached by the AM system, the VGSTUDIO MAX 3.4.3 foam analysis module was used. This module allows for the determined surface of the XCT volume data to be segmented into topologically disconnected components. The isolated components can be holistically analysed statistically and also individually visualised. The main analyses parameter in this case is the merge threshold percentage which was kept in this case at the default 5%. The merge threshold value affects the tolerance for local fluctuations and defines the number of segmentations to generated for the analysed cells. For example, if the merge threshold values was set to 100%, all of the external pores will be merged and considered as one.

It can be seen from the analysis results, seen in Figure 146 B1, that the chosen default merge threshold percentage led to a gradient external pore distribution, which complied with the expected segmentation. From qualitative visual analysis of the colour maps shown in Figure 146, it was clear how the 0.4 mm layer height print setting (Figure 146 B3) had missing struts, leading to most external pores to be of a smaller size, which was clearly reflected in the histogram results seen in Figure 146 (A3). Quantitatively, close to 80% of external pores of the of 0.4 mm layer height print setting had a volume less than 1.5 mm^3. This means that while the 0.06 mm layer height print setting histogram seen in Figure 146 (A2) was not perfectly matching the CAD histogram seen in Figure 146 (A1), it still clearly had visually closer histogram values to CAD compared to 0.4 setting to CAD. This shows the expected higher fidelity of the finer layer height at keeping external pore distribution closer to the original CAD one. This is further reflected in the 2D cross sections of the external porosity analysis in Figure 147, where the 0.06 mm layer height setting had a smallest achievable external pore size of 0.05 mm, compared to the 0.4 mm layer height smallest achievable external pore size value of 0.98mm, seen in Figure 147 (b). Also, as seen in the 2D cross sections of the external porosity analysis in Figure 147, the 0.06 mm layer height setting had a smallest achievable external pore size of 0.05 mm. In contrast, and using the 0.4 mm layer height setting, the smallest achievable external pore size was 0.98mm. Both of these two external pores were located at the lower half of the lattice, which was expected from the gradient design, their annotations can be seen in Figure 147. While the visual comparison between the different histograms in Figure 145 and Figure 146 was visually clear, statistical methods like QQ plot [374] can allow us to know if a distribution is normal. If the distribution is not normal, non-parametric methods like Kolmogorov-Smirnov [374] can still allow for a distribution comparison. While VGSTUDIO MAX limits the use of these tests as it only allows for the export of already binned data and not the complete data of each individual voxel, future work can investigate the use of other methods oe software that allow for the export of complete data as well as the analysis using parametric or non-parametric methods like Kolmogorov-Smirnov, depending on the type of the distribution.

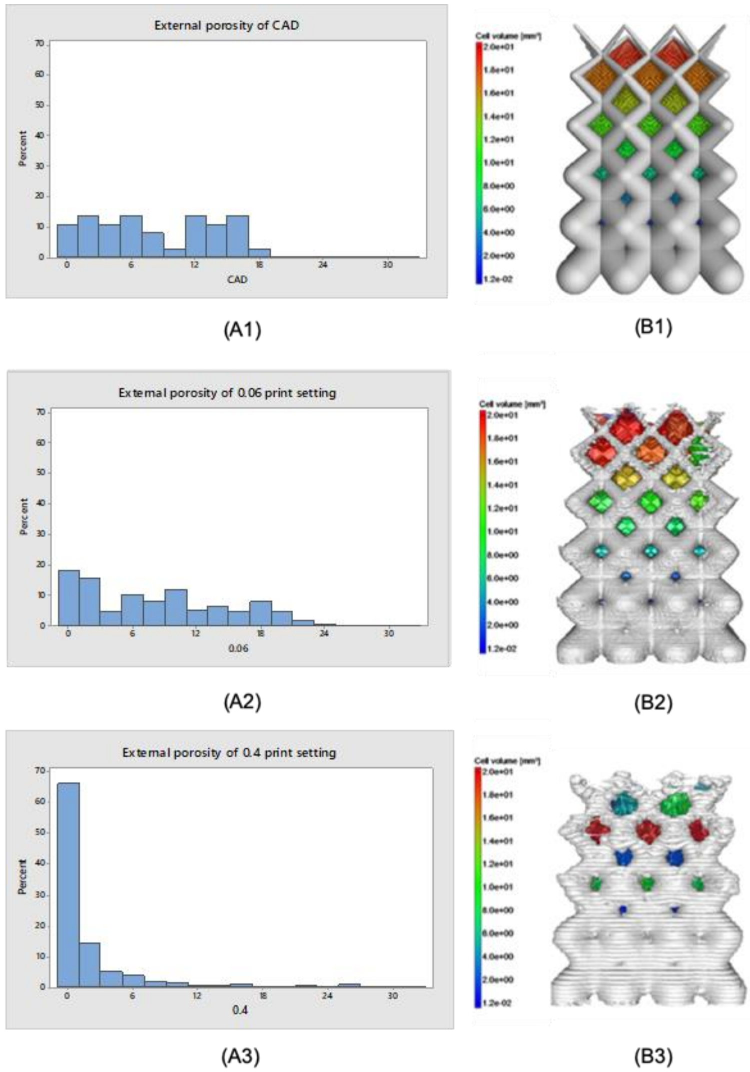

Figure 146: External porosity histogram and equivalent analysis 3D model of CAD, 0.06 setting and 0.4 setting shown in (A1) (B1), (A2) (B2) and (A3) (B3) respectively.

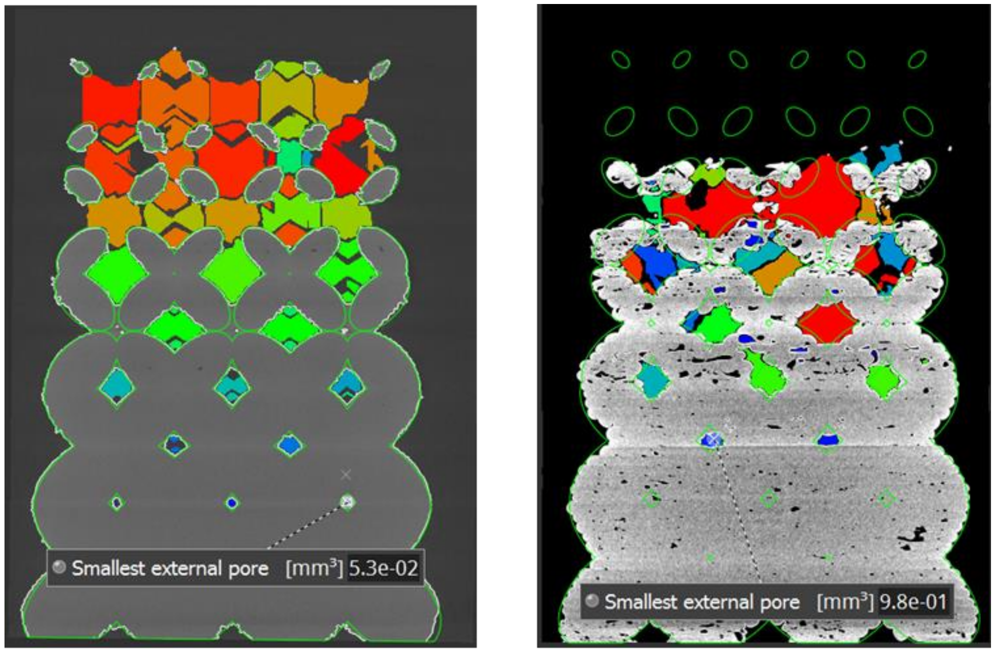

(a) (b)

Figure 147: Smallest external pore measured for the 0.06mm layer height print (a) and 0.4 mm layer height print (b). The green outline in both (a) and (b) represent the CAD outline.

d) Lattice node positioning error

As previously discussed, the lattice node positioning error was calculated using node spheres that are already existing in the lattice design, removing the need of designing additional ones. To extract these node spheres, intervals were applied in the applied wall thickness analysis histogram shown above. The applied intervals allowed the isolation of a specific volume geometry. This means that when isolating a specific layer height and choosing the highest wall thickness interval, the node sphere connecting the struts were isolated since they have higher diameter than the struts.

By applying this protocol, it was possible to isolate all of the CAD node spheres which can be seen in Figure 148 a, 11 node spheres of the 0.06 mm layer height setting seen in Figure 148 b and only four node spheres of the 0.4 mm layer height setting. The result quality of this method is highly dependent on the print quality. This means that in the case of the 0.4 mm layer height print setting, and due to fine external pores not printing correctly, the node spheres that were supposed to be at the lower part of the lattice were merged with other features as clearly seen in the wall thickness analysis 2D results in B2 and B3. Eventually, four node spheres were enough to be used in each model and complete the analysis in this section, although more of them would have allowed a further repeatability comparison between different heights of the same printed lattice.

Also due to not being able to extract most node spheres of the printed lattices, especially at the 0.4 mm layer height, it was not possible to use the same node spheres and have an exact back-to-back comparison. This was however only a challenge for the sphere named S4, which was still obtained from the same layer height as can be clearly seen in Figure 148 with the S4_0.06 and S4_0.4 node spheres. The rest of the node spheres which are from S1 to S3 for either the 0.06 mm or 0.4 mm layer height settings were all from the same position and layer height.

From Table 18, it is possible to see the linear positioning error results, for each of the X, Y or Z axis separately. The linear positioning error was assessed by comparing node sphere centre to centre distance in different axes. For example, the X axis linear positioning error was assessed by using the S1 to S2 sphere distance, the Z axis linear positioning error by using S1 to S3 and the Z axis linear positioning error one by using the S1 to S4 node spheres in each of the lattices. Also, from Table 18, it can be clearly seen how the node sphere centre to centre error in the 0.06 mm layer height print setting ranged from 0.02% to a maximum of 1.79%. This was significantly lower when compared to the 0.4 mm layer height setting of which the node sphere centre to centre error was ranged from 1.02 % to 7.12 %.

In addition to analysing the linear positioning error, an evaluation of the isolated node spheres position was carried out compared to their equivalent CAD node sphere position. This comparison results can be seen in Table 19 where the difference to CAD in the 0.06 mm layer height setting ranged from 0.04 mm to 0.15 mm which was again significantly lower in regard to the 0.4 mm layer height setting of which the difference to CAD ranged from 0.18 mm to 0.56 mm. From both these two types of analyses, the 0.06 mm layer height print setting had the closest and least error to the CAD node sphere positioning as well as axis centre to centre positioning error. These results are not unexpected but are evidence of the efficacy of the principle of the methods developed. For a better visualisation of the results, a subtraction was done to obtain the vector between each node sphere and its CAD equivalent. The results can be seen in Figure 149 where all vectors start from the graph origin, making the direction of the error in space comparable and clearer. Also, Figure 149 shows how the 0.06 mm layer height print had a consistent error direction while the 0.4 mm layer height print setting had error vector in multiple directions, making it harder to estimate a potential design adjustment or machine calibration solution.

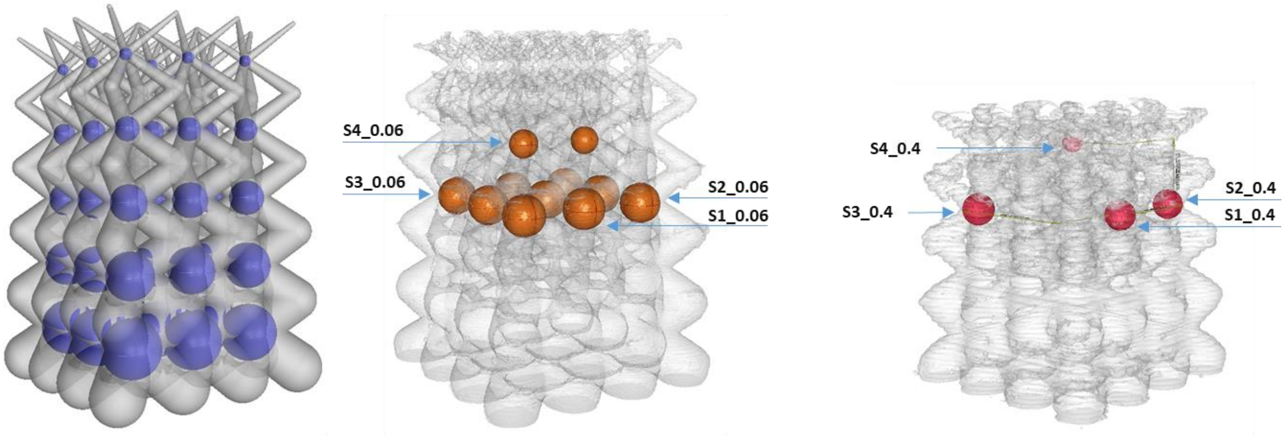

(a) (b) (c)

Figure 148: Extracted sphere nodes from AM benchmark lattice artefact CAD.

Table 18: X axis, Y axis and Z axis linear positioning error and comparison with CAD, which has a unit cell (node to node distance) of 5mm in X, Y and Z.

Layer height setting (mm)	Axis linear error	Value (mm)
0.06	X axis linear error (S1_0.06 to S2_0.06) Absolute difference to CAD in (%)	5.00 (0.02%)
	Y axis linear error (S1_0.06 to S3_0.06) Absolute difference to CAD in (%)	4.96 (0.75%)
	Z axis linear error (S1_0.06 to S4_0.06) Absolute difference to CAD in (%)	4.93 (1.79%)
0.4	X axis linear error (S1_0.4 to S2_0.4) Absolute difference to CAD in (%)	5.28 (5.66%)
	Y axis linear error (S1_0.4 to S3_0.4) Absolute difference to CAD in (%)	5.05 (1.02%)
	Z axis linear error (S1_0.4 to S4_0.4) Absolute difference to CAD in (%)	5.37 (7.12%)

Table 19: Centre to centre distance between node spheres of CAD versus 0.06 setting and CAD versus 0.4 setting.

Layer height setting (mm)	Node spheres	Centre to centre distance between node sphere and its CAD node sphere equivalent (mm)
0.06	S1_0.06	0.11
	S2_0.06	0.18
	S3_0.06	0.06
	S4_0.06	0.17
0.4	S1_0.4	0.21
	S2_0.4	0.55
	S3_0.4	0.25
	S4_0.4	0.26

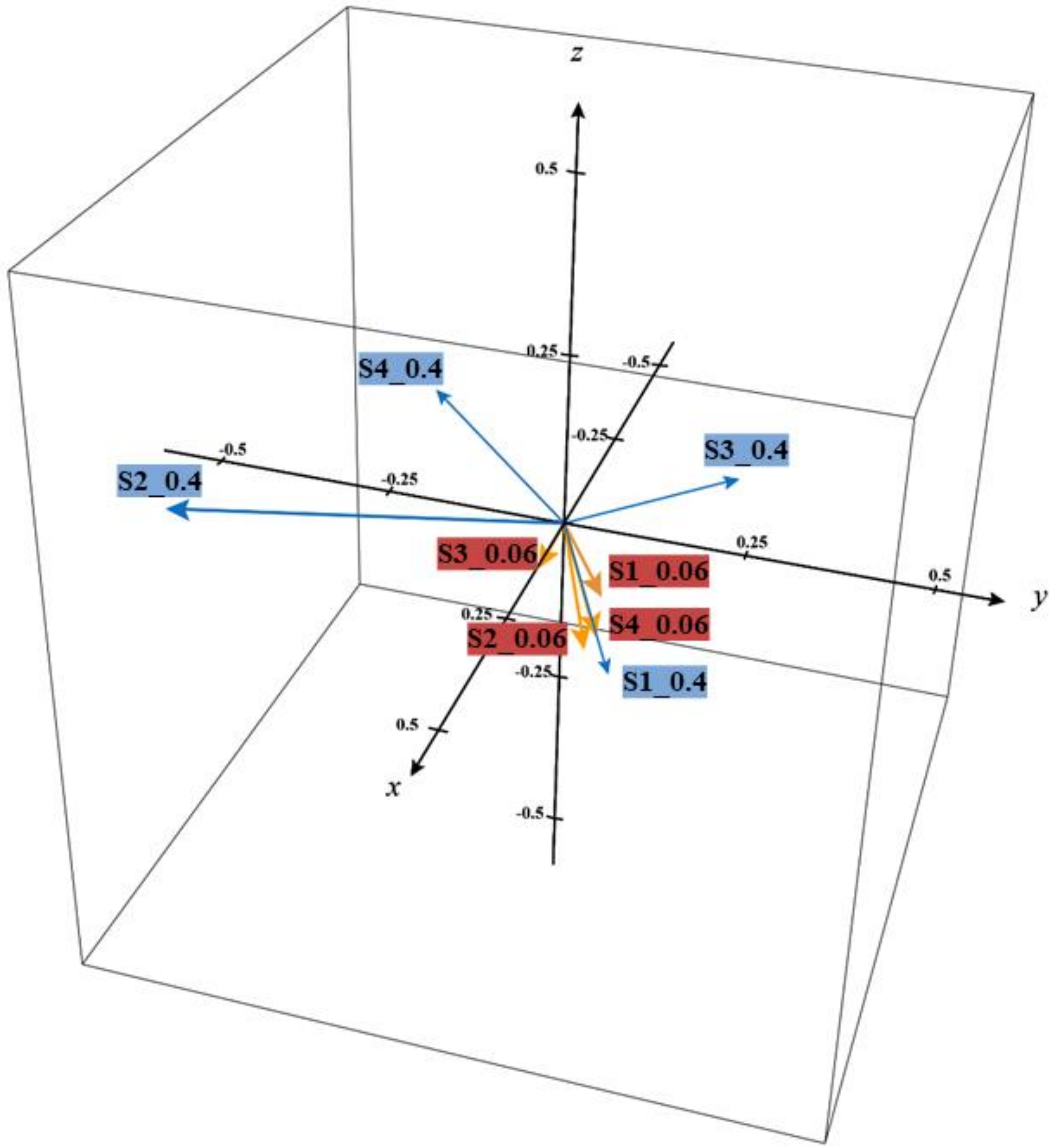

Figure 149: Centre to centre vector between node sphere and its CAD node sphere equivalent, all starting from origin.

e) Dimensional deviation from the original CAD

As mentioned above, a wall thickness analysis will give an idea on the strut diameter distribution on the whole CAD allowing the evaluation of the AM system resolution. However, a deviation analysis like shown below allows for a detailed investigation of the local areas where features were oversized or undersized. A dimensional deviation analysis starts by a Gaussian best fit registration that allows for alignment of the XCT volume scan to the CAD. A search distance of ± 1mm was chosen as well as the “consider surface orientation” parameter. The latter allows for mainly the surfaces that have the same orientation to be compared, increasing results accuracy.

Initial qualitative analysis can be seen in Figure 150 where a colour map with a set ± 0.5 mm scale for better contrast. The deviation analysis highlights locations of oversizing (positive deviation in red) and undersizing (negative deviation in blue), which can be a useful addition to the wall thickness analysis. The colour map showed from Figure 150 (b) for the 0.4 mm layer height setting shows how the thick layer height affected the accuracy of the deposited layers leading to local areas where material was missing. This was more significant in the 0.4 mm layer height setting than the 0.06 mm layer height one. This can be directly visualised in histogram shown in Figure 151, where it is clear how the 0.4 mm setting has higher deviation values in both positive and negative directions. The obtained deviation analysis results from VGSTUDIO MAX highlighted for the 0.06 setting a mean deviation of 20.8 μm with a standard deviation of 92.1 μm which were both lower than the 0.4 mm setting mean deviation of 27.1 and standard deviation of 204.8 μm, suggesting less error and improved accuracy of the 0.06 setting. However, the effect of the applied registration has not been investigated and could be affecting the deviation analysis results. Future work can include a thorough investigation of the registration impact on the results of the deviation analysis.

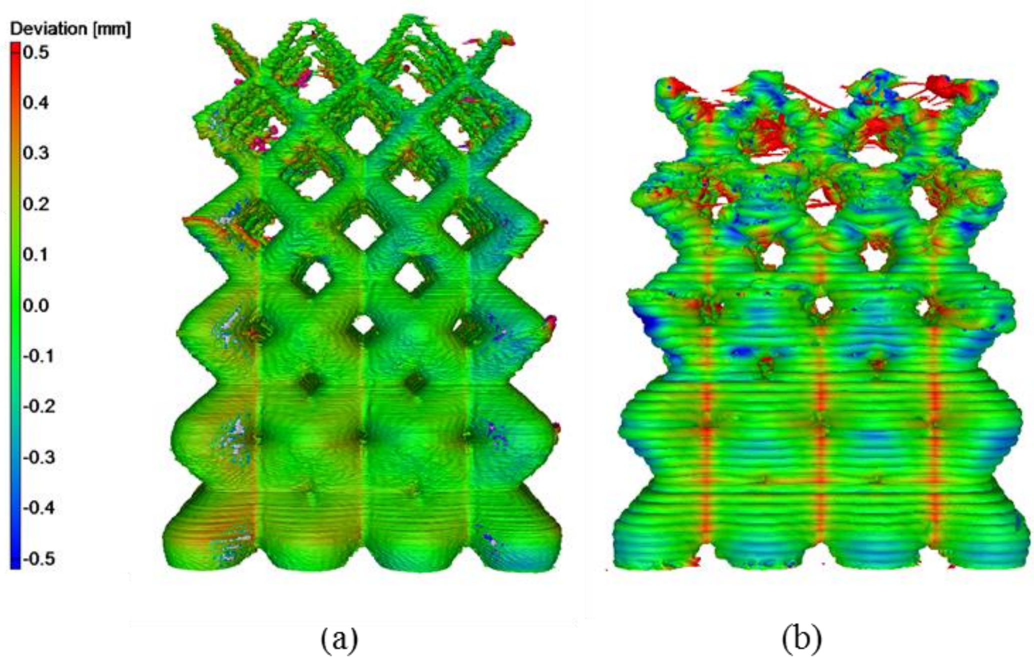

Figure 150: Colour map showing the deviation analysis of 0.06 setting vs CAD (left) and 0.4 setting vs CAD (right).

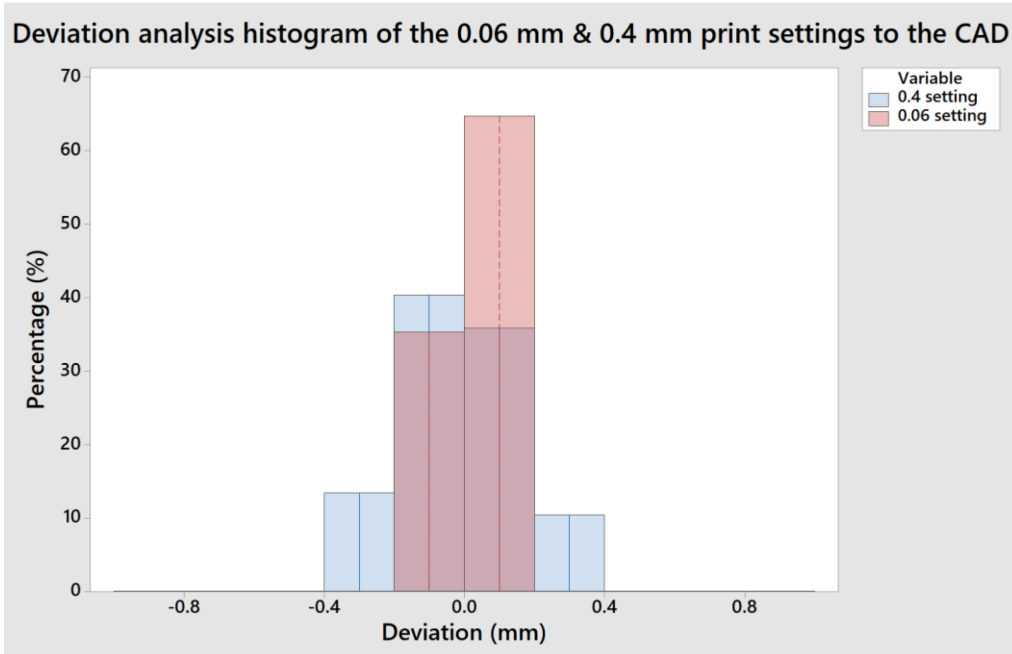

Figure 151: Histogram comparison of deviation analysis of CAD to 0.06 mm setting and CAD to 0.4 mm setting.

f) Surface roughness

As outlined previously, 24 down skin surfaces were isolated, 12 for each lattice where each four surfaces formed an ROI cluster as seen in Figure 152. To isolate these surfaces, a Boolean Intersect with the XCT thresholded model was performed as previously used by the author in section 6.3b), only this time to more struts positioned at different layer heights. The form removal and areal surface parameter extraction was done by Luca Pagani. The extracted Sa and Spd value of each ROI cluster for each layer height setting can be seen in Figure 153 and Figure 154 respectively. It can be clearly seen in Sa results in Figure 153 how the Sa values of 0.4 mm layer height setting of each ROI had higher value than its ROI cluster equivalent from the 0.06 mm layer height setting. This can be associated to the thick layer height adding extra material that is further from the nominal CAD form. Also from the two figures, it can be clearly seen how the smaller lattice struts of each layer height print setting had a higher Sa value than its equivalent larger strut diameters. This can be associated to the higher waviness and deviation that was clear as in the analyses performed above especially on the higher fine features.

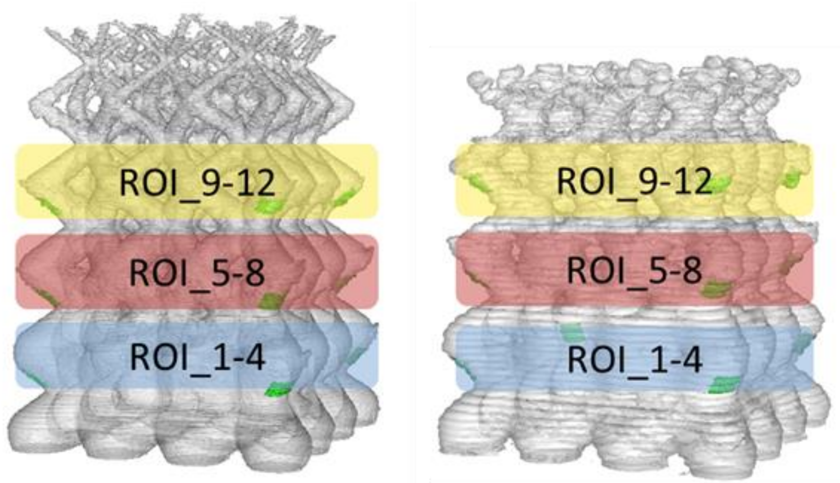

Figure 152: 24 down skins highlighted in green, 12 for each lattice. Each four downskins form an ROI cluster.

In contrast, the Spd values had an opposite trend compared to Sa. For example, it can be seen how in Figure 154, the Spd value was smaller in 0.4 mm layer height setting compared to the 0.06 mm layer height one. This can be related to the larger nozzle leading to fewer peaks and their frequency of appearance per similar area and also to the Wolf pruning, which may add to this trend by having rough peaks not appearing above the background surface.

Also, since each cluster had four down skins, it was possible add error bars that give an idea on the process repeatability at each strut diameter cluster and for each layer height setting. For example, it can be clearly seen from Figure 153 related to Sa how the standard deviation for both layer height settings was mainly getting higher with smaller features, decreasing chances of repeatability and process stability.

While down skin surface of the lattice struts was the only one analysed due to being the usual significant one, the up skin can additionally be analysed as shown in the previous study in section 6.3.b) and seen in figure Figure 125. Using XCT for surface data analysis has can allow for extraction and analysis of features that are not accessible using conventional tools like line-of-sight optical ones. By using the suggested design and analysis method, the user can evaluate the AM system surface roughness quality and have a clear Sa expectation for different strut diameters using different print settings. This method allows for simultaneous assessment of different strut diameters using the same design but differing print conditions. In case the user requires higher resolution for more accurate surface roughness data, the additively manufactured lattice benchmark artefact can be sliced, leading to multiple parts isolating the different ROI clusters. These separated part clusters can be XCT scanned separately for increased magnification and eventually smaller voxel size that is more accurate. Also, a few of the external down skin struts can be measured using a conventional instrument like focus variation microscopy for a further back to back comparison with XCT obtained surface measurement results to improve the s confidence level or to initially decide on the ideal voxel size as previously described in literature [86,264]. Using the suggested design in this case can assist in reducing chances of print process failure due to the finest struts existing at the top of the design with less impact on the lower thicker struts. However, there could be scenarios where it is already known that the fine features will not fail the print process and where it would be ideal to print different strut diameters separately, without using the suggested design, for increased surface measurement resolution mentioned above and without the need for sectioning.

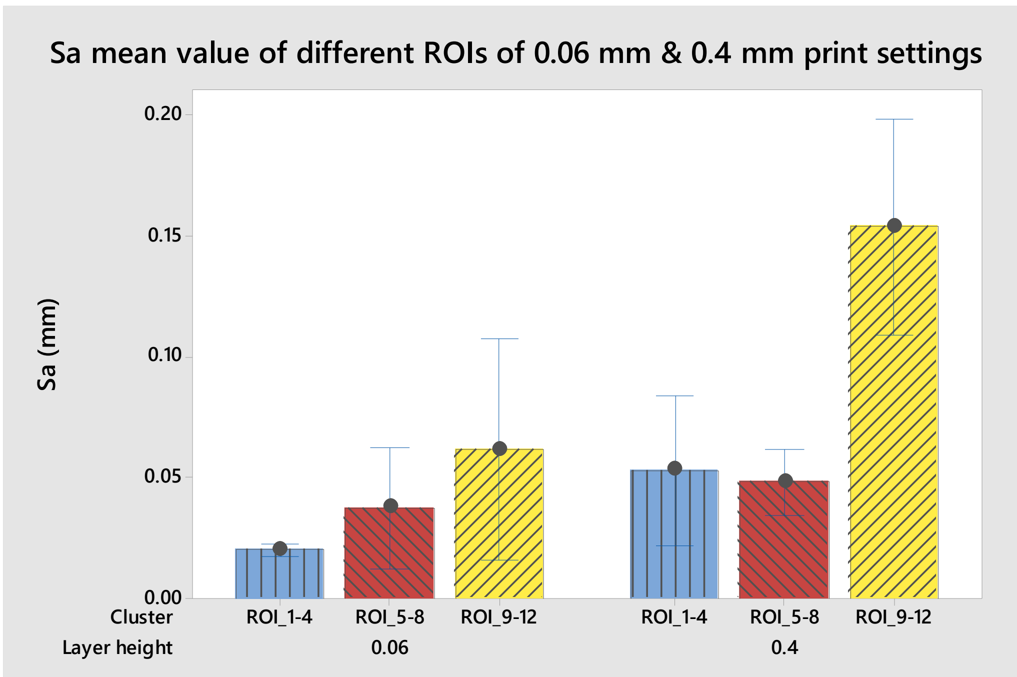

Figure 153: Sa mean value of different ROI clusters for both the 0.06 mm and 0.4 mm print settings.

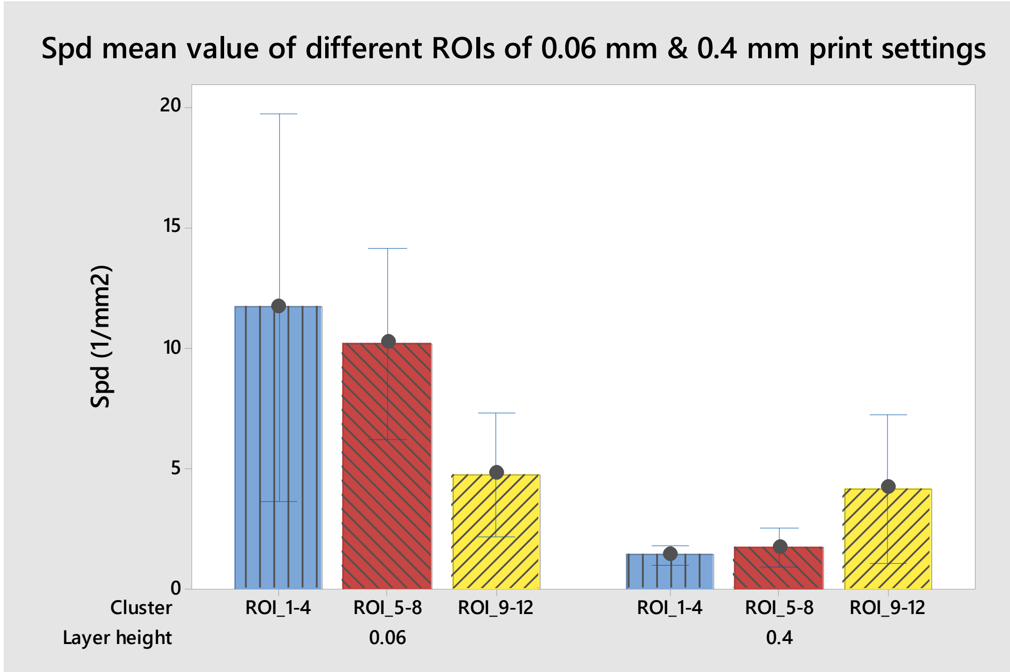

Figure 154: Spd mean value of different ROI clusters for both the 0.06 mm and 0.4 mm print settings.

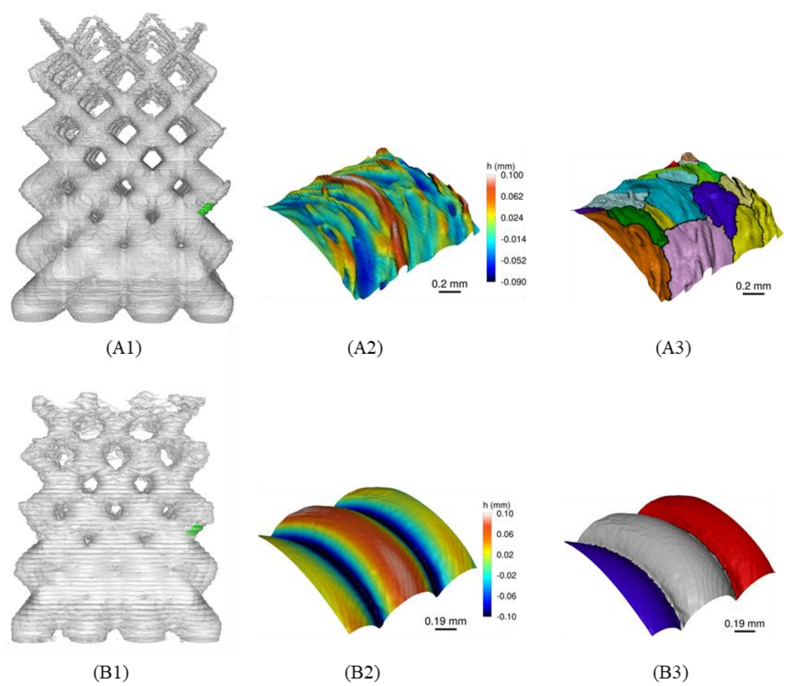

Figure 155: Green colour in (A1) and (B1) shows ROI_5 location. Colour map in (A2) and (B2) shows height distance between points to the estimated nominal form. Watershed segmentation shown in (A3) and (B3) after estimation of nominal form.

g) Internal Porosity analysis

The existence of internal porosity especially in fine features can be detrimental to the structural integrity of the produced part. Internal pores are voids, cracks or delamination existing between layers creating unwanted gaps/stress concentrations inside the printed material that are non-existent in the CAD. Initial qualitative results can be seen from the rendering in Figure 156 where both 0.06 mm and 0.4 mm layer height print settings can be visualized with 50 % transparency. The internal pores can be visualized in a scale similar for both models and on a mm^3 volume unit. Only pores that had a diameter 10 times bigger than the voxel size were assessed to increase accuracy and reduce chances of counting noise. The chosen value is higher than the recommended ratio of 6 mentioned in literature [364], shown to reduce pore volume errors. The segmentation method is a proprietary algorithm by VGSTUDIO MAX which is explained in the manual by defining pores as a group of voxels with grey values lower than the surrounding material [330]. Upon contacting VGSTUDIO MAX, the steps followed by the used algorithm segmentation were provided. The segmentation algorithm used starts by placing seed points all over the data set in positions with a local minimum. From this minimum, the seed point is then flooded in all directions (3D) until a certain threshold is reached, similar to a watershed algorithm. Whether the area flooded based on the seed point is deemed a pore is dependent on the probability criterium chosen. There are three criteria: contrast, roundness and size. The used default setting has a balance between the three, allowing for the pore to be assigned a probability value, to determine whether the detected pore is an actual pore.

Visually from Figure 156, it is clear how the 0.4 mm layer height print setting model has more, and bigger porosity distributed all over the lattice height compared to the 0.06 mm layer height setting. This is also reflected in the histogram generated in Figure 157 showing clearly how most pores for both models had a small volume, while the 0.4 mm setting had a higher percentage of larger pore volumes.

To summarize the internal porosity distribution, the volume percentage of the extracted internal pore defects can be seen in Table 20. The table shows how the 0.4 mm layer height print setting had an internal porosity percentage of 1.36 % which was ten times the value extracted from the 0.06 mm layer height setting, which was 0.08 %. The internal porosity percentage calculation was defined as a ratio of defect volume to the material volume. The material volume was also calculated and compared to the CAD as also seen in Table 20. The material volume of the 0.06 mm layer height print setting had a +0.61 % positive deviation from CAD showing a general oversizing to the CAD volume. The 0.4 mm print setting however had a negative material volume deviation from CAD volume of -4.07 % which can mainly be linked to the non-manufactured lattice struts at the top.

When most of the model is additively manufactured and dimensional CAD deviation analysis is small, material volume calculation can give a good indication of amount of porosity in the model as well as being a good basis for experimental comparisons. Alternatively, this could be achieved using comparable ROI where all struts are printed. This can be compared to internal porosity assessed indirectly by measuring the part density and applying an Archimedes' method for further comparison with an XCT porosity measurement [315]. Nevertheless, work by James et al. shows that significant deviation can be observed when comparing Archimedes' and micrograph analysis to XCT porosity analysis due to very small pores not being able to be captured [317]. This highlights the further need of more research in the field of smallest possible detectable pore size using XCT. The use of XCT porosity analysis is often more challenging when used in LPBF AM parts especially in cases where surface determination is not straightforward to apply on pores since the "pores" can be unfused or semi-fused powder, a challenge that often requires the use of porosity focused AM artefacts [375]. The reason for this challenge is that the XCT scanned internal unfused or semi-fused powder has a closer grey value to the part instead of a background level grey value that is easier to threshold.

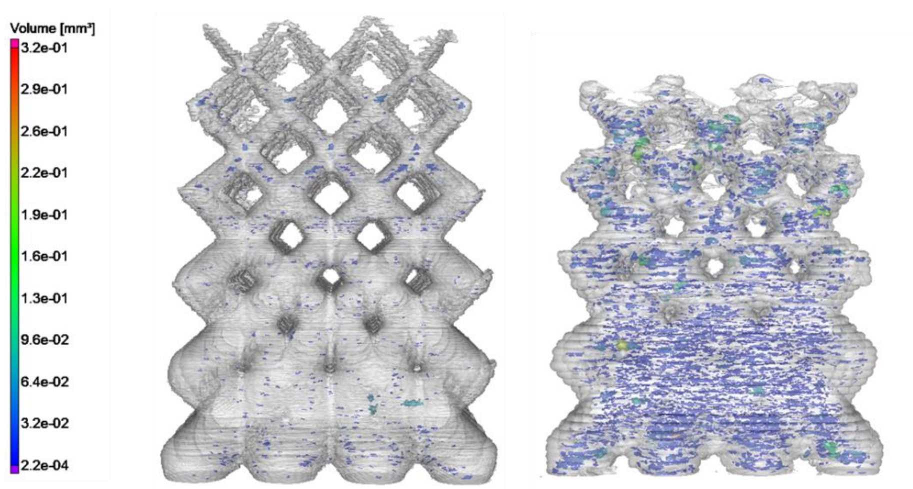

Figure 156: Internal porosity analysis

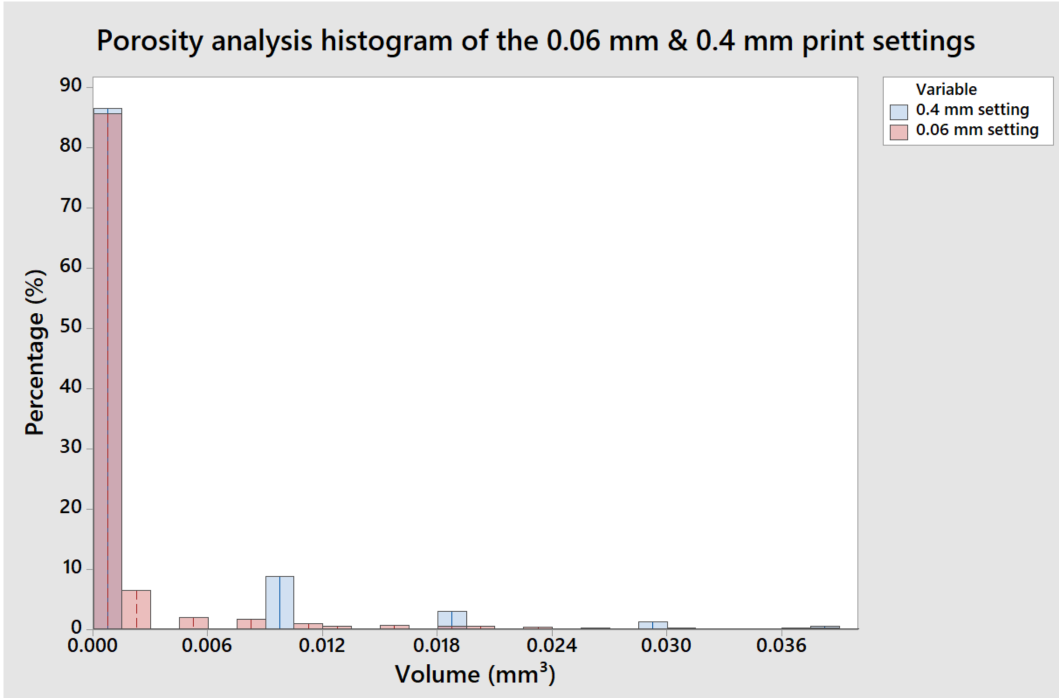

Figure 157: Porosity analysis histogram of both the 0.06mm layer height setting and 0.4 mm one.

Table 20: Material volume and defect volume percentage for both print settings

Layer height setting (mm)	0.06	0.4
Material volume (mm^3) Difference to CAD volume (%)	3782.22 (0.61%)	3606.06 (-4.07%)
Defect volume percentage (%)	0.08%	1.36%

7.5. Further AM lattice benchmark artefact design for TPMS and stochastic AM lattices and use of Chapter 5 contributions

In the two previous sections, the AM lattice benchmark artefact was additive manufactured and measured using XCT. This section will take the findings further and discuss AM lattice benchmark artefact designs for TPMS and stochastic lattices as well as measurement strategy that uses findings from Chapter 5.

While the AM lattice benchmark artefact above was a strut based one, it was done by developing a workflow in Ntop software, making the design parametric. This means that the unit cell or strut thickness can be efficiently and easily changed. For example, as seen in Figure 158 below, the unit cell could be instantly changed to other types like face centred cubic (b) or kelvin cell (c) while also changing the strut thickness, chosen in this case to range from 3 mm at the bottom to 0.3 mm at the top. While BCC and FCC is based on the crystal molecular body structure, the kelvin cell is proposed by Sir William Thomson (Lord Kelvin) in 1887 used to describe the equal sized bubble foam [4]. The kelvin cell is a tetrakaidecahedron (polyhedron with 14 faces) consisting of 6 squares and 8 hexagons. A different unit cell can have different mechanical properties and uses, for example, kelvin cell can be used in energy absorption applications like in cushioning and packaging [4]. The developed script in Ntop software ecosystem allows for increased flexibility and adaptability that can allow AM engineers to save time when designing other lattices to be tested on AM machines or to be used to develop unit cell specific measurement protocols.

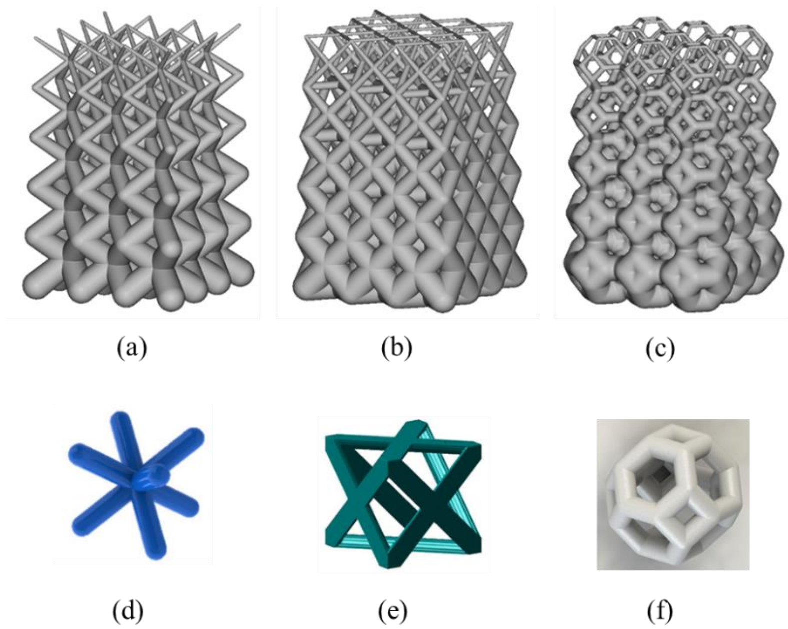

Figure 158: Developed parametric design BCC (a), face centred cubic (b) and kelvin cell (c) all shown as gradual strut from 3mm at the bottom to 0.3mm at the top of the lattice. Equivalent unit cell of BCC (d) [123], FCC (e) [376] and kelvin cell (f) [4].

This method can also be applied for TPMS type lattice structures which have improved functionality in applications with high fatigue [137] or ones that need heat dissipation [17]. As seen in Figure 159, not only it was possible to adapt the design for TPMS gyroid (a) and diamond type (b), but it was also easier to integrate it as a cylinder shape, which is more efficient to be used for XCT. This is because a cylindrical geometry would have an approximately similar penetration length while being rotated compared to a cubic shape, making it easier to XCT scan. While most of the developed measurement strategy shown above can be applied on TPMS lattices, it is expected that future work can unveil specific challenges that will need to be overcome, mainly in the case of surface roughness analysis and positioning error. It will for example be more challenging if not impossible in the case of TPMS structures to threshold nodes that can be used in node positioning error developed in this study. This is because TPMS lattices don't necessarily form sphere nodes in their connections compared to strut-based lattices. This challenge might require alternative ways to assess the positioning error which might include designing additional spheres on the TPMS benchmark lattice artefact as previously done on non-lattice and general AM benchmark artefacts [282].

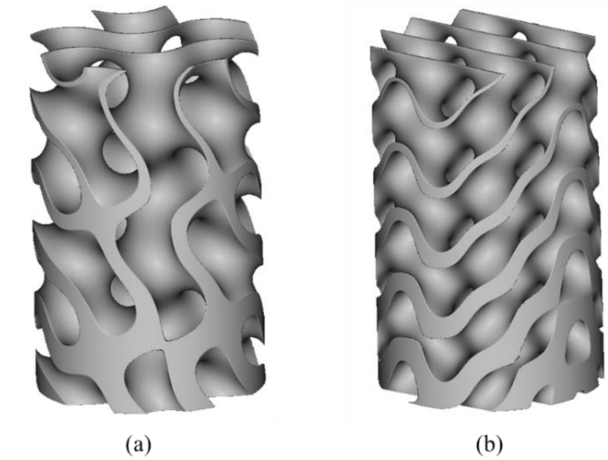

Figure 159: AM lattice benchmark artefact of TPMS gyroid (a) and diamond (b) with gradual strut thickness

The gradual strut thickness and measurement strategy developed above can also be used for stochastic lattices, which are also strut based and commonly used in implants due to their resemblance to bone geometry and properties [94]. Instead of varying only the strut thickness which only minimally changes the external pore size, the unit cell size can also be altered. Researching this topic can lead to better manufacturing optimisation for stochastic lattices, as well as improved and custom measurement strategies. Developing a stochastic AM lattice benchmark artefact can also assist significantly in current research done about post process surface treatment like chemical etching and [80,204]. Future work in this field can assist in testing the AM system in a range of stochastic strut diameters or unit cells without use of supports as well as DOE experiments focused on testing and optimising different post processing methods. These tests would be cost effective when using a single AM stochastic benchmark artefact with a gradient strut diameter and unit cell size compared to printing multiple lattices with individual properties. Figure 158 shows an example of a gradient AM stochastic lattice benchmark artefact that was designed in Ntop, additive manufactured in Aluminium, XCT scanned as well as analysed using wall thickness algorithm.

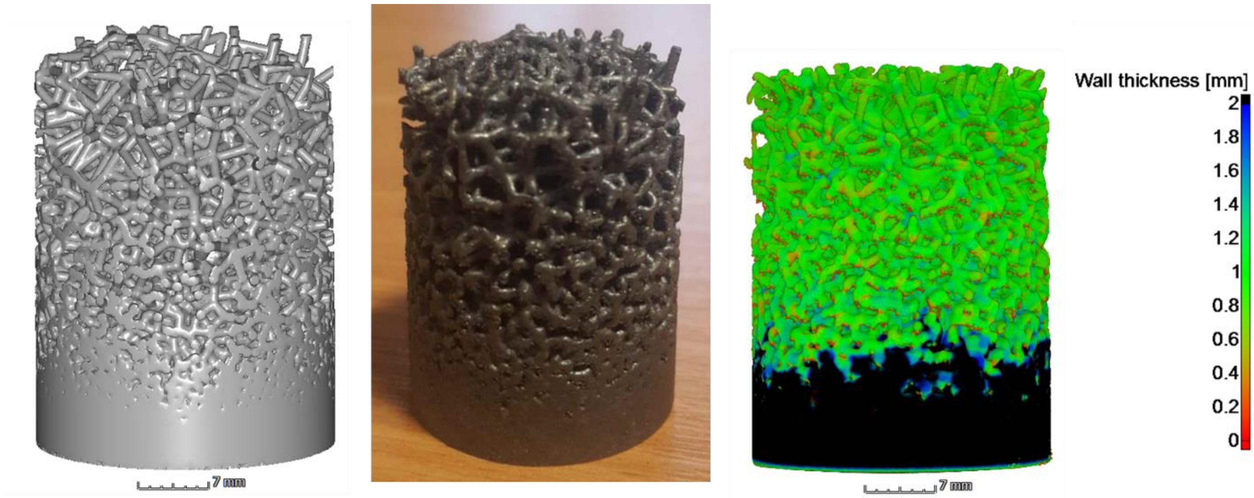

Figure 160: Example of AM stochastic lattice benchmark artefact with a gradient strut thickness.

Finally, and as previously applied in Chapter 5, the chosen AM lattice benchmark artefact design can be additive manufactured in metal and held using the developed fixture assembly alongside a dimensional workpiece previously measured using conventional instrument like CMM, as seen in Figure 161. This can assist in optimising XCT settings in a cost-effective manner as well as assisting in differentiating the AM errors with measurement errors caused by XCT, using dimensional workpiece. Expected challenges in this case include that the polymer fixture can only be used with metal prints of the lattice benchmark artefact and another material with lower attenuation will have to be used when holding lattice benchmark made in polymer material. Another challenge is that the dimensional workpiece has a fixed diameter which makes the XCT setting optimisation method developed in Chapter 5 optimised for a single diameter. A solution to tackle this challenge can be the use of a dimensional workpiece that also has a gradual strut thickness with approximately the same range as the one used in the dimensional workpiece. An additional suggestion for future work is to XCT at different magnifications. This could be especially advantageous for the fine lattice struts, which can benefit from a smaller voxel size. Further future work discussion can be found in Chapter 10 section 10.3

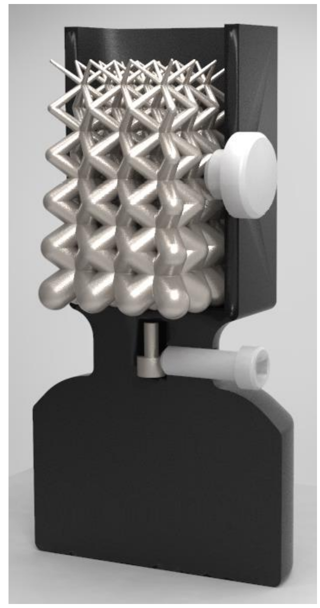

Figure 161: Rendering of the AM lattice benchmark artefact assembled with the XCT scan fixture and the dimensional workpiece.

7.6. Chapter summary

In this chapter, a novel AM benchmark artefact that is solely based on lattice structures, especially strut-based ones, has been designed, additively manufactured in both LPBF and FDM processes and measured using XCT, while following ISO/ASTM 52902:2019 as the main guideline. The AM lattice benchmark artefact can assist AM users to evaluate AM system capability as well as calibration of the system when it comes to AM of lattices. This is especially relevant when purchasing an AM system and looking to evaluate machine limits and optimize print settings before embarking on larger lattice parts, especially in the expensive LPBF process. The proposed design can also be used to compare cost effective and fast print settings versus slower and accurate ones, which has been successfully done in the FDM print section. For example, initial visual inspection clearly showed how the finer 0.06 mm layer height in the FDM print setting resulted in better resolution when printing the lattice struts as well as external pores. As for the faster 0.4 mm layer height setting, the fine features located at the top of the part were not printed but the lower half was additively manufactured, and at a significantly faster speed. This result can give the AM user great confidence on the expectations when printing different strut diameters of an AM lattice at different print settings. While results like smallest achievable strut diameter or pore size can be achieved by simpler AM benchmark artefacts that has simpler pin and hole designs, the suggested design goes further to allow for the quantification of holistic dimensional deviation, surface roughness and porosity, distributed across the whole lattice, which can be crucial before embarking on a larger complex lattice design. While the XCT use can be often expensive and a drawback for industrial environments, the proposed design has a gradual strut diameter that can be also measured by using simpler calliper or gauge tools or visually, to indicate to the AM user the approximate limitations of the AM machines and comparison results of different print settings.

The novel design was proven to be suitable for different AM technologies and not being process specific, which is an important milestone for an initial AM lattice benchmark artefact, making it more accessible to evaluate lattice structures. Future work can improve on the design and develop it to be more process specific to individual AM technologies, taking in consideration the features and workflows that are unique to each process. Novel protocols were also developed and applied to measure and evaluate the part dimensionally, as well as by analysing their surface roughness and porosity. This study aims at a research gap strictly aimed at designing a lattice focused AM benchmark as highlighted by De Pastre et al. [116]. As mentioned in literature review, and from the 65 AM benchmark artefacts existing in literature, there are only two added lattice designs but only as complementary designs with no clear measurement strategy optimized for them. Therefore, this study also offers a measurement strategy to fill the gap regarding the approaches and measurement evaluation methods for lattices which is still highlighted by the AMSC and named “Gap D26” in the standardization roadmap for AM [97].

From the developed measurement protocol, the geometric fidelity was also assessed and identified the minimum strut diameter that could be reliably manufactured by the AM machine. The minimum external pore size was also identified under different layer height print settings as well as their positioning linear error in different X, Y and Z axis. To summarise the dimensional metrology of the lattice, the XCT volume was aligned to the original CAD allowing for a holistic deviation analysis clearly highlighting the local analysis of the printed part. This analysis allowed for a clearer visualization as well as quantification of the often under sizing or oversizing, that AM lattices are subjected caused by different print settings.

Beside dimensional measurement, surface measurement was also applied on 24 down skin surfaces representing 12 surfaces from each layer height print setting. Each four of the 12 isolated down skin surfaces of an AM lattice formed an ROI cluster that represented a specific lattice strut diameter range. The obtained results allow an AM user to have clear expectations on the surface roughness Sa and Spd value as well as its repeatability across a layer height regarding different strut diameter values. Extracting areal surface data from XCT is still a relatively new process, and was first applied on lattices in this research since previous literature either measured surface data on cross sectioned strut using SEM or using XCT for profile measurement parameters like Ra. This research comes also as a complementary addition to the previous experiment in which both up skin and down skin was measured but only for one unit cell. When combining these two methods, both up and down skin measurements can be performed on multiple cluster ROIs of the whole lattice. Improvements can be achieved to this method by introducing further automation to it especially in the surface ROIs isolation stage. This stage of the process is currently done manually, however, the next time a similar lattice is XCT scanned the isolation can be implemented automatically by using the same Boolean Intersect that only needs to be prepared once and applied after an alignment of the XCT scanned lattice to original CAD.

Also, while XCT is ideal for lattices as it can reach internal features, its resolution and voxel size is still limiting a factor that should further researched and addressed [86]. A potential way to tackle this challenge is to use the newly suggested two-stage magnification 3D X-ray microscopes in XCT systems as suggested in study published by Villarraga-Gómez et al. [377]. Common good XCT resolutions at the moment can be around 3-10 µm while by using 3D X-ray microscopes significantly better resolutions can be reached better than 1 µm where for example 0.5 µm with the Versa 620 model [377]. To also tackle this challenge and increase the porosity analysis measurement fidelity, a calibrated reference part with micro drilled pores that is previously measured can be included with the AM part to be measured [241], which can be the AM lattice benchmark artefact in this case. Using this method can significantly reduce errors caused by surface determination which is often challenging and can greatly affect the results especially when it comes to additive manufactured components. Scanning artefacts like scattering or beam hardening can also be a challenge when using XCT and more research is needed to reduce them [343,378].

Finally, instead of printing multiple lattices as previously done in literature [121], the proposed novel gradient design offers increased simplicity when testing an AM system resolution and linear node positioning error when additively manufacturing lattice structures. The proposed design removes the need of having to manufacture multiple lattices with different strut diameter and having to individually XCT scan them, significantly increasing print time, material usage and measurement time. Using the proposed design can for example cut the time needed for AM and measurement if four lattices would have had to be assessed individually.

Also, a great benefit from using the proposed design is the minimisation of chances of a print failure or damage of the AM system hardware like re-coater blade. For example, if four lattices with different strut had to be additive manufactured, the one with the finest features might fail during the printing process. Since the lattices are separate, the failure will start from the beginning of the AM build, increasing its chances of a total failure or negatively affecting the parts next to it as well as the machine hardware. Having a gradient design means that the strut diameters that are challenging to the machine and have less chances to be additive manufactured are kept at the top of the part. This means that even in the case of a failure at that area, most of the AM benchmark lattice artefact bigger struts are already printed and will less likely be affected by the failure at the top of the part. This can also encourage the ease of additively manufacturing multiple gradient lattices at different corners of the AM build bed to assess for the process stability and chances of build plate position affecting the print quality due to laser focus shift or non-equal heat distribution across the X and Y axis of the AM build plate as well as in its Z axis representing the height.

AM lattice benchmark artefacts can play the role of a much-needed catalyst accelerating the adoption of not only lattices but also of AM in general in the different automotive, aerospace and medical industries, currently heavily increasing their AM capabilities. The AM benchmark lattice artefact not only assists in being able to understand the AM system limitations but also to improve and run DOE experiments with the aim of optimizing hatch scanning strategies, slicing methods, post processing processes and more. Doing so will also allow the AM user to choose the right AM print setting for the right AM lattice geometry depending on its geometry resolution and also depending on the part functionality and provided budget The budget can have a direct impact when additively manufacturing a part, this can be seen in the study above where the more accurate 0.06 mm layer height print setting led to a 13-fold increase in time needed to print compared to the 0.4 mm layer height setting. This means that especially for thicker lattice struts and if a part does not need tight tolerances, faster print settings one can be used while knowing the expected dimensional, surface and porosity defects to be expected, allowing for a much-needed cost effective and efficient AM process.

In terms of measurement accuracy, future work can focus on separating errors due to XCT and ones related to AM process. While using XCT for metrology allows measurement protocols unachievable using conventional methods, it also opens the door for traceability and repeatability challenges that should be accounted for. As suggested and performed in Chapter 5, a dimensional workpiece previously measured in CMM can accompany the developed AM lattice benchmark artefact to apply any necessary voxel corrections and evaluate the performed measurement. Since the AM lattice benchmark artefact has a gradient strut diameter, using a dimensional workpiece with fixed diameter as done in Chapter 5 can be limiting. To tackle this challenge, future work can include designing a dimensional workpiece like the one in Chapter 5 but this time, with a gradual strut that is similar to the range set for the lattice strut diameter.

Since measurements on the AM lattice benchmark artefact were more than just dimensional ones, a dimensional workpiece, even with a gradual strut, can be improved upon to be used as a reference for other type of measurements like surface or porosity ones. Future research improvements can include micro drilled holes that are previously conventionally measured. The hole resolution can be approximately similar to the one expected for the AM lattice to further evaluate the obtained porosity analysis. Future research in this field can be a great addition to work previously performed by Hermanek et al. [245] who looked at traceable porosity measurements using an artifact with holes, assisting in the surface determination phase. To improve upon the surface measurements done on the proposed study, up skin and down skin like LPBF surfaces can be also added to the dimensional workpiece alongside the micro drilled holes. This might however be challenging due to the range of surface topography needed to represent a lattice with gradient strut. To overcome this challenge, and as previously done by Townsend et al. [86] for areal surface measurements for XCT, voxel correction can be done to improve upon areal surface measurements. Using a dimensional artefact as seen in Figure 161, with a feature that is not affected by surface determination like the distance between two parallel planes can separate global voxel scaling errors and surface determination errors allowing for further XCT areal surface measurement correction [86].

Beside including a dimensional workpiece for the AM lattice benchmark artefact measurement, another optimisation can include the use of image analysis method developed in Chapter 5. Since the developed AM lattice benchmark artefact is expected to be used for different AM processes and materials, the XCT measurement operation can be further automated, especially in the settings optimisation stage. This means that further work can include testing the developed method and optimise it to work for a gradual strut diameter. Advances in this field can lead to a custom optimisation that can increase CNR across all different strut diameters instead of just one. Adapting this method can be crucial to make sure that the XCT measurement works for the whole lattice and is not only optimised for a specific range of strut diameters in the lattice. Finally, future work can include designing AM lattice benchmark artefacts that work for TPMS structures and also for stochastic strut-based lattices as can be seen in the designs suggested in Figure 159 and Figure 160 respectively. Further discussion can be found in Chapter 8 section 8.2d) and further future work discussion in Chapter 10 section 10.3.

8. Chapter : Discussion

8.1. Context of research

AM has been often viewed as a prototyping-only tool, hence the previous "Rapid Prototyping" naming. However, the AM field is currently offering end use production part quality in a range of industries, which can be considered as an important milestone. Nevertheless, the end use market, especially for parts that require high load or positioned in fatigue heavy environment would often require a case-by-case way of inspection and process validation. Breaking this pattern can only be done by developing advanced tools that assist in increasing the AM system stability as well as quality inspection methods especially for unconventional part geometries like lattice structures.

8.2. Discussion

a) Review on latest trends and research gaps in AM, XCT and their relation to lattice structures

The extensive review presented in this research represents a strong foundation and reference for AM lattice structures. The review starts with a strong foundation summarising AM market, technologies, applications, general workflow of both LPBF and FDM technologies, different AM standards and research gaps as well as DfAM methods. The review is then followed by a sole focus on lattice structures applications, design workflow, mechanical properties as well as advanced AM strategies optimised for lattice structures. The last part of the review starts by an introduction of XCT technology and its applications. This was followed by discussing the metrology side of lattices where XCT optimised inspection methods are investigated and summarised in three main sections that include dimensional metrology, surface metrology and porosity analysis.

b) XCT dimensional metrology optimisation for AM lattice structures

The initial work presented in Chapter 5 allowed for a first-hand identification of limitations when using conventional tools like focus variation microscope on lattice structures. Subsequently, it was clear how XCT had a high promise of solving metrology challenges for AM lattice structures. However, it was also clear after further research that using XCT and choosing its setup settings can often be subjective, and depending on user experience, leading to possible discrepancies [271]. Since most studies in this research were planned to be done using XCT, it was only reasonable to research and examinate a method that can semi automatically assist users in choosing XCT settings, making the process more objective and reducing user influence.

The two main experiments in Chapter 5 had a combined total of 42 XCT scans. The initial 30 XCT scans were done on a machined part and highlighted the possibility of using 2D image analysis prior to XCT reconstruction. The results showed a method that assists in ranking XCT settings using a developed "SFN" equation. The method was then extended to work for lattices and also extended by using the CNR equations from ISO 15708-3:2019 [339]. The results also showed high correlation between 2D image analysis evaluation results and 3D volume reconstruction quality, verified in this case using a substitution method of dimensional workpiece previously measured by CMM methods and which was subsequently published with ASTM [321], as seen in Appendix 12.2.

The results shown from this chapter contribute to the work reported in the literature to improve XCT accuracy and stability, especially when choosing scan settings, initially for machined parts and also for AM lattice structures. Compared to other methods like the use of XCT simulation software or conventional methods where volume XCT scans are compared using a substitution method, the developed method is not only faster and cost effective but also developed to be used on complex geometries like lattice structures. While showing good promise for future use, XCT simulation techniques currently only provide reasonable uncertainty predictions for simple measurement tasks and still show deviations when used on complex ones [379]. As reported in the literature, this is mainly due to the lack of holistic models that can correlate the effects of different scanning parameters on measurement uncertainty [231]. Due to these challenges in uncertainty assessment and XCT measurement procedures, the substitution method remains highly favourable. However, the substitution method is time consuming and non-generalizable [380], which means that different reference models have to be made whose geometry are dependent on the part of interest. Along these lines and using the developed method, the substitution method application time is consequentially reduced by applying the developed 2D image analysis procedures prior to volume reconstruction, saving a significant amount of setup time and reducing the chances of human error. The developed method, shows also how a verification process was performed, giving the user the possibility to verify the results leading to a high confidence standard when performing dimensional measurement on AM lattice structures. Also, and in the context of literature, this research comes as a great addition to the work performed by Kraemer et al. [340] where the authors also applied image quality parameters like CNR prior to reconstruction but the accuracy of the method did not allow for ideal XCT settings ranking. This research also comes as a significant addition to work carried out by Buratti et al. [332] who looked at individual influences of XCT parameters on scan quality and most importantly, developed a method to optimise XCT scan parameters and predict the parameters that will maximise the CNR value. This method however requires information on the nominal workpiece geometry, which is not a requirement in the method developed in this research.

Finally, both studies from Chapter 5 where the first one was performed mainly on machined parts and second one was focused on lattices, showed capability to make XCT setup efficient and cost effective.

The results also showed further compliance with literature findings like local surface determination being more accurate [262] and CNR being an adequate parameter to assess scan quality [332]. The developed protocol shown in this research has a significant potential to be used in industrial XCT machine scenarios to assist in cutting XCT scanning setups, reduce time needed to choose XCT settings while minimising user error and allowing the process to semi-automated instead of manual. This research can also set a solid ground for further upcoming studies aimed at making XCT scanning process not only semi-automated but fully automated, thus greatly increasing productivity and cost effectiveness of the process, indirectly leading to further adoption of AM processes and use of the functionally superior lattice geometries. Finally, findings from Chapter 5 contributed not only to the literature mentioned above but also directly to objective 2 set in this PhD study (seen in Chapter 1) and also to research GAP NDE4 [381] set by AMSC, related to NDE tools like XCT for complex geometries like AM lattices. Nevertheless, future work can be done to take further the developed method, which can be seen in Chapter 10 section 10.1.

c) XCT surface metrology optimisation for AM lattice structures

The work in Chapter 6 revolved around optimising the surface metrology aspect of lattice structures. This choice was a sensible step and a complementary one to the previous study in Chapter 5 optimising XCT dimensional metrology for AM lattices. This part of the research was approached after further literature examination highlighting the impact that surface roughness can have on lattice structures. This study was also developed to show the importance of including CAD with designed surface when optimise to simulation and also more generally in the design phase.

To better understand the impact of the study, the latter can be summarised in three components. The first component focused on developing a DOE, allowing for the study of 54 samples, leading to the capability to design custom surface topography on any CAD using areal surface roughness parameters as inputs. The second main component of the study focused on developing a method to extract both up and down skin areal surface data from lattice structures using XCT. As for the third component of the study, a process was developed to combine the two previous components and outline a method to design custom LPBF process up and down skin surface topography on CAD of lattice structures. The result of applying these three main components was a CADwDS that had less surface as well as less dimensional deviation compared of the lattice compared to the original CAD.

The findings of this study add to the knowledge base and contribute to the work completed regarding printed AM deviations during the design phase. Compared to published work which mainly focused on varying strut diameter or centroid of strut along its axis [205–207], this study investigated the resulting areal surface roughness on top of dimensional deviation of the CADwDS. Also, instead of using XCT as direct input to design a varying cross section as done in literature [175], this study relies on a novel script developed to design LPBF like up or down skin surface texture using areal surface parameters as inputs. Finally, instead of using XCT for profile surface measurements on lattices as previously reported in the literature [203,221,309], this study shows a novel method to extract areal surface parameters of both up and down skin of AM lattices.

Furthermore, and from a wider context of the literature, this study results come to enhance the currently researched methods and capabilities with respect to design of custom surface roughness on a chosen CAD. This capability can not only be used as a predictive method in the design phase, as done in this study, but also as a way to have further control and add custom surface roughness and textures to the surface of CAD with the intention of actually producing it. The work done by Modaresifar et al. [382] is a great example of how a custom nanopatterned surface can be designed on the CAD and additively manufactured, as a texture capable of repelling bacteria. This level of control, although still limited to small scale and high resolution AM systems [382] can be crucial when applied on the surface of medical AM implants [383].

Another application from the developed methods in this study is the possibility to reliably generate large databases of virtual and synthetic surfaces on different CAD shapes or lattices. These generated surfaces can for example represent either up or down skins and be used to form datasets useful for training machine learning models. These trained models can have a positive impact and for example assist in optimising AM process parameters to obtain functionally optimised surface textures [384]. They can also be used to optimise in-line surface measurement techniques as reported by Liu et al. [216,385]. As highlighted by Eastwood et al. [386], the capability to generate synthetic surface data can be cost effective and especially crucial during events like the recent COVID-19 pandemic which led to most lab access to be paused, leading to a lack of training data. Finally, findings from Chapter 6 contributed not only to the literature mentioned above but also directly to objective 3 set in this PhD study (seen in Chapter 1) and also to research GAP P4 [381] set by AMSC, related to developing metrology tools that are adapted and optimised for geometries like AM lattice structures. Further work suggestions related to this study can be seen in Chapter 10 section 10.2.

d) Development of benchmark artifact for AM lattice structures

The work presented in Chapter 7 presents a novel AM lattice benchmark artefact. The developed novel design was subsequently manufactured in both LPBF and FDM processes, measured using XCT, and analysed using a measurement strategy that was refined and optimised for lattices by using ISO/ASTM 52902:2019 [360] as a guideline.

Using the suggested design and measurement strategy means that by additively manufacturing only one part, the print quality of a range of strut diameters could be tested and analysed, simultaneously. This result comes as an addition to the work presented by Teeter et al. [121] in which multiple lattices with different strut diameters had to be additively manufactured. As outlined above, the ISO/ASTM 52902:2019 was used as a guideline where for example, the suggested test geometry for pin and hole diameter resolution was translated to strut diameter resolution and external pore resolution, respectively. This adaptation meant that the developed measurement strategy and analyses were optimised for lattice structures.

Another example of this measurement optimization is the developed lattice node positioning error evaluation, adapted from the ISO/ASTM 52902:2019 linear position accuracy measurement. In this case, node spheres that are already existing in the nodes connecting the designed lattice struts were thresholded and used for the measurement. This approach comes as a practical alternative to the method of adding or using prismatic protrusions to AM benchmark artefact designs as suggested by ISO/ASTM 52902:2019. The developed lattice node positioning method also complements and comes as a significant addition to previous work in literature suggesting the design of additional spheres in an AM benchmark artefact [282]. Taking advantage of features already existing in the design lead to reduction of print time and material use as well as ease of measurement, which is not necessarily possible when adding overlapping features for an XCT scan.

Also, the surface roughness data analyses was optimized for the suggested gradient strut diameter design by splitting the lattice into cluster ROIs. In this case, 24 down skin surfaces were isolated and analysed. This developed method was a crucial step to include, since the surface roughness properties across the lattice are not the same and are affected by the strut diameter or thickness, as also observed in literature [387].

Nevertheless, the findings of this study implies that to assess an AM system in terms of lattices, general AM benchmark artefacts can be avoided and lattice focused benchmark artefacts like the one developed can be used. This is significant since the most AM benchmark artefacts features suggested in literature [116,118] or by ISO/ASTM 52902:2019 [360] are not necessarily representative of a lattice geometry which often requires further process optimisation from laser settings in manufacturing stage to post-processing options. Also, conventional general AM benchmark artefacts are sometimes susceptible to manufacturability challenges like warping [118]. Also, most AM benchmark artefacts have a range of pin diameters [116,118], as advised by ISO/ASTM 52902:2019 [360], which can be used as an approximate reference for lattice printability. However, these isolated features and test geometries are provided with measurement strategies that are not methodically optimised for lattices. Furthermore, only two AM benchmark artefacts in literature [121,388] included a lattice as a complementary design and with no lattice focused optimised measurement method.

Finally, the suggested developed AM benchmark artefact with its measurement strategy comes as a clear addition to those highlighted in the literature, due to being solely focused on lattice structures and especially in the strut-based lattices. The findings of this study can not only assist in understanding and calibrating AM systems for lattices and comparing print settings as done in this study but also for optimizing the adequate post processing options available for lattices like blasting, chemical etching and more [80,204], which cannot be achieved if a conventional and general AM benchmark artefact is used. Suggested designs for TPMS and stochastic lattice structures can also play an important role for future AM lattice benchmark artefacts which can also take in consideration the suggested use of findings from Chapter 5. This include the use of a dimensional workpiece to separate measurement errors from manufacturing ones as well as using the developed image analysis tool to optimise XCT scan settings for the measured AM lattice.

Another application of the developed study is for the AM user to test the capability of making strut based “supports” which are existing in most builds. The application of this study in this field contributes to the existing literature in this area of research [149,389]. Advances in this field can also allow for using smaller and thinner supports at the are touching the part, allowing for an easier support removal, reducing time and cost needed for this post processing phase. The developed AM benchmark artefact can also assist existing AM users to experiment and develop DOE studies to innovate optimized scanning strategies as previously highlighted by Ghouse et al. [213,224] and post processing protocols especially for end use AM parts like medical implants as previously discussed by Farber et al [80]. Finally, the gap highlighted by De. Pastre et al. [116] regarding a lattice focused AM benchmark artefact design and measurement strategy has been met in this study. Finally, findings from Chapter 7 contributed not only to the literature mentioned above but also directly to objective 4 set in this PhD study (seen in Chapter 1) and also this time to multiple research gaps highlighted by AMSC [20], related to AM lattice measurement challenges which is named GAPD26, as well as ones related to using XCT for dimensional metrology of internal features, which is named Gap NDE4. Another one is “Gap P4: surface finish” which highlights the development of surface measurement methods adapted for lattice structures, which was successfully done in this study. Studies shared in Chapter 5, 6 were applied on as printed Aluminium lattice structure while the metal Titanium lattice in Chapter 7 had a stress relieving but no addition heat treatment. In this study, the focus was on developing measurement methods for lattices without emphasis on specific applied heat treatment. However, future work can consider multiple lattices with different heat treatments like HIP or surface treatments like chemical etching. Investigating these post processing methods can reveal more challenges, like the required measurement resolution or measurement strategy that could be then optimised for each chosen workflow. Further research suggestions can be seen in Chapter 10 section 10.3.

9. Chapter: Conclusion

The presented research forms a strong basis that can accelerate AM transition into developing more protocols to semi-automate and ideally automate most pre-processing as well as post-processing stages of the AM process, especially the metrology one. The main contributions can be briefly summarised below:

- Contribution 1 (Chapter 2-4): Identifying the latest trends as well as research gaps related to AM lattices in terms of design, manufacturing and especially metrology using XCT.
- Contribution 2 (Chapter 5): Development of novel semi-automatic method to assist XCT user and optimise scan settings for dimensional AM lattice metrology.
- Contribution 3 (Chapter 6): Development of procedure to extract both up and down skin areal surface data from AM lattices using XCT.
- Contribution 4 (Chapter 6): Development of procedure to design surface topography on any CAD and also for lattice structures up and down skin using areal surface parameters as design inputs.
- Contribution 5 (Chapter 7): Design of lattice focused AM lattice benchmark artefact with novel gradient strut thickness applicable for dimensional, surface and porosity analysis.
- Contribution 6 (Chapter 7): Development of lattice focused measurement strategy based on ISO/ASTM 52902:2019 and applying it using XCT and on prints done in both FDM and LPBF.

In response to objectives shown in Chapter 1, the first objective of laying out a state of art identification and summary of latest trends as well as research gaps related to AM and XCT in relation to lattices was successfully met As shown in Chapter (2-4), it was clear how adopting highly functional AM lattices relied on developing metrology tools not only DfAM ones. It was also clear how XCT was the ideal tool for investigating and holistically analysing AM lattice structures both internally and externally.

The second objective shown in Chapter 1 was successfully met with contribution 2, summarised above. Due to lack of XCT standards and heavy reliance on manual user input, Chapter 5 focused on developing a semi-automatic tool that assists users in optimising XCT settings prior to reconstruction [321]. This was done using 2D image analysis based on ISO 15708-3:2019 [339] CNR equation as well as verification using a dimensional workpiece previously measured in CMM. The developed method was initially applied on machined parts and then adapted for lattice structures. The developed method is highly efficient, cost effective and can allow as seen in Chapter 5 to go from a 7-hour process to 35min one when compared to conventional methods. The developed method was not only developed and optimised for lattices but also compared and verified against conventional methods using a designed and manufactured dimensional workpiece and fixture. This contribution comes as a great addition to existing literature related to reducing influence of user experience or subjectivity when using XCT [271] or maximising CNR by analysing the nominal workpiece geometry [332]. The findings also meet Gap NDE4 [381] related to using NDE tools like XCT for internal features, especially parts with complex geometries like lattice structures.

The third objective shown in Chapter 1 was met by contribution 3 and 4 summarised above. As seen in Chapter 6, the developed protocols did not only allow for successful extraction of areal up skin and down skin surface data of AM lattices using XCT but also to parametrically design surface topography on general CAD geometries as well as on CAD of AM lattice structures. This contribution was a result of extensive DOE done on different geometries, allowing for design of surface topography using areal surface parameters as inputs. This contribution comes as a great addition to existing literature which mainly focused on incorporating dimensional variations in the CAD of AM lattices [205–207].Also, contribution 3 and 4 specifically met Gap P4 set by AMSC [20], which is mainly focused on developing surface related metrology tools optimised for complex geometries like AM lattice structures.

Finally, objective four shown in Chapter 1 was successfully met with contribution 5 and 6 summarised above. As seen in Chapter 7, a novel AM lattice benchmark artefact was designed, additive manufactured in both LPBF/FDM processes, and measured using a novel lattice adequate measurement strategy. The measurement strategy was based on ISO/ASTM 52902:2019, applied using XCT and adequate volume analysis tools optimised for the metrology of AM lattice structures. Findings related to developing adequate surface measurement for lattices using XCT shown in Chapter 6 was taken further and applied on the novel gradual strut design. Chapter 7 also include in section 7.5 designs for AM lattice benchmark artefact optimised for TPMS or stochastic lattices as well as method to include and use findings from Chapter 5 related to the measurement strategy. Using findings from Chapter 5 and 6 allowed for an integrated Chapter 7 where it was possible to summarise multiple findings related to metrology of AM lattice structures, possible challenges as well as future work suggestions. This contribution comes as a great addition to existing literature where only two AM benchmark artefact included a lattice [116,118] without a suitable measurement strategy, which highlights the need of a lattice focused benchmark artefact as mentioned by De. Pastre et al. [116]. The findings can be used to not only evaluate different AM systems but also to optimise print settings as done by Ghouse et al. [213,224] or post processing options as done by Farber et al. [80]. This means that contribution 5 and 6 meet Gap D26 which is related to developing adequate measurement procedures optimised for AM lattice structures and also targets Gap P4 and Gap NDE4 shown above.

Furthermore, the proposed novel dimensional optimisation, surface extraction/design and AM lattice benchmark artefact research allowed to meet the aim of this PhD study, which was to develop and optimise measurement techniques, to enable a clear, repeatable and reliable approach of measuring or comparing produced AM lattice structures. Presented research and contribution in this field will participate in accelerating further adoption of AM and use of lattices in industry. Research in this field will allow AM users to be focused on developing ground-breaking applications with less cost and time spent on the process stability, post-processing, and quality inspection tools.

Nevertheless, AM market has significantly grew in the previous decade but, it still only represent less than 1% of the global manufacturing economy [6] and more research will be needed especially when it comes to lattices. Examples of promising research can include Nikon automated CT lines [390], EOS industry 4.0 integrated smart AM factory [391] or high speed XCT scan technology [392]. Future work related to each section of this study can be seen in the following Chapter.

10. Chapter : Future work

The work presented in this study aims at accelerating the adoption of AM and increase its use in the existing fields by embracing more of the unique capabilities of AM, in this case lattice structures. Following the presented research multiple future work paths can be followed as described below.

10.1. Further work regarding XCT dimensional metrology optimisation for AM lattice structures

Further work related to this Chapter can initially include doing a larger study with more variables in a structured DOE. Few adaptations are expected of the developed method like the option of changing ROI size when magnification is also a parameter. Another future study can include involving more XCT systems and users, leading to an ideal interlaboratory experiment. This will allow for the assessment of the developed method reliability and repeatability with different users. This can allow for improved efficiency that can assist users of all experience levels to take reliable XCT scans, especially for complex geometries like AM lattice structures. Future studies can also inspect the possibility of automating the process steps like the one related to user choosing the ROI regions and automatic comparison of CNR. This can greatly assist in research aiming at making XCT scanning process reliable and with reduced dependency on user experience or subjectivity as well as automated, making it cost effective.

10.2. Further work regarding XCT surface metrology study for AM lattice structures

The performed study was effective, and to take it further, future work can expand the range of strut-based lattices and their overhang angles allowing for further process repeatability quantification. Since the design is parametric, this can be done instantly by changing the unit cell type of strut diameter range without need for manual redesign. Also, the proposed study used AlSi10Mg and LPBF process. However, Since the challenging surface roughness on the overhang of lattices is not limited to the LPBF process, future research can investigate further AM processes such as electron beam [393] or even binder jetting [394]. As a result, DfAM engineers can have clear expectations of different AM processes and materials when additively manufacturing lattices as previously reported in the literature for non-lattice AM parts [108]. In the context of the present study, research in this field will enable designing CADwDS of AM lattices specifying the type of AM process and print settings as inputs or retain of areal surface roughness parameters to define process parameters. Also, when using LPBF process, it is not uncommon to have slightly different part quality depending on the part position on the print bed [395], in fact, most AM machines when calibrated, have an ideal spot that is usually in the middle, where heat distribution is more stable. The positioning in the build platform in regard to the powder spreading direction and purging gas can also affect the resulting part properties due to the distribution of powder particle sizes and packing density of the layers and gas flow [396] . In this regard, future research can investigate how this change in part position across build platform can affect quality and surface topography of AM lattices using the proposed design and measurement strategy. It is expected for example that with further research on the AM machine quality and repeatability across the bed platform, the designed CADwDS will not only be dependent on the AM process and print settings as mentioned above but also on the planned print bed location. Research in this field can possibly lead to the development of another parameter or coefficient that can be directly added to the developed script to affect the surface topography, and for example increase Sa on down skin surface because the part is not in an ideal build bed position.

10.3. Further work regarding AM lattice benchmark artefact

Regarding the study shared in Chapter 7, the design was proven to not be exclusive to one AM process as it was additive manufactured in both LPBF and FDM systems. Since the XCT penetration of the Titanium part was challenging, few suggestions made above included testing it in Aluminium, since a lattice of approximately similar box size was successfully XCT scanned in Chapter 6. Another suggestion was the use of XCT machine with higher voltage, which might be challenging due to contrasting fine and thick features but can be achievable by using dual energy methods shown in literature [370]. Another alternative was to adapt the design for denser metals and only have two-unit cells in X and Y axis as seen in as seen in Figure 141. Future work can also include the design and adaptation of measurement strategy for TPMS lattice structures. While the TPMS lattice benchmark artefact can also have a gradual thickness, measurements developed for strut-based type unit cells are not necessarily applicable in this case. Finally, and while the findings of Chapter 6 related to surface extraction was used in the AM lattice benchmark artefact, the findings of Chapter 5 can also be adapted in future experiments and be used to include a dimensional workpiece and XCT setting optimisation step before measurement. This will allow for improved separation of manufacturing errors and measurement errors, which can be critical for the usual fine features of AM lattice structures.

11. References

[1] ISO - ISO/ASTM 52900:2015 - Additive manufacturing — General principles — Terminology, (n.d.). https://www.iso.org/standard/69669.html (accessed January 27, 2021).

[2] M. Chiumenti, X. Lin, M. Cervera, W. Lei, Y. Zheng, W. Huang, Numerical simulation and experimental calibration of additive manufacturing by blown powder technology. Part I: thermal analysis, Rapid Prototyp. J. 23 (2017) 448–463. https://doi.org/10.1108/RPJ-10-2015-0136.

[3] A.H. Schoen, Infinite periodic minimal surfaces without self-intersections, National Aeronautics and Space Administration, 1970.

[4] C. Ge, L. Priyadarshini, D. Cormier, L. Pan, J. Tuber, A preliminary study of cushion properties of a 3D printed thermoplastic polyurethane Kelvin foam, Packag. Technol. Sci. 31 (2018) 361–368.

[5] L. Tan, Image file formats, Biomed. Imaging Interv. J. 2 (2006) e6. https://doi.org/10.2349/biij.2.1.e6.

[6] A. Wohlers, Wohlers Report 2020 3D Printing and Additive Manufacturing Global State of the Industry, n.d. https://wohlersassociates.com/2020report.htm (accessed April 13, 2021).

[7] A.W. Gebisa, H.G. Lemu, Design for manufacturing to design for Additive Manufacturing: Analysis of implications for design optimality and product sustainability, Procedia Manuf. 13 (2017) 724–731. https://doi.org/10.1016/j.promfg.2017.09.120.

[8] J. Plocher, A. Panesar, Review on design and structural optimisation in additive manufacturing: Towards next-generation lightweight structures, Mater. Des. 183 (2019) 108164. https://doi.org/10.1016/j.matdes.2019.108164.

[9] D. Mahmoud, M.A. Elbestawi, Lattice Structures and Functionally Graded Materials Applications in Additive Manufacturing of Orthopedic Implants: A Review, J. Manuf. Mater. Process. 1 (2017) 13. https://doi.org/10.3390/jmmp1020013.

[10] C. Pan, Y. Han, J. Lu, Design and Optimization of Lattice Structures: A Review, Appl. Sci. 10 (2020) 6374. https://doi.org/10.3390/app10186374.

[11] Architected Materials, NTopology. (n.d.). https://ntopology.com/architected-materials/ (accessed July 28, 2021).

[12] X. Wang, S. Xu, S. Zhou, W. Xu, M. Leary, P. Choong, M. Qian, M. Brandt, Y.M. Xie, Topological design and additive manufacturing of porous metals for bone scaffolds and orthopaedic implants: A review, Biomaterials. 83 (2016) 127–141. https://doi.org/10.1016/j.biomaterials.2016.01.012.

[13] S. Arabnejad, B. Johnston, M. Tanzer, D. Pasini, Fully porous 3D printed titanium femoral stem to reduce stress-shielding following total hip arthroplasty, J. Orthop. Res. 35 (2017) 1774–1783. https://doi.org/10.1002/jor.23445.

[14] C. Emmelmann, P. Scheinemann, M. Munsch, V. Seyda, Laser Additive Manufacturing of Modified Implant Surfaces with Osseointegrative Characteristics, Phys. Procedia. 12 (2011) 375–384. https://doi.org/10.1016/j.phpro.2011.03.048.

[15] Case Study: Air Force Optimizes CubeSat Bus, NTopology. (n.d.). https://ntopology.com/case-studies/air-force-optimizes-cubesat-using-architected-materials/ (accessed May 18, 2021).

[16] K.J. Maloney, K.D. Fink, T.A. Schaedler, J.A. Kolodziejska, A.J. Jacobsen, C.S. Roper, Multifunctional heat exchangers derived from three-dimensional micro-lattice structures, Int. J. Heat Mass Transf. 55 (2012) 2486–2493. https://doi.org/10.1016/j.ijheatmasstransfer.2012.01.011.

[17] S. Catchpole-Smith, R.R.J. Sélo, A.W. Davis, I.A. Ashcroft, C.J. Tuck, A. Clare, Thermal conductivity of TPMS lattice structures manufactured via laser powder bed fusion, Addit. Manuf. 30 (2019) 100846. https://doi.org/10.1016/j.addma.2019.100846.

[18] D.A. Ramirez, L.E. Murr, S.J. Li, Y.X. Tian, E. Martinez, J.L. Martinez, B.I. Machado, S.M. Gaytan, F. Medina, R.B. Wicker, Open-cellular copper structures fabricated by additive manufacturing using electron beam melting, Mater. Sci. Eng. A. 528 (2011) 5379–5386. https://doi.org/10.1016/j.msea.2011.03.053.

[19] R.K. Leach, D. Bourell, S. Carmignato, A. Donmez, N. Senin, W. Dewulf, Geometrical metrology for metal additive manufacturing, CIRP Ann. 68 (2019) 677–700. https://doi.org/10.1016/j.cirp.2019.05.004.
[20] AMSC, April 2021 Progress Report AMSC Roadmap v2 Gaps, 2021. https://share.ansi.org/Shared%20Documents/Standards%20Activities/AMSC/April_2021_Progress_Report_AMSC_Roadmap_v2_Gaps.pdf (accessed July 28, 2021).
[21] A. Bandyopadhyay, S. Bose, Additive Manufacturing, Second Edition, CRC Press, 2019.
[22] D. Piñero Vega, M. Batista Ponce, A.P. Valerga Puerta, J.M. Vazquez Martinez, S.R. Fernandez Vidal, A COMPARISON OF MACRO AND MICROGEOMETRICAL PROPERTIES OF SPECIMENS MADE WITH A FDM COMMERCIAL PRINTER AND ITS OPENSOURCE RETROFIT VERSION., Ann. DAAAM Proc. 29 (2018).
[23] Dr Adrian Bowyer to receive Outstanding Contribution to 3D Printing Award, 3D Print. Ind. (2017). https://3dprintingindustry.com/news/dr-adrian-bowyer-receive-outstanding-contribution-3d-printing-award-107673/ (accessed January 27, 2021).
[24] TCT Hall of Fame | Dr Adrian Bowyer | Founder of the RepRap Project, TCT Mag. (2017). https://www.tctmagazine.com/api/content/7b2d1a02-dc2a-11e7-8829-125f88921b3c/ (accessed January 27, 2021).
[25] Best Budget 3D Printers 2021 (April), All3DP. (2021). https://all3dp.com/1/best-cheap-budget-3d-printer-affordable-under-500-1000/ (accessed June 2, 2021).
[26] A. Vafadar, F. Guzzomi, A. Rassau, K. Hayward, Advances in Metal Additive Manufacturing: A Review of Common Processes, Industrial Applications, and Current Challenges, Appl. Sci. 11 (2021) 1213. https://doi.org/10.3390/app11031213.
[27] J.J. Lewandowski, M. Seifi, Metal additive manufacturing: a review of mechanical properties, Annu. Rev. Mater. Res. 46 (2016) 151–186.
[28] J.V. Gordon, S.P. Narra, R.W. Cunningham, H. Liu, H. Chen, R.M. Suter, J.L. Beuth, A.D. Rollett, Defect structure process maps for laser powder bed fusion additive manufacturing, Addit. Manuf. 36 (2020) 101552. https://doi.org/10.1016/j.addma.2020.101552.
[29] L.E. Criales, Y.M. Arısoy, B. Lane, S. Moylan, A. Donmez, T. Özel, Laser powder bed fusion of nickel alloy 625: Experimental investigations of effects of process parameters on melt pool size and shape with spatter analysis, Int. J. Mach. Tools Manuf. 121 (2017) 22–36. https://doi.org/10.1016/j.ijmachtools.2017.03.004.
[30] P. Edwards, M. Ramulu, Fatigue performance evaluation of selective laser melted Ti–6Al–4V, Mater. Sci. Eng. A. 598 (2014) 327–337. https://doi.org/10.1016/j.msea.2014.01.041.
[31] H. Masuo, Y. Tanaka, S. Morokoshi, H. Yagura, T. Uchida, Y. Yamamoto, Y. Murakami, Influence of defects, surface roughness and HIP on the fatigue strength of Ti-6Al-4V manufactured by additive manufacturing, Int. J. Fatigue. 117 (2018) 163–179. https://doi.org/10.1016/j.ijfatigue.2018.07.020.
[32] A. du Plessis, E. Macdonald, Hot isostatic pressing in metal additive manufacturing: X-ray tomography reveals details of pore closure, Addit. Manuf. 34 (2020) 101191. https://doi.org/10.1016/j.addma.2020.101191.
[33] S. Tammas-Williams, P.J. Withers, I. Todd, P.B. Prangnell, Porosity regrowth during heat treatment of hot isostatically pressed additively manufactured titanium components, Scr. Mater. 122 (2016) 72–76. https://doi.org/10.1016/j.scriptamat.2016.05.002.
[34] S. Tammas-Williams, P.J. Withers, I. Todd, P.B. Prangnell, The Effectiveness of Hot Isostatic Pressing for Closing Porosity in Titanium Parts Manufactured by Selective Electron Beam Melting, Metall. Mater. Trans. A. 47 (2016) 1939–1946. https://doi.org/10.1007/s11661-016-3429-3.
[35] Q. Han, R. Mertens, M.L. Montero-Sistiaga, S. Yang, R. Setchi, K. Vanmeensel, B. Van Hooreweder, S.L. Evans, H. Fan, Laser powder bed fusion of Hastelloy X: Effects of hot isostatic pressing and the

hot cracking mechanism, Mater. Sci. Eng. A. 732 (2018) 228–239. https://doi.org/10.1016/j.msea.2018.07.008.
[36] J. Benzing, N. Hrabe, T. Quinn, R. White, R. Rentz, M. Ahlfors, Hot isostatic pressing (HIP) to achieve isotropic microstructure and retain as-built strength in an additive manufacturing titanium alloy (Ti-6Al-4V), Mater. Lett. 257 (2019) 126690. https://doi.org/10.1016/j.matlet.2019.126690.
[37] C. de Formanoir, M. Suard, R. Dendievel, G. Martin, S. Godet, Improving the mechanical efficiency of electron beam melted titanium lattice structures by chemical etching, Addit. Manuf. 11 (2016) 71–76. https://doi.org/10.1016/j.addma.2016.05.001.
[38] S. Hwang, E.I. Reyes, K. Moon, R.C. Rumpf, N.S. Kim, Thermo-mechanical Characterization of Metal/Polymer Composite Filaments and Printing Parameter Study for Fused Deposition Modeling in the 3D Printing Process, J. Electron. Mater. 44 (2015) 771–777. https://doi.org/10.1007/s11664-014-3425-6.
[39] Y. Thompson, J. Gonzalez-Gutierrez, C. Kukla, P. Felfer, Fused filament fabrication, debinding and sintering as a low cost additive manufacturing method of 316L stainless steel, Addit. Manuf. 30 (2019) 100861. https://doi.org/10.1016/j.addma.2019.100861.
[40] 3D printing for foot, MOJ Proteomics Bioinforma. Volume 5 (2017). https://doi.org/10.15406/mojpb.2017.05.00176.
[41] K.V. Wong, A. Hernandez, A Review of Additive Manufacturing, ISRN Mech. Eng. 2012 (2012) e208760. https://doi.org/10.5402/2012/208760.
[42] Boeing: Additive manufacturing insight, (n.d.). https://www.boeing.com/features/innovation-quarterly/2019_q4/btj-additive-manufacturing.page (accessed July 19, 2021).
[43] J.C. Najmon, S. Raeisi, A. Tovar, 2 - Review of additive manufacturing technologies and applications in the aerospace industry, in: F. Froes, R. Boyer (Eds.), Addit. Manuf. Aerosp. Ind., Elsevier, 2019: pp. 7–31. https://doi.org/10.1016/B978-0-12-814062-8.00002-9.
[44] Boeing: 3D printing done right, (n.d.). https://www.boeing.com/features/innovation-quarterly/nov2017/feature-thought-leadership-3d-printing.page (accessed April 13, 2021).
[45] New technology campus for 3D printing goes on stream: BMW Group builds on additive manufacturing, with skills consolidated at single site, (n.d.). https://www.press.bmwgroup.com/global/article/detail/T0309872EN/new-technology-campus-for-3d-printing-goes-on-stream:-bmw-group-builds-on-additive-manufacturing-with-skills-consolidated-at-single-site?language=en (accessed April 13, 2021).
[46] J.B. April 2019, Customising production, Automot. Manuf. Solut. (n.d.). https://www.automotivemanufacturingsolutions.com/joining/customising-production/31218.article (accessed April 13, 2021).
[47] BMW's new S58 engine features cylinder head made with 3D printing » 3D Printing Media Network - The Pulse of the AM Industry, 3D Print. Media Netw. - Pulse AM Ind. (2019). https://www.3dprintingmedia.network/bmw-s58-engine-3d-printed-cylinder/ (accessed April 13, 2021).
[48] Innovative pistons from a 3D printer for increased power and efficiency, Porsche Newsroom. (n.d.). https://newsroom.porsche.com/en/2020/technology/porsche-cooperation-mahle-trumpf-pistons-3d-printer-power-efficiency-911-gt2-rs-21462.html (accessed April 13, 2021).
[49] NanoHack, an open-source 3D printed mask against COVID-19, 3Dnatives. (2020). https://www.3dnatives.com/en/mask-against-covid-19-180320205/ (accessed July 23, 2021).
[50] Coronavirus: 3D printers save hospital with valves, BBC News. (2020). https://www.bbc.com/news/technology-51911070 (accessed June 3, 2021).
[51] 3D printing nasal swabs - Make Parts Fast, (n.d.). https://www.makepartsfast.com/3d-printing-nasal-swabs/ (accessed June 3, 2021).

[52] M.K. Thompson, G. Moroni, T. Vaneker, G. Fadel, R.I. Campbell, I. Gibson, A. Bernard, J. Schulz, P. Graf, B. Ahuja, F. Martina, Design for Additive Manufacturing: Trends, opportunities, considerations, and constraints, CIRP Ann. 65 (2016) 737–760. https://doi.org/10.1016/j.cirp.2016.05.004.
[53] M. Paulic, T. Irgolic, J. Balic, F. Cus, A. Cupar, T. Brajlih, I. Drstvensek, Reverse Engineering of Parts with Optical Scanning and Additive Manufacturing, Procedia Eng. 69 (2014) 795–803. https://doi.org/10.1016/j.proeng.2014.03.056.
[54] F. Bauer, M. Schrapp, J. Szijarto, Accuracy analysis of a piece-to-piece reverse engineering workflow for a turbine foil based on multi-modal computed tomography and additive manufacturing, Precis. Eng. 60 (2019) 63–75. https://doi.org/10.1016/j.precisioneng.2019.07.008.
[55] J.W.H. Tangelder, P. Ermes, G. Vosselman, F.A.V.D. Heuvel, CAD-Based Photogrammetry for Reverse Engineering of Industrial Installations, Comput.-Aided Civ. Infrastruct. Eng. 18 (2003) 264–274. https://doi.org/10.1111/1467-8667.00316.
[56] L. Chougrani, J.-P. Pernot, P. Véron, S. Abed, Lattice structure lightweight triangulation for additive manufacturing, Comput.-Aided Des. 90 (2017) 95–104. https://doi.org/10.1016/j.cad.2017.05.016.
[57] B. Zhang, A. Goel, O. Ghalsasi, S. Anand, CAD-based design and pre-processing tools for additive manufacturing, J. Manuf. Syst. 52 (2019) 227–241. https://doi.org/10.1016/j.jmsy.2019.03.005.
[58] A.C. Brown, D. de Beer, Development of a stereolithography (STL) slicing and G-code generation algorithm for an entry level 3-D printer, in: 2013 Africon, 2013: pp. 1–5. https://doi.org/10.1109/AFRCON.2013.6757836.
[59] M. Givi, J.R.R. Mayer, Volumetric error formulation and mismatch test for five-axis CNC machine compensation using differential kinematics and ephemeral G-code, Int. J. Adv. Manuf. Technol. 77 (2015) 1645–1653. https://doi.org/10.1007/s00170-014-6558-0.
[60] Ultimaker Cura: Powerful, easy-to-use 3D printing software, Ultimaker.Com. (n.d.). https://ultimaker.com/software/ultimaker-cura (accessed March 16, 2021).
[61] N.E. Gorji, P. Saxena, M. Corfield, A. Clare, J.-P. Rueff, J. Bogan, P.G.M. González, M. Snelgrove, G. Hughes, R. O'Connor, R. Raghavendra, D. Brabazon, A new method for assessing the recyclability of powders within Powder Bed Fusion process, Mater. Charact. 161 (2020) 110167. https://doi.org/10.1016/j.matchar.2020.110167.
[62] E. Kim, Y.-J. Shin, S.-H. Ahn, The effects of moisture and temperature on the mechanical properties of additive manufacturing components: fused deposition modeling, Rapid Prototyp. J. 22 (2016) 887–894. https://doi.org/10.1108/RPJ-08-2015-0095.
[63] C.L.A. Leung, S. Marussi, M. Towrie, R.C. Atwood, P.J. Withers, P.D. Lee, The effect of powder oxidation on defect formation in laser additive manufacturing, Acta Mater. 166 (2019) 294–305. https://doi.org/10.1016/j.actamat.2018.12.027.
[64] N.A. Pohlman, J.A. Roberts, M.J. Gonser, Characterization of titanium powder: Microscopic views and macroscopic flow, Powder Technol. 228 (2012) 141–148. https://doi.org/10.1016/j.powtec.2012.05.009.
[65] A. Strondl, O. Lyckfeldt, H. Brodin, U. Ackelid, Characterization and Control of Powder Properties for Additive Manufacturing, JOM. 67 (2015) 549–554. https://doi.org/10.1007/s11837-015-1304-0.
[66] S. Vock, B. Klöden, A. Kirchner, T. Weißgärber, B. Kieback, Powders for powder bed fusion: a review, Prog. Addit. Manuf. 4 (2019) 383–397. https://doi.org/10.1007/s40964-019-00078-6.
[67] Why Pre-Build Calibration is Critical to Part Quality for Metal Additive Manufacturing, (n.d.). https://www.qualitymag.com/articles/96242-why-pre-build-calibration-is-critical-to-part-quality-for-metal-additive-manufacturing?v=preview (accessed June 3, 2021).
[68] REVIEW: The Zortrax M300 Plus, a well designed machine for large volume desktop 3D printing, 3D Print. Ind. (2019). https://3dprintingindustry.com/news/review-the-zortrax-m300-plus-a-well-designed-machine-for-large-volume-desktop-3d-printing-155138/ (accessed June 3, 2021).

[69] M. Grasso, A. Remani, A. Dickins, B. Colosimo, R. Leach, In-situ measurement and monitoring methods for metal powder bed fusion – an updated review, (2021).
[70] X. Wang, K. Chou, The effects of stress relieving heat treatment on the microstructure and residual stress of Inconel 718 fabricated by laser metal powder bed fusion additive manufacturing process, J. Manuf. Process. 48 (2019) 154–163. https://doi.org/10.1016/j.jmapro.2019.10.027.
[71] T. DebRoy, H.L. Wei, J.S. Zuback, T. Mukherjee, J.W. Elmer, J.O. Milewski, A.M. Beese, A. Wilson-Heid, A. De, W. Zhang, Additive manufacturing of metallic components – Process, structure and properties, Prog. Mater. Sci. 92 (2018) 112–224. https://doi.org/10.1016/j.pmatsci.2017.10.001.
[72] J. Jiang, X. Xu, J. Stringer, Support Structures for Additive Manufacturing: A Review, J. Manuf. Mater. Process. 2 (2018) 64. https://doi.org/10.3390/jmmp2040064.
[73] J. Jiang, F. Weng, S. Gao, J. Stringer, X. Xu, P. Guo, A support interface method for easy part removal in directed energy deposition, Manuf. Lett. 20 (2019) 30–33. https://doi.org/10.1016/j.mfglet.2019.04.002.
[74] S. Nelaturi, M. Behandish, A.M. Mirzendehdel, J. de Kleer, Automatic Support Removal for Additive Manufacturing Post Processing, Comput.-Aided Des. 115 (2019) 135–146. https://doi.org/10.1016/j.cad.2019.05.030.
[75] O.J. Hildreth, A.R. Nassar, K.R. Chasse, T.W. Simpson, Dissolvable Metal Supports for 3D Direct Metal Printing, 3D Print. Addit. Manuf. 3 (2016) 90–97. https://doi.org/10.1089/3dp.2016.0013.
[76] A. Hussein, L. Hao, C. Yan, R. Everson, P. Young, Advanced lattice support structures for metal additive manufacturing, J. Mater. Process. Technol. 213 (2013) 1019–1026. https://doi.org/10.1016/j.jmatprotec.2013.01.020.
[77] Z.-C. Fang, Z.-L. Wu, C.-G. Huang, C.-W. Wu, Review on residual stress in selective laser melting additive manufacturing of alloy parts, Opt. Laser Technol. 129 (2020) 106283. https://doi.org/10.1016/j.optlastec.2020.106283.
[78] I. Alexander, G. Vladimir, P. Petr, K. Mihail, I. Yuriy, V. Andrey, Machining of Thin-walled Parts Produced by Additive Manufacturing Technologies, Procedia CIRP. 41 (2016) 1023–1026. https://doi.org/10.1016/j.procir.2015.08.088.
[79] G. Pyka, A. Burakowski, G. Kerckhofs, M. Moesen, S.V. Bael, J. Schrooten, M. Wevers, Surface Modification of Ti6Al4V Open Porous Structures Produced by Additive Manufacturing, Adv. Eng. Mater. 14 (2012) 363–370. https://doi.org/10.1002/adem.201100344.
[80] E. Farber, D. Nazarov, I. Mitrofanov, V. Sufiiarov, A. Popovich, M. Maximov, Development of the titanium meshes by selective laser melting and chemical etching for using as medical implants, Mater. Today Proc. 30 (2020) 746–751. https://doi.org/10.1016/j.matpr.2020.01.558.
[81] HIP for Additive Manufacturing, Quintus Technol. (2015). https://quintustechnologies.com/hot-isostatic-pressing/applications/additive-manufacturing (accessed April 17, 2021).
[82] T. Hirata, T. Kimura, T. Nakamoto, Effects of hot isostatic pressing and internal porosity on the performance of selective laser melted AlSi10Mg alloys, Mater. Sci. Eng. A. 772 (2020) 138713. https://doi.org/10.1016/j.msea.2019.138713.
[83] B.S. Rupal, N. Anwer, M. Secanell, A.J. Qureshi, Geometric tolerance and manufacturing assemblability estimation of metal additive manufacturing (AM) processes, Mater. Des. 194 (2020) 108842. https://doi.org/10.1016/j.matdes.2020.108842.
[84] M. Praniewicz, J. Fox, G. Ameta, F. Kim, P. Witherell, C. Saldana, Exploring Registration of Optical, CMM and XCT for Verification of Supplemental Surfaces to Define AM Lattices: Application to Cylindrical and Spherical Surfaces, Procedia CIRP. 92 (2020) 181–186. https://doi.org/10.1016/j.procir.2020.05.182.
[85] A. Townsend, N. Senin, L. Blunt, R.K. Leach, J.S. Taylor, Surface texture metrology for metal additive manufacturing: a review, Precis. Eng. 46 (2016) 34–47. https://doi.org/10.1016/j.precisioneng.2016.06.001.

[86] A. Townsend, R. Racasan, R. Leach, N. Senin, A. Thompson, A. Ramsey, D. Bate, P. Woolliams, S. Brown, L. Blunt, An interlaboratory comparison of X-ray computed tomography measurement for texture and dimensional characterisation of additively manufactured parts, Addit. Manuf. 23 (2018) 422–432. https://doi.org/10.1016/j.addma.2018.08.013.
[87] S.T. McClain, D.R. Hanson, E. Cinnamon, J.C. Snyder, R.F. Kunz, K.A. Thole, Flow in a Simulated Turbine Blade Cooling Channel With Spatially Varying Roughness Caused by Additive Manufacturing Orientation, in: American Society of Mechanical Engineers Digital Collection, 2021. https://doi.org/10.1115/GT2020-16069.
[88] F. Cabanettes, A. Joubert, G. Chardon, V. Dumas, J. Rech, C. Grosjean, Z. Dimkovski, Topography of as built surfaces generated in metal additive manufacturing: A multi scale analysis from form to roughness, Precis. Eng. 52 (2018) 249–265. https://doi.org/10.1016/j.precisioneng.2018.01.002.
[89] J.A. Slotwinski, E.J. Garboczi, Porosity of additive manufacturing parts for process monitoring, AIP Conf. Proc. 1581 (2014) 1197–1204. https://doi.org/10.1063/1.4864957.
[90] A. Thompson, I. Maskery, R.K. Leach, X-ray computed tomography for additive manufacturing: a review, Meas. Sci. Technol. 27 (2016) 072001. https://doi.org/10.1088/0957-0233/27/7/072001.
[91] R. plc, Renishaw: Renishaw announces a new version of the REVO® multi-sensor 5-axis measurement system at EMO 2015, Renishaw. (n.d.). http://www.renishaw.com/en/renishaw-announces-a-new-version-of-the-revo-multi-sensor-5-axis-measurement-system-at-emo-2015--35917 (accessed June 4, 2021).
[92] G. Govind, J. Henckel, H. Hothi, S. Sabah, J. Skinner, A. Hart, Method for the location of primary wear scars from retrieved metal on metal hip replacements, BMC Musculoskelet. Disord. 16 (2015) 173. https://doi.org/10.1186/s12891-015-0622-2.
[93] Nikon Metrology qualifies 3D printed hip implants at Ortho Baltic, 3D Print. Ind. (2017). https://3dprintingindustry.com/news/nikon-metrology-qualifies-3d-printed-hip-implants-ortho-baltic-119841/ (accessed June 4, 2021).
[94] N. Kourra, J.M. Warnett, A. Attridge, G. Dibling, J. McLoughlin, S. Muirhead-Allwood, R. King, M.A. Williams, Computed tomography metrological examination of additive manufactured acetabular hip prosthesis cups, Addit. Manuf. 22 (2018) 146–152. https://doi.org/10.1016/j.addma.2018.04.033.
[95] M. Seifi, M. Gorelik, J. Waller, N. Hrabe, N. Shamsaei, S. Daniewicz, J.J. Lewandowski, Progress Towards Metal Additive Manufacturing Standardization to Support Qualification and Certification, JOM. 69 (2017) 439–455. https://doi.org/10.1007/s11837-017-2265-2.
[96] Cross-Committee Collaboration: ISO/TC 261, ASTM F42 and ISO/TC 44/SC 14/WG 1, (n.d.). https://committee.iso.org/sites/tc261/home/news/content-left-area/news-and-updates/cross-committee-collaboration-is.html (accessed June 4, 2021).
[97] America Makes & ANSI Additive Manufacturing Standardization Collaborative – AMSC, Am. Natl. Stand. Inst. - ANSI. (n.d.). https://www.ansi.org/standards-coordination/collaboratives-activities/additive-manufacturing-collaborative (accessed March 25, 2021).
[98] ISO/ASTM Additive Manufacturing Standards Structure, (n.d.). https://committee.iso.org/sites/tc261/home/projects.html (accessed June 4, 2021).
[99] C. for D. and R. Health, Technical Considerations for Additive Manufactured Medical Devices, US Food Drug Adm. (2020). https://www.fda.gov/regulatory-information/search-fda-guidance-documents/technical-considerations-additive-manufactured-medical-devices (accessed April 28, 2021).
[100] MSFC-STD-3716 | NASA Technical Standards System (NTSS), (n.d.). https://standards.nasa.gov/standard/msfc/msfc-std-3716 (accessed April 28, 2021).
[101] O. of the Commissioner, 3D Printing in FDA's Rapid Response to COVID-19, FDA. (2020). https://www.fda.gov/emergency-preparedness-and-response/coronavirus-disease-2019-covid-19/3d-printing-fdas-rapid-response-covid-19 (accessed April 28, 2021).

[102] ISO - ISO/TC 261 - Additive manufacturing, (n.d.). https://www.iso.org/committee/629086/x/catalogue/p/0/u/0/w/0/d/0 (accessed April 28, 2021).
[103] Additive Manufacturing Standards, (n.d.). https://www.additivemanufacturing.media/articles/standards-for-additive-manufacturing (accessed April 28, 2021).
[104] The 5 Most Important Standards in Additive Manufacturing, ASTM Stand. News. (2019). https://sn.astm.org/?q=features/5-most-important-standards-additive-manufacturing-.html (accessed April 28, 2021).
[105] AMSC Gaps: Design, (n.d.). https://www.ansi.org/portal/amsc/AMSC-Gaps-Design (accessed April 28, 2021).
[106] G. Kerckhofs, G. Pyka, M. Moesen, S.V. Bael, J. Schrooten, M. Wevers, High-Resolution Microfocus X-Ray Computed Tomography for 3D Surface Roughness Measurements of Additive Manufactured Porous Materials, Adv. Eng. Mater. 15 (2013) 153–158. https://doi.org/10.1002/adem.201200156.
[107] 14:00-17:00, ISO/ASTM AWI TR 52905, ISO. (n.d.). https://www.iso.org/cms/render/live/en/sites/isoorg/contents/data/standard/08/25/82539.html (accessed April 29, 2021).
[108] P. Shah, R. Racasan, P. Bills, Comparison of different additive manufacturing methods using computed tomography, Case Stud. Nondestruct. Test. Eval. 6 (2016) 69–78. https://doi.org/10.1016/j.csndt.2016.05.008.
[109] M. Mahesh, Y.S. Wong, J.Y.H. Fuh, H.T. Loh, Benchmarking for comparative evaluation of RP systems and processes, Rapid Prototyp. J. 10 (2004) 123–135. https://doi.org/10.1108/13552540410526999.
[110] J.-P. Kruth, B. Vandenbroucke, J. Van Vaerenbergh, P. Mercelis, Benchmarking of different SLS/SLM processes as rapid manufacturing techniques, in: Proc. Int. Conf. Polym. Moulds Innov. PMI 2005, 2005.
[111]E.C. Santos, M. Shiomi, K. Osakada, T. Laoui, Rapid manufacturing of metal components by laser forming, Int. J. Mach. Tools Manuf. 46 (2006) 1459–1468.
[112] J. Delgado, J. Ciurana, C. Reguant, B. Cavallini, Studying the repeatability in DMLS technology using a complete geometry test part, Innov. Dev. Des. Manuf. Adv. Res. Virtual Rapid Prototyp.--Proc. VRP4 Oct 2009 Leir. Port. (2009) 349.
[113] W.M. Johnson, M. Rowell, B. Deason, M. Eubanks, Benchmarking evaluation of an open source fused deposition modeling additive manufacturing system, in: Proceeding 22nd Annu. Int. Solid Free. Fabr. Symp., 2011: pp. 197–211.
[114] S.P. Moylan, J.A. Slotwinski, A.L. Cooke, K.K. Jurrens, M.A. Donmez, Proposal for a standardized test artifact for additive manufacturing machines and processes, (2012). https://www.nist.gov/publications/proposal-standardized-test-artifact-additive-manufacturing-machines-and-processes (accessed March 15, 2021).
[115] M. MAHESH, Rapid prototyping and manufacturing benchmarking, Thesis, 2005. https://scholarbank.nus.edu.sg/handle/10635/14697 (accessed March 15, 2021).
[116] M.-A. de Pastre, S.-C. Toguem Tagne, N. Anwer, Test artefacts for additive manufacturing: A design methodology review, CIRP J. Manuf. Sci. Technol. 31 (2020) 14–24. https://doi.org/10.1016/j.cirpj.2020.09.008.
[117] J.P. Kruth, Material Incress Manufacturing by Rapid Prototyping Techniques, CIRP Ann. 40 (1991) 603–614. https://doi.org/10.1016/S0007-8506(07)61136-6.
[118] L. Rebaioli, I. Fassi, A review on benchmark artifacts for evaluating the geometrical performance of additive manufacturing processes, Int. J. Adv. Manuf. Technol. 93 (2017) 2571–2598. https://doi.org/10.1007/s00170-017-0570-0.

[119] M. Mahesh, Y.S. Wong, J.Y.H. Fuh, H.T. Loh, A Six-sigma approach for benchmarking of RP&M processes, Int. J. Adv. Manuf. Technol. 31 (2006) 374–387. https://doi.org/10.1007/s00170-005-0201-z.
[120] 14:00-17:00, ISO 12781-2:2011, ISO. (n.d.). https://www.iso.org/cms/render/live/en/sites/isoorg/contents/data/standard/05/36/53625.html (accessed March 15, 2021).
[121] M.G. Teeter, A.J. Kopacz, H.N. Nikolov, D.W. Holdsworth, Metrology test object for dimensional verification in additive manufacturing of metals for biomedical applications, (n.d.) 8.
[122] Toward a common laser powder bed fusion qualification test artifact, Addit. Manuf. 39 (2021) 101803. https://doi.org/10.1016/j.addma.2020.101803.
[123] K.G. Mostafa, G.A. Momesso, X. Li, D.S. Nobes, A.J. Qureshi, Dual Graded Lattice Structures: Generation Framework and Mechanical Properties Characterization, Polymers. 13 (2021) 1528. https://doi.org/10.3390/polym13091528.
[124] J. Feng, J. Fu, C. Shang, Z. Lin, X. Niu, B. Li, Efficient generation strategy for hierarchical porous scaffolds with freeform external geometries, Addit. Manuf. 31 (2020) 100943. https://doi.org/10.1016/j.addma.2019.100943.
[125] Design for AM DfAM steps: additive manufacturing solutions centres 3D printing metal powder bed fusion Solutions Center, (n.d.). https://resources.renishaw.com/en/details/Design%20for%20AM%20DfAM%20steps(90442) (accessed June 4, 2021).
[126] D. Bhate, C.A. Penick, L.A. Ferry, C. Lee, Classification and Selection of Cellular Materials in Mechanical Design: Engineering and Biomimetic Approaches, Designs. 3 (2019) 19. https://doi.org/10.3390/designs3010019.
[127] L.J. Gibson, M.F. Ashby, Cellular Solids by Lorna J. Gibson, Camb. Core. (1997). https://doi.org/10.1017/CBO9781139878326.
[128] W. Tao, M. Leu, Design of lattice structure for additive manufacturing, 2016 Int. Symp. Flex. Autom. ISFA. (2016). https://doi.org/10.1109/ISFA.2016.7790182.
[129] M.F. Ashby, The properties of foams and lattices, Philos. Trans. R. Soc. Lond. Math. Phys. Eng. Sci. 364 (2006) 15–30. https://doi.org/10.1098/rsta.2005.1678.
[130] O. Al-Ketan, R. Rowshan, R.K. Abu Al-Rub, Topology-mechanical property relationship of 3D printed strut, skeletal, and sheet based periodic metallic cellular materials, Addit. Manuf. 19 (2018) 167–183. https://doi.org/10.1016/j.addma.2017.12.006.
[131] L. Zhang, S. Feih, S. Daynes, S. Chang, M.Y. Wang, J. Wei, W.F. Lu, Energy absorption characteristics of metallic triply periodic minimal surface sheet structures under compressive loading, Addit. Manuf. 23 (2018) 505–515. https://doi.org/10.1016/j.addma.2018.08.007.
[132] X. Wang, T.J. Lu, Optimized acoustic properties of cellular solids, J. Acoust. Soc. Am. 106 (1999) 756–765. https://doi.org/10.1121/1.427094.
[133] P. Göransson, Acoustic and vibrational damping in porous solids, Philos. Trans. R. Soc. Math. Phys. Eng. Sci. 364 (2006) 89–108. https://doi.org/10.1098/rsta.2005.1688.
[134] L.E. Murr, S.M. Gaytan, E. Martinez, F. Medina, R.B. Wicker, Next Generation Orthopaedic Implants by Additive Manufacturing Using Electron Beam Melting, Int. J. Biomater. 2012 (2012) e245727. https://doi.org/10.1155/2012/245727.
[135] V.S. Deshpande, N.A. Fleck, M.F. Ashby, Effective properties of the octet-truss lattice material, J. Mech. Phys. Solids. 49 (2001) 1747–1769. https://doi.org/10.1016/S0022-5096(01)00010-2.
[136] Y. Sun, Q.M. Li, Dynamic compressive behaviour of cellular materials: A review of phenomenon, mechanism and modelling, Int. J. Impact Eng. 112 (2018) 74–115. https://doi.org/10.1016/j.ijimpeng.2017.10.006.
[137] C.N. Kelly, J. Francovich, S. Julmi, D. Safranski, R.E. Guldberg, H.J. Maier, K. Gall, Fatigue behavior of As-built selective laser melted titanium scaffolds with sheet-based gyroid microarchitecture

for bone tissue engineering, Acta Biomater. 94 (2019) 610–626. https://doi.org/10.1016/j.actbio.2019.05.046.
[138] I. Maskery, A.O. Aremu, L. Parry, R.D. Wildman, C.J. Tuck, I.A. Ashcroft, Effective design and simulation of surface-based lattice structures featuring volume fraction and cell type grading, Mater. Des. 155 (2018) 220–232. https://doi.org/10.1016/j.matdes.2018.05.058.
[139] P. Zhang, J. Toman, Y. Yu, E. Biyikli, M. Kirca, M. Chmielus, A.C. To, Efficient Design-Optimization of Variable-Density Hexagonal Cellular Structure by Additive Manufacturing: Theory and Validation, J. Manuf. Sci. Eng. 137 (2015). https://doi.org/10.1115/1.4028724.
[140] B. Wang, G. Cheng, Design of cellular structures for optimum efficiency of heat dissipation, Struct. Multidiscip. Optim. 30 (2005) 447–458. https://doi.org/10.1007/s00158-005-0542-0.
[141] A.G. Evans, J.W. Hutchinson, N.A. Fleck, M.F. Ashby, H.N.G. Wadley, The topological design of multifunctional cellular metals, Prog. Mater. Sci. 46 (2001) 309–327. https://doi.org/10.1016/S0079-6425(00)00016-5.
[142] I. Maskery, L. Sturm, A.O. Aremu, A. Panesar, C.B. Williams, C.J. Tuck, R.D. Wildman, I.A. Ashcroft, R.J.M. Hague, Insights into the mechanical properties of several triply periodic minimal surface lattice structures made by polymer additive manufacturing, Polymer. 152 (2018) 62–71. https://doi.org/10.1016/j.polymer.2017.11.049.
[143] J. Calì, D.A. Calian, C. Amati, R. Kleinberger, A. Steed, J. Kautz, T. Weyrich, 3D-printing of non-assembly, articulated models, ACM Trans. Graph. 31 (2012) 130:1-130:8. https://doi.org/10.1145/2366145.2366149.
[144] S. Yang, Y. Tang, Y.F. Zhao, A new part consolidation method to embrace the design freedom of additive manufacturing, J. Manuf. Process. 20 (2015) 444–449. https://doi.org/10.1016/j.jmapro.2015.06.024.
[145] D. Lehmhus, T. Wuest, S. Wellsandt, S. Bosse, T. Kaihara, K.-D. Thoben, M. Busse, Cloud-Based Automated Design and Additive Manufacturing: A Usage Data-Enabled Paradigm Shift, Sensors. 15 (2015) 32079–32122. https://doi.org/10.3390/s151229905.
[146] The World's First 3D Printed Turbocharger | TD Blog, (n.d.). https://www.turbodynamics.co.uk/media/blog/3d-printed-turbocharger (accessed June 4, 2021).
[147] C. Duran, V. Subbian, M.T. Giovanetti, J.R. Simkins, F.R. Beyette Jr, Experimental desktop 3D printing using dual extrusion and water-soluble polyvinyl alcohol, Rapid Prototyp. J. 21 (2015) 528–534. https://doi.org/10.1108/RPJ-09-2014-0117.
[148] J.-P. Järvinen, V. Matilainen, X. Li, H. Piili, A. Salminen, I. Mäkelä, O. Nyrhilä, Characterization of Effect of Support Structures in Laser Additive Manufacturing of Stainless Steel, Phys. Procedia. 56 (2014) 72–81. https://doi.org/10.1016/j.phpro.2014.08.099.
[149] T.A. Krol, M.F. Zaeh, C. Seidel, Optimization of supports in metal-based additive manufacturing by means of finite element models, Bourell DL. (2012).
[150] Application field Additive Manufacturing, or 3D Printing - Simufact software solutions, (n.d.). https://www.simufact.com/additive-manufacturing.html (accessed April 17, 2021).
[151] J. Wu, N. Aage, R. Westermann, O. Sigmund, Infill Optimization for Additive Manufacturing—Approaching Bone-Like Porous Structures, IEEE Trans. Vis. Comput. Graph. 24 (2018) 1127–1140. https://doi.org/10.1109/TVCG.2017.2655523.
[152] Croft Filters – Custom Filtration Solutions for Oil,Gas & Energy, Chemical, Pharmaceuticals and Food & Beverage industries, Croft Filters. (n.d.). https://filters.co.uk/ (accessed June 4, 2021).
[153] C. Zhang, S. Wang, J. Li, Y. Zhu, T. Peng, H. Yang, Additive manufacturing of products with functional fluid channels: A review, Addit. Manuf. 36 (2020) 101490. https://doi.org/10.1016/j.addma.2020.101490.

[154] How to Design High-Performance Filters for Additive Manufacturing | nTopology, (n.d.). https://ntopology.com/blog/2021/05/06/designing-high-performance-filters-for-additive-manufacturing/ (accessed June 4, 2021).
[155] Layer Manufacturing | Layer By Layer Manufacture | Croft AM |Croft Additive Manufacturing | | Additive Manufacturing | 3D Printing | Croft AM |Croft Additive Manufacturing, (2019). https://www.croftam.co.uk/designing-to-add-value/ (accessed May 11, 2021).
[156] Additive Manufacturing – helping to reduce waste in aircraft production, (n.d.). https://www.open.ac.uk/blogs/design/additive-manufacturing-helping-to-reduce-waste-in-aircraft-production/ (accessed May 11, 2021).
[157] Cobra AERO, Cobra AERO. (n.d.). https://www.cobra-aero.com (accessed June 4, 2021).
[158] Case Study: Cobra Aero Reimagines the Combustion Engine Cylinder using Multiphysics Simulation, NTopology. (n.d.). https://ntopology.com/case-studies/cobra-aero-multiphysics-simulation-drone-engine/ (accessed April 23, 2021).
[159] CubeSat 101: Basic Concepts and Processes for First-Time CubeSat Developers, (n.d.) 96.
[160] R. Begg, Lattice Design Enables 3D-Printed Nasal Swab Production, Mach. Des. (2021). https://www.machinedesign.com/medical-design/article/21162932/lattice-design-enables-3dprinted-nasal-swab-production (accessed July 23, 2021).
[161] Massachusetts startup OPT Industries is perfecting a 3D-printed nasal swab for COVID-19 tests, TechCrunch. (n.d.). https://social.techcrunch.com/2021/07/14/massachusetts-startup-opt-industries-is-perfecting-a-3d-printed-nasal-swab-for-covid-19-tests/ (accessed July 27, 2021).
[162] Orthopaedic Implants, Betatype. (n.d.). https://www.betaty.pe/case-studies/orthopaedic-implants/ (accessed May 18, 2021).
[163] R. Karunakaran, S. Ortgies, A. Tamayol, F. Bobaru, M.P. Sealy, Additive manufacturing of magnesium alloys, Bioact. Mater. 5 (2020) 44–54. https://doi.org/10.1016/j.bioactmat.2019.12.004.
[164] A. Gefen, Computational simulations of stress shielding and bone resorption around existing and computer-designed orthopaedic screws, Med. Biol. Eng. Comput. 40 (2002) 311–322. https://doi.org/10.1007/BF02344213.
[165] I. Sanli, J.J.C. Arts, J. Geurts, Clinical and Radiologic Outcomes of a Fully Hydroxyapatite-Coated Femoral Revision Stem: Excessive Stress Shielding Incidence and its Consequences, J. Arthroplasty. 31 (2016) 209–214. https://doi.org/10.1016/j.arth.2015.08.037.
[166] Betatype - Technology for Complex Additive Manufacturing, Betatype. (n.d.). https://www.betaty.pe/ (accessed June 7, 2021).
[167] M. Regis, E. Marin, L. Fedrizzi, M. Pressacco, Additive manufacturing of Trabecular Titanium orthopedic implants, MRS Bull. 40 (2015) 137–144. https://doi.org/10.1557/mrs.2015.1.
[168] How to Design and Optimize a Patient Specific Additively Manufactured Hip Implant Stem, NTopology. (2020). https://ntopology.com/blog/2020/04/27/how-to-design-and-optimize-a-patient-specific-additively-manufactured-hip-implant-stem/ (accessed May 18, 2021).
[169] Design Challenge 2020, (n.d.). additiveworld.com/Design-challenge/Design-challenge-2020 (accessed May 18, 2021).
[170] STL File Format (3D Printing) – Simply Explained, All3DP. (2019). https://all3dp.com/what-is-stl-file-format-extension-3d-printing/ (accessed June 7, 2021).
[171] J.D. Hiller, H. Lipson, Stl 2.0: A proposal for a universal multi-material additive manufacturing file format, in: Mech. Aerosp. Eng., 2009: pp. 266–278.
[172] A.H. Azman, F. Vignat, F. Villeneuve, CAD TOOLS AND FILE FORMAT PERFORMANCE EVALUATION IN DESIGNING LATTICE STRUCTURES FOR ADDITIVE MANUFACTURING, J. Teknol. 80 (2018). https://doi.org/10.11113/jt.v80.12058.
[173] S. Hällgren, L. Pejryd, J. Ekengren, 3D Data Export for Additive Manufacturing - Improving Geometric Accuracy, Procedia CIRP. 50 (2016) 518–523. https://doi.org/10.1016/j.procir.2016.05.046.

[174] 3MF Consortium FAQ, 3MF Consort. (n.d.). https://3mf.io/resources/faq/ (accessed June 7, 2021).
[175] B. Lozanovski, M. Leary, P. Tran, D. Shidid, M. Qian, P. Choong, M. Brandt, Computational modelling of strut defects in SLM manufactured lattice structures, Mater. Des. 171 (2019) 107671. https://doi.org/10.1016/j.matdes.2019.107671.
[176] Enabling the full potential of 3D printing, 3MF Consort. (n.d.). https://3mf.io/ (accessed April 23, 2021).
[177] nTop Platform Supports the 3MF File Format with Beam Extension, NTopology. (2020). https://ntopology.com/blog/2020/09/10/ntop-platform-supports-the-3mf-file-format-with-beam-extension/ (accessed April 23, 2021).
[178] How to Eliminate STL files from Your 3D Printing Process, NTopology. (2019). https://ntopology.com/blog/2019/08/23/eliminate-stl-files-from-your-printing-process/ (accessed June 7, 2021).
[179] Netfabb Software | Get Prices & Buy Netfabb 2022 | Autodesk, (n.d.). https://www.autodesk.co.uk/products/netfabb/overview (accessed July 19, 2021).
[180] STL Editor | STL Repair Software | Materialise Magics, (n.d.). https://www.materialise.com/en/software/magics (accessed June 7, 2021).
[181] Understanding the basics of B-reps and Implicits, NTopology. (2019). https://ntopology.com/blog/2019/03/12/understanding-the-basics-of-b-reps-and-implicits/ (accessed April 23, 2021).
[182] A New Approach to Modelling Lattices and Other Complex Geometry, Eng. Rule. (2019). https://www.engineersrule.com/a-new-approach-to-modelling-lattices-and-other-complex-geometry/ (accessed June 7, 2021).
[183] How implicits succeed where B-reps fail, NTopology. (2019). https://ntopology.com/blog/2019/03/28/how-implicits-succeed-where-b-reps-fail/ (accessed June 7, 2021).
[184] Field-Driven Design: Product Data Models for Rapid, Collaborative Development, NTopology. (2019). https://ntopology.com/blog/2019/03/04/field-driven-design-product-data-models-for-rapid-collaborative-development/ (accessed April 23, 2021).
[185] B. Hanks, J. Berthel, M. Frecker, T.W. Simpson, Mechanical properties of additively manufactured metal lattice structures: Data review and design interface, Addit. Manuf. 35 (2020) 101301. https://doi.org/10.1016/j.addma.2020.101301.
[186] F. Tamburrino, S. Graziosi, M. Bordegoni, The Design Process of Additively Manufactured Mesoscale Lattice Structures: A Review, J. Comput. Inf. Sci. Eng. 18 (2018). https://doi.org/10.1115/1.4040131.
[187] S. Krish, A practical generative design method, Comput.-Aided Des. 43 (2011) 88–100. https://doi.org/10.1016/j.cad.2010.09.009.
[188] Design Automation for Engineering & Manufacturing, NTopology. (n.d.). https://ntopology.com/design-automation-software/ (accessed April 26, 2021).
[189] 14:00-17:00, ISO 17340:2020, ISO. (n.d.). https://www.iso.org/cms/render/live/en/sites/isoorg/contents/data/standard/08/03/80372.html (accessed April 26, 2021).
[190] 14:00-17:00, ISO 13314:2011, ISO. (n.d.). http://www.iso.org/cms/render/live/en/sites/isoorg/contents/data/standard/05/36/53669.html (accessed January 20, 2020).
[191] Image-Based Geometrical Characterization of Nodes in Additively Manufactured Lattice Structures | 3D Printing and Additive Manufacturing, (n.d.). https://www.liebertpub.com/doi/10.1089/3dp.2020.0091 (accessed April 26, 2021).

[192] L. Cheng, X. Liang, E. Belski, X. Wang, J.M. Sietins, S. Ludwick, A. To, Natural Frequency Optimization of Variable-Density Additive Manufactured Lattice Structure: Theory and Experimental Validation, J. Manuf. Sci. Eng. 140 (2018). https://doi.org/10.1115/1.4040622.
[193] Simulation Series - How to Accelerate FE Simulations of Lattices using Homogenization, NTopology. (n.d.). https://ntopology.com/videos/video/simulation-series-how-to-accelerate-fe-simulations-of-lattices-using-homogenization/ (accessed June 7, 2021).
[194] I. Echeta, X. Feng, B. Dutton, S. Piano, R. Leach, Review of defects in lattice structures manufactured by powder bed fusion, Int. J. Adv. Manuf. Technol. (2019).
[195] M. Mazur, M. Leary, M. McMillan, S. Sun, D. Shidid, M. Brandt, 5 - Mechanical properties of Ti6Al4V and AlSi12Mg lattice structures manufactured by Selective Laser Melting (SLM), in: M. Brandt (Ed.), Laser Addit. Manuf., Woodhead Publishing, 2017: pp. 119–161. https://doi.org/10.1016/B978-0-08-100433-3.00005-1.
[196] I. Yadroitsev, I. Yadroitsava, 3 - A step-by-step guide to the L-PBF process, in: I. Yadroitsev, I. Yadroitsava, A. du Plessis, E. MacDonald (Eds.), Fundam. Laser Powder Bed Fusion Met., Elsevier, 2021: pp. 39–77. https://doi.org/10.1016/B978-0-12-824090-8.00026-3.
[197] A. Charles, A. Elkaseer, L. Thijs, V. Hagenmeyer, S. Scholz, Effect of process parameters on the generated surface roughness of down-facing surfaces in selective laser melting, Appl. Sci. 9 (2019) 1256.
[198] S.L. Sing, F.E. Wiria, W.Y. Yeong, Selective laser melting of lattice structures: A statistical approach to manufacturability and mechanical behavior, Robot. Comput.-Integr. Manuf. 49 (2018) 170–180. https://doi.org/10.1016/j.rcim.2017.06.006.
[199] I. Echeta, X. Feng, B. Dutton, R. Leach, S. Piano, Review of defects in lattice structures manufactured by powder bed fusion, Int. J. Adv. Manuf. Technol. 106 (2020) 2649–2668. https://doi.org/10.1007/s00170-019-04753-4.
[200] D. Melancon, Z.S. Bagheri, R.B. Johnston, L. Liu, M. Tanzer, D. Pasini, Mechanical characterization of structurally porous biomaterials built via additive manufacturing: experiments, predictive models, and design maps for load-bearing bone replacement implants, Acta Biomater. 63 (2017) 350–368. https://doi.org/10.1016/j.actbio.2017.09.013.
[201] Mechanical and microstructural properties of polycaprolactone scaffolds with one-dimensional, two-dimensional, and three-dimensional orthogonally oriented porous architectures produced by selective laser sintering | Elsevier Enhanced Reader, (n.d.). https://doi.org/10.1016/j.actbio.2010.02.002.
[202] B. Partee, S.J. Hollister, S. Das, Selective Laser Sintering Process Optimization for Layered Manufacturing of CAPA® 6501 Polycaprolactone Bone Tissue Engineering Scaffolds, J. Manuf. Sci. Eng. 128 (2006) 531–540. https://doi.org/10.1115/1.2162589.
[203] G. Pyka, G. Kerckhofs, I. Papantoniou, M. Speirs, J. Schrooten, M. Wevers, Surface Roughness and Morphology Customization of Additive Manufactured Open Porous Ti6Al4V Structures, Materials. 6 (2013) 4737–4757. https://doi.org/10.3390/ma6104737.
[204] P. Lhuissier, C. de Formanoir, G. Martin, R. Dendievel, S. Godet, Geometrical control of lattice structures produced by EBM through chemical etching: Investigations at the scale of individual struts, Mater. Des. 110 (2016) 485–493. https://doi.org/10.1016/j.matdes.2016.08.029.
[205] M.R. Karamooz Ravari, M. Kadkhodaei, M. Badrossamay, R. Rezaei, Numerical investigation on mechanical properties of cellular lattice structures fabricated by fused deposition modeling, Int. J. Mech. Sci. 88 (2014) 154–161. https://doi.org/10.1016/j.ijmecsci.2014.08.009.
[206] G. Campoli, M.S. Borleffs, S. Amin Yavari, R. Wauthle, H. Weinans, A.A. Zadpoor, Mechanical properties of open-cell metallic biomaterials manufactured using additive manufacturing, Mater. Des. 49 (2013) 957–965. https://doi.org/10.1016/j.matdes.2013.01.071.

[207] M.R. Karamooz Ravari, M. Kadkhodaei, A Computationally Efficient Modeling Approach for Predicting Mechanical Behavior of Cellular Lattice Structures, J. Mater. Eng. Perform. 24 (2015) 245–252. https://doi.org/10.1007/s11665-014-1281-4.
[208] Z. Xiao, Y. Yang, R. Xiao, Y. Bai, C. Song, D. Wang, Evaluation of topology-optimized lattice structures manufactured via selective laser melting, Mater. Des. 143 (2018) 27–37. https://doi.org/10.1016/j.matdes.2018.01.023.
[209] R. plc, Renishaw: QuantAM build preparation software, Renishaw. (n.d.). http://www.renishaw.com/en/quantam-build-preparation-software--35455 (accessed June 7, 2021).
[210] C. Qiu, S. Yue, N.J.E. Adkins, M. Ward, H. Hassanin, P.D. Lee, P.J. Withers, M.M. Attallah, Influence of processing conditions on strut structure and compressive properties of cellular lattice structures fabricated by selective laser melting, Mater. Sci. Eng. A. 628 (2015) 188–197. https://doi.org/10.1016/j.msea.2015.01.031.
[211] S. Tsopanos, R.A.W. Mines, S. McKown, Y. Shen, W.J. Cantwell, W. Brooks, C.J. Sutcliffe, The Influence of Processing Parameters on the Mechanical Properties of Selectively Laser Melted Stainless Steel Microlattice Structures, J. Manuf. Sci. Eng. 132 (2010). https://doi.org/10.1115/1.4001743.
[212] S. Li, H. Xiao, K. Liu, W. Xiao, Y. Li, X. Han, J. Mazumder, L. Song, Melt-pool motion, temperature variation and dendritic morphology of Inconel 718 during pulsed- and continuous-wave laser additive manufacturing: A comparative study, Mater. Des. 119 (2017) 351–360. https://doi.org/10.1016/j.matdes.2017.01.065.
[213] S. Ghouse, S. Babu, R.J. Van Arkel, K. Nai, P.A. Hooper, J.R.T. Jeffers, The influence of laser parameters and scanning strategies on the mechanical properties of a stochastic porous material, Mater. Des. 131 (2017) 498–508. https://doi.org/10.1016/j.matdes.2017.06.041.
[214] T. Abe, H. Sasahara, Layer geometry control for the fabrication of lattice structures by wire and arc additive manufacturing, Addit. Manuf. 28 (2019) 639–648. https://doi.org/10.1016/j.addma.2019.06.010.
[215] S.K. Everton, M. Hirsch, P. Stravroulakis, R.K. Leach, A.T. Clare, Review of in-situ process monitoring and in-situ metrology for metal additive manufacturing, Mater. Des. 95 (2016) 431–445. https://doi.org/10.1016/j.matdes.2016.01.099.
[216] Y. Liu, L. Blunt, Z. Zhang, H.A. Rahman, F. Gao, X. Jiang, In-situ areal inspection of powder bed for electron beam fusion system based on fringe projection profilometry, Addit. Manuf. 31 (2020) 100940. https://doi.org/10.1016/j.addma.2019.100940.
[217] H. Ghasemi-Tabasi, J. Jhabvala, E. Boillat, T. Ivas, R. Drissi-Daoudi, R.E. Logé, An effective rule for translating optimal selective laser melting processing parameters from one material to another, Addit. Manuf. 36 (2020) 101496. https://doi.org/10.1016/j.addma.2020.101496.
[218] Z. Zhu, N. Anwer, L. Mathieu, Deviation Modeling and Shape Transformation in Design for Additive Manufacturing, Procedia CIRP. 60 (2017) 211–216. https://doi.org/10.1016/j.procir.2017.01.023.
[219] M. Dallago, B. Winiarski, F. Zanini, S. Carmignato, M. Benedetti, On the effect of geometrical imperfections and defects on the fatigue strength of cellular lattice structures additively manufactured via Selective Laser Melting, Int. J. Fatigue. 124 (2019) 348–360. https://doi.org/10.1016/j.ijfatigue.2019.03.019.
[220] M. Dallago, V. Fontanari, E. Torresani, M. Leoni, C. Pederzolli, C. Potrich, M. Benedetti, Fatigue and biological properties of Ti-6Al-4V ELI cellular structures with variously arranged cubic cells made by selective laser melting, J. Mech. Behav. Biomed. Mater. 78 (2018) 381–394. https://doi.org/10.1016/j.jmbbm.2017.11.044.
[221] M. Leary, M. Mazur, J. Elambasseril, M. McMillan, T. Chirent, Y. Sun, M. Qian, M. Easton, M. Brandt, Selective laser melting (SLM) of AlSi12Mg lattice structures, Mater. Des. 98 (2016) 344–357. https://doi.org/10.1016/j.matdes.2016.02.127.

[222] A. El Elmi, D. Melancon, M. Asgari, L. Liu, D. Pasini, Experimental and numerical investigation of selective laser melting–induced defects in Ti–6Al–4V octet truss lattice material: the role of material microstructure and morphological variations, J. Mater. Res. 35 (2020) 1900–1912.
[223] A. Yadollahi, N. Shamsaei, Additive manufacturing of fatigue resistant materials: Challenges and opportunities, Int. J. Fatigue. 98 (2017) 14–31. https://doi.org/10.1016/j.ijfatigue.2017.01.001.
[224] S. Ghouse, S. Babu, K. Nai, P.A. Hooper, J.R.T. Jeffers, The influence of laser parameters, scanning strategies and material on the fatigue strength of a stochastic porous structure, Addit. Manuf. 22 (2018) 290–301. https://doi.org/10.1016/j.addma.2018.05.024.
[225] S. Tammas-Williams, P.J. Withers, I. Todd, P.B. Prangnell, The Influence of Porosity on Fatigue Crack Initiation in Additively Manufactured Titanium Components, Sci. Rep. 7 (2017) 7308. https://doi.org/10.1038/s41598-017-06504-5.
[226] Z. Dong, Y. Liu, W. Li, J. Liang, Orientation dependency for microstructure, geometric accuracy and mechanical properties of selective laser melting AlSi10Mg lattices, J. Alloys Compd. 791 (2019) 490–500. https://doi.org/10.1016/j.jallcom.2019.03.344.
[227] Y. Amani, S. Dancette, P. Delroisse, A. Simar, E. Maire, Compression behavior of lattice structures produced by selective laser melting: X-ray tomography based experimental and finite element approaches, Acta Mater. 159 (2018) 395–407. https://doi.org/10.1016/j.actamat.2018.08.030.
[228] The Nobel Prize in Physiology or Medicine 1979, NobelPrize.Org. (n.d.). https://www.nobelprize.org/prizes/medicine/1979/summary/ (accessed February 23, 2021).
[229] C.L. Vaughan, Imagining the Elephant: A Biography of Allan MacLeod Cormack, AJNR Am. J. Neuroradiol. 30 (2009) E122–E123. https://doi.org/10.3174/ajnr.A1668.
[230] R. Dundon, Early X-rays revealed a hidden world just beneath the skin—and amazed the public, Medium. (2017). https://timeline.com/early-xrays-hidden-world-6bbc3a3fb267 (accessed June 8, 2021).
[231] J.P. Kruth, M. Bartscher, S. Carmignato, R. Schmitt, L. De Chiffre, A. Weckenmann, Computed tomography for dimensional metrology, CIRP Ann. 60 (2011) 821–842. https://doi.org/10.1016/j.cirp.2011.05.006.
[232] Werth Messtechnik GmbH - Werth Messtechnik, (n.d.). https://www.werth.de/de/unser-angebot/produkte-nach-kategorie.html (accessed February 23, 2021).
[233] C.A. Roobottom, G. Mitchell, G. Morgan-Hughes, Radiation-reduction strategies in cardiac computed tomographic angiography, Clin. Radiol. 65 (2010) 859–867. https://doi.org/10.1016/j.crad.2010.04.021.
[234] Director, History of CT Scans | Evolution of CT Technology, Radiol. Assist. (n.d.). https://radiologyassist.com/learn-about-ct-scans/history-of-ct-scans/ (accessed June 8, 2021).
[235] BIPM - Guide to the Expression of Uncertainty in Measurement (GUM), (n.d.). https://www.bipm.org/en/publications/guides/gum.html (accessed February 23, 2021).
[236] L. De Chiffre, S. Carmignato, J.-P. Kruth, R. Schmitt, A. Weckenmann, Industrial applications of computed tomography, CIRP Ann. 63 (2014) 655–677. https://doi.org/10.1016/j.cirp.2014.05.011.
[237] Nikon Metrology - 3D scanning - 3D inspection - CMM - Computed Tomography – Shop floor inspection – Video measurement - Nikon Metrology, (n.d.). https://www.nikonmetrology.com/en-gb/ (accessed June 8, 2021).
[238] H. Villarraga-Gómez, E.L. Herazo, S.T. Smith, X-ray computed tomography: from medical imaging to dimensional metrology, Precis. Eng. 60 (2019) 544–569. https://doi.org/10.1016/j.precisioneng.2019.06.007.
[239] 14:00-17:00, ISO 15530-3:2011, ISO. (n.d.). http://www.iso.org/cms/render/live/en/sites/isoorg/contents/data/standard/05/36/53627.html (accessed March 12, 2019).

[240] P. Müller, J. Hiller, Y. Dai, J.L. Andreasen, H.N. Hansen, L.D. Chiffre, Estimation of measurement uncertainties in X-ray computed tomography metrology using the substitution method, CIRP J. Manuf. Sci. Technol. 3 (2014) 222–232. https://doi.org/10.1016/j.cirpj.2014.04.002.
[241] P. Hermanek, F. Zanini, S. Carmignato, Traceable Porosity Measurements in Industrial Components Using X-Ray Computed Tomography, J. Manuf. Sci. Eng. 141 (2019) 051004. https://doi.org/10.1115/1.4043192.
[242] M. Berger, Q. Yang, A. Maier, X-ray Imaging, in: A. Maier, S. Steidl, V. Christlein, J. Hornegger (Eds.), Med. Imaging Syst. Introd. Guide, Springer, Cham (CH), 2018. http://www.ncbi.nlm.nih.gov/books/NBK546155/ (accessed February 23, 2021).
[243] R. Christoph, H.J. Neumann, X-ray tomography in industrial metrology precise, economical and universal, 2011.
[244] P.J. Bills, Introduction to Computed Tomography as an aid to Forensic Analysis, in: University of Huddersfield, UK, 2016. https://eprints.hud.ac.uk/id/eprint/28556/ (accessed February 23, 2021).
[245] P. Hermanek, J.S. Rathore, V. Aloisi, S. Carmignato, Principles of X-ray Computed Tomography, in: S. Carmignato, W. Dewulf, R. Leach (Eds.), Ind. X-Ray Comput. Tomogr., Springer International Publishing, Cham, 2018: pp. 25–67. https://doi.org/10.1007/978-3-319-59573-3_2.
[246] W. Sun, S.B. Brown, R.K. Leach, An overview of industrial X-ray computed tomography., (2012).
[247] M. Beckers, B. Weise, S. Kalapis, T. Gries, G. Seide, C.-A. Bunge, 2 - Basics of light guidance, in: C.-A. Bunge, T. Gries, M. Beckers (Eds.), Polym. Opt. Fibres, Woodhead Publishing, 2017: pp. 9–46. https://doi.org/10.1016/B978-0-08-100039-7.00002-6.
[248] Radiopaedia.org, the wiki-based collaborative Radiology resource, Radiopaedia. (n.d.). https://radiopaedia.org/?lang=gb (accessed June 8, 2021).
[249] S. Carmignato, W. Dewulf, R. Leach, eds., Industrial X-Ray Computed Tomography, Springer International Publishing, 2018. https://www.springer.com/gb/book/9783319595719 (accessed April 12, 2019).
[250] J. Wiegert, U. Ohm, Scattered radiation in cone-beam computed tomography: analysis, quantification and compensation, Publ. Serv. RWTH Aachen Univ. (2007).
[251] M.F. L'Annunziata, Radioactivity: Introduction and History, Elsevier, 2007.
[252] S. Price, Pair production | Radiology Reference Article | Radiopaedia.org, Radiopaedia. (n.d.). https://radiopaedia.org/articles/pair-production?lang=gb (accessed June 8, 2021).
[253] K. Buchtela, RADIOCHEMICAL METHODS|Gamma-Ray Spectrometry☆, in: P. Worsfold, C. Poole, A. Townshend, M. Miró (Eds.), Encycl. Anal. Sci. Third Ed., Academic Press, Oxford, 2019: pp. 15–22. https://doi.org/10.1016/B978-0-12-409547-2.11333-2.
[254] T. Yanagida, Y. Fujimoto, T. Ito, K. Uchiyama, K. Mori, Development of X-ray-induced afterglow characterization system, Appl. Phys. Express. 7 (2014) 062401.
[255] A. du Plessis, M. Tshibalanganda, S.G. le Roux, Not all scans are equal: X-ray tomography image quality evaluation, Mater. Today Commun. 22 (2020) 100792. https://doi.org/10.1016/j.mtcomm.2019.100792.
[256] S. Zehani, A. Ouahabi, M. Oussalah, M. Mimi, A. Taleb-Ahmed, Bone microarchitecture characterization based on fractal analysis in spatial frequency domain imaging, Int. J. Imaging Syst. Technol. 31 (2021) 141–159.
[257] D. Thanh, P. Surya, A review on CT and X-ray images denoising methods, Informatica. 43 (2019).
[258] M. Beister, D. Kolditz, W.A. Kalender, Iterative reconstruction methods in X-ray CT, Phys. Med. 28 (2012) 94–108.
[259] M.J. Willemink, P.B. Noël, The evolution of image reconstruction for CT—from filtered back projection to artificial intelligence, Eur. Radiol. 29 (2019) 2185–2195.

[260] J.J. Lifton, T. Liu, Evaluation of the standard measurement uncertainty due to the ISO50 surface determination method for dimensional computed tomography, Precis. Eng. 61 (2020) 82–92. https://doi.org/10.1016/j.precisioneng.2019.10.004.
[261] M.L. Mather, S.P. Morgan, L.J. White, H. Tai, W. Kockenberger, S.M. Howdle, K.M. Shakesheff, J.A. Crowe, Image-based characterization of foamed polymeric tissue scaffolds, Biomed. Mater. 3 (2008) 015011.
[262] A. Townsend, L. Pagani, L. Blunt, P.J. Scott, X. Jiang, Factors affecting the accuracy of areal surface texture data extraction from X-ray CT, CIRP Ann. 66 (2017) 547–550. https://doi.org/10.1016/j.cirp.2017.04.074.
[263] VGStudio MAX 2.2 reference manual Ch. 5, (2013).
[264] A. Townsend, L. Pagani, P. Scott, L. Blunt, Areal surface texture data extraction from X-ray computed tomography reconstructions of metal additively manufactured parts, Precis. Eng. 48 (2017) 254–264. https://doi.org/10.1016/j.precisioneng.2016.12.008.
[265] A. Du Plessis, P. Sperling, A. Beerlink, W.B. Du Preez, S.G. Le Roux, Standard method for microCT-based additive manufacturing quality control 4: Metal powder analysis, MethodsX. 5 (2018) 1336–1345.
[266] P.A. Rometsch, D. Pelliccia, D. Tomus, X. Wu, Evaluation of polychromatic X-ray radiography defect detection limits in a sample fabricated from Hastelloy X by selective laser melting, NDT E Int. 62 (2014) 184–192.
[267] W.B. Zbijewski, Model-based image reconstruction in X-ray Computed Tomography, Utrecht University, 2006.
[268] U. Zscherpel, M. NAZARZADEHMOAFI, M. YUAN, A. WASKE, X-ray back scatter techniques for additive manufacturing, (2019).
[269] X. Cai, A.A. Malcolm, B.S. Wong, Z. Fan, Measurement and characterization of porosity in aluminium selective laser melting parts using X-ray CT, Virtual Phys. Prototyp. 10 (2015) 195–206.
[270] A. Du Plessis, S.G. le Roux, J. Waller, P. Sperling, N. Achilles, A. Beerlink, J.-F. Métayer, M. Sinico, G. Probst, W. Dewulf, Laboratory X-ray tomography for metal additive manufacturing: Round robin test, Addit. Manuf. 30 (2019) 100837.
[271] R. Schmitt, C. Isenberg, C. Niggemann, Knowledge-Based System to improve dimensional CT Measurements, (2012) 10.
[272] S. Carmignato, A. Pierobon, E. Savio, First International Intercomparison of Computed Tomography Systems for Dimensional Metrology, (2011) 4.
[273] J.S. Rathore, C. Vienne, Y. Quinsat, C. Tournier, Influence of resolution on the X-ray CT-based measurements of metallic AM lattice structures, Weld. World. 64 (2020) 1367–1376. https://doi.org/10.1007/s40194-020-00920-4.
[274] G.-R. Jaenisch, C. Bellon, U. Samadurau, McRay - A Monte Carlo Model Coupled to CAD for Radiation Techniques, (2006) 8.
[275] U. Hilpert, M. Bartscher, M. Neugebauer, J. Goebbels, G. Weidemann, C. Bellon, Simulation-aided computed tomography (CT) for dimensional measurements, in: 2007: p. 15.
[276] J. Tabary, Sindbad - a realistic multi-purpose and scalable X-ray simulation tool for NDT applications, in: 2007: p. 10.
[277] M. Reiter, B. Harrer, C. Heinzl, J. Kastner, C. Kuhn, D. Salaberger, Simulation Aided Study for Optimising Industrial X-ray CT Scan Parameters for Non-Destructive Testing and Materials Characterisation, in: 2011: p. 9.
[278] F. Timischl, The contrast-to-noise ratio for image quality evaluation in scanning electron microscopy, Scanning. 37 (2015) 54–62. https://doi.org/10.1002/sca.21179.

[279] B. Bechara, C.A. McMahan, W.S. Moore, M. Noujeim, H. Geha, F.B. Teixeira, Contrast-to-noise ratio difference in small field of view cone beam computed tomography machines, J. Oral Sci. 54 (2012) 227–232. https://doi.org/10.2334/josnusd.54.227.
[280] T. Vorburger, Optical Methods of Surface Measurement, (2012). https://www.nist.gov/system/files/documents/oles/3-Vorburger-Ted-Optical-Methods-of-Surface-Measurement-MSSFAA-10jul12.pdf (accessed June 8, 2021).
[281] G. Moroni, S. Petrò, Design for X-Ray Computed Tomography, Procedia CIRP. 84 (2019) 173–178. https://doi.org/10.1016/j.procir.2019.04.342.
[282] V.M. Rivas Santos, A. Thompson, D. Sims-Waterhouse, I. Maskery, P. Woolliams, R. Leach, Design and characterisation of an additive manufacturing benchmarking artefact following a design-for-metrology approach, Addit. Manuf. 32 (2020) 100964. https://doi.org/10.1016/j.addma.2019.100964.
[283] P.J. Swornowski, A critical look at the coordinate measuring technique, Mechatronics. 23 (2013) 80–93. https://doi.org/10.1016/j.mechatronics.2012.11.002.
[284] A. Küng, F. Meli, R. Thalmann, Ultraprecision micro-CMM using a low force 3D touch probe, Meas. Sci. Technol. 18 (2007) 319–327. https://doi.org/10.1088/0957-0233/18/2/S01.
[285] D. Weiß, Q. Shi, C. Kuhn, Measuring the 3D resolution of a micro-focus X-ray CT setup, (n.d.) 9.
[286] S. Kasperl, J. Hiller, M. Krumm, Computed Tomography Metrology in Industrial Research and Development, Mater. Test. 51 (2009) 405–411. https://doi.org/10.3139/120.110053.
[287] D. Cooper, J. Thornby, N. Blundell, R. Henrys, M.A. Williams, G. Gibbons, Design and manufacture of high performance hollow engine valves by Additive Layer Manufacturing, Mater. Des. 69 (2015) 44–55. https://doi.org/10.1016/j.matdes.2014.11.017.
[288] ImageJ, (n.d.). https://imagej.nih.gov/ij/ (accessed April 16, 2019).
[289] T. Hildebrand, P. Rüegsegger, A new method for the model-independent assessment of thickness in three-dimensional images, J. Microsc. 185 (1997) 67–75. https://doi.org/10.1046/j.1365-2818.1997.1340694.x.
[290] S. Van Bael, G. Kerckhofs, M. Moesen, G. Pyka, J. Schrooten, J.P. Kruth, Micro-CT-based improvement of geometrical and mechanical controllability of selective laser melted Ti6Al4V porous structures, Mater. Sci. Eng. A. 528 (2011) 7423–7431. https://doi.org/10.1016/j.msea.2011.06.045.
[291] J. Parthasarathy, B. Starly, S. Raman, A. Christensen, Mechanical evaluation of porous titanium (Ti6Al4V) structures with electron beam melting (EBM), J. Mech. Behav. Biomed. Mater. 3 (2010) 249–259. https://doi.org/10.1016/j.jmbbm.2009.10.006.
[292] C. Yan, L. Hao, A. Hussein, P. Young, Ti–6Al–4V triply periodic minimal surface structures for bone implants fabricated via selective laser melting, J. Mech. Behav. Biomed. Mater. 51 (2015) 61–73. https://doi.org/10.1016/j.jmbbm.2015.06.024.
[293] A. du Plessis, I. Yadroitsava, I. Yadroitsev, Ti6Al4V lightweight lattice structures manufactured by laser powder bed fusion for load-bearing applications, Opt. Laser Technol. 108 (2018) 521–528. https://doi.org/10.1016/j.optlastec.2018.07.050.
[294] C. Han, Y. Li, Q. Wang, S. Wen, Q. Wei, C. Yan, L. Hao, J. Liu, Y. Shi, Continuous functionally graded porous titanium scaffolds manufactured by selective laser melting for bone implants, J. Mech. Behav. Biomed. Mater. 80 (2018) 119–127. https://doi.org/10.1016/j.jmbbm.2018.01.013.
[295] S. Arabnejad, R. Burnett Johnston, J.A. Pura, B. Singh, M. Tanzer, D. Pasini, High-strength porous biomaterials for bone replacement: A strategy to assess the interplay between cell morphology, mechanical properties, bone ingrowth and manufacturing constraints, Acta Biomater. 30 (2016) 345–356. https://doi.org/10.1016/j.actbio.2015.10.048.
[296] C. Yan, L. Hao, A. Hussein, P. Young, D. Raymont, Advanced lightweight 316L stainless steel cellular lattice structures fabricated via selective laser melting, Mater. Des. 55 (2014) 533–541. https://doi.org/10.1016/j.matdes.2013.10.027.

[297] Z.S. Bagheri, D. Melancon, L. Liu, R.B. Johnston, D. Pasini, Compensation strategy to reduce geometry and mechanics mismatches in porous biomaterials built with Selective Laser Melting, J. Mech. Behav. Biomed. Mater. 70 (2017) 17–27. https://doi.org/10.1016/j.jmbbm.2016.04.041.
[298] L. Liu, P. Kamm, F. García-Moreno, J. Banhart, D. Pasini, Elastic and failure response of imperfect three-dimensional metallic lattices: the role of geometric defects induced by Selective Laser Melting, J. Mech. Phys. Solids. 107 (2017) 160–184. https://doi.org/10.1016/j.jmps.2017.07.003.
[299] A. Cuadrado, A. Yánez, O. Martel, S. Deviaene, D. Monopoli, Influence of load orientation and of types of loads on the mechanical properties of porous Ti6Al4V biomaterials, Mater. Des. 135 (2017) 309–318. https://doi.org/10.1016/j.matdes.2017.09.045.
[300] T.B. Sercombe, X. Xu, V.J. Challis, R. Green, S. Yue, Z. Zhang, P.D. Lee, Failure modes in high strength and stiffness to weight scaffolds produced by Selective Laser Melting, Mater. Des. 67 (2015) 501–508. https://doi.org/10.1016/j.matdes.2014.10.063.
[301] D.A. Hollander, M. von Walter, T. Wirtz, R. Sellei, B. Schmidt-Rohlfing, O. Paar, H.-J. Erli, Structural, mechanical and in vitro characterization of individually structured Ti–6Al–4V produced by direct laser forming, Biomaterials. 27 (2006) 955–963. https://doi.org/10.1016/j.biomaterials.2005.07.041.
[302] C.-Y. Lin, T. Wirtz, F. LaMarca, S.J. Hollister, Structural and mechanical evaluations of a topology optimized titanium interbody fusion cage fabricated by selective laser melting process, J. Biomed. Mater. Res. A. 83A (2007) 272–279. https://doi.org/10.1002/jbm.a.31231.
[303] A. Townsend, L. Pagani, P.J. Scott, L. Blunt, Introduction of a Surface Characterization Parameter Sdrprime for Analysis of Re-entrant Features, J. Nondestruct. Eval. 38 (2019) 58. https://doi.org/10.1007/s10921-019-0573-x.
[304] G. Pyka, G. Kerckhofs, A. Braem, T. Mattheys, J. Schrooten, M. Wevers, Novel micro-ct based characterization tool for surface roughness measurements of porous structures, in: n.d.
[305] F. Borges de Oliveira, A. Stolfi, M. Bartscher, L. De Chiffre, U. Neuschaefer-Rube, Experimental investigation of surface determination process on multi-material components for dimensional computed tomography, Case Stud. Nondestruct. Test. Eval. 6 (2016) 93–103. https://doi.org/10.1016/j.csndt.2016.04.003.
[306] A. Thompson, N. Senin, C. Giusca, R. Leach, Topography of selectively laser melted surfaces: A comparison of different measurement methods, CIRP Ann. 66 (2017) 543–546. https://doi.org/10.1016/j.cirp.2017.04.075.
[307] K. Yang, J. Wang, L. Jia, G. Yang, H. Tang, Y. Li, Additive manufacturing of Ti-6Al-4V lattice structures with high structural integrity under large compressive deformation, J. Mater. Sci. Technol. 35 (2019) 303–308. https://doi.org/10.1016/j.jmst.2018.10.029.
[308] J. Stringer, X. Xu, P. Zheng, J. Jiang, A benchmarking part for evaluating and comparing support structures of additive manufacturing, in: Int. Conf. Prog. Addit. Manuf. Pro-AM 2018, 2018: p. 201.
[309] A. Alghamdi, D. Downing, M. McMillan, M. Brandt, M. Qian, M. Leary, Experimental and numerical assessment of surface roughness for Ti6Al4V lattice elements in selective laser melting, Int. J. Adv. Manuf. Technol. 105 (2019) 1275–1293. https://doi.org/10.1007/s00170-019-04092-4.
[310] X. Han, H. Zhu, X. Nie, G. Wang, X. Zeng, Investigation on Selective Laser Melting AlSi10Mg Cellular Lattice Strut: Molten Pool Morphology, Surface Roughness and Dimensional Accuracy, Materials. 11 (2018) 392. https://doi.org/10.3390/ma11030392.
[311] T. Tancogne-Dejean, A.B. Spierings, D. Mohr, Additively-manufactured metallic micro-lattice materials for high specific energy absorption under static and dynamic loading, Acta Mater. 116 (2016) 14–28. https://doi.org/10.1016/j.actamat.2016.05.054.
[312] A. Zargarian, M. Esfahanian, J. Kadkhodapour, S. Ziaei-Rad, Numerical simulation of the fatigue behavior of additive manufactured titanium porous lattice structures, Mater. Sci. Eng. C. 60 (2016) 339–347. https://doi.org/10.1016/j.msec.2015.11.054.

[313] S. Siddique, M. Imran, M. Rauer, M. Kaloudis, E. Wycisk, C. Emmelmann, F. Walther, Computed tomography for characterization of fatigue performance of selective laser melted parts, Mater. Des. 83 (2015) 661–669. https://doi.org/10.1016/j.matdes.2015.06.063.
[314] J.A. Slotwinski, E.J. Garboczi, K.M. Hebenstreit, Porosity Measurements and Analysis for Metal Additive Manufacturing Process Control, J. Res. NIST JRES - 119019. (2014). https://www.nist.gov/publications/porosity-measurements-and-analysis-metal-additive-manufacturing-process-control (accessed November 19, 2018).
[315] W.W. Wits, S. Carmignato, F. Zanini, T.H.J. Vaneker, Porosity testing methods for the quality assessment of selective laser melted parts, CIRP Ann. 65 (2016) 201–204. https://doi.org/10.1016/j.cirp.2016.04.054.
[316] S. Khademzadeh, S. Carmignato, N. Parvin, F. Zanini, P.F. Bariani, Micro porosity analysis in additive manufactured NiTi parts using micro computed tomography and electron microscopy, Mater. Des. 90 (2016) 745–752.
[317] J. Damon, S. Dietrich, F. Vollert, J. Gibmeier, V. Schulze, Process dependent porosity and the influence of shot peening on porosity morphology regarding selective laser melted AlSi10Mg parts, Addit. Manuf. 20 (2018) 77–89. https://doi.org/10.1016/j.addma.2018.01.001.
[318] J. Kastner, B. Plank, D. Salaberger, J. Sekelja, Defect and porosity determination of fibre reinforced polymers by X-ray computed tomography, in: 2nd Int. Symp. NDT Aerosp., 2010: pp. 1–12.
[319] L. Lin, M. Luo, H.T. Tian, X.M. Li, G.P. Guo, Experimental investigation on porosity of carbon fiber-reinforced composite using ultrasonic attenuation coefficient, in: Proc. World Conf. Nondestruct. Test., Citeseer, 2008.
[320] P. Delroisse, P.J. Jacques, E. Maire, O. Rigo, A. Simar, Effect of strut orientation on the microstructure heterogeneities in AlSi10Mg lattices processed by selective laser melting, Scr. Mater. 141 (2017) 32–35. https://doi.org/10.1016/j.scriptamat.2017.07.020.
[321] Y. Chahid, A. Townsend, A. Liu, P. Bills, P. Sperling, R. Racasan, Optimizing X-Ray Computed Tomography Settings for Dimensional Metrology Using 2D Image Analysis, in: N. Shamsaei, M. Seifi (Eds.), Struct. Integr. Addit. Manuf. Mater. Parts, ASTM International, 100 Barr Harbor Drive, PO Box C700, West Conshohocken, PA 19428-2959, 2020: pp. 88–101. https://doi.org/10.1520/STP163120190141.
[322] InfiniteFocus - Dimensional accuracy & surface finish measurement, (n.d.). https://www.alicona.com/en/products/infinitefocus/ (accessed July 19, 2021).
[323] Fiji is just ImageJ, (2020). http://web.archive.org/web/20200519164153/https://fiji.sc/ (accessed April 16, 2019).
[324] N. Otsu, A threshold selection method from gray-level histograms, IEEE Trans. Syst. Man Cybern. 9 (1979) 62–66.
[325] S. Petrò, C. Reina, G. Moroni, X-ray CT-Based Defect Evaluation of Continuous CFRP Additive Manufacturing, J. Nondestruct. Eval. 40 (2021) 1–9.
[326] A. Pascual, N. Ortega, S. Plaza, I. Holgado, J.I. Arrizubieta, A RE Methodology to achieve Accurate Polygon Models and NURBS Surfaces by Applying Different Data Processing Techniques, Metals. 10 (2020) 1508. https://doi.org/10.3390/met10111508.
[327] Optical Methods of Surface Measurement, (n.d.). https://webcache.googleusercontent.com/search?q=cache:dobH4IUF2mQJ:https://www.nist.gov/sites/default/files/documents/oles/3-Vorburger-Ted-Optical-Methods-of-Surface-Measurement-MSSFAA-10jul12.pdf+&cd=1&hl=en&ct=clnk&gl=uk&client=firefox-b-d (accessed June 3, 2019).
[328] Optical Methods of Surface Measurement nist - Google Search, (n.d.). https://www.google.com/search?q=Optical+Methods+of+Surface+Measurement+nist&client=firefox-b-

d&source=lnms&tbm=isch&sa=X&ved=0ahUKEwiW9Yf6ts3iAhWMnhQKHTL4Cz4Q_AUIECgB&biw=1216&bih=612#imgrc=_v45zVw-EVmLVM: (accessed June 3, 2019).
[329] Y. Chahid, Method to choose X-ray computed tomography settings for dimensional metrology using 2D image analysis prior to reconstruction, in: Univ. Hudders. Res. Portal, 2019. https://pure.hud.ac.uk/en/activities/method-to-choose-x-ray-computed-tomography-settings-for-dimension (accessed July 23, 2021).
[330] VGSTUDIO MAX - Products - volumegraphics.com, (n.d.). https://www.volumegraphics.com/en/products/vgstudio-max.html (accessed April 16, 2019).
[331] XT H 225 | Computed Tomography | X-ray and CT inspection | Nikon Metrology, (2020). http://web.archive.org/web/20200519163626/https://www.nikonmetrology.com/en-gb/product/xt-h-225 (accessed May 19, 2020).
[332] A. Buratti, N. Grozmani, C. Voigtmann, L.V. Sartori, R.H. Schmitt, Determination of the optimal imaging parameters in industrial computed tomography for dimensional measurements on monomaterial workpieces, Meas. Sci. Technol. 29 (2018) 115009. https://doi.org/10.1088/1361-6501/aae4d6.
[333] ROI Manager Tools, (n.d.). https://imagej.nih.gov/ij/plugins/roi-manager-tools/index.html (accessed April 16, 2019).
[334] Software | Nikon Metrology, (2020). http://web.archive.org/web/20200519162151/https://www.nikonmetrology.com/en-gb/products/x-ray-and-ct-inspection/software-x-ray-and-ct-inspection (accessed May 19, 2020).
[335] blender.org - Home of the Blender project - Free and Open 3D Creation Software, (n.d.). https://www.blender.org/ (accessed July 27, 2021).
[336] Autodesk - Meshmixer, Inspector. (2019). https://help.autodesk.com/view/MSHMXR/2019/ENU/?guid=GUID-83BC663B-FA1C-46D3-8C2F-82EB6892DFC3 (accessed June 3, 2019).
[337] EWI Adds Second EOS M290 DMLS Machine, (n.d.). https://additivemanufacturingtoday.com/ewi-adds-second-eos-m290-dmls-machine (accessed June 3, 2019).
[338] M. Dallago, S. Raghavendra, V. Luchin, G. Zappini, D. Pasini, M. Benedetti, Geometric assessment of lattice materials built via Selective Laser Melting, Mater. Today Proc. 7 (2019) 353–361. https://doi.org/10.1016/j.matpr.2018.11.096.
[339] BS EN ISO 15708-3:2019 Non-destructive testing. Radiation methods for computed tomography. Operation and interpretation, (n.d.). https://shop.bsigroup.com/ProductDetail/?pid=000000000030380394 (accessed October 15, 2019).
[340] A. Kraemer, E. Kovacheva, G. Lanza, Projection based evaluation of CT image quality in dimensional metrology, in: 2015: p. 10.
[341] P. Gajjar, IPC Quick Start Guide: IPC programming for Inspect-X, The University of Manchester, 2017. https://doi.org/10.3927/59340663.
[342] Archiveddocs, Visual Basic 6.0 Documentation, (n.d.). https://docs.microsoft.com/en-us/previous-versions/visualstudio/visual-basic-6/visual-basic-6.0-documentation (accessed July 5, 2021).
[343] Y. Zhang, H. Yu, Convolutional Neural Network Based Metal Artifact Reduction in X-Ray Computed Tomography, IEEE Trans. Med. Imaging. 37 (2018) 1370–1381. https://doi.org/10.1109/TMI.2018.2823083.
[344] Y. Chahid, R. Racasan, L. Pagani, A. Townsend, A. Liu, P. Bills, L. Blunt, Parametrically designed surface topography on CAD models of additively manufactured lattice structures for improved design validation, Addit. Manuf. 37 (2021) 101731. https://doi.org/10.1016/j.addma.2020.101731.
[345] T. Maconachie, M. Leary, B. Lozanovski, X. Zhang, M. Qian, O. Faruque, M. Brandt, SLM lattice structures: Properties, performance, applications and challenges, Mater. Des. 183 (2019) 108137. https://doi.org/10.1016/j.matdes.2019.108137.

[346] D. Schillinger, M. Ruess, The Finite Cell Method: A review in the context of higher-order structural analysis of CAD and image-based geometric models, Arch. Comput. Methods Eng. 22 (2015) 391–455.
[347] J. Fieres, P. Schumann, C. Reinhart, Predicting failure in additively manufactured parts using X-ray computed tomography and simulation, Procedia Eng. 213 (2018) 69–78.
[348] 3d Print Aluminum | Metal 3D printing, (n.d.). https://www.eos.info/en/additive-manufacturing/3d-printing-metal/dmls-metal-materials/aluminium-al (accessed June 18, 2021).
[349] S. Gustavson, Simplex noise demystified, (n.d.) 17.
[350] ISO 25178-2:2012(en), Geometrical product specifications (GPS) — Surface texture: Areal — Part 2: Terms, definitions and surface texture parameters, (n.d.). https://www.iso.org/obp/ui/#iso:std:iso:25178:-2:ed-1:v1:en (accessed March 30, 2020).
[351] S. Lou, L. Pagani, W. Zeng, X. Jiang, P.J. Scott, Watershed segmentation of topographical features on freeform surfaces and its application to additively manufactured surfaces, Precis. Eng. 63 (2020) 177–186. https://doi.org/10.1016/j.precisioneng.2020.02.005.
[352] S10Z (Ten-Point Height) | Area Roughness Parameters | Introduction To Roughness | KEYENCE America, (n.d.). https://www.keyence.com/ss/products/microscope/roughness/surface/s10z-ten-point-height.jsp (accessed November 12, 2021).
[353] X.J. Jiang, P.J. Scott, Reference form computation, in: Adv. Metrol. Free. Surf., Academic Press, 2020: p. 249.
[354] Towards a new definition of areal surface texture parameters on freeform surface: Re-entrant features and functional parameters - ScienceDirect, (n.d.). https://www.sciencedirect.com/science/article/pii/S026322411930329X (accessed March 30, 2020).
[355] M. Shukla, I. Todorov, D. Kapletia, Application of additive manufacturing for mass customisation: understanding the interaction of critical barriers, Prod. Plan. Control. 29 (2018) 814–825. https://doi.org/10.1080/09537287.2018.1474395.
[356] Z. Alomar, F. Concli, A Review of the Selective Laser Melting Lattice Structures and Their Numerical Models, Adv. Eng. Mater. 22 (2020) 2000611. https://doi.org/10.1002/adem.202000611.
[357] Structural Analysis for Rapid Design Iterations | Altair SimSolid, (n.d.). https://www.altair.com/simsolid/ (accessed February 10, 2020).
[358] A. Tawfik, R. Racasan, D. Bacheva, L. Blunt, A. Beerlink, P. Bills, Challenges in Inspecting Internal Features for SLM Additive Manufactured Build Artifacts, in: 4th ASTM Symp. Struct. Integr. Addit. Manuf. Mater. Parts, ASTM International, 2020: pp. 102–121.
[359] How does the ramp block work?, NTopology. (n.d.). https://support.ntopology.com/hc/en-us/articles/360041676813-How-does-the-ramp-block-work- (accessed March 16, 2021).
[360] 14:00-17:00, ISO/ASTM 52902:2019, ISO. (n.d.). https://www.iso.org/cms/render/live/en/sites/isoorg/contents/data/standard/06/72/67287.html (accessed March 25, 2021).
[361] What's New in VGSTUDIO MAX 3.4.x, Ind. CT Softw. Vol. Graph. (n.d.). https://www.volumegraphics.com/en/products/vgsm/what-s-new-in-vgstudio-max-3-4-x.html (accessed November 13, 2021).
[362] P. Kumar Nayak, A. Kumar Sahu, S. Sankar Mahapatra, Effect of Process Parameters on the Mechanical Behavior of FDM and DMLS Build Parts, Mater. Today Proc. 22 (2020) 1443–1451. https://doi.org/10.1016/j.matpr.2020.01.502.
[363] I.J. Solomon, P. Sevvel, J. Gunasekaran, A review on the various processing parameters in FDM, Mater. Today Proc. 37 (2021) 509–514. https://doi.org/10.1016/j.matpr.2020.05.484.
[364] S. Guddati, A.S.K. Kiran, M. Leavy, S. Ramakrishna, Recent advancements in additive manufacturing technologies for porous material applications, Int. J. Adv. Manuf. Technol. 105 (2019) 193–215. https://doi.org/10.1007/s00170-019-04116-z.

[365] F. Zanini, E. Sbettega, S. Carmignato, X-ray computed tomography for metal additive manufacturing: challenges and solutions for accuracy enhancement, Procedia CIRP. 75 (2018) 114–118. https://doi.org/10.1016/j.procir.2018.04.050.
[366] A. Hernandez-Contreras, L. Ruiz-Huerta, A. Caballero-Ruiz, V. Moock, H.R. Siller, Extended CT Void Analysis in FDM Additive Manufacturing Components, Materials. 13 (2020) 3831. https://doi.org/10.3390/ma13173831.
[367] C.R. Knowles, T.H. Becker, R.B. Tait, The effect of heat treatment on the residual stress levels within direct metal laser sintered Ti-6Al-4V as measured using the hole-drilling strain gauge method, in: Proc. 13th Int. RAPDASA Conf., 2012: pp. 1–10.
[368] VDI/VDE 2630 Blatt 1.1 - Computed tomography in dimensional measurement - Fundamentals and definitions, 2016. https://www.vdi.de/en/home/vdi-standards/details/vdivde-2630-blatt-11-computed-tomography-in-dimensional-measurement-fundamentals-and-definitions (accessed November 15, 2021).
[369] Nikon, Nikon MCT225 Brochure, (n.d.). https://www.nikonmetrology.com/images/brochures/mct225-en.pdf (accessed November 15, 2021).
[370] K. Naresh, K.A. Khan, R. Umer, W.J. Cantwell, The use of X-ray computed tomography for design and process modeling of aerospace composites: A review, Mater. Des. 190 (2020) 108553. https://doi.org/10.1016/j.matdes.2020.108553.
[371] B. Akhoundi, A.H. Behravesh, A. Bagheri Saed, Improving mechanical properties of continuous fiber-reinforced thermoplastic composites produced by FDM 3D printer, J. Reinf. Plast. Compos. 38 (2019) 99–116.
[372] A.F. Barreno-Avila, M. Monar-Naranjo, E.M. Barreno-Avila, Fusion deposition modeling (FDM) 3D printing parameters correlation: An analysis of different polymers surface roughness, in: IOP Conf. Ser. Mater. Sci. Eng., IOP Publishing, 2021: p. 012071.
[373] V.E. Kuznetsov, A.N. Solonin, O.D. Urzhumtsev, R. Schilling, A.G. Tavitov, Strength of PLA components fabricated with fused deposition technology using a desktop 3D printer as a function of geometrical parameters of the process, Polymers. 10 (2018) 313.
[374] N.M. Razali, Y.B. Wah, Power comparisons of shapiro-wilk, kolmogorov-smirnov, lilliefors and anderson-darling tests, J. Stat. Model. Anal. 2 (2011) 21–33.
[375] A. Tawfik, P. Bills, L. Blunt, R. Racasan, Development of an Additive Manufactured Artifact to Characterize Unfused Powder Using Computed Tomography, Int. J. Autom. Technol. 14 (2020) 439–446. https://doi.org/10.20965/ijat.2020.p0439.
[376] A. Panesar, M. Abdi, D. Hickman, I. Ashcroft, Strategies for functionally graded lattice structures derived using topology optimisation for additive manufacturing, Addit. Manuf. 19 (2018) 81–94.
[377] H. Villarraga-Gómez, N. Kotwal, V. Ninov, L. Omlor, A. Mishra, B. Johnson, R. Zarnetta, D. Weiss, W. Kimmig, M. Krenkel, C. Graf, High-precision Metrology with High-resolution Computed Tomography Using 3D X-ray Microscopes, 2020.
[378] X. Zhang, J. Wang, L. Xing, Metal artifact reduction in x-ray computed tomography (CT) by constrained optimization, Med. Phys. 38 (2011) 701–711. https://doi.org/10.1118/1.3533711.
[379] F. Wohlgemuth, E. Haltenberger, C. Klein, T. Hausotte, Numerical determination of task-specific measurement uncertainty using a virtual metrological X-ray computed tomography system, in: Sens. Meas. Syst. 19th ITGGMA-Symp., 2018: pp. 1–4.
[380] M. Ferrucci, E. Ametova, Charting the course towards dimensional measurement traceability by x-ray computed tomography, Meas. Sci. Technol. 32 (2021) 092001. https://doi.org/10.1088/1361-6501/abf058.
[381] AMSC Gaps: Nondestructive Evaluation, (n.d.). https://www.ansi.org/portal/amsc/AMSC-Gaps-Nondestructive-Evaluation (accessed April 29, 2021).

[382] K. Modaresifar, L.B. Kunkels, M. Ganjian, N. Tümer, C.W. Hagen, L.G. Otten, P.-L. Hagedoorn, L. Angeloni, M.K. Ghatkesar, L.E. Fratila-Apachitei, A.A. Zadpoor, Deciphering the Roles of Interspace and Controlled Disorder in the Bactericidal Properties of Nanopatterns against Staphylococcus aureus, Nanomaterials. 10 (2020) 347. https://doi.org/10.3390/nano10020347.
[383] Intentional Design of Surface Roughness for Orthopedic Parts | nTopology, (n.d.). https://ntopology.com/blog/2019/05/24/intentional-design-of-surface-roughness-for-orthopedic-parts/ (accessed February 7, 2020).
[384] L. Cao, J. Li, J. Hu, H. Liu, Y. Wu, Q. Zhou, Optimization of surface roughness and dimensional accuracy in LPBF additive manufacturing, Opt. Laser Technol. 142 (2021) 107246. https://doi.org/10.1016/j.optlastec.2021.107246.
[385] Y. Liu, L.A. Blunt, F. Gao, X. (Jane) Jiang, High-dynamic-range 3D measurement for E-beam fusion additive manufacturing based on SVM intelligent fringe projection system, Surf. Topogr. Metrol. Prop. (2021). https://doi.org/10.1088/2051-672X/ac0c62.
[386] J. Eastwood, L. Newton, R. Leach, S. Piano, The generation of representative synthetic surface texture data using machine learning, 2021. https://doi.org/10.13140/RG.2.2.20113.97120.
[387] P. Jiang, M. Rifat, S. Basu, Impact of Surface Roughness and Porosity on Lattice Structures Fabricated by Additive Manufacturing- A Computational Study, Procedia Manuf. 48 (2020) 781–789. https://doi.org/10.1016/j.promfg.2020.05.114.
[388] H.C. Taylor, E.A. Garibay, R.B. Wicker, Toward a common laser powder bed fusion qualification test artifact, Addit. Manuf. 39 (2021) 101803.
[389] H.T. Tran, X. Liang, A.C. To, Efficient prediction of cracking at solid-lattice support interface during laser powder bed fusion via global-local J-integral analysis based on modified inherent strain method and lattice support homogenization, Addit. Manuf. 36 (2020) 101590. https://doi.org/10.1016/j.addma.2020.101590.
[390] Nikon Metrology Showcase Semi - Automated CT Inspection, Metrol. Qual. News - Online Mag. (2017). https://metrology.news/nikon-metrology-semi-automated-ct-inspection/ (accessed June 28, 2021).
[391] Digital Factory: Industry 4.0 & Additive Manufacturing, (n.d.). https://www.eos.info/en/innovations/digital-manufacturing-production (accessed June 28, 2021).
[392] University of Warwick, EPSRC Strategic Equipment - High Speed CT, (n.d.). https://gtr.ukri.org/projects?ref=EP%2FS010076%2F1 (accessed June 28, 2021).
[393] X. Gong, T. Anderson, K. Chou, Review on powder-based electron beam additive manufacturing technology, in: Int. Symp. Flex. Autom., American Society of Mechanical Engineers, 2012: pp. 507–515.
[394] M. Ziaee, N.B. Crane, Binder jetting: A review of process, materials, and methods, Addit. Manuf. 28 (2019) 781–801.
[395] S. Franchitti, R. Borrelli, C. Pirozzi, L. Carrino, W. Polini, L. Sorrentino, A. Gazzerro, Investigation on Electron Beam Melting: Dimensional accuracy and process repeatability, Vacuum. 157 (2018) 340–348. https://doi.org/10.1016/j.vacuum.2018.09.007.
[396] S. Pal, N. Gubeljak, T. Bončina, R. Hudák, T. Toth, J. Zivcak, G. Lojen, N. Leben, I. Drstvenšek, The effects of locations on the build tray on the quality of specimens in powder bed additive manufacturing, Int. J. Adv. Manuf. Technol. 112 (2021) 1159–1170. https://doi.org/10.1007/s00170-020-06563-5.

12. Appendices

12.1. Appendix 1: DOE 54 sample data (Chapter 6)

DOE sample	Frequency	Amplitude (mm)	Shape	Seed	Sa (µm)	Sq (µm)	Sp (µm)	Sv (µm)	Spd (10% Treshold) (1/ mm²)	Max(Sp,Sv) (µm)
1	1750	0.1	Plane	2	21.84	26.82	86.81	81.97	3.84	86.81
2	1250	0.3	Plane	1	66.22	81.54	253.19	260.35	1.97	260.35
3	1750	0.3	Plane	3	65.93	80.60	263.54	248.33	3.38	263.54
4	1250	0.1	Plane	3	22.49	27.45	83.73	84.47	1.99	84.47
5	1750	0.2	Plane	2	43.57	53.63	174.58	171.10	3.88	174.58
6	1250	0.2	Plane	1	44.17	54.29	166.90	161.55	2.12	166.90
7	1750	0.3	Plane	1	66.34	81.10	258.15	276.03	3.36	276.03
8	1750	0.1	Plane	1	22.41	27.40	87.88	84.57	3.79	87.88
9	1500	0.1	Plane	2	22.32	27.31	84.60	80.70	3.11	84.60
10	1250	0.3	Plane	3	66.17	80.93	256.32	248.18	2.01	256.32
11	1500	0.1	Plane	3	22.22	27.23	87.42	85.32	2.76	87.42
12	1750	0.2	Plane	3	44.30	54.16	169.88	172.72	3.90	172.72
13	1250	0.1	Plane	2	22.57	27.50	82.64	81.86	2.09	82.64
14	1500	0.2	Plane	1	43.86	53.89	160.29	161.22	3.15	161.22
15	1250	0.2	Plane	3	44.57	54.47	173.47	171.35	2.01	173.47
16	1500	0.3	Plane	1	65.91	81.06	244.31	250.64	2.77	250.64
17	1500	0.3	Plane	2	67.45	82.60	245.61	246.02	2.84	246.02
18	1500	0.2	Plane	3	44.71	54.75	171.12	178.70	2.82	178.70
19	1750	0.3	Plane	2	64.75	79.69	264.28	249.72	3.34	264.28
20	1750	0.2	Plane	1	44.76	54.77	174.12	172.71	3.72	174.12
21	1250	0.1	Plane	1	22.12	27.13	85.41	83.37	2.15	85.41
22	1500	0.1	Plane	1	21.99	26.99	87.10	84.32	3.00	87.10
23	1750	0.1	Plane	3	22.33	27.29	84.58	84.62	4.00	84.62
24	1250	0.2	Plane	2	45.24	55.29	180.38	167.24	1.99	180.38
25	1500	0.3	Plane	3	66.61	81.59	260.01	246.62	2.58	260.01
26	1500	0.2	Plane	2	44.87	54.95	163.17	169.34	3.00	169.34
27	1250	0.3	Plane	2	67.84	83.15	251.47	251.35	1.97	251.47

28	1750	0.1	Cylinder	2	22.24	27.23	88.18	89.39	3.63	89.39
29	1250	0.3	Cylinder	1	68.15	83.25	256.10	260.93	2.04	260.93
30	1750	0.3	Cylinder	3	66.65	81.40	255.69	261.86	3.45	261.86
31	1250	0.1	Cylinder	3	22.89	27.99	87.51	87.81	2.01	87.81
32	1750	0.2	Cylinder	2	44.59	54.57	174.02	177.83	3.72	177.83
33	1250	0.2	Cylinder	1	45.52	55.69	169.70	175.02	2.04	175.02
34	1750	0.3	Cylinder	1	66.51	81.44	255.74	253.88	3.28	255.74
35	1750	0.1	Cylinder	1	22.32	27.34	87.76	86.10	3.68	87.76
36	1500	0.1	Cylinder	2	22.19	27.18	85.90	84.96	2.83	85.90
37	1250	0.3	Cylinder	3	68.40	83.36	263.75	257.65	1.96	263.75
38	1500	0.1	Cylinder	3	22.28	27.29	85.49	85.69	2.89	85.69
39	1750	0.2	Cylinder	3	44.89	54.88	170.73	178.19	3.71	178.19
40	1250	0.1	Cylinder	2	22.24	27.28	83.47	87.67	2.04	87.67
41	1500	0.2	Cylinder	1	44.41	54.30	180.10	174.33	2.74	180.10
42	1250	0.2	Cylinder	3	45.70	55.76	175.34	176.59	2.04	176.59
43	1500	0.3	Cylinder	1	65.95	80.75	256.80	254.72	2.62	256.80
44	1500	0.3	Cylinder	2	66.00	81.01	257.27	257.87	2.60	257.87
45	1500	0.2	Cylinder	3	44.51	54.56	172.45	171.45	2.88	172.45
46	1750	0.3	Cylinder	2	66.70	81.56	254.38	258.85	3.39	258.85
47	1750	0.2	Cylinder	1	44.75	54.84	166.65	173.45	3.77	173.45
48	1250	0.1	Cylinder	1	22.64	27.71	89.38	91.85	1.98	91.85
49	1500	0.1	Cylinder	1	22.36	27.30	85.07	84.62	2.94	85.07
50	1750	0.1	Cylinder	3	22.45	27.42	87.33	87.54	3.71	87.54
51	1250	0.2	Cylinder	2	44.56	54.55	173.18	173.77	2.08	173.77
52	1500	0.3	Cylinder	3	66.36	81.35	260.79	258.71	2.66	260.79
53	1500	0.2	Cylinder	2	44.13	54.08	173.00	176.06	2.84	176.06
54	1250	0.3	Cylinder	2	66.83	81.80	256.03	254.88	2.00	256.03

12.2. Appendix 2: ASTM Book Chapter Publication (Chapter 5)

STP 1631, 2020 / available online at www.astm.org / doi: 10.1520/STP163120190141

Younes Chahid,[1] Andrew Townsend,[2] Alexander Liu,[3]
Paul Bills,[1] Philip Sperling,[4] and Radu Racasan[1]

Optimizing X-Ray Computed Tomography Settings for Dimensional Metrology Using 2D Image Analysis

Citation

Y. Chahid, A. Townsend, A. Liu, P. Bills, P. Sperling, and R. Racasan, "Optimizing X-Ray Computed Tomography Settings for Dimensional Metrology Using 2D Image Analysis," in *Structural Integrity of Additive Manufactured Materials and Parts*, ed. N. Shamsaei and M. Seifi (West Conshohocken, PA: ASTM International, 2020), 88–101. http://doi.org/10.1520/STP163120190141[5]

ABSTRACT

The current way to choose X-ray computed tomography (XCT) scanning settings is usually manual and prone to operator errors. This paper presents an effective semiautomatic protocol that proves a high correlation between the local contrast-to-noise (CNR) of XCT two-dimensional (2D) projection image (prior to reconstruction) quality and the resulting XCT 3D volume scan quality. This high correlation allowed the comparison of four XCT settings to determine the one with the smallest error, solely by locally using the CNR equation on one 2D projection (prior to reconstruction) of an additive manufactured lattice structure. Verification of the protocol was done by using a workpiece and comparing the chosen XCT setting reconstructed workpiece dimensions to the ones measured

Manuscript received November 6, 2019; accepted for publication May 27, 2020.

[1]EPSRC Future Metrology Hub, School of Computing and Engineering, University of Huddersfield, Queensgate, HD1 3DH Huddersfield, UK, Y. C. http://orcid.org/0000-0002-1816-4869, P. B. http://orcid.org/0000-0002-5468-6330, R. R. http://orcid.org/0000-0001-5067-9494

[2]Nondestructive Evaluation Group, Nondestructive Characterization Institute, Lawrence Livermore National Laboratory, 7000 East Ave., Livermore, CA 94550, USA http://orcid.org/0000-0002-1215-3018

[3]NTU Innovation Centre, 71 Nanyang Dr. #04-01, Singapore 638075

[4]Product Management Additive Manufacturing, Volume Graphics GmbH, Speyerer Str. 4-6, 69115 Heidelberg, Germany http://orcid.org/0000-0001-9944-264X

[5]Fourth ASTM Symposium on *Structural Integrity of Additive Manufactured Materials and Parts* on October 7–10, 2019 in National Harbor, MD, USA.

using a coordinate-measuring machine (CMM). This new method can reduce the operator error and time needed to compare different XCT setting combinations. The proposed protocol is a step closer to an automated XCT parameter selection procedure, limiting user dependency and error while increasing accuracy and fidelity.

Keywords
quality control, metrology, X-ray computed tomography (XCT), additive manufacturing

Introduction

X-ray computed tomography (XCT) is one of the few tools that can assist in measuring and assessing both external and internal features. With the advancements in design techniques and additive manufacturing methods, the industry has become capable of producing parts such as custom lattice structures with extreme complexity that cannot be measured with common metrology tools. Lattice structures are usually topologically ordered and repeated unit cells;[1] their unique geometry can, for example, be beneficial for patient-specific orthopedic implants[2] or in aerospace.[3,4]

However, while XCT is usually the tool used to measure these geometries in a nondestructive way, there is still no clear model correlating the effects of different XCT parameters on the measurement uncertainty.[5] This means that:

- Current users cannot usually provide an uncertainty statement.[6]
- No holistic model can currently aid the user in choosing settings for a part where the material and internal features are unknown.
- Most XCT settings are being chosen by the user, leading to a great influence and large variation in the measurements.[7]
- A considerable amount of time can be spent choosing the XCT settings optimized for scanning a given part.

CURRENT PROCEDURES AND CHALLENGES WHEN CHOOSING XCT SETTINGS

When faced with a new part, of which the material and internal features are unknown, an experienced user can usually limit the range of the different combinations of settings that should be used, following common initial user guidelines provided in the machine manufacturer manuals. These guidelines suggest, for example, that X-rays penetrate the part from all angles without saturating any of the projections used for reconstruction or that the X-ray spot stays smaller than the effective pixel size.*

After limiting the choice of settings to be used, a user is usually not capable of accurately deciding from this range of settings which one results in the highest contrast and minimum noise—therefore leading to less artifacts and measurement

*Nikon Metrology, "Inspect-X: X-Ray and CT Acquisition and Processing Software," 2020, http://web.archive.org/web/20200519163325/https://www.nikonmetrology.com/en-us/product/inspect-x error. The reason is that it can be challenging for the user to detect subtle changes in contrast and noise from the histogram alone or the two dimensional (2D) image displayed on the machine screen without relying on image analysis tools before starting the XCT scan.

Currently, to choose the XCT machine settings, different approaches can be considered. Alongside the manufacturer's XCT guidelines, the ISO 15708-2:2019[8] descriptive table can be used as a starting point. The latter links the approximate adequate voltages, screen scintillators, and filtration values to different materials. The materials, however, are described as pure elements, which makes it hard to choose the ideal parameter for an alloy composed of a combination of different elements.

Another approach is to use simulation techniques and software such as aRTist (BAM, Germany) to estimate or optimize the scan quality. Usually, based on the attenuation law for the primary radiation and Monte Carlo models for scattered radiation,[9] different part positions and scan parameters can be simulated to effectively reduce beam hardening and ring artifacts and to increase scan quality.[10–12] However, this method is only feasible if the part outer, internal features, and material with its element percentages are known prior to scanning.

A semiempirical approach has also been suggested in the literature. Called a knowledge-based system (KBS), the method assists in choosing the XCT settings of a part aided by the use of available knowledge of the XCT device to be used and previously scanned parts of a similar shape. The aforementioned paper also showed that the method provided more accurate results compared to relying on user experience only.[7] Another solution is, of course, user experience. Experienced users yield more accurate results.[7]

EVALUATING 2D IMAGE QUALITY OF XCT PROJECTIONS OR RECONSTRUCTIONS

Using 2D image quality to discern the scan quality has been used numerous times in the literature. The contrast-to-noise ratio (CNR) equation is a common tool in this field.[9,10,13] The two parameters in the CNR equation (1) are μ_{1-2}, mean gray value, and σ_{1-2}, standard deviation of both the part and the background values extracted locally from the image, as used in the medical field[14] or when using a scanning electron microscope (SEM).[15] An experienced user is often needed to avoid choosing a region of interest (ROI) with a local artifact leading to it not representing the quality of the whole image. To minimize the user input error when choosing an ROI, the CNR equation parameters can be extracted directly from the histogram peaks of a reconstructed 2D image.[16]

$$CNR = \frac{Contrast}{Noise} = \frac{|\mu_1 - \mu_2|}{\sqrt{\sigma_1^2 + \sigma_2^2}} \tag{1}$$

CNR and signal to noise ratio (SNR) alongside other 2D image quality quantifiers have been used to analyze the effect of different XCT settings on each image quality parameter.[17] The research showed that the image quality parameters correlated with XCT scanning settings, but the accuracy was not enough to rank the ideal XCT settings purely from evaluating the 2D image projections.

The method proposed in this paper not only assists the user in choosing from a range of XCT settings based on the image quality of the projections (prior to reconstruction) but also represents a crucial step closer to a closed-loop XCT, where the settings are automatically chosen, by comparing a range of XCT settings and choosing the ideal one, in an optimized procedure.

Methodology

INTRODUCTION

The proposed protocol, as shown in figure 1, starts by taking 2D XCT images of the part at different settings; CNR is then calculated for each one using nonreconstructed 2D XCT images. The setting with the highest CNR is considered the ideal XCT setting.

To validate the proposed protocol, the obtained results were compared to the conventional protocol where 3D XCT reconstructed scans of a dimensional workpiece (previously measured using a coordinate-measuring machine [CMM]) and the lattice are taken at the same time with different settings. The 3D reconstructed and thresholded volume XCT scans are then analyzed, and the one with the least difference from the CMM measurement is considered the ideal one.

THE DIMENSIONAL WORKPIECE

The dimensional workpiece (fig. 2) was computer numerical control (CNC) machined from aluminum bar stock to produce a consistent gray value during XCT scans and

FIG. 1 Suggested and conventional protocol used to compare four XCT setting combinations to find the one with the least error. Total time is calculated if each of the four scans is only done once.

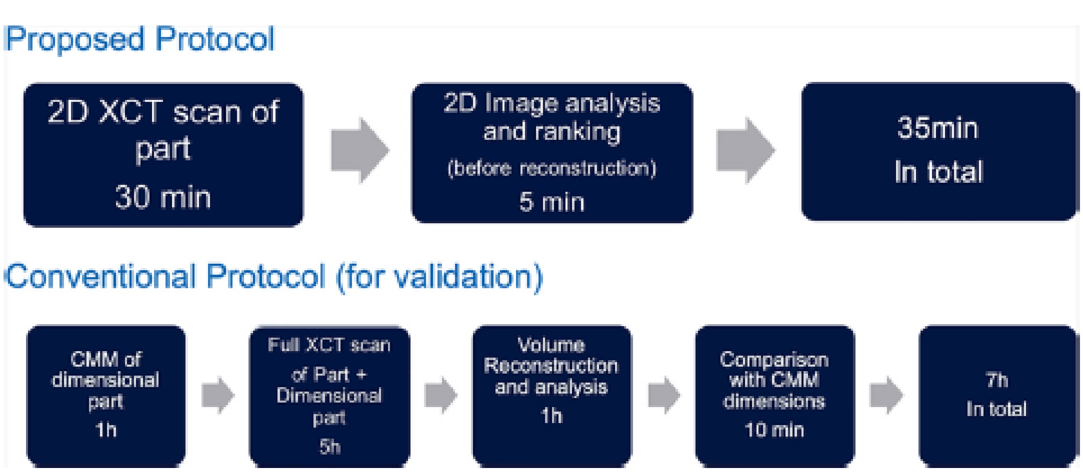

FIG. 2 (*A*) The dimensional workpiece dimensions (in mm) used in the experiment. (*B*) Manufactured dimensional workpiece with pencil tip.[19]

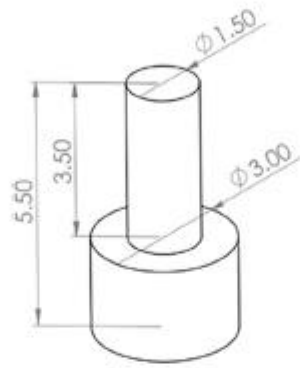

(*A*)

(*B*)

to have less chance of porosity. The part has a 1.5-mm outer diameter (OD), the same as the lattice truss diameter, with the aim of achieving almost the same gray value when XCT scanning both parts. This allows an edge detection that is consistent for both parts. Designing and scanning a dimensional workpiece from the same material as the main scanned part (in this case, the lattice structure) is a common method used in the literature, especially for XCT porosity measurements.[18]

The CMM, a Zeiss Prismo Access, was used to measure the OD. The CMM measured mean OD after five repeat measurements was 1.5117 mm (0.0001 mm standard deviation). To determine the OD, as shown in figure 3, four circles were measured (five times each) to then extract the cylinder they formed.

FIG. 3 Measurement strategy for CMM to extract the outer cylinder diameter (OD).

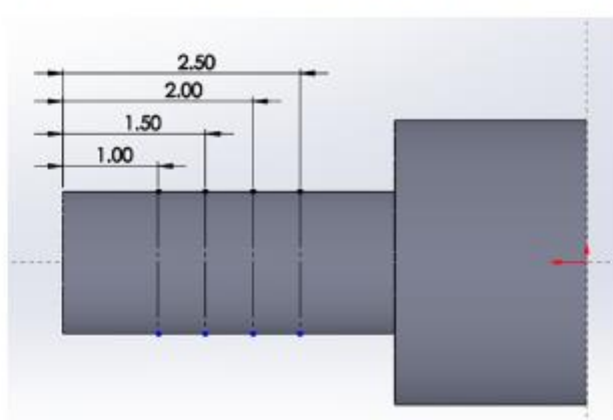

LATTICE STRUCTURE AND FIXTURING

The cube vertex centroid lattice structure, as shown in figure 4, was designed in Ntop (Ntopology, New York) with a dimension of 15 by 15 by 25 mm and a truss diameter of 1.5 mm. The lattice was additive manufactured using an EOS M290 in AlSi10Mg material (fig. 4*B*).

The lattice structure and the dimensional workpiece, as seen in figure 5, were held using an additive manufactured polyactide (PLA) plastic fixture using a fused

FIG. 4 (*A*) Rendering and (*B*) additive manufactured lattice structure with 15-by-15-by-25-mm box dimension and 1.5-mm truss diameter.

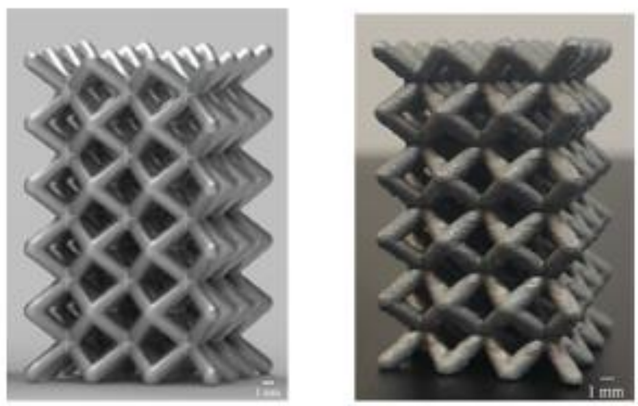

(*A*) (*B*)

FIG. 5 (*A*) The FDM 3D-printed holder used to grip both the lattice and dimensional workpiece. (*B*) Rendering of the fixed position.

(*A*) (*B*) 252

deposition modeling (FDM) process. The fixture minimized the movement of the part without being in direct contact with the measured features, allowing for better surface determination.

XCT MEASUREMENT PROTOCOL

The XCT machine used was a Nikon XT H 225 (Nikon Metrology), and the different XCT settings used in this study are shown in table 1.

The voxel size, exposure time, and number of projections were fixed to 0.023 mm, 2,829 ms, and 1,583 projections, respectively, with no filter. Each setting combination was done three times. This resulted in a total of 12 scans that were all performed in a random order. The magnification was fixed in order to avoid the need to scale the ROIs analyzed. More settings will be simultaneously changed in future research, especially exposure time and number of projections, two factors usually decisive in scan times.

2D XCT MEASUREMENTS

Using the Nikon XT H 225, three 2D XCT projections (after shading correction) were taken of each XCT setting combination mentioned in table 1. The analysis of the 2D projections was done using Fiji software.* The projection images used were 16-bit TIFF images, each with a size of 1008 by 1008 pixels. The gray value of each pixel ranged from 0 to 65,536.

The CNR equation used is from ISO 15708-3:2019.[20] The higher the CNR, the higher the image quality. In this case, and as seen in equation (2), an absolute value is calculated between the mean gray value of the part and mean gray value of the background and is divided by the noise of the background. The goal is to have an image with a high gray value difference between the part and the background but with a small noise value.

$$CNR = \frac{|\mu_f - \mu_b|}{\sigma_b} \tag{2}$$

To extract these values from the 2D nonreconstructed XCT projection image, four different ROIs were defined, as shown in figure 6:

TABLE 1 Setting combinations used in the study

Setting Combinations	Voltage (kV)	Power (W)
100_6 (3 meas.)	100	6
120_7 (3 meas.)	120	7
140_8 (3 meas.)	140	8
160_9 (3 meas.)	160	9

*Fiji (ImageJ 2.0), https://web.archive.org/web/20200729223035/https://fiji.sc/

FIG. 6 Regions of interest used in CNR formula shown in two different 2D projections: (A) one for dimensional and (B) one for lattice structure.

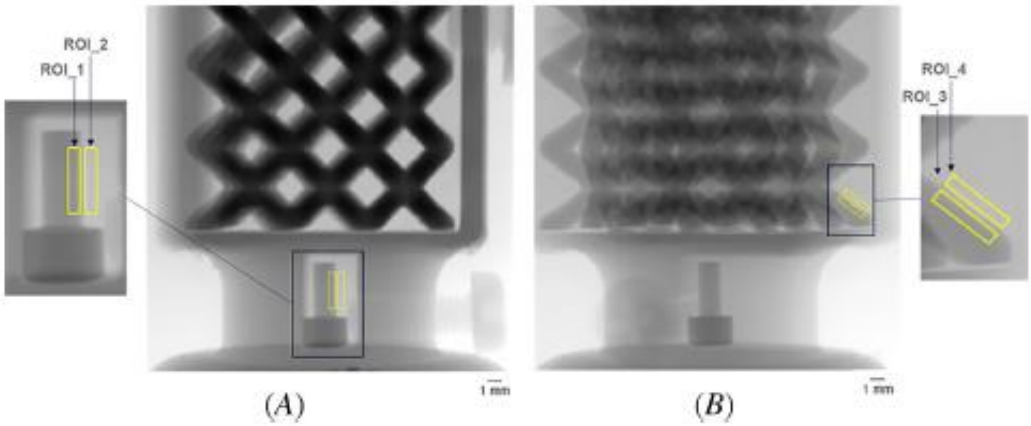

- **ROI_1 and ROI_3**: Used to extract the local mean gray value (μ_f) of the workpiece (ROI_1) and of the lattice part (ROI_3).
- **ROI_2 and ROI_4**: Used to extract both the local gray value of the background (μ_b) and the noise of the background (σ_b) for the workpiece (ROI_2) or the lattice (ROI_4).

As mentioned previously, the dimensional workpiece diameter and material were chosen to have almost the same gray value of the lattice strut. To limit the impact of the chosen projection on the gray value, it was made sure that the chosen projection angle for the lattice did not have superimposed struts (making the pixels darker). The chosen projection isolated the strut so that its gray value was closer to the dimensional workpiece.

The individual effects of different XCT parameters on the 2D projection image quality has not been discussed in this study and has been previously addressed.[21] This study does not individually look at the cause and effect of each parameter and their influence on the CT scan; the purpose was to rather assess if there is a strong correlation between the 2D image quality (before reconstruction) using CNR and CT settings (voltage and power, in this case) to assist in swiftly selecting parameters before each scan.

The proposed method is semiautomated in the sense that the user chooses the XCT parameters to be compared and defines the 2D image ROIs, while the XCT scanning and CNR extraction are done as a batch. The batch process was done using Inspect-X software (Nikon Metrology) for automating XCT scans and Fiji software for automating the extraction of CNR from 2D images.

3D VOLUME XCT SCANS AND ANALYSIS

Using Nikon XT H 225, three 3D volume XCT scans were taken of each XCT setting combination mentioned in table 1. Reconstruction was performed using

Nikon XCT Pro 3D (Nikon Metrology), and no beam hardening or noise reduction algorithm was applied during the reconstruction. Since the XCT machine used is not a metrology one, and to reduce reproducibility errors, the manipulator and the part were not moved during measurements and all 12 XCT scans were done as a batch. For surface determination, local iterative surface determination was chosen using VGSTUDIO MAX3.1 (Volume Graphics, Heidelberg, Germany). This type of surface determination delivers the most accurate results during reconstruction.[22] A global surface determination was also applied, and both methods were compared.

Results

2D XCT PROJECTION ANALYSIS

Using equation (2) on the ROIs described in figure 6, the CNR of each 2D projection for each setting was determined. Because three 2D projections were taken per XCT setting, table 2 shows the average CNR value as well as the standard deviation. It can be seen from table 2 that the setting with 160 kV and 9 W had the highest CNR for both the dimensional workpiece and the lattice. The raw data used to calculate CNR can be seen in table A.1 and table A.2 in the Appendix.

3D XCT SCAN RESULTS AND MEASUREMENTS USED FOR VALIDATION

To verify the results of the 2D XCT projection analysis, the extracted OD from 3D volume analysis was compared to the CMM measured OD. The calculated difference (using two types of surface determinations) for each XCT setting combination can be seen in figure 7. Because each setting was taken three times, the standard deviation intervals are also plotted, showing the repeatability of the method. The standard deviation of all settings was 0.0001 mm except in automatic surface determination where two settings (100_6 and 120_7) have a standard deviation of 0.0003 mm and 0.0005 mm. Based on the results in figure 7, the XCT setting combination of 160 kV and 9 W has the smallest error—in this case, meaning the least difference from CMM measurement.

It can also be seen from figure 7 that the mean difference value to the CMM using automatic global surface determination was higher compared to using local

TABLE 2 Average CNR value per XCT setting for dimensional workpiece (left) and lattice (right)

XCT Settings	Dimensional Workpiece CNR [Std. Dev.] (Gray Value)	Lattice CNR [Std. Dev.] (Gray Value)
100_6 (3 meas.)	16.3 [0.3]	19.3 [0.5]
120_7 (3 meas.)	16.3 [0.6]	18.4 [0.6]
140_8 (3 meas.)	20.2 [0.9]	19.5 [1.2]
160_9 (3 meas.)	21.6 [0.2]	20.1 [0.2]

FIG. 7 Mean OD difference between XCT volume data and CMM data with standard deviation.

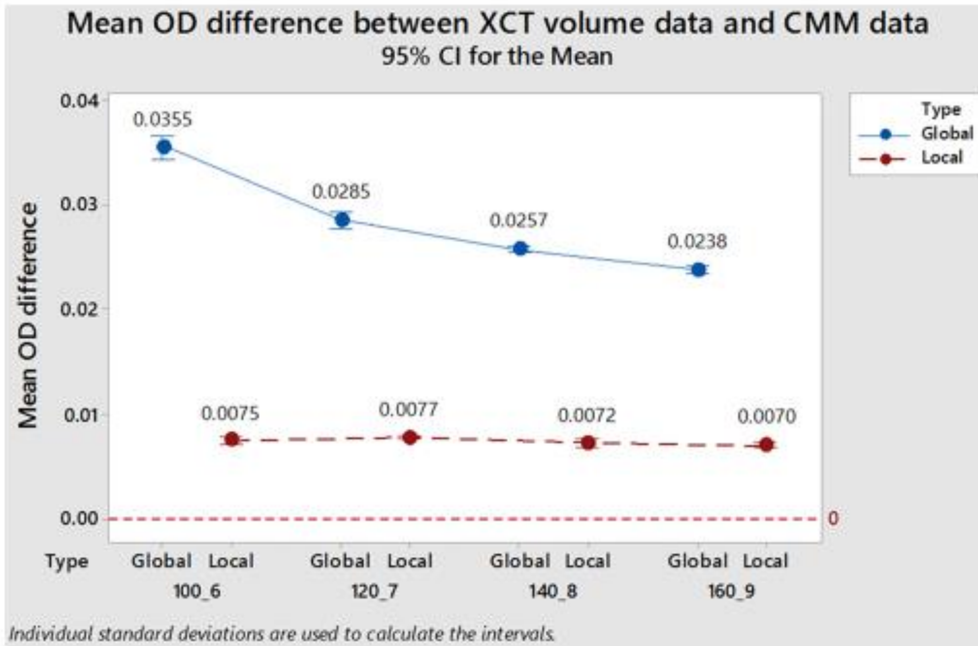

iterative surface determination, which was expected and conforms to previous findings published in the literature.[22]

Discussion

Based on the aforementioned results, the XCT setting combination determined by the 2D projection analysis (table 2) matches the XCT setting combination determined using the 3D volume analysis with both surface determinations (fig. 2). This proves a high correlation between the 2D projections' image quality (prior to reconstruction) and the reconstructed 3D volume quality. These results also prove that before a XCT scan, comparing the local CNR of one 2D projection (prior to reconstruction) of each XCT setting combination (voltage and power in this case) can assist in finding the ideal XCT scan setting.

The X-ray voltage affects the contrast between low density materials and the background noise level.[23]

As expected, the ideal setting was the one with the highest power (W). Higher power leads to the broadening of the histogram peaks, leading to more contrast in the 2D projections, an easier edge detection, and smaller surface determination error after reconstruction and thresholding. However, measuring the contrast alone can be misleading because the noise can induce artificial high differences between pixels, hence the importance of using the CNR equation because it takes the noise value into consideration.

To minimize noise, one of the user guidelines from ISO 15708-2:2019 is to have a minimal X-ray transmission of 10%.[8] Minimal X-ray transmission is calculated by comparing the screen gray value when the X-ray is off with the scanned part's lowest gray value.

While the suggested protocol assists in comparing different XCT settings and deciphering the ideal one, it does not suggest which XCT settings should initially be considered for comparison. This means that when getting a new part, it is expected that the user selects the range of XCT setting combinations needed. The number and selected values for these combinations will depend on the user's experience as well as on the maximum allowed time, cost of the experiment, and allowable error.

Due to the XCT repeatability error when scanning after long intervals[5] (impacted by filament life and other factors), it is expected, when using this protocol, that the XCT scan is performed shortly after performing the suggested protocol.

As seen in figure 1 and in this study, the XCT scanning and 3D volume comparison of four XCT scans (if each scan is only done once) took around 7 h. Alternatively, the time needed for the 2D projection analysis (prior to reconstruction) of four XCT scans took only 35 min.

While a low standard deviation was achieved when analyzing three samples of each scan (in both 3D volume and 2D analysis), the verification method relied solely on the difference between the CMM measured OD and the XCT 3D volume extracted OD. This means that the CNR method produces accurate results when the goal is to have XCT scans with the least dimensional measurement error.

Conclusion

This paper presents and verifies a new protocol for evaluating XCT setting combinations in order to find the optimum voltage (kV) and power (W) (prior to reconstruction). While the results were expected, this study proved the high correlation between the 2D nonreconstructed image CNR and reconstructed 3D volume. While an experienced user can choose better XCT settings than a nonexperienced one, the suggested protocol of batch scanning and batch analyzing 2D projections prior to reconstruction can be used on a range of settings set by the experienced user, taking advantage of the user's experience, saving even more time, and increasing the machine accuracy while limiting user input and error.

This paper compared setting combinations in which only two XCT parameters were altered in the combinations. More parameters need to be considered in the future alongside their impact on the CNR equation. It is expected, for example, that if the magnification is changed, the ROI needs to be scaled accordingly as well. The protocol also does not take in consideration artifacts that can only be visible after reconstruction (e.g., beam hardening, ring artifacts, and so on). The proposed protocol needs to be assessed for other scenarios such as having minimal error when calculating porosity or extracting areal surface roughness. Implementing this protocol will provide a closer step to a semiautomated and, ideally in the future, a fully automated XCT setup process, limited in terms of user input and error, with a high accuracy and minimal noise.

ACKNOWLEDGEMENTS

The authors gratefully acknowledge the UK's Engineering and Physical Sciences Research Council (EPSRC) funding of the Future Metrology Hub (Grant Ref: EP/P006930/1). This work was performed under the auspices of the U.S. Department of Energy by Lawrence Livermore National Laboratory under Contract DE-AC52-07NA27344. LLNL Document number LLNL-BOOK-811638. The authors also gratefully acknowledge Ntopology for providing the license of Ntop.

Appendix

TABLE A.1 Dimensional workpiece ROI_1, ROI_2, and CNR raw data

XCT Setting	Mean Part (ROI_1)	Mean Back Part (ROI_2)	St. Dev. Back Part (ROI_2)	CNR Part
100_6	43546.8	52576.1	563.7	16.0
100_6	43520.3	52554.0	545.6	16.6
100_6	43552.6	52504.1	545.7	16.4
120_7	45313.6	52885.2	471.2	16.1
120_7	45253.0	52740.0	439.0	17.1
120_7	45300.3	52876.1	478.2	15.8
140_8	45614.6	51854.9	311.8	20.0
140_8	45481.7	51757.6	297.2	21.1
140_8	45572.2	51801.6	320.8	19.4
160_9	46099.1	51782.4	264.0	21.5
160_9	45762.6	51383.4	263.3	21.3
160_9	46172.9	51893.1	262.6	21.8

TABLE A.2 Lattice ROI_3, ROI_4, and CNR raw data

XCT Setting	Mean Lattice (ROI_3)	Mean Lattice Background (ROI_4)	Std. Dev. (Lattice Back) ROI_4	CNR
100_6	42178.6	50507.6	422.8	19.7
100_6	42216.6	50540.3	426.7	19.5
100_6	42277.7	50512.3	439.8	18.7
120_7	44206.5	51245.8	369.5	19.1
120_7	44213.8	51212.3	381.7	18.3
120_7	44278.0	51272.1	391.2	17.9
140_8	44947.3	50853.2	292.1	20.2
140_8	44890.1	50901.3	298.6	20.1
140_8	45119.4	51016.3	327.4	18.0
160_9	45880.2	51410.8	277.6	19.9
160_9	46119.5	51633.9	271.4	20.3
160_9	47880.0	53590.3	285.1	20.0

References

1. T. Maconachie, M. Leary, B. Lozanovski, X. Zhang, M. Qian, O. Faruque, and M. Brandt, "SLM Lattice Structures: Properties, Performance, Applications and Challenges, *Materials & Design* 183 (2019): 1–18.
2. E. Alabort, D. Barba, and R. C. Reed, "Design of Metallic Bone by Additive Manufacturing," *Scripta Materialia* 164 (2019): 110–114.
3. M. Bici, S. Brischetto, F. Campana, C. G. Ferro, C. Secli, S. Varetti, P. Maggiore, and A. Mazza, "Development of a Multifunctional Panel for Aerospace Use through SLM Additive Manufacturing," *Procedia CIRP* 67 (2018): 215–220.
4. H. Zhou, X. Zhang, H. Zeng, H. Yang, H. Lei, X. Li, and Y. Wang, "Lightweight Structure of a Phase-Change Thermal Controller Based on Lattice Cells Manufactured by SLM," *Chinese Journal of Aeronautics* 32 (2019): 1727–1732.
5. J. P. Kruth, M. Bartscher, S. Carmignato, R. Schmitt, L. De Chiffre, and A. Weckenmann, "Computed Tomography for Dimensional Metrology," *CIRP Annals* 60 (2011): 821–842.
6. S. Carmignato, A. Pierobon, and E. Savio, "First International Intercomparison of Computed Tomography Systems for Dimensional Metrology," in *Proceedings of the Eleventh International Conference of the European Society for Precision Engineering and Nanotechnology, EUSPEN 2011*, ed. H. Spaan (Bedfordshire, UK: EUSPEN, 2011), 84–87.
7. R. Schmitt, C. Isenberg, and C. Niggemann, "Knowledge-Based System to Improve Dimensional CT Measurements," in *Proceedings of the Fourth Conference on Industrial Computed Tomography*, (Düren, Germany: Shaker Verlag GmbH, 2012), 363–372.
8. *Non-Destructive Testing. Radiation Methods for Computed Tomography. Principles, Equipment and Samples*, BS EN ISO 15708-2:2019 (London: British Standards Institution, 2019).
9. G.-R. Jaenisch, C. Bellon, and U. Samadurau, "McRay—A Monte Carlo Model Coupled to CAD for Radiation Techniques," in *Proceedings of the 9th European Conference on Non-Destructive Testing ECNDT* (Berlin, Germany: ECNDT, 2006), 1–8.

10. U. Hilpert, M. Bartscher, M. Neugebauer, J. Goebbels, G. Weidemann, and C. Bellon, "Simulation-Aided Computed Tomography (CT) for Dimensional Measurements" (paper presentation, International Symposium on Digital Industrial Radiology and Computed Tomography, Lyon, France, June 25–27, 2007).
11. J. Tabary, "Sindbad—A Realistic Multi-Purpose and Scalable X-Ray Simulation Tool for NDT Applications" (paper presentation, International Symposium on Digital Industrial Radiology and Computed Tomography, Lyon, France, June 25–27, 2007).
12. M. Reiter, B. Harrer, C. Heinzl, D. Salaberger, C. Gusenbauer, C. Kuhn, and J. Kastner, "Simulation Aided Study for Optimising Industrial X-Ray CT Scan Parameters for Non-Destructive Testing and Materials Characterisation" (poster, International Symposium on Digital Industrial Radiology and Computed Tomography, Berlin, Germany, June 20–22, 2011).
13. A. du Plessis, M. Tshibalanganda, and S. G. le Roux, "Not All Scans Are Equal: X-Ray Tomography Image Quality Evaluation," *Materials Today Communications* 22 (2020): 1–10.
14. B. Bechara, C. A. McMahan, W. S. Moore, M. Noujeim, H. Geha, and F. B. Teixeira, "Contrast-to-Noise Ratio Difference in Small Field of View Cone Beam Computed Tomography Machines," *Journal of Oral Science* 54 (2012): 227–232.
15. F. Timischl, "The Contrast-To-Noise Ratio for Image Quality Evaluation in Scanning Electron Microscopy," *The Journal of Scanning Microscopies* 37 (2015): 54–62.
16. M. Reiter, D. Weiss, C. Gusenbauer, M. Erler, C. Kuhn, S. Kasperl, and J. Kastner, "Evaluation of a Histogram-Based Image Quality Measure for X-Ray Computed Tomography" (paper presentation, Fifth Conference on Industrial Computed Tomography, Wels, Austria, February 25–28, 2014).
17. A. Kraemer, E. Kovacheva, and G. Lanza, "Projection Based Evaluation of CT Image Quality in Dimensional Metrology" (paper presentation, International Symposium on Digital Industrial Radiology and Computed Tomography, Lyon, France, June 25–27, 2007).
18. P. Hermanek, F. Zanini, and S. Carmignato, "Traceable Porosity Measurements in Industrial Components Using X-Ray Computed Tomography," *Journal of Manufacturing Science and Engineering* 141 (2019): 1–8.
19. A. Townsend, R. Racasan, R. Leach, N. Senin, A. Thompson, A. Ramsey, D. Bate, P. Woolliams, S. Brown, and L. Blunt, "An Interlaboratory Comparison of X-Ray Computed Tomography Measurement for Texture and Dimensional Characterisation of Additively Manufactured Parts," *Additive Manufacturing* 23 (2018): 422–432.
20. *Non-Destructive Testing. Radiation Methods for Computed Tomography. Operation and Interpretation*, BS EN ISO 15708-3:2019 (London: British Standards Institution, 2019).
21. A. Buratti, N. Grozmani, C. Voigtmann, L. V. Sartori, and R. H. Schmitt, "Determination of the Optimal Imaging Parameters in Industrial Computed Tomography for Dimensional Measurements on Monomaterial Workpieces," *Measurement Science and Technology* 29 (2018): 1–13.
22. A. Townsend, L. Pagani, L. Blunt, P. J. Scott, and X. Jiang, "Factors Affecting the Accuracy of Areal Surface Texture Data Extraction from X-Ray CT," *CIRP Annals* 66 (2017): 547–550.
23. S. Carmignato, W. Dewulf, and R. Leach, *Industrial X-Ray Computed Tomography* (Cham, Switzerland: Springer International, 2018).

12.3. Appendix 3: Additive Manufacturing Journal Paper published in 2020 (Chapter 6)

Additive Manufacturing 37 (2021) 101731

Contents lists available at ScienceDirect

Additive Manufacturing

journal homepage: www.elsevier.com/locate/addma

Research Paper

Parametrically designed surface topography on CAD models of additively manufactured lattice structures for improved design validation

Younes Chahid [a,*], Radu Racasan [a], Luca Pagani [a], Andrew Townsend [b], Alexander Liu [c], Paul Bills [a], Liam Blunt [a]

[a] EPSRC Future Metrology Hub, School of Computing and Engineering, University of Huddersfield, HD1 3DH Huddersfield, UK
[b] Nondestructive Evaluation Group, Nondestructive Characterisation Institute, Lawrence Livermore National Laboratory, Livermore, CA 94550, USA
[c] ASTM International, Singapore

ARTICLE INFO

Keywords:
Metrology
Lattice structures
Surface topography
Computer aided design (CAD)
X-ray computed tomography
Defect modelling

ABSTRACT

Additively Manufactured (AM) lattice structures of the laser powder bed fusion (LPBF) process generally have different surface geometries depending on the overhang angle and location. This means that the design validation stage is often challenging, considering it is based on an ideal Computer Aided Design (CAD) model that is not truly representative, since the AM part will be different in terms of dimensional accuracy and surface finish. Previous studies have relied on the design of surface textures that are independent of the overhang angle, or techniques based on directly using X-ray Computed Tomography (XCT) data. In this paper, a new technique for designing surface texture on the CAD of lattices has been investigated and correlated with areal surface roughness parameters. After extracting areal surface parameters from the XCT data of the lattice, the method allowed for the design of this surface texture on the part CAD taking in consideration if its up skin or down skin, without using XCT data as the main input. By applying this method, it is possible to obtain a lattice CAD model with a designed surface texture and geometry that is more representative of the actual AM lattice. The mean deviation between the CAD model with the designed surface and the XCT was a third of the one between the XCT and the initial CAD. The proposed method allows for designing and replicating LPBF AM surfaces on the CAD of a lattice, taking into consideration the dimensional deviation caused by AM surfaces, especially on overhangs. Assuming that an LPBF AM process is stable and produces approximately the same AM surface, this method can be used to predict the geometry of a lattice, providing a cost-effective and efficient methodology that minimizes the time needed for design validation.

1. Introduction

Additive manufacturing (AM) has allowed the production of custom cellular solids [1] of increased complexity and functionality. These 3D cellular solids are usually categorized as either strut-based lattices or Triply Periodic Minimal Surfaces (TPMS) like Gyroid structures, which can be used in engineering applications such as those that require high absorption of mechanical energy or heat transfer [2]. As an illustrative example, cellular solids when optimized appropriately can also be used in medical implants to reduce stress shielding effects and increase osseointegration [3,4].

The manufacturing of cellular solids using laser powder bed fusion LPBF AM process can sometimes be prone to defects usually attributed to various sources [5] and in the case of (LPBF) process, up to 130 variables have been shown to affect the print quality [2]. These defects can be described as undesired dimensional deviation, surface roughness or pores affecting the part quality. Variables such as the scanning speed, layer thickness or more, especially laser power [6], affect the melt pool size. Also, powder particles that are in contact with the overhangs but outside of the melt pool still get heated and sintered to the down skin of the struts leading to a dross formation which increases surface roughness and decreases dimensional accuracy [7,8].

During the LPBF process of strut based lattices, the relative density (density percentage when compared to nominal CAD) of the manufactured lattice would usually be bigger than the CAD by between 20% and 30% [2]. This difference can be attributed to the over melting of the powder in horizontal struts that are supported at two ends as seen in Fig. 1, this is especially the case on the down skin side of the strut. In

* Corresponding author.
E-mail address: Younes.chahid@hud.ac.uk (Y. Chahid).

https://doi.org/10.1016/j.addma.2020.101731
Received 19 June 2020; Received in revised form 1 November 2020; Accepted 22 November 2020
Available online 27 November 2020

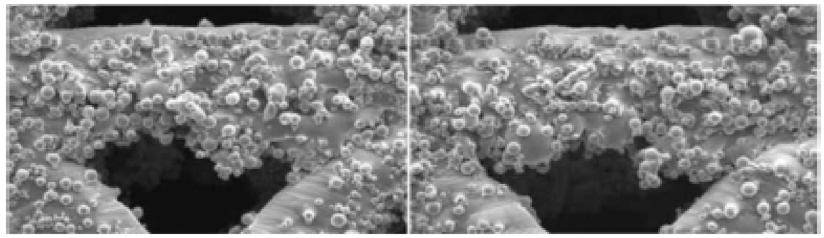

Fig. 1. Lattice strut of Ti6Al4V showing the horizontal defects like down skin oversizing and un-melted powder on a 2 mm cell size [2].

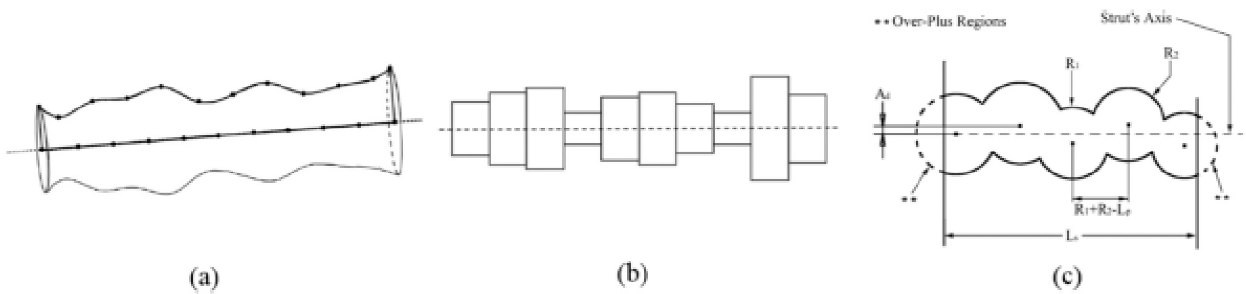

Fig. 2. Example of methods used to generate varying strut diameter and surface texture defects [23–25].

parallel to this, vertical struts tend to be undersized [5].

Beside vertical struts and horizontal bridges (struts supported in two ends), angles from 35° degrees to 90° degrees from horizontal can also be additively manufactured [9,10]. However, the additive manufacture of these angles produces the "staircase effect" [11], in both the up skin and down skin side of the strut, significantly reducing the dimensional accuracy and surface finish quality of the manufactured lattice when compared to the CAD. This often results in a negative impact on the cellular solid mechanical properties [10–12] making the design validation stage very challenging. Overhang surface roughness not only impacts lattices structures but also internal geometries and channels, affecting the expected fluid flow or heat transfer [12]. Consequently, there is a clear need for methods that allows for the design of LPBF AM surface finish and its superposition onto CAD designs as part of the complete design process. Surface texture is defined as the scale-limited surface obtained after series of operations on the primary surface [13,14]. Measuring surfaces is usually done either using profile [15] or areal parameters [13] with the latter being better at the describing the three dimensional nature of surface topographies and complex AM surfaces.

To reduce the deviation of the AM part from the original (CAD), a compensation method can be developed. Compensation strategies can be divided to three categories: *(i)* A design compensation phase facilitated by altering the strut diameter depending on its angle [16], *(ii)* AM process setting optimization [17,18] or, *(iii)* using a chemical post-processing phase to smooth the surface, by controlling chemical etching solution concentration and time [19–21]. These three approaches can assist in producing a more predictable cellular solid design dimension and surface finish. However, to develop suitable benchmarking methods for AM produced parts, it is important to understand the impact of these defects on the function and structural integrity. This requires the development of cost-effective tools that incorporate the expected dimensional deviation and surface finish during the design validation stage. Unfortunately at present these tools do not fully exist [22]. Several tools have been suggested that incorporate AM dimensional deviation or surface finish in the design phase and these are reviewed in the following sections.

1.1. Design of defects on the CAD of an AM lattice structure

Several methods reported in the literature allow for the continuous alteration of the strut diameter of a lattice, making the CAD more representative of the as-manufactured AM lattice. These methods include, a revolution from a spline of *n* points (Fig. 2a), beam elements with various cross section (Fig. 2b) or a Boolean of *N* number of spheres (Fig. 2c) [23–25]. Inclusion of dimensional inaccuracies can be done using a stochastic modelling approach which can increase finite element (FE) model accuracy [22,24,26].

The methods above focus on varying the strut diameter or centroid of the strut along its axis without varying the cross-sectional shape. Alternatively, historical XCT data can be used to extract the lattice strut cross sectional shape and this can then be inputted in the CAD, allowing for not only a variable strut diameter but also a variable cross section [22].

However, the cited methods did not investigate the areal surface roughness of the resulting CAD or its dimensional deviation to the actual manufactured AM part. Also, the cited method [22] that allows for the design of a varying strut cross section, depends on using XCT determined surface as the main input.

The presented work of this paper facilitates the design of a varying cross section that can be directly and parametrically applied within the CAD model without using XCT determined surface data, making the process faster and more cost-effective. The resulting CAD model areal surface roughness and dimensional deviation was investigated and then compared with the actual manufactured AM part.

The following summarizes the approach of this paper in the context of previously published work:

- Script to design surface texture on CAD using areal surface parameters: there is currently no method to design surface topography using areal surface parameters. Ntopology, the main software used in this study, is one of the few programs that allows for the design of a surface texture on any CAD geometry, however, using input parameters like amplitude and frequency, of which the relationship to areal surface roughness parameters has not been previously investigated. In this paper, this relationship has been investigated, allowing for the direct input of areal surface parameters when designing a texture on a CAD, assisting greatly in the design validation stage of lattice structures.
- Method to extract up and down skin of a lattice using XCT: most lattice structures have internal features that cannot be reached and

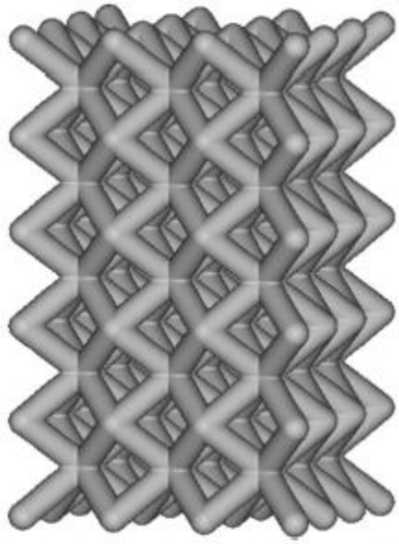

Fig. 3. Rendering of the BCC strut-based lattice structure.

measured without using XCT, especially, if the lattice is totally enclosed, with no exposed struts. The presented method assumes the scenario where no strut is in reach and shows a protocol to extract the areal surface parameters of the up and down skin of an internal lattice strut. The extracted surface roughness values can be then inputted in the developed Ntopology script to design a similar surface topography on any CAD, assisting in the design validation of the following parts to be produced using the same environment.

- Improving the design stage of lattice structures: lattices structures are one of the geometries that take full advantage of AM capabilities. However, the usual small size of the struts, make lattices more sensitive to surface defects, impacting their fatigue resistance [27]. While the surface of parts with simpler geometries and more accessible surfaces can be treated or polished, the same operation on a lattice can be more expensive or nearly impossible (when lattice is enclosed inside, like in the example of an infill). Therefore, a lattice shape was chosen for this study, since the surface of a simpler geometry can be easily treated or manufactured in another method beside AM.

2. Methodology

2.1. Design of the lattice

A Body Centered Cubic (BCC) lattice was designed from a box size of (15×15×25) mm with a cell size of 5 mm and a strut diameter of 1.5 mm. The software used for the design is Ntopology [28]. The BCC lattice is one of the most common lattices due to its printability and the lack of the need for supports (Fig. 3). The 45° angle, however, usually leaves an unwanted surface texture. This undesirable as-built surface texture will be measured and added to the CAD model for the component.

2.2. Additive manufacturing and X-ray CT

The design file of the CAD shown in Fig. 3 was converted to an STL file and additively manufactured using an EOS M290 in AlSi10Mg material. No compensation methods have been applied to the LPBF manufactured lattice structure and standard manufacturer recommended settings for the material were used. The surface texture remained "as manufactured", with no post-processing being applied. Due to the 45° degrees angles of the lattice struts, and as expected from literature, the manufactured lattice (Fig. 4a) exhibited a significant down skin surface texture.

To obtain the volume file of the additive manufactured lattice (Fig. 4b), which will be used to extract surface parameters, an XCT machine (Nikon XT H 225) was used. The XCT scanning parameters were 100 kV acceleration voltage, 90 µA filament current, 1415 ms exposure, 1583 projections and a voxel size of 0.030 mm while using a 1008 × 1008 pixel detector and no filter. The detector pixel pitch is 200 µm. The source to object distance was 149 mm and source to detector 972 mm making the geometric magnification 6.5. The obtained XCT volume file was thresholded using the local iterative technique implemented in VGSTUDIO MAX 3.3 [29], which delivers less errors when compared to the automatic ISO 50 method [30].

Many options are available (focus variation, confocal microscopy and more) to extract areal surface parameters from LPBF AM surfaces

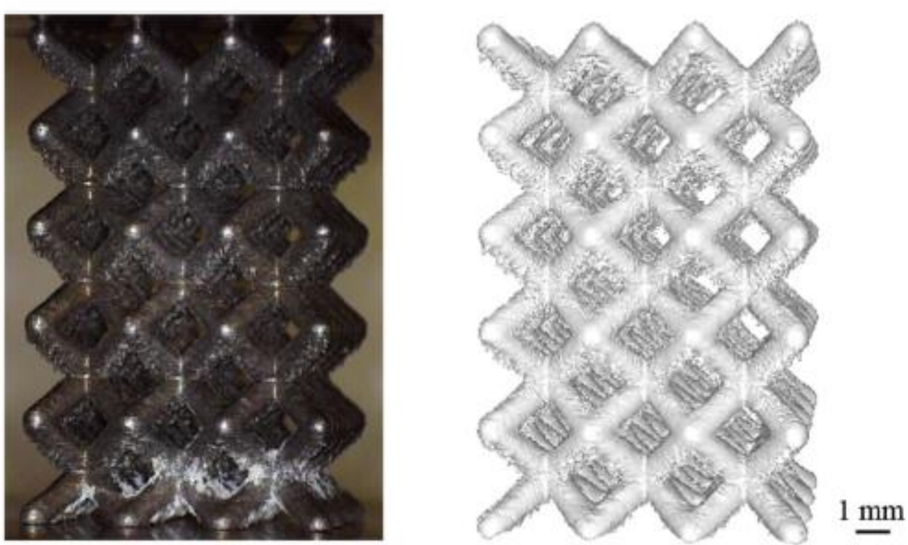

(a) (b)

Fig. 4. Additive manufactured BCC lattice (a) and X-ray CT volume rendering (b).

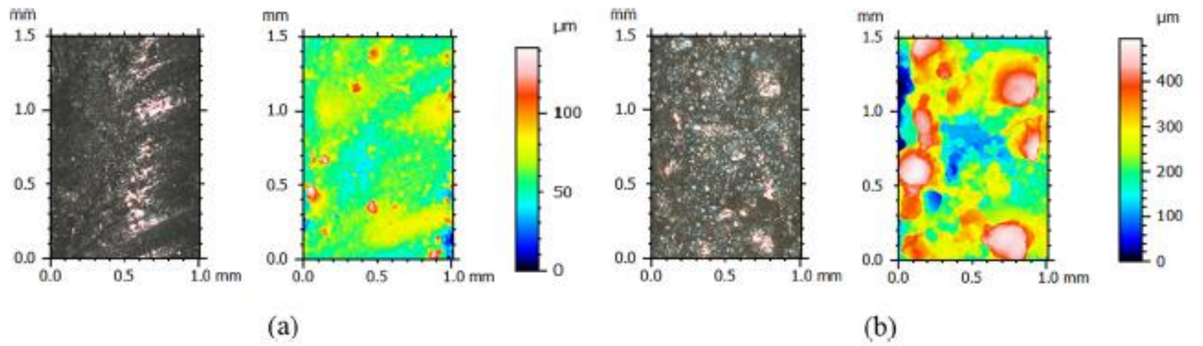

Fig. 5. Focus Variation Alicona G4 measurements of the up skin (a) and down skin of one lattice strut (b) where the left image is the as viewed texture and right image the height map after form removal.

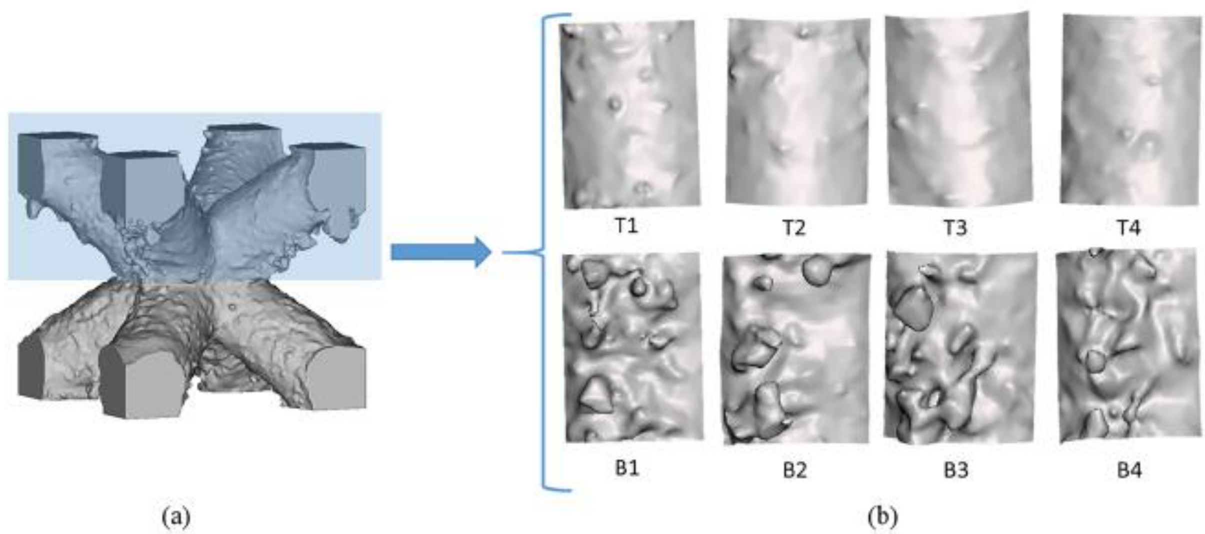

Fig. 6. Extraction of X-ray CT AM lattice surface roughness parameters from four struts resulting in four up skins (T1, T2, T3, T4) and four down skins (B1, B2, B3, B4).

[30]. The reason for using XCT in this paper to extract surface parameters, is the common scenario where the lattice structures are internal and inaccessible, making it impossible to use line-of-sight instrumentation. While not being a conclusive method, and when extracting surface texture parameters from XCT, it is preferable to have a scan voxel size that is one half or less than the expected areal surface roughness (*Sa*) [31]. For this reason, and before extracting surface parameters from XCT, a focus variation measurement (Fig. 5) was completed using an

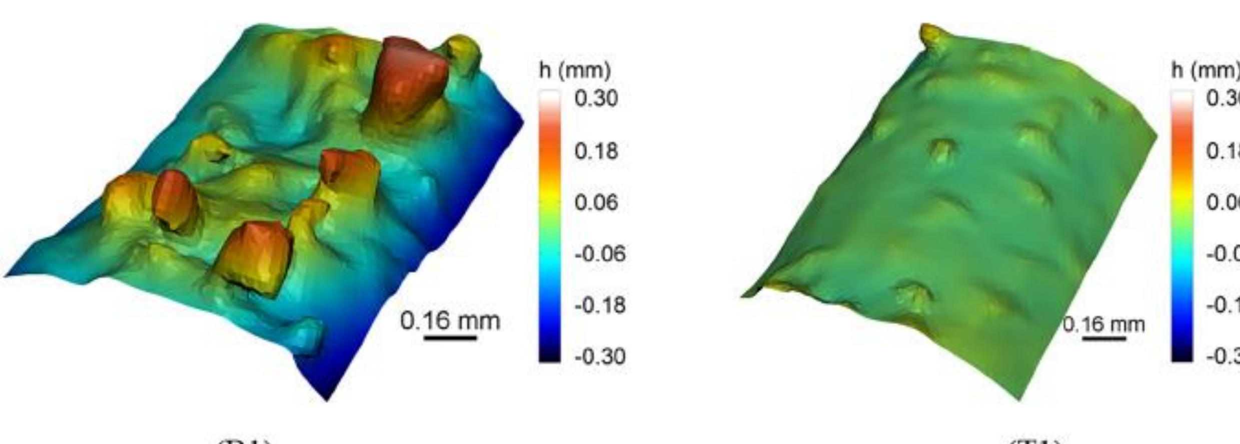

Fig. 7. From the left to the right, a height map example of the down skin surface (obtained from Fig. 7 B1) and of the up skin surface (obtained from Fig. 7 T1). The colour represents the distance between the measured points and the estimated nominal form.

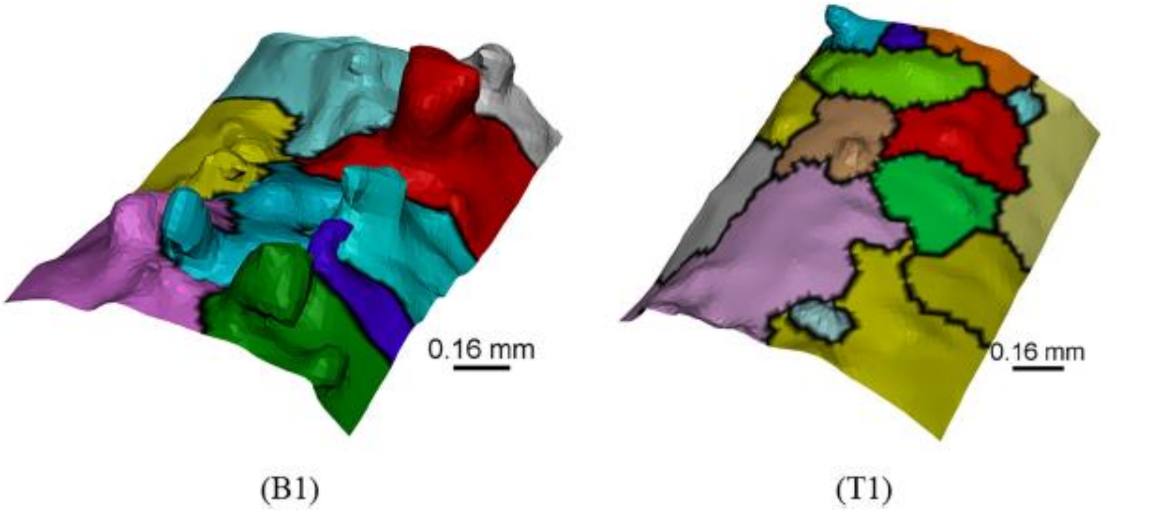

Fig. 8. Watershed segmentation performed on mesh once nominal form is estimated for the Spd parameter.

Alicona G4 on both the up skin and down skin of one externally visible strut using a rectangular region of interest (ROI) of 1.5 mm × 1 mm and a lateral spacing of 1.75 µm, no cut off filter was used. The form of the measured surface was removed using an approximated nominal cylinder (more details in Section 2.3). While the measured Sa of the down skin ($Sa = 0.081$ mm) is more than double the voxel size of the XCT scan (0.030 mm), the Sa of the up skin ($Sa = 0.013$ mm) is significantly lower than the voxel size. Since the down skin surface is considered more significant in affecting the dimensional accuracy of AM prints, making it more important, the voxel size in this study will be deemed sufficient if not ideal. The up skin surface will be nevertheless studied in the next sections of this paper while acknowledging the XCT resolution limitation in the acquired values. While surface features were captured by XCT as clearly seen in Fig. 12a, it is likely to be missing small features due to possible resolution limitations or surface determination. More information about possible discrepancies between XCT and focus variation surface measurement results can be found in [31,32].

2.3. Extracting surface roughness parameters from X-ray CT of AM lattice

To extract surface parameters, the XCT determined surface (Fig. 4b) was exported to a mesh format and one unit cell was isolated using a Boolean operation as seen in (Fig. 6a). Four struts from the isolated unit cell (shaded in Fig. 6a) were measured, resulting in eight regions of

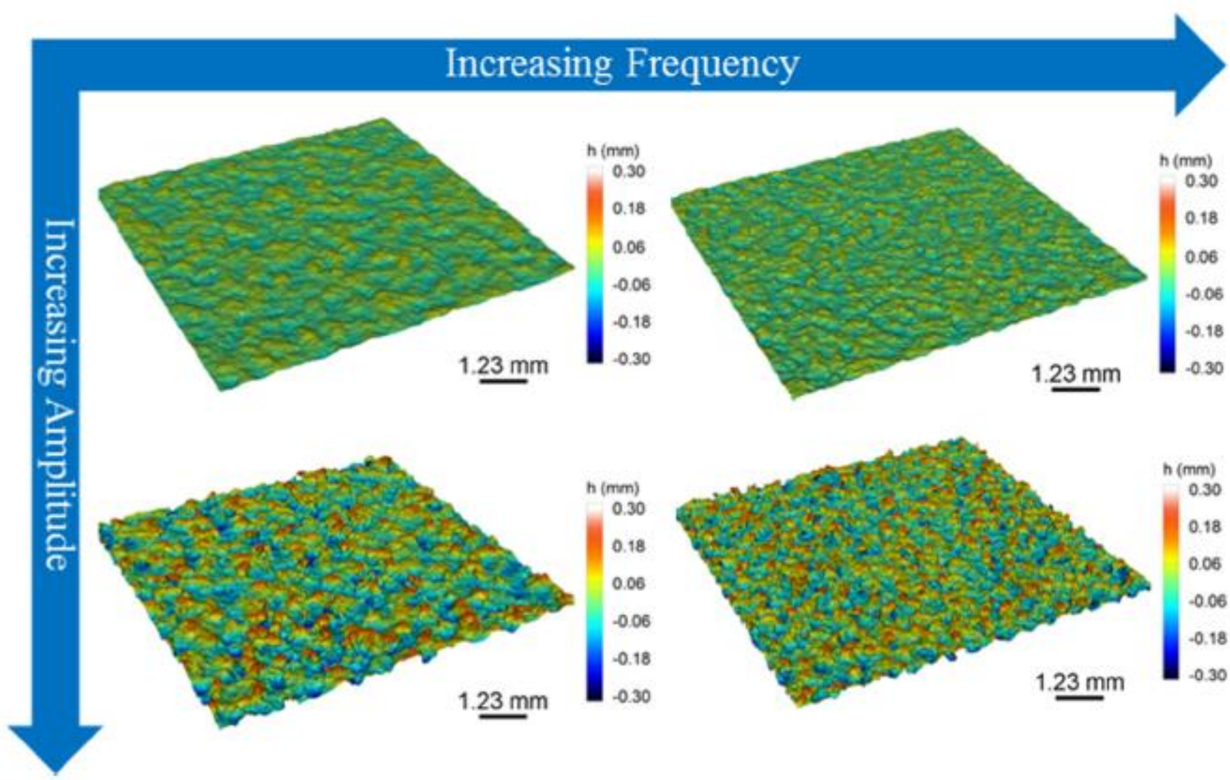

Fig. 9. Example of different surface roughness designs with increasing frequency, amplitude and fixed seed number on a 10 × 10 mm planar surface.

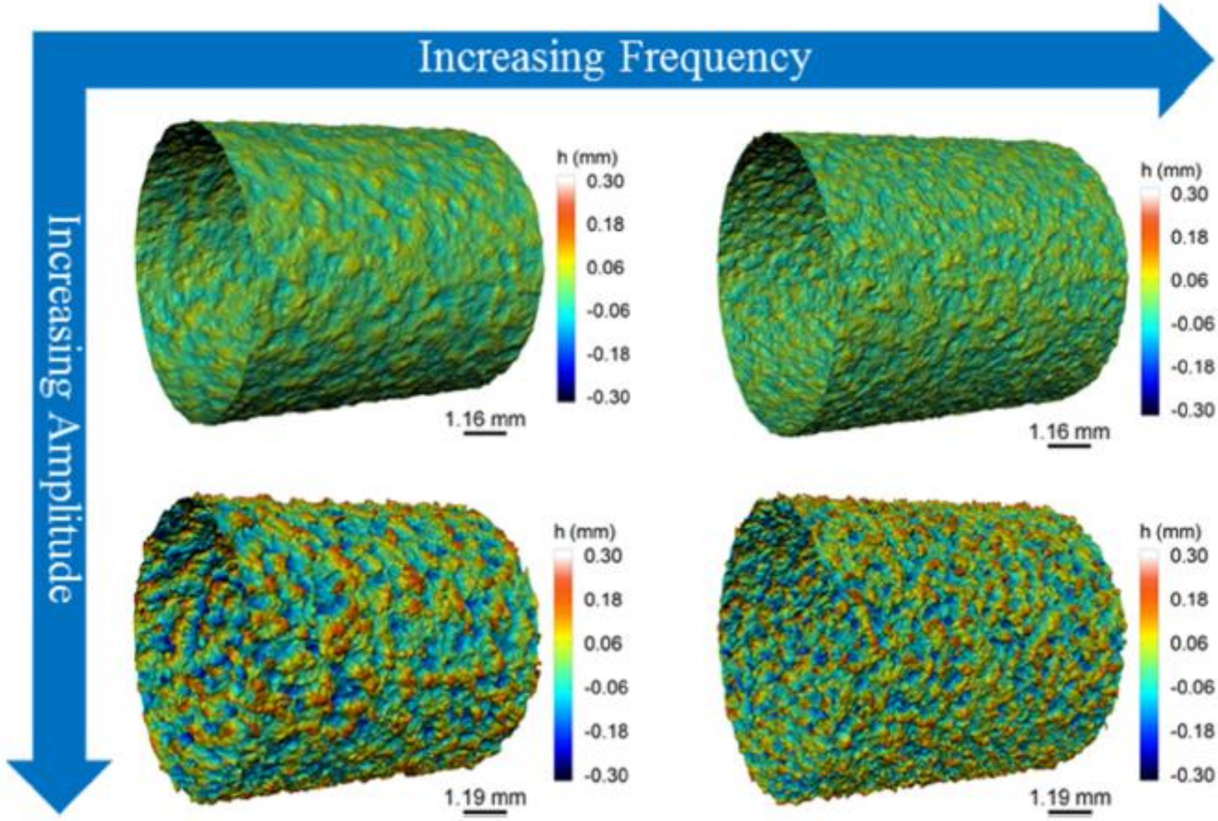

Fig. 10. Example of different surface roughness designs with increasing frequency, amplitude and fixed seed number on a cylindrical surface with a diameter of 8 mm and height of 10 mm.

interests, four up strut skins (T1,T2,T3,T4) and four down strut skins (B1,B2,B3,B4) all shown in Fig. 6b. The size of each of the isolated regions of interest is also 1.5 mm × 1 mm, which was placed at the center and limited by the strut diameter. No significant differences between different locations along the strut was observed. For this study, to avoid shifting the focus to the distribution of surface roughness on a lattice, the four isolated struts shown in blue in Fig. 6 are assumed to represent the surface roughness of the whole lattice (Fig. 4b).

A cylinder was used as nominal form. After estimating the cylinder coefficients using the orthogonal least squares approach, the manifold parameters were then directly computed on the mesh [33] using parameters that are a generalization of ISO 25178. Fig. 7 shows a height map example of the down skin B1 and the up skin T1 isolated above (Fig. 6). The color for the following height maps represents the distance between the measured points and the estimated nominal form.

After removing the form, common surface parameters were extracted such as the average areal surface roughness me (*Sa*) or root mean square surface height (*Sq*). However, and as a result of the performed design of experiment (explained in more detail in section 0), the two main parameters used in this paper to design surface texture are $\hat{a}$ (Eq. (1)) and *Spd* (Eq. (2)) of which the formulas are shown below. $\hat{a}$ is the maximum deviation from the reference geometry, either *Sp* (maximum peak height) or *Sv* (maximum pit height) whichever is the highest. While *Spd*, is the density of the peaks, the area *A* in the *Spd* formula is of the surface form (cylinder) and *#peaks* is the number of the peaks computed after performing the Wolf pruning of the watershed segmentation [13].

$$\hat{a} = max\{Sp, Sv\} \tag{1}$$

$$Spd = \frac{\#peaks}{A} \tag{2}$$

Watershed segmentation can be easily defined on a mesh, once the nominal form is estimated [34] allowing for the *Spd* parameter to be computed. Fig. 8 shows the segmented regions of the down skin B1 and the up skin T1 isolated above (Fig. 6), facilitated by applying a 10% Wolf pruning of the original watershed segmentation. For a formal definition of the parameters the reader can refer to Pagani et al. [33].

2.4. Design of experiment on designing custom surface roughness

The design of a custom surface can be achieved using the "Surface Roughness" tool from Ntopology (software called nTop), which is based on the Simplex Noise algorithm [35]. This tool has three main inputs, frequency, amplitude and seed (used for the pseudorandom number generator). In nTop software, the frequency parameter is defined as a unitless scalar that affects the coarseness of the surface, amplitude (mm) as a scalar field with higher amplitudes resulting in greater affected area, and seed value as unitless integer used to generate randomness. An example of the effect of changing the frequency and amplitude on a planar shape or cylindrical one can be seen in Figs. 9 and 10 respectively.

However, since the direct connection between the input values in Ntopology software (frequency, amplitude, seed) and the outputted surface parameters have not been previously investigated, an investigation using a design of experiment (DOE) [36] has been carried out. A full factorial design of experiment was completed using four factors where each has three levels (beside the shape factor, which only has two levels): frequency (1750, 1500 and 1250), amplitude (0.1 mm, 0.2 mm and 0.3 mm), seed (one, two and three) and finally shape factor (plane and cylinder). The relationship between Ntopology software surface parameters (frequency, amplitude, seed, shape) and areal surface parameters (*Sa, Sq, Spd,* $\hat{a}$) was developed by analyzing the 54 DOE

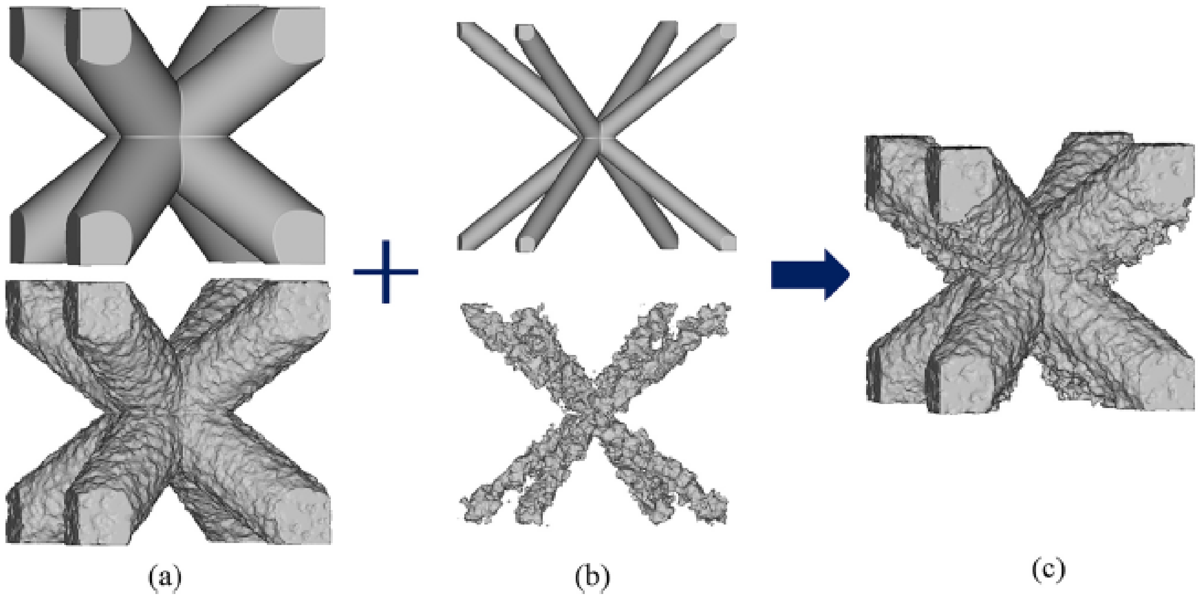

Fig. 11. Steps of applying two types of surface roughness. In (a), the general up skin texture is applied, in (b), the down skin is applied on a smaller diameter, in (c), a Boolean union is carried out to combine (a) and (b).

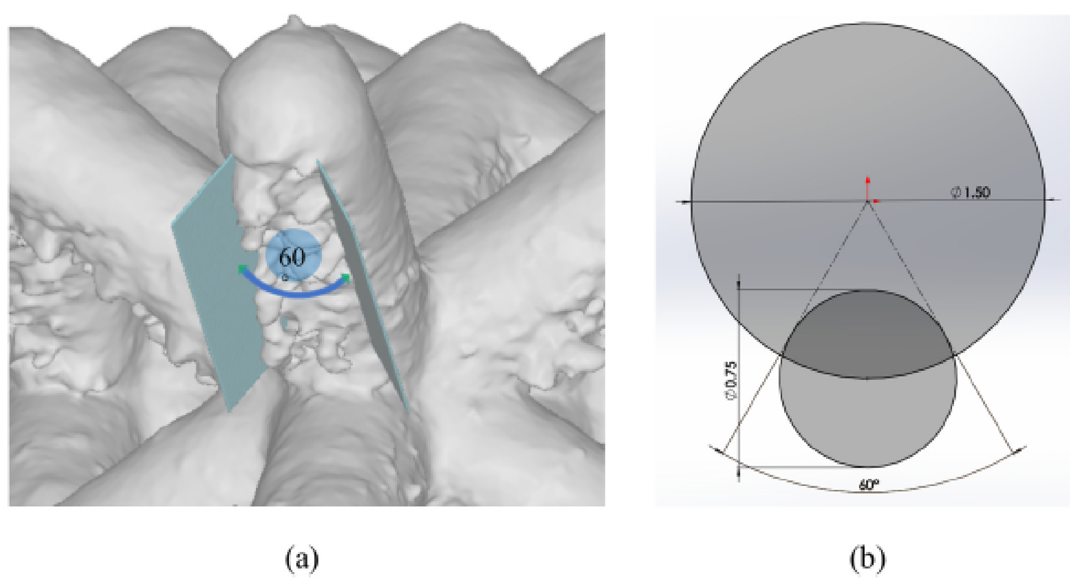

Fig. 12. Angle of the down skin rough surface from XCT (a), Cross profile representation of the original lattice and smaller one used in Fig. 11.

generated surfaces. The mesh feature size used was 0.03 mm. The size of the planar and cylindrical surfaces was chosen to be approximately around the size of the whole lattice box dimension size.

To design a surface roughness on a lattice, three steps are required (shown step by step on one-unit lattice). In step one (Fig. 11 a) a general surface roughness of the up skin value is applied on the whole part. In step two (Fig. 11 b) another smaller lattice is generated with the down skin surface roughness values. This smaller lattice is then moved down to have its centroid touching the bigger lattice surface. The final step (Fig. 11 c) applies a Boolean union between the whole unit lattice, which has the up skin surface roughness values and the smaller unit lattice which has the down skin surface roughness values.

While surface roughness was designed on the whole plane and cylinder in the DOE, it is more challenging in the case of a lattice strut composed of an up skin and localized rougher down skin. For this study, the down skin angle where most rough surface exist was measured to be around 60° degrees (Fig. 12 a) from XCT real geometry. This meant that the smaller strut centroid was designed to be touching the surface of the original lattice surface while covering only 60° degrees of the down skin leading to a diameter of 0.75 mm. More samples and research will need

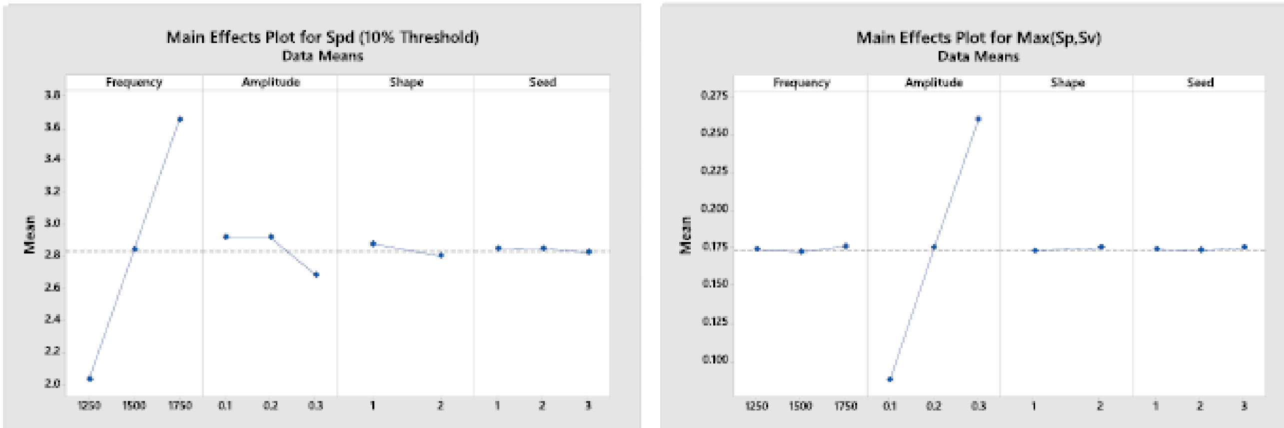

Fig. 13. Main effects plot of Spd and Max(Sp, Sv). The shape factor (1) is for the plane and the shape factor (2) is for the Cylinder.

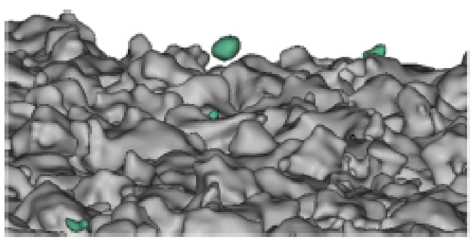

Fig. 14. Example of planar surface roughness design (Grey) used in the DOE showing non-connected particles (Green). The input settings of the image above are 0.3 mm amplitude and frequency of 1500.

to be investigated in future studies in order to develop a robust repeatable method of sizing and placing the smaller lattice for all strut sizes.

3. Results

3.1. DOE results

The DOE results can be seen using the main effects plot in Fig. 13, allowing for the following deductions to be done:

- $\widehat{a}$:$max\{Sp, Sv\}$: as expected, this parameter shows a clear connection to the amplitude. While the obtained value is slightly lower than the set amplitude, it is consistent, and a trendline can be used to predict the values.
- *Spd*: again, as expected, the *Spd* surface parameter showed a clear connection to the frequency value and can be used to measure it. It was slightly affected by amplitude especially at the 0.3 mm value. This is due to the creation of extra particles from the surface roughness tool as seen in Fig. 14. Since these particles do not have any physical meaning, they were removed (by isolating non connected manifolds) causing a drop in the *Spd* value at 0.3 mm amplitude, as seen in Fig. 13. While the impact of these non-connected manifolds is not highly significant and only appears at high amplitudes, future research will investigate its cause and ways to minimize it.
- Seed and Shape: as expected, the seed number and the shape did not have a significant effect on the resulting surface extracted parameters. While the design process generates stochastic surfaces, the extracted parameters remain constant when changing the seed as seen in Fig. 13.

In this paper, the amplitude parameter not only correlated with the $\widehat{a}$ developed surface parameter (due to the close value and dependency) but also to the individual parameters *Sa* and *Sq* as can be seen in the main effect plot below in Fig. 17 in the Appendix.

3.2. Design of surface roughness on the lattice CAD

After investigating the effect of each factor, a model that links the frequency (f) and the amplitude (a) to the roughness parameters can be estimated using linear regression [37] and seen in the two equations shown below. The R-squared values were 96.1% and 99.6% for the estimated models in Eqs. (3) and (4) respectively (Fig. 15).

$$Spd = 0.0032f - 2.013 \tag{3}$$

$$\widehat{a} = max\{Sp, Sv\} = 0.8616a + 0.0009 \tag{4}$$

Using the equations above and the extracted average *Spd* and $\widehat{a}$ of the manufactured lattice from the created ROIs in (Table 1). The interpolated frequency and amplitude that needs to be used to replicate the manufactured AM lattice surface finish (in this case) is reported in Table 2.

After generating the CAD with designed surface (CADwDS), surface parameters were extracted (Fig. 16) from the latter using the same methodology and ROI size used in (Fig. 6). The result of this extraction can be seen below in Table 3.

From the results shown in Table 3 the *Spd* of the CADwDS up skin has a difference of 56.7% to the actual manufactured lattice up skin *Spd* (Table 1). This relatively high difference was expected and attributed to the frequency 2964 used in the interpolation in Table 2, being far above the maximum frequency (1750) and outside the bounds investigated in the DOE, therefore impacting the obtained *Spd* value, suggesting that the relationship might not be linear.

For the down skin however, all values correlated much closer to the XCT extracted surface parameters, with a difference of 2.0% for the *Spd* and a maximum difference of 15.1% for $\widehat{a}$ of up skin and 9.5% for down skins. This makes the *Spd* value of the up skin, the only value that is not close to the actual manufactured AM lattice one. These results show a better surface roughness representation especially in the down skin of the struts compared to the original CAD, which has no surface roughness and all comparison to real geometry would have a 100% difference.

Finally, to assess the dimensional difference between the original CAD (Fig. 3) versus the manufactured AM lattice (XCT) and the proposed CADwDS versus the manufactured AM lattice (XCT), a deviation analysis was performed subsequent to an alignment using a Gaussian best fit registration. A maximum search distance of ± 0.5 mm was selected based on the strut diameter. The results from Table 4, show how the average deviation of the XCT versus the proposed CADwDS was

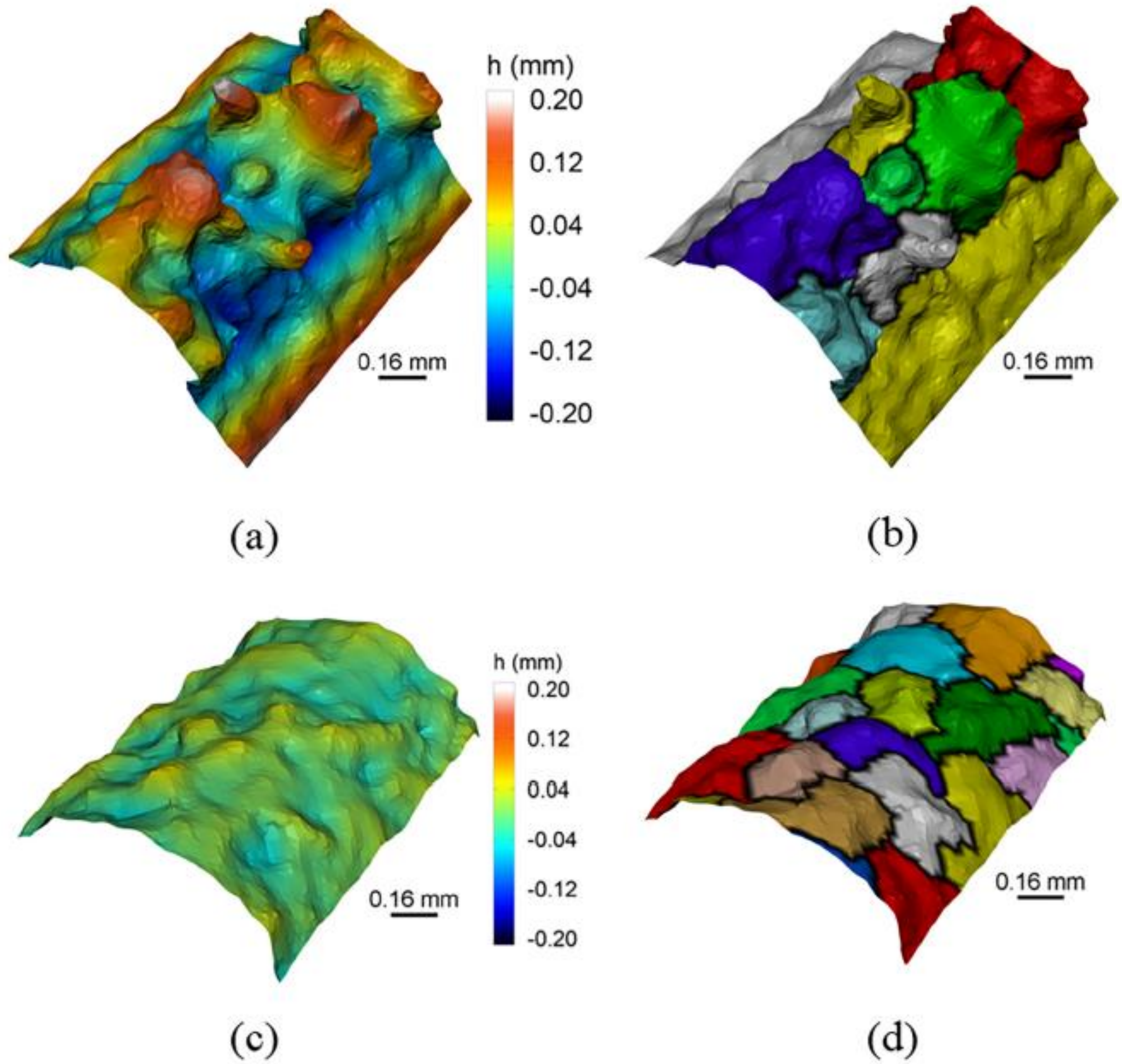

Fig. 15. Example of down skin (a and b) and up skin (c and d) designed surfaces on the CAD lattice strut. On the left side (a and c) is shown the signed distance to the estimated reference form, while on the right side (b and d) is shown the watershed segmentation.

Table 1
Sa, Sq, Spd and max(Sp, Sv) values of the ROIs shown in Fig. 6.

	XCT lattice surface parameters							
	Up skin (T)				Down skin (B)			
	Sa (mm)	*Sq* (mm)	*Spd* ($1/mm^2$)	$\breve{a}$ (mm)	*Sa* (mm)	*Sq* (mm)	*Spd* ($1/mm^2$)	$\breve{a}$ (mm)
Strut 1	0.010	0.013	7.815	0.108	0.065	0.087	5.030	0.295
Strut 2	0.009	0.011	6.739	0.050	0.069	0.085	2.895	0.300
Strut 3	0.009	0.011	8.886	0.042	0.054	0.070	3.647	0.212
Strut 4	0.009	0.011	7.901	0.050	0.049	0.064	4.556	0.285
Average	0.009	0.012	7.835	0.062	0.059	0.076	4.032	0.273

approximately a third of the average deviation of the XCT versus the original CAD. When analysing the colour map shown in Fig. 16, it can be seen how from image (a) to (b), the positive deviation in the down skin gets less intense while a small increase in the negative deviation (bright blue) can be seen. This negative deviation was expected and is due to the designed surface texture not exactly overlaying the AM XCT one. This study was focused on designing surface roughness and combining it with compensation methods from literature mentioned in introduction section is expected to result in improved dimensional deviation results.

Table 2
Interpolated frequency and amplitude using the Spd and $\hat{a}$ equations shown above.

CAD with designed surface (CADwDS) interpolated frequency and amplitude			
Up skin		Down skin	
Interpolated frequency	Interpolated amplitude (mm)	Interpolated frequency	Interpolated amplitude (mm)
2964	0.072	1850	0.315

4. Conclusion and future developments

In this paper, a new method of designing surface texture on CAD models has been investigated and correlated with areal surface roughness parameters for additive manufactured parts. This method was used to design and reproduce LPBF manufacturing surface finish by controlling the amplitude, frequency and location. Assuming an AM process where surface parameter values are approximately repeatable, only one part needs to be measured once for parts printed in the same build. The measured surface finish for that specific AM process can then be replicated on the next CAD models expected to be manufactured under the same conditions to allow for their design validation. The method allowed for the variation of the strut diameter, centroid of the strut and the variation of the cross section. Future work will investigate different print settings and assess the repeatability of the suggested protocol on different samples with different overhang angles (Only 45° degrees strut angle was studied). A single material and machine were used in this study, future research will look at different materials and machines and their impact on the surface roughness. Due to the repeatability challenge of an LPBF process across a build platform, future research can also look at isolating the window of minimum to maximum obtained surface roughness. This can be inputted back to the developed script to generate a least versus worst case scenario, or even a heterogeneous model with a range of surface roughness instead of unique one for up and down skin.

While the cited literature methods allow for designing a variable strut diameter, this method allows for designing and replicating the expected LPBF surface finish in a parametric way and depending on the strut skin side (up or down) all without using XCT data as the main input in the design process. The script within Ntopology developed in this study allows for the direct input of surface roughness parameters to design a parametric surface topography on a chosen CAD. Alternatively, the lookup tables (Tables 5, 6) can be used to understand the obtained surface roughness parameters when choosing a certain amplitude or frequency. For values that are not in the lookup tables, the trendline (Eqs. (3)–(6)) of Spd, $\hat{a}$, Sa, Sq trendline equations can be used. Future research will investigate broader limits in the DOE study to increase the accuracy of the interpolations.

The dimensional difference was also investigated, showing improved mean deviation of the manufactured lattice to the CADwDS compared to the manufactured lattice to the original CAD. The proposed method can allow for the creation of a virtual printed model that incorporates

Table 3
Surface parameters extracted from CADwDS and compared to surface parameters extracted from XCT data in Table 1.

	CAD with designed Surface (CADwDS)	
	Up skin	Down skin
Spd average of four struts (1/ mm^2)	12.274	3.951
Average Spd Difference to XCT in (%)	(56.7%)	(2.0%)
$\hat{a}$ average of four struts (mm)	0.053	0.247
Difference to XCT average $\hat{a}$ in (%)	(15.1%)	(9.5%)

Table 4
Mean deviation of the XCT vs. CAD and XCT vs. CADwDS obtained using VGSTUDIO 3.3.

	XCT versus CAD	XCT versus CADwDS
Mean Deviation (mm)	0.044	0.014

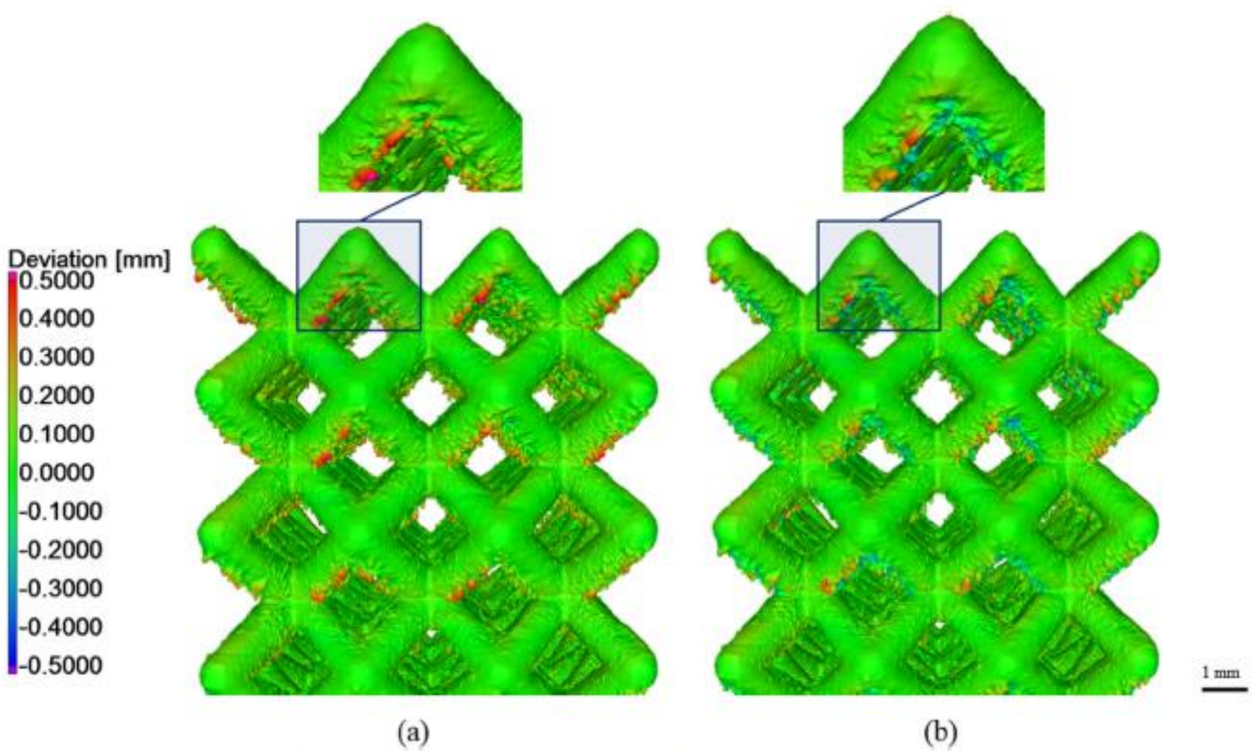

Fig. 16. Colour map of the deviation analysis of the XCT vs. CAD (a) and of the XCT vs. CADwDS (b).

dimensional and surface finish deviations often obtained in AM processes in the design phase and before manufacturing, allowing for a cost-effective and quicker design validation phase. Future work will also investigate the use of the CADwDS in FE simulations by converting the latter to a tetrahedral mesh or using the CADwDS model directly in faster meshless simulations studies in software like Altair Simsolid [38].

The suggested method can also allow for the design validation of rough surface textures, for example, one resulting from a faster printing speed, to then evaluate if this rougher surface texture would still respect the desired dimensional and surface texture tolerances constrained in the design phase. Due to the current high cost of post processing limitations especially for the surface finish of internal lattices, it is important to be able to design and validate the predicted surface texture in the design phase.

Finally, designing and simulating defects will become more critical because of the expected use of AM in the mass customization of products, and topology optimized designs [39]. This means that validating a design with physical testing or even X-ray CT might not be feasible since the next produced part is not necessarily identical. The proposed method was completed on one lattice design, further work will include studying multiple lattices with different geometries and evaluating them dimensionally, in FE and fracture simulations and physical compression tests (ISO 13314 standard [40]) to compare results of the original CAD, CADwDS and the manufactured AM lattice.

CRediT authorship contribution statement

Younes Chahid: Project concept and design. **Younes Chahid, Radu Racasan, Liam Blunt:** Methodology. **Alexander Liu:** Resources. **Luca Pagani, Younes Chahid:** Acquisition of data. **Luca Pagani, Younes Chahid, Radu Racasan, Liam Blunt:** Data analysis and interpretation. **Younes Chahid:** Writing (first draft). **Radu Racasan, Liam Blunt, Luca Pagani, Andrew Townsend, Paul Bills:** Writing - review & editing. **Radu Racasan, Liam Blunt, Andrew Townsend, Paul Bills:** Supervision.

Declaration of Competing Interest

The authors declare that they have no known competing financial interests or personal relationships that could have appeared to influence the work reported in this paper.

Acknowledgements

The authors gratefully acknowledge the UK's Engineering and Physical Sciences Research Council (EPSRC) funding of the Future Metrology Hub (Grant Ref: EP/P006930/1). This work was performed under the auspices of the U.S. Department of Energy by Lawrence Livermore National Laboratory under Contract DE-AC52–07NA27344, LDRD-20-SI-001. LLNL Document number LLNL-JRNL-812397. The authors also gratefully acknowledge Ntopology for providing the license of Ntop and Volume Graphics for providing the license of their VGSTUDIO MAX 3.3 software.

Appendix

Below is lookup tables and equations based on the DOE study that can assist in choosing the right amplitude and frequency to get a specific Sa, Sq, max(Sp, Sv) and Spd. (Fig. 17 and Table 5,6).

$$Sa = 0.2214\ a + 0.0002 \tag{5}$$

$$Sq = 0.2712\ a + 0.0003 \tag{6}$$

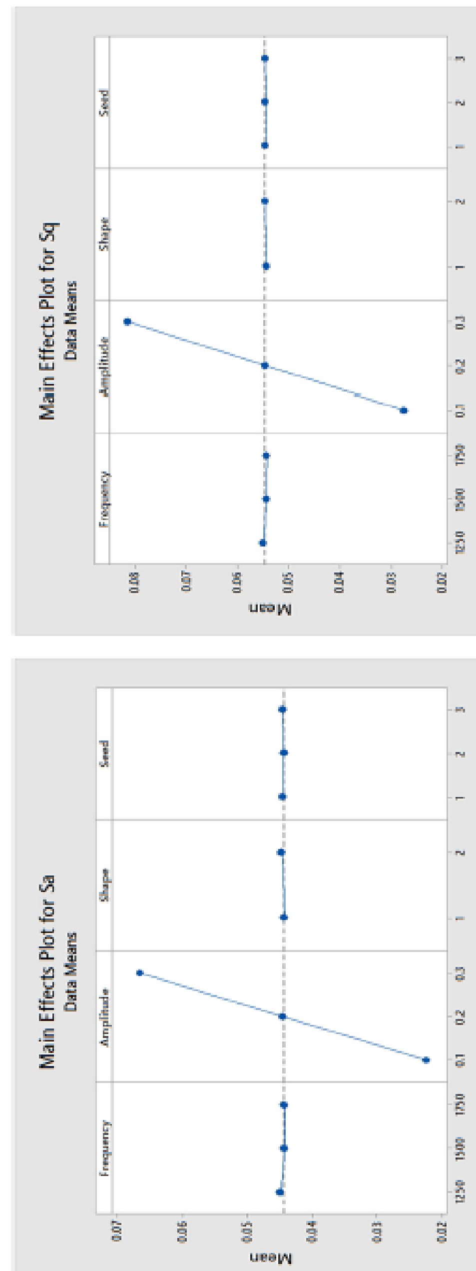

Fig. 17. Main effects plot showing a significant dependency of the Sa and Sq value to the amplitude one.

Table 5
Lookup table based on DOE results showing Max (Sp,Sv), Sa or Sq when selecting an amplitude between 0.05 mm and 0.3 mm in the surface roughness tool in Ntopology Software.

Lookup table for amplitude			
Amplitude (mm)	*max (Sp, Sv)* (mm)	*Sa* (mm)	*Sq* (mm)
0.05	0.0440	0.0113	0.0138
0.1	0.0871	0.0224	0.0274
0.15	0.1301	0.0334	0.0409
0.2	0.1732	0.0445	0.0545
0.25	0.2163	0.0556	0.0681
0.3	0.2594	0.0666	0.0816

Table 6
Lookup table based on DOE results to give an idea on the obtained Spd when selecting a frequency between 1250 and 1700 in the surface roughness tool in Ntopology Software.

Lookup table for frequency	
Frequency	*Spd* ($1/mm^2$)
1250	1.987
1300	2.147
1350	2.307
1400	2.467
1450	2.627
1500	2.787
1550	2.947
1600	3.107
1650	3.267
1700	3.427

References

[1] L.J. Gibson, M.F. Ashby, in: Lorna J. Gibson (Ed.), Cellular Solids, Cambridge Core, 1997, https://doi.org/10.1017/CBO9781139878326.

[2] M. Mazur, M. Leary, M. McMillan, S. Sun, D. Shidid, M. Brandt, 5 – Mechanical properties of Ti6Al4V and AlSi12Mg lattice structures manufactured by Selective Laser Melting (SLM), in: M. Brandt (Ed.), Laser Additive Manufacturing, Woodhead Publishing, 2017, pp. 119–161, https://doi.org/10.1016/B978-0-08-100433-3.00005-1.

[3] X.P. Tan, Y.J. Tan, C.S.L. Chow, S.B. Tor, W.Y. Yeong, Metallic powder-bed based 3D printing of cellular scaffolds for orthopaedic implants: a state-of-the-art review on manufacturing, topological design, mechanical properties and biocompatibility, Mater. Sci. Eng. C 76 (2017) 1328–1343, https://doi.org/10.1016/j.msec.2017.02.094.

[4] L.E. Murr, S.M. Gaytan, F. Medina, H. Lopez, E. Martinez, B.I. Machado, D. H. Hernandez, L. Martinez, M.I. Lopez, R.B. Wicker, J. Bracke, Next-generation biomedical implants using additive manufacturing of complex, cellular and functional mesh arrays, Philos. Trans. R. Soc. A Math. Phys. Eng. Sci. 368 (2010) 1999–2032, https://doi.org/10.1098/rsta.2010.0010.

[5] I. Echeta, X. Feng, B. Dutton, S. Piano, R. Leach, Review of defects in lattice structures manufactured by powder bed fusion, Int. J. Adv. Manuf. Technol. (2019).

[6] S.L. Sing, F.E. Wiria, W.Y. Yeong, Selective laser melting of lattice structures: a statistical approach to manufacturability and mechanical behavior, Robot. Comput. Integr. Manuf. 49 (2018) 170–180, https://doi.org/10.1016/j.rcim.2017.06.006.

[7] A.M. Kamat, Y. Pei, An analytical method to predict and compensate for residual stress-induced deformation in overhanging regions of internal channels fabricated using powder bed fusion, Addit. Manuf. 29 (2019), 100796, https://doi.org/10.1016/j.addma.2019.100796.

[8] D. Wang, S. Mai, D. Xiao, Y. Yang, Surface quality of the curved overhanging structure manufactured from 316-L stainless steel by SLM, Int J. Adv. Manuf. Technol. 86 (2016) 781–792, https://doi.org/10.1007/s00170-015-8216-6.

[9] A. Sarker, N. Tran, A. Rifai, J. Elambasseril, M. Brandt, R. Williams, M. Leary, K. Fox, Angle defines attachment: switching the biological response to titanium interfaces by modifying the inclination angle during selective laser melting, Mater. Des. 154 (2018) 326–339, https://doi.org/10.1016/j.matdes.2018.05.043.

[10] M. Dallago, B. Winiarski, F. Zanini, S. Carmignato, M. Benedetti, On the effect of geometrical imperfections and defects on the fatigue strength of cellular lattice structures additively manufactured via Selective Laser Melting, Int. J. Fatigue 124 (2019) 348–360, https://doi.org/10.1016/j.ijfatigue.2019.03.019.

[11] On the effects of geometry, defects, and material asymmetry on the mechanical response of shape memory alloy cellular lattice structures, IOPscience, 2019. (https://iopscience.iop.org/article/10.1088/0964-1726/25/2/025008/pdf) accessed December 8.

[12] J.C. Snyder, C.K. Stimpson, K.A. Thole, D. Mongillo, Build direction effects on additively manufactured channels, J. Turbomach. 138 (2016), https://doi.org/10.1115/1.4032168.

[13] ISO 25178-2:2012(en), Geometrical product specifications (GPS) — surface texture: areal — Part 2: terms, definitions and surface texture parameters, n.d.. (https://www.iso.org/obp/ui/#iso:std:iso:25178:-2:ed-1:v1:en) (accessed March 30, 2020).

[14] A. Townsend, N. Senin, L. Blunt, R.K. Leach, J.S. Taylor, Surface texture metrology for metal additive manufacturing: a review, Precis. Eng. 46 (2016) 34–47, https://doi.org/10.1016/j.precisioneng.2016.06.001.

[15] 14:00-17:00, ISO 4287:1997, ISO. n.d.. (https://www.iso.org/cms/render/live/en/sites/isoorg/contents/data/standard/01/01/10132.html) (accessed September 12, 2020).

[16] Z.S. Bagheri, D. Melancon, L. Liu, R.B. Johnston, D. Pasini, Compensation strategy to reduce geometry and mechanics mismatches in porous biomaterials built with Selective Laser Melting, J. Mech. Behav. Biomed. Mater. 70 (2017) 17–27, https://doi.org/10.1016/j.jmbbm.2016.04.041.

[17] Mechanical and microstructural properties of polycaprolactone scaffolds with one-dimensional, two-dimensional, and three-dimensional orthogonally oriented porous architectures produced by selective laser sintering | Elsevier Enhanced Reader, n.d.. (https://doi.org/10.1016/j.actbio.2010.02.002).

[18] B. Partee, S.J. Hollister, S. Das, Selective laser sintering process optimization for layered manufacturing of CAPA® 6501 polycaprolactone bone tissue engineering scaffolds, J. Manuf. Sci. Eng. 128 (2006) 531–540, https://doi.org/10.1115/1.2162589.

[19] G. Pyka, G. Kerckhofs, I. Papantoniou, M. Speirs, J. Schrooten, M. Wevers, Surface roughness and morphology customization of additive manufactured open porous Ti6Al4V structures, Materials 6 (2013) 4737–4757, https://doi.org/10.3390/ma6104737.

[20] G. Pyka, A. Burakowski, G. Kerckhofs, M. Moesen, S.V. Bael, J. Schrooten, M. Wevers, Surface modification of Ti6Al4V open porous structures produced by additive manufacturing, Adv. Eng. Mater. 14 (2012) 363–370, https://doi.org/10.1002/adem.201100344.

[21] P. Lhuissier, C. de Formanoir, G. Martin, R. Dendievel, S. Godet, Geometrical control of lattice structures produced by EBM through chemical etching: Investigations at the scale of individual struts, Mater. Des. 110 (2016) 485–493, https://doi.org/10.1016/j.matdes.2016.08.029.

[22] B. Lozanovski, M. Leary, P. Tran, D. Shidid, M. Qian, P. Choong, M. Brandt, Computational modelling of strut defects in SLM manufactured lattice structures, Mater. Des. 171 (2019), 107671, https://doi.org/10.1016/j.matdes.2019.107671.

[23] M.R. Karamooz Ravari, M. Kadkhodaei, M. Badrossamay, R. Rezaei, Numerical investigation on mechanical properties of cellular lattice structures fabricated by fused deposition modeling, Int. J. Mech. Sci. 88 (2014) 154–161, https://doi.org/10.1016/j.ijmecsci.2014.08.009.

[24] G. Campoli, M.S. Borleffs, S. Amin Yavari, R. Wauthle, H. Weinans, A.A. Zadpoor, Mechanical properties of open-cell metallic biomaterials manufactured using additive manufacturing, Mater. Des. 49 (2013) 957–965, https://doi.org/10.1016/j.matdes.2013.01.071.

[25] M.R. Karamooz Ravari, M. Kadkhodaei, A computationally efficient modeling approach for predicting mechanical behavior of cellular lattice structures, J. Mater. Eng. Perform. 24 (2015) 245–252, https://doi.org/10.1007/s11665-014-1281-4.

[26] Z. Xiao, Y. Yang, R. Xiao, Y. Bai, C. Song, D. Wang, Evaluation of topology-optimized lattice structures manufactured via selective laser melting, Mater. Des. 143 (2018) 27–37, https://doi.org/10.1016/j.matdes.2018.01.023.
[27] T. Persenot, A. Burr, E. Plancher, J.-Y. Buffière, R. Dendievel, G. Martin, Effect of ultrasonic shot peening on the surface defects of thin struts built by electron beam melting: consequences on fatigue resistance, Addit. Manuf. 28 (2019) 821–830, https://doi.org/10.1016/j.addma.2019.06.014.
[28] Engineering Software Designed for Advanced Manufacturing, NTopology, n.d.. ⟨https://ntopology.com/⟩ (accessed January 20, 2020).
[29] VGSTUDIO MAX – Products – volumegraphics.com, n.d.. ⟨https://www.volumegraphics.com/en/products/vgstudio-max.html⟩ (accessed April 16, 2019).
[30] A. Townsend, L. Pagani, L. Blunt, P.J. Scott, X. Jiang, Factors affecting the accuracy of areal surface texture data extraction from X-ray CT, CIRP Ann. 66 (2017) 547–550, https://doi.org/10.1016/j.cirp.2017.04.074.
[31] A. Townsend, R. Racasan, R. Leach, N. Senin, A. Thompson, A. Ramsey, D. Bate, P. Woolliams, S. Brown, L. Blunt, An interlaboratory comparison of X-ray computed tomography measurement for texture and dimensional characterisation of additively manufactured parts, Addit. Manuf. 23 (2018) 422–432, https://doi.org/10.1016/j.addma.2018.08.013.
[32] A. Townsend, L. Pagani, P. Scott, L. Blunt, Areal surface texture data extraction from X-ray computed tomography reconstructions of metal additively manufactured parts, Precis. Eng. 48 (2017) 254–264, https://doi.org/10.1016/j.precisioneng.2016.12.008.
[33] Towards a new definition of areal surface texture parameters on freeform surface: re-entrant features and functional parameters – ScienceDirect, n.d.. ⟨https://www.sciencedirect.com/science/article/pii/S026322411930329X⟩ (accessed March 30, 2020).
[34] S. Lou, L. Pagani, W. Zeng, X. Jiang, P.J. Scott, Watershed segmentation of topographical features on freeform surfaces and its application to additively manufactured surfaces, Precis. Eng. 63 (2020) 177–186, https://doi.org/10.1016/j.precisioneng.2020.02.005.
[35] S. Gustavson, Simplex noise demystified, (n.d.) 17.
[36] E.J. Williams, Experimental designs balanced for pairs of residual effects, AuSRA 3 (1950) 351, https://doi.org/10.1071/PH500351.
[37] S. Konishi, Introduction to multivariate analysis: linear and nonlinear modeling, CRC Press, 2014.
[38] Structural Analysis for Rapid Design Iterations | Altair SimSolid, n.d.. ⟨https://www.altair.com/simsolid/⟩ (accessed February 10, 2020).
[39] M. Shukla, I. Todorov, D. Kapletia, Application of additive manufacturing for mass customisation: understanding the interaction of critical barriers, Prod. Plan. Control 29 (2018) 814–825, https://doi.org/10.1080/09537287.2018.1474395.
[40] 14:00–17:00, ISO 13314:2011, ISO. n.d. ⟨http://www.iso.org/cms/render/live/en/sites/isoorg/contents/data/standard/05/36/53669.html⟩ (accessed January 20, 2020).

12.4. Appendix 4: Euspen 2021 Advancing Precision in Additive Manufacturing (Chapter 7)

Joint Special Interest Group meeting between euspen and ASPE
Advancing Precision in Additive Manufacturing
Inspire AG, St. Gallen, Switzerland 2021
www.euspen.eu

Design and measurement strategy of additive manufacturing lattice benchmark artefact

Younes Chahid[1], Radu Racasan[1], Paul Bills[1], Liam Blunt[1]

[1]*EPSRC Future Metrology Hub, School of Computing and Engineering, University of Huddersfield, HD1 3DH Huddersfield, UK*

Younes.chahid@hud.ac.uk

Abstract
Currently, no additive manufacturing (AM) benchmark artefact has been solely made for lattices. The objective of this research is to design an AM lattice benchmark artefact that AM users can use to assess their machine's capability, accompanied by a measurement strategy to evaluate the lattice characteristics using X-ray computed tomography (XCT). This novel AM benchmark lattice artefact design allows for a simplified method to evaluate the machine's capability in manufacturing different strut thicknesses or type of unit cells by only having to print one part. The parametric and gradient nature of the design allows engineers to easily choose and merge different types of lattices and strut thickness ranges. This method removes the need of printing multiple parts, resulting in decreased powder use, reduced print/measurement time while limiting chances of a print failure.

Keywords: Lattice structures; Additive Manufacturing; Benchmark artefact; X-ray Computed Tomography; Metrology.

1. Introduction:

When commissioning a new additive manufacturing (AM) machine or when using a new powder material, it is common practice to additively manufacture different types of benchmark artefacts for different purposes such as assessing the mechanical properties of the produced part, optimising the different printing/post processing workflows, or to evaluate the AM machine geometric resolution limits, surface roughness and more. While more than 65 AM benchmark artefacts have been reported in literature [1], only a few have included a lattice as a complimentary design. The objective of this research is to design an AM lattice benchmark artefact that AM users can use to assess their machine's capability, accompanied by a measurement strategy to assess the dimensional, surface and porosity of the produced lattice using X-ray computed tomography (XCT).

2. Methodology

This paper starts by analysing the previous AM geometric benchmark artefacts and assessing their strengths and weaknesses. Secondly, this research investigates and uses ISO/ASTM 52902 [2] "Additive manufacturing - Test artifacts - Geometric capability assessment of additive manufacturing systems" as a guide to develop design constraints, features, and measurement strategies that are optimised for lattice structures. These features include, but are not limited to strut diameter resolution, node positioning error, surface roughness and porosity. Measurement strategy was optimised for XCT as it could match the measurement complexity needed to assess internal features or porosity of lattices.

A lattice is composed of uniformly repeated unit cell designs composed of different nodes and struts forming the general geometry. While ISO/ASTM 52902 does not provide information about measuring lattices, some suggested designs and measurement methods can be translated to achieving the task.

For example, the pin diameter resolution, hole resolution and linear axis accuracy from the standard can be translated respectively to strut resolution, external porosity (designed internal lattice spacings) resolution and linear node positioning error.

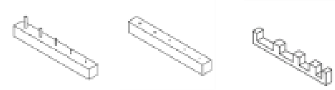

Figure 1. Example of ISO/ASTM 52902 suggested reference geometries as shown from left to right the pin diameter resolution, hole resolution and linear axis accuracy [2].

To represent the features shown in figure 1, the suggested design in this study has a gradient field to incorporate into one design, a range of lattice strut diameters and external pores sizes as can be seen in figure 2. This gradient approach is different from previously suggested designs in literature where multiple lattices with different strut and cell sizes have to be produced.

2.2. Results and discussion

The resulting design has Body Centred Cubic (bcc) type unit cell, this being one of the most used type of lattices in literature [1] and a box size 18.7 x 18.7 x 27 mm. Ntopology software was used to design a gradient that resulted in a varying strut diameter and cell size seen in figure 2.

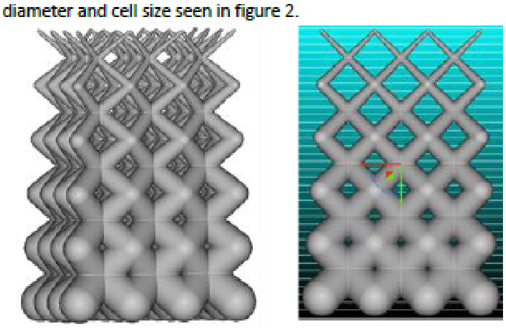

Figure 2. Suggested AM lattice benchmark artefact showing the gradient strut thickness and cell size.

The measurement strategy relies on using X-ray computed tomography (XCT) to image the additive manufactured part. While the gradient design allows for a visual and qualitative inspection, a quantitative inspection using XCT will be more thorough, especially when it comes to internal features that are inaccessible using conventional measurement instruments.

To simulate the measurement strategy beforehand, the measurements were applied on the produced CAD. For example, the lattice strut resolution can be measured using a wall thickness analysis as seen in figure 3. The external pore resolution can be measured using foam analysis module here performed using VGStudio MAX 3.4.3 as seen in figure 4.

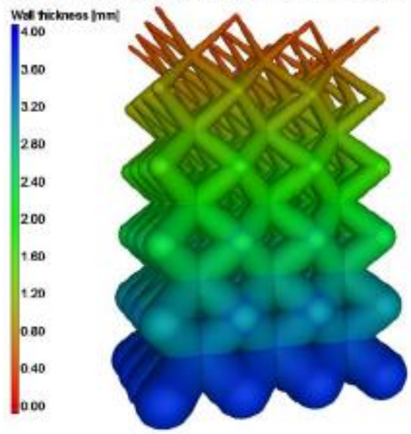

Figure 3. Wall thickness analysis performed on the AM lattice benchmark artefact CAD showing the strut resolution.

To evaluate the node positioning axis error, and instead of adding spheres to the design, the nodes can be thresholded from the wall thickness analysis to isolate the spheres already existing in each node. The measurement strategy in this case can include measuring the centre distance between multiple spheres in each X, Y and Z axis to evaluate the axis node positioning error. Another measurement can include the overlay of CAD and produced AM node spheres and compare their centre-to-centre distance. Example of spheres thresholded from the CAD nodes can be seen in figure 4.

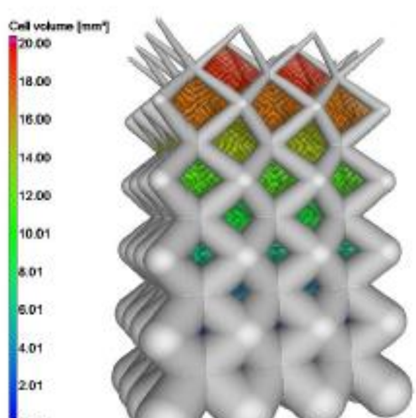

Figure 4. Foam analysis performed on the AM lattice benchmark artefact CAD showing the external porosity resolution.

Finally, deviation analysis can also be performed as well as surface data analysis as previously completed by the author [3]. Also, and while not mentioned in ISO/ASTM 52902, porosity analysis can also be performed on the produced AM lattice since the small geometry can be easily affected by the existence of internal pores.

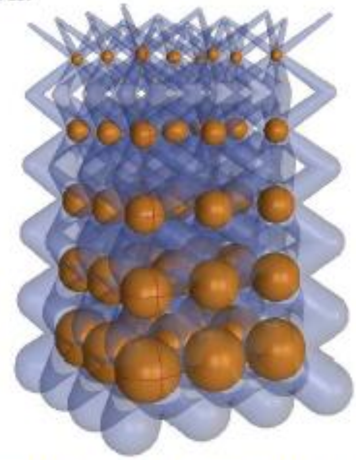

Figure 5. Isolated spheres existing in every lattice node used for node positioning error measurement.

3. Conclusion and future work

This study suggests a novel AM lattice benchmark artefact that can be used for assessing the machine capability using for example different hatching methods and layer height to evaluate parameters like the smallest achievable lattice strut or external pore. Process repeatability and stability can also be assessed since lattice designs already have duplicated features across each layer.

Instead of producing multiple lattices, each with a fixed strut and cell size, the suggested design is based on a gradient that allows for reduction of the number of specimens and print time making the process cost efficient. The suggested design also minimises the chances of print failure since the fine features are at the top and are printed last. The paper also suggests, a measurement strategy based on XCT and applied as seen above on the CAD design converted to a virtual volume.

Future work will include the additive manufacturing of the AM lattice benchmark design and demonstration of the suggested measurement strategy. Dimensional deviations and defects are expected to be predominant at the top part of the lattice due to minimising lattice strut diameter.

4. Acknowledgements

The authors gratefully acknowledge the UK's Engineering and Physical Sciences Research Council (EPSRC) funding of the Future Metrology Hub (Grant Ref: EP/P006930/1).The authors also gratefully acknowledge Ntopology for providing the license of Ntop and Volume Graphics for providing the license of their VGSTUDIO MAX 3.4 software.

4. References

[1] Toward a common laser powder bed fusion qualification test artifact, Addit. Manuf. 39 (2021) 101803. https://doi.org/10.1016/j.addma.2020.101803.

[2] 14:00-17:00, ISO/ASTM 52902:2019, ISO. (n.d.). https://www.iso.org/cms/render/live/en/sites/isoorg/contents/data/standard/06/72/67287.html (accessed March 25, 2021).

[3] Y. Chahid, R. Racasan, L. Pagani, A. Townsend, A. Liu, P. Bills, L. Blunt, Parametrically designed surface topography on CAD models of additively manufactured lattice structures for improved design validation, Addit. Manuf. 37 (2021) 101731. https://doi.org/10.1016/j.addma.2020.101731.

12.5. Appendix 5: Article published in 2020 about Webinar presented with Ntopology

Design for Metrology in Additive Manufacturing

Designing for AM, in general, has its challenges. One challenge is ensuring that your designs will be measurable using X-ray Computed Tomography (XCT). Below, I briefly go over this and invite you to watch my presentation diving deeper into the subject.

Younes Chahid
August 12, 2020 • 3 min read

With the rise of design for additive manufacturing (DfAM) awareness, more efficient and functional designs are being made taking advantage of additive manufacturing (AM) complexity. However, at the same time, since these designs are usually complex enough to not be manufactured using conventional manufacturing methods, they are also complex enough to not be measurable using conventional metrology tools.

Figure 1: Additive manufactured steel joints designed by Arup. All designed to carry the same load [1].

To tackle this challenge, a non-conventional metrology tool is usually used, X-ray Computed Tomography (XCT). While XCT still lacks standardisation and needs more research to better generate uncertainty statements, it is becoming more and more popular in the AM field.

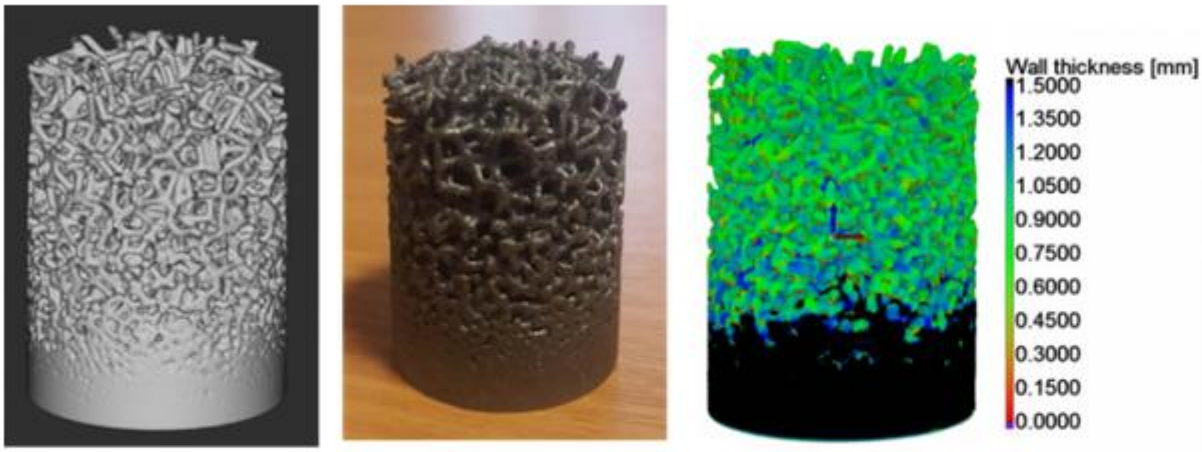

Figure 2: Design in nTop (left), additive manufacturing in aluminium (middle), XCT and wall thickness analysis using VGStudio.

In my webinar available on-demand Tuesday, August 18, there will be a general introduction to metrology, where XCT fits in the scope of measurement tools, and finally, ways to design for metrology. In this case, design for metrology will mean taking in consideration XCT measurement limitations during the design phase, making sure that your important function related features are measurable using XCT.

References

[1] Mercuri, Valentina. (2018). Form and structural optimization: from beam modeling to 3D printing of reinforced concrete members.

WRITTEN BY

Younes Chahid

Younes Chahid has a first class Mechanical Engineering degree and is currently a final year PhD student on the topic of Design and Metrology of AM Lattice and Trabecular Structures at the University of Huddersfield. Younes has been selected in iMeche 2019 Rising Stars list and is also the winner of the international Additive World Design for AM 2020 challenge. Younes is also the founder and mentor of the award-winning University of Huddersfield 3D Printing Society. His experiences are in generative design, design for AM using topology optimisation, lattice structures and metrology using X-ray CT for dimensional, surface roughness and porosity analysis.

12.6. Appendix 6: Article published in 2020 with Ntopology about surface metrology of AM lattices

Design of surface roughness on CAD of AM lattices using areal surface parameters for better design validation

AM lattices often have a down skin surface roughness different from the up skin one. The workflow shown below enables the design of a virtual "CAD with Designed Surface". The latter has a surface roughness closer to the actual AM lattice, measured using X-ray Computed Tomography.

Younes Chahid

December 16, 2020

Structural or fluid simulations in the Additive Manufacturing (AM) field are performed a utilizing Computer-aided design (CAD) models of lattice structures that do not contain any information related to the surface roughness. During the Laser Powder Bed Fusion (LPBF) significant surface roughness is produced especially in low overhangs and down skin of lattice structures as can be seen in Fig. 1.

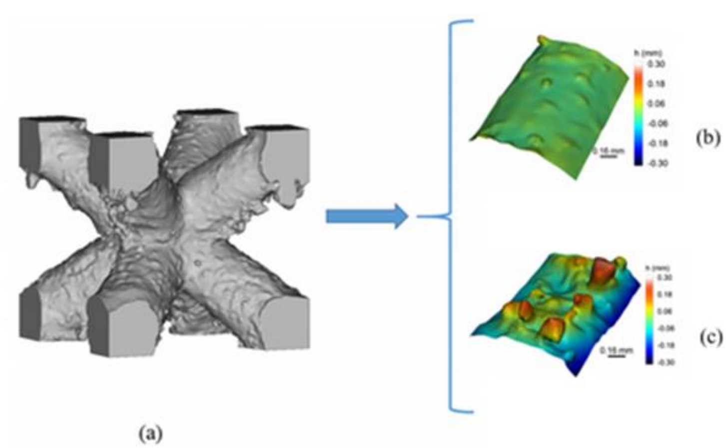

Fig. 1: Example of a Boolean subtracted one-unit cell of an AM lattice (a) obtained using X-ray Computed Tomography (XCT) showing different up (b) and down skin (c) surface roughness.

To account for these differences, the expected surface roughness can be designed before the manufacturing process on the CAD of the AM part (Fig. 2), creating a virtual "CAD with Designed Surface" (CADwDS).

In this study, a full factorial Design of Experiment (DOE) has been performed to correlate nTop Platform surface roughness block parameters (frequency, amplitude, seed) with the conventional engineering ISO 25178 areal surface parameters (Sa, Sq, Sp, Sv, Spd). A total of 54 DOE surfaces were generated on both a planar and cylindrical geometry.

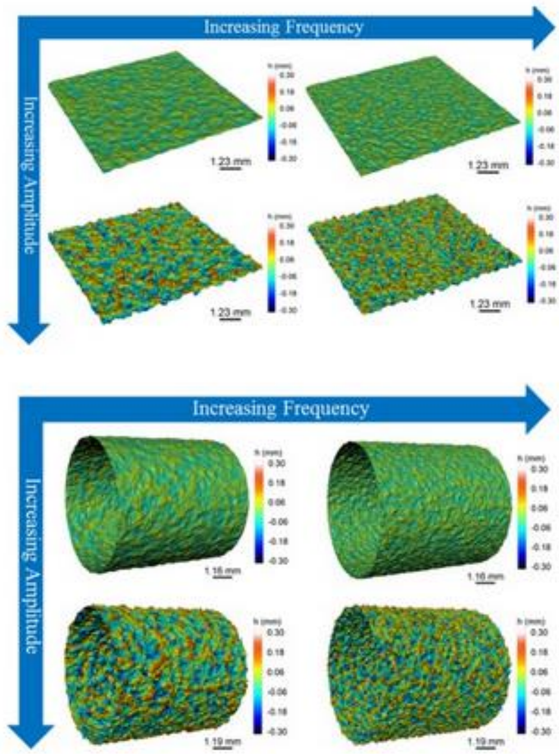

Fig. 2: Example of surface roughness design with increasing amplitude, frequency and fixed seed on both planar and cylindrical surfaces.

The results of the study show a successful correlation between the frequency parameter and the conventional areal surface parameter "Spd" and a separate correlation between amplitude and a developed "max(Sp,Sv)" parameter (also to Sa and Sq). These results demonstrate that it is possible to design surface roughness on CAD models using areal surface roughness parameters in such a way as to replicate the surface that is produced during Powder Bed Fusion.

In order to design surface roughness on CAD models of lattice structures two workflows have been developed: one to extract surface roughness from an AM lattice using X-ray Computed Tomography (XCT) as seen in Fig. 1 and another one to design a different upper and down skin surface roughness on a strut-based lattice as seen below.

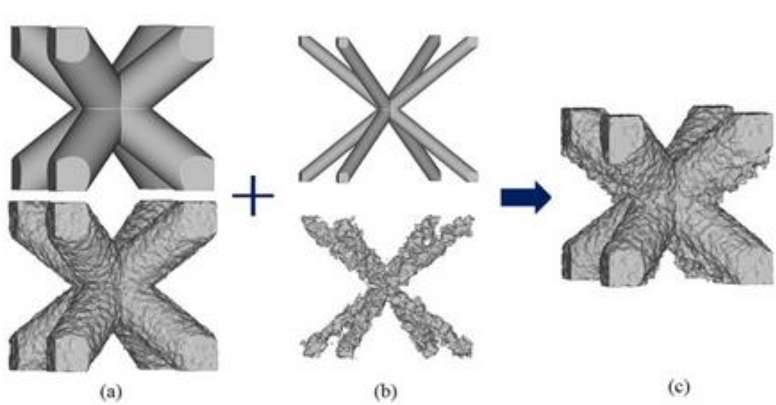

Fig. 3: Workflow of adding up skin and general surface roughness (a) combined (c) with down skin one (b) using areal surface parameters as inputs (Spd, Sa, Sq...) and a custom nTop workflow.

The result was a CADwDS that had a closer surface roughness and smaller mean deviation (Fig.4) to the XCT of the AM lattice compared to the original perfect CAD versus the XCT. More information can be found in my published research paper, *Parametrically designed surface topography on CAD models of additive manufactured lattice structures for improved design validation.*

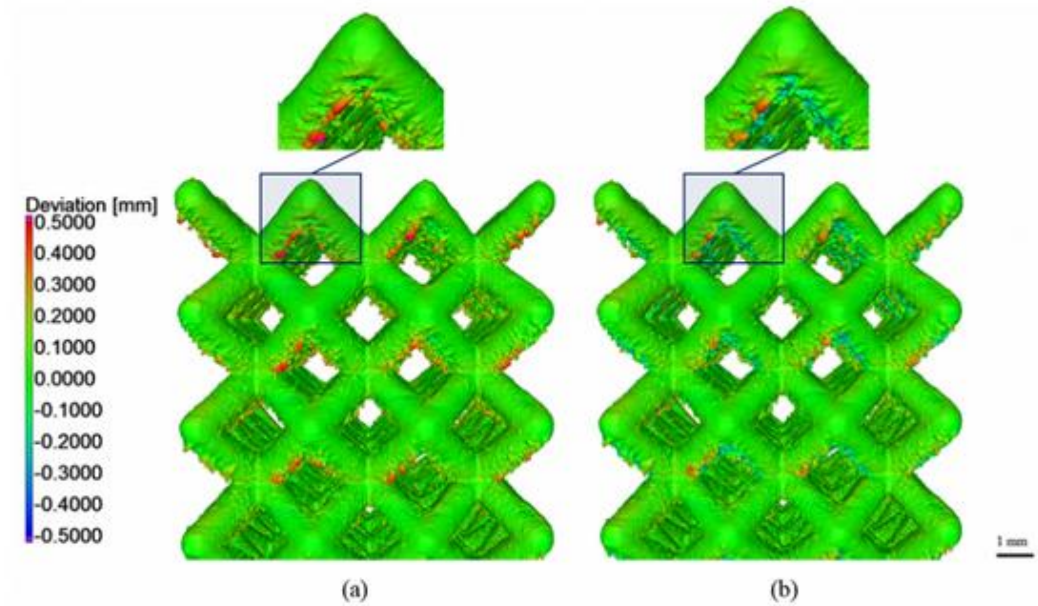

Fig. 4: Colour map of the deviation analysis of the XCT vs. original CAD (a) and of the XCT vs. CADwDS (b) showing less deviation.

In conclusion, the research in this field will enable the design of virtual CAD models that contain a realistic and better expectation of the anticipated defects or deviations prior to the AM process, assisting in the design validation process and cost-effectively assessing different printing parameters, strategies, surface treatments and behavior of AM parts.

> If this interests you, read my first nTop guest blog, *How to Design and Optimize a Patient Specific Additively Manufactured Hip Implant Stem.*
>
> You can also check out my presentation from nTop's Metal DfAM series, *Metrology and DfAM for Lattice Structures.*

WRITTEN BY

Younes Chahid

Younes Chahid has a first class Mechanical Engineering degree and is currently a final year PhD student on the topic of Design and Metrology of AM Lattice and Trabecular Structures at the University of Huddersfield. Younes has been selected in iMeche 2019 Rising Stars list and is also the winner of the international Additive World Design for AM 2020 challenge. Younes is also the founder and mentor of the award-winning University of Huddersfield 3D Printing Society. His experiences are in generative design, design for AM using topology optimisation, lattice structures and metrology using X-ray CT for dimensional, surface roughness and porosity analysis.

12.7. Appendix 7: Article published in 2020 about award winning AM lattice implant design

How to Design and Optimize a Patient Specific Additively Manufactured Hip Implant Stem

Read below to see how a student used nTop Platform to design a novel hip implant stem and won an award for his design

Younes Chahid
April 27, 2020 • 5 min read

Figure 1: AM optimised hip implant stem design in Ti-6Al-4V. Winner of the 2020 Additive World student category DfAM challenge

The advancement of Additive Manufacturing (AM) is allowing us to materialise ideas and designs previously thought impossible to manufacture. Combined with the spirit of Biomimetics, which can be described as the art and science of mimicking biological systems or nature in general, a user can run a custom experiment with specific constraints to then run a tiny "natural selection" lab, all using a laptop.

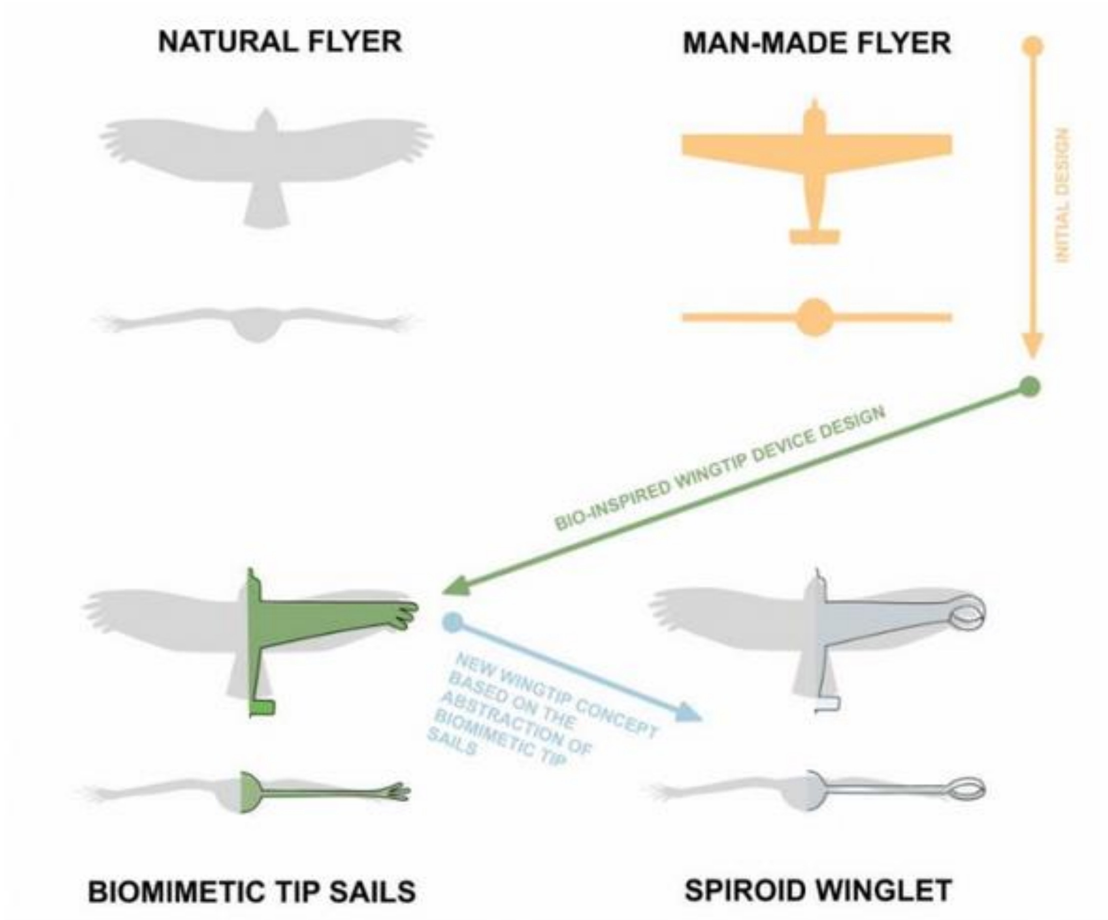

Figure 2: Spiroid winglet design through biomimetics abstraction [1]

Traditional Hip Implant Design Problems

Traditional hip implant stem designs usually cause stress shielding, meaning that they absorb most of the load that the body exercises on the hip joint. This means that lower bones in the body stop receiving their usual load and start resorbing or shrinking due to Wolff's law. This causes the hip implant to start dislocating, leading to another surgery.

Solving that Problem

To solve this challenge, the goal was to design a hip implant stem that is as close as possible to the human trabecular bone, allowing for both the reduction of stress shielding effect and increasing the chance of osseointegration.

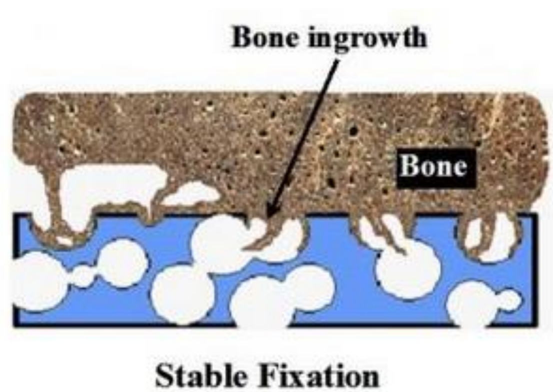

Figure 3: Bone ingrowth in a foam like structure [2]

Using nTop Platform and beginning with a full stem (Figure 4 a), the design was initially converted to a stochastic Voronoi pattern (Figure 4 b). After applying a structural analysis in Simsolid software, the stress color scale map was then used as an input to vary both the density distribution (Figure 4 d) and the thickness distribution in a linear way (Figure 4 e). This resulted in a design that can absorb more load by sharing it through its connected lattice struts thereby avoiding a concentration of stress and decreasing the possibility of a second surgery.

The final design has an average pore size of 1.1 or mm, increasing the chances of osseointegration which usually happens in pore sizes between 0.64 mm and 1.4 mm [3]. In comparison with the initial full stem (Figure 4 a), the final design allowed for a reduction of Maximum Von Mises Stress by 23%, Maximum Displacement of 15%, and total volume of 30%. The final design (Figure 1) takes full advantage of AM capability in manufacturing custom, internal lattice structures impossible to achieve any other way, while reducing both lead time and manufacturing waste and increasing patient success.

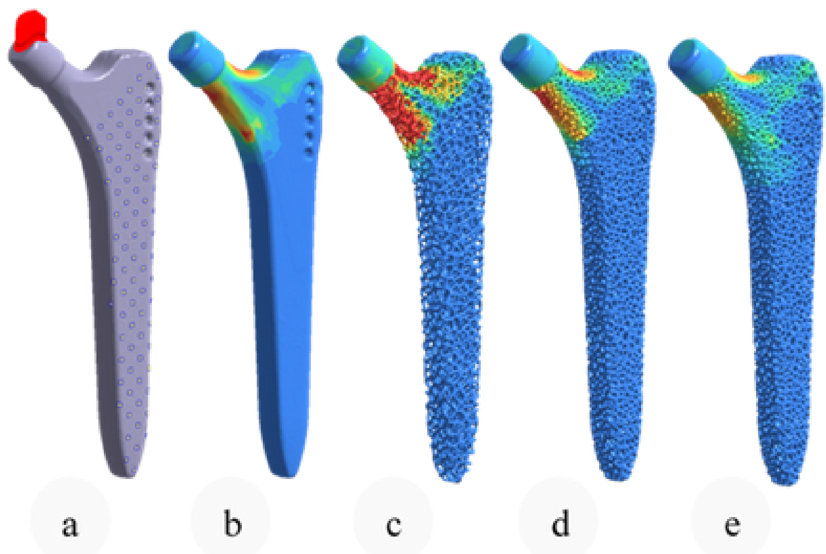

Figure 4: Same Von mises color scale from Simsolid FEA. Boundary conditions (0), initial stem FEA (1), Stochastic lattice FEA (2), Optimised density (3), Optimised strut thickness (4)

How to Achieve Patient Specific Implants

AM allows for a parametric way of design and opens the door for a future of mass customization, but at the same time, it creates more challenges and sometimes represents a nightmare for quality control engineers and for the metrology field in general. A field that is not adapted yet to mass customization, internal features, high surface roughness and sometimes random porosity.

For this reason, a significant part of my research lays in developing or testing new inspection tools for the metrology and quality validation of AM lattice structures. I use an industrial Computed Tomography (CT) machine due to the presence of internal features that cannot be viewed using traditional tools. While not fully standardized or traceable, industrial CT machines and applications have been improving at a great pace, assisting in performing a range of measurements like wall thickness (example in Figure 6), porosity analysis and sometimes even extracting areal surface roughness parameters.

Finally, design software like nTopology allows for designing lattice structures in a dynamic and parametric way. For this example, by using blocks and notebooks, a whole workflow can theoretically be built from the import of the patient CT to designing and validating hundreds of designs, to finally reach one that works specifically for the concerned patient while respecting design for AM (DfAM) rules and metrology ones.

Figure 5: Prototyping a sectioned version of the design steps shown in Figure 4 using FDM technology

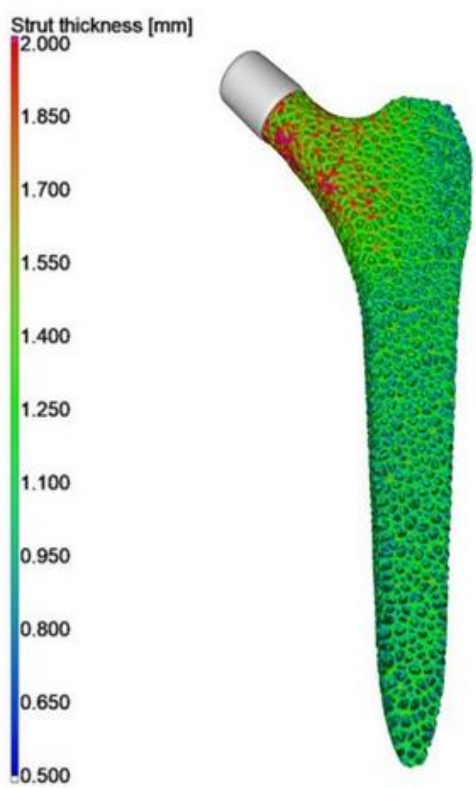

Figure 6: Strut thickness distribution of the optimized stem. (Dataset from Younes Chahid – Analysis by Philip Sperling Vgstudio)

Figure 6: Strut thickness distribution of the optimized stem. (Dataset from Younes Chahid – Analysis by Philip Sperling Vgstudio)

References

[1] J.E. Guerrero, D. Maestro, A. Bottaro, Biomimetic spiroid winglets for lift and drag control, Comptes Rendus Mécanique. 340 (2012) 67–80. https://doi.org/10.1016/j.crme.2011.11.007.

[2] A. Nouri, P.D. Hodgson, C. Wen, Biomimetic Porous Titanium Scaffolds for Orthopedic and Dental Applications, Biomim. Learn. Nat. (2010). https://doi.org/10.5772/8787.

[3] M. Regis, E. Marin, L. Fedrizzi, M. Pressacco, Additive manufacturing of Trabecular Titanium orthopedic implants, MRS Bull. 40 (2015) 137–144. https://doi.org/10.1557/mrs.2015.1.

WRITTEN BY

Younes Chahid

Younes Chahid has a first class Mechanical Engineering degree and is currently a final year PhD student on the topic of Design and Metrology of AM Lattice and Trabecular Structures at the University of Huddersfield. Younes has been selected in iMeche 2019 Rising Stars list and is also the winner of the international Additive World Design for AM 2020 challenge. Younes is also the founder and mentor of the award-winning University of Huddersfield 3D Printing Society. His experiences are in generative design, design for AM using topology optimisation, lattice structures and metrology using X-ray CT for dimensional, surface roughness and porosity analysis.

12.8. Appendix 7: Article published in 2021 about advances and research in medical AM

AM brings a new dawn to surgical procedures

Additive Manufacturing (AM) has provided previously unconceivable design freedom for the creation of complex freeform geometries that have traditionally been limited by the capabilities of conventional machine tools. This design freedom is currently allowing designers in fields such as biotechnology and medical engineering to follow a process called design for AM (DfAM) to optimise existing production methods and incorporate revolutionary new features. Here, **Younes Chahid** takes a closer look at the impact 3D printing is having on the evolution of the medical industry.

From left to right: A) Anatomical model, (B) custom fit AM implant, (C) additive manufactured surgical guides

The recent increase in the use of advanced techniques such as X-Ray computed tomography (XCT) or other medical imaging tools that are being combined with AM has led to a sharp increase in the development of applications that include different custom fit products for the benefit of patients. Some of these applications include:

- Anatomical models: These can be replicas of the patient's soft tissue or bones captured by medical imaging techniques as seen above in Figure A. They can be additively manufactured to be used by surgeons as guides for better planning of treatment and surgical operations.
- Custom implant designs: Instead of the traditionally handmade designs from anatomical models or standard size implants, medical imaging techniques are again used to reverse engineer the patient's bone model to help develop bespoke designs that are custom-fitted to work better for the patient as seen in Figure B.
- Custom surgery guides: Using the anatomical models mentioned above, the operating team can better simulate the whole procedure before the surgery and further design/3D print custom instruments, surgical guides or custom tools as seen in Figure C.

When designing hip or dental implants, natural human bones are usually used as a reference due to their extremely high optimisation that is shaped by millions of years of evolution. Along similar lines, AM has been heavily used in biomimetic approaches to try and replicate the similar porous structures existing in the human body trabecular bone tissue – as found at the end of long bones like the femur.

Of course, designers don't have millions of years to wait to develop optimised designs. Fortunately, advanced software can be used to simulate various loads and operating constraints to test designs and add or remove material where it is most beneficial. It should come as no surprise that designs created by this method look almost organic in structure, with modern engineering accomplishing in hours

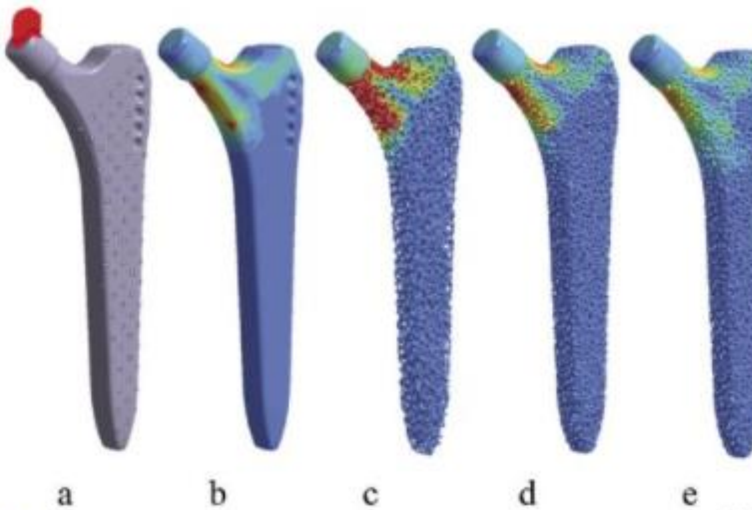

Designed in Ntop software and same Von mises colour scale from Simsolid FEA. (a) boundary conditions, (b) initial stem FEA, (c) stochastic lattice FEA, (d) optimised density distribution, (e) optimised strut thickness distribution

what would take millennia in nature.

Having control over the implant lattice structure design or topology optimisation tools opens the door for engineers to take conventionally heavy titanium implants and make them lighter – even incorporating properties that are closer to the human bone structure as seen above.

The advantages of having more design freedom in the design of medical implants include:

- Reduction of stress shielding: When a conventional fully solid titanium hip implant takes the whole load without distributing it to the lower bones, the latter weakens and suffers from bone resorption. Using a porous design with closer properties to human bone allows for improved stress distribution and reduction of the stress shielding effect.
- Porous surface: Imitating human bone porosity using lattices assists bone fixation and locking as well as facilitating bone ingrowth in some instances.
- Custom surface roughness: Instead of adding a custom surface roughness with minimal control, recent research has been looking at designing and 3D printing implants with custom surfaces with different functions to support post-processes like plasma spray coatings. These offer several potential benefits such as reducing bacterial adhesion.

With more than 160,000 hip replacement operations in the UK every year as well as hundreds of thousands of other bone structure procedures being undertaken – the advancements in AM and its ability to improve stress distribution, bone fixation and ingrowth as well as the potential to reduce bacterial adhesion has far-reaching benefits for patients, their recovery process and post-operation quality of life. Furthermore, the benefits for the NHS could also be far-reaching with shorter post-operation recovery times increasing patient and bed capacity.

Finally, this increase in design freedom has led to new challenges. For instance, parts with internal features are substantially more complex to inspect, requiring further research into the optimum metrology strategy to determine product quality. This forms a significant portion of my doctoral programme and I am currently researching the use of volume analysis methods on AM implants or lattices to assess their build quality as seen in the below diagram.

Another aspect of my research has been looking at including the expected surface roughness in the design stage before the manufacturing stage for improved design validation. This work was recently published in the Journal of Additive Manufacture under the title "Parametrically designed surface topography on CAD models of additively manufactured lattice structures for improved design validation".

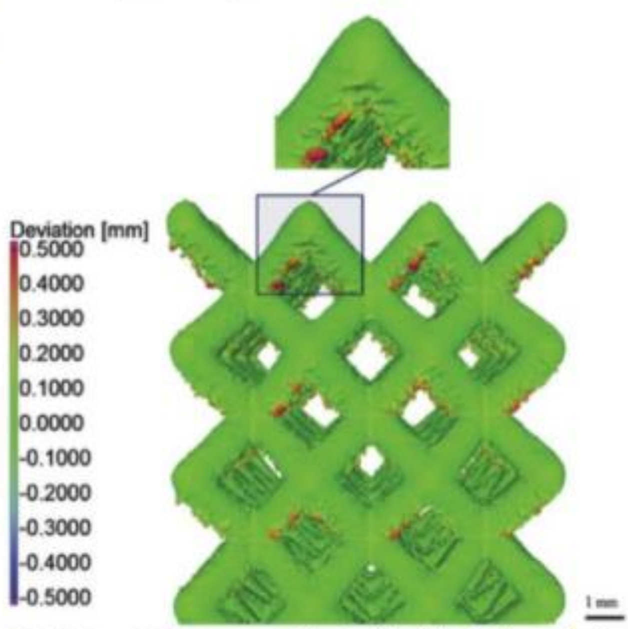

Deviation analysis to compare AM part with original design, red colour shows unwanted material not existing in original CAD.

12.9. Appendix 9: Article published in 2020 with Philip Sperling (VGSTUDIO MAX) about metrology in medical AM field

cem contrôles essais mesures

73

La revue des technologies et applications de contrôles pour les laboratoires et l'industrie

N°73 • Novembre 2020 • 25 €

www.controles-essais-mesures.fr

DOSSIER

La fabrication additive au chevet des patients

Comme le rappelle Dassault Systèmes, spécialiste mondial de la simulation numérique, « il est possible de prédire les distorsions de pièces ainsi que les contraintes résiduelles et le comportement des matériaux construits, en simulant le processus d'impression virtuelle pour améliorer la qualité globale pendant le processus d'impression. (...) Il est en outre possible de simuler les traitements post-impression à l'aide de technologies de suppression progressive des éléments, pour vérifier le processus de bout en bout. »

Le scanner 3D, gage de fiabilité pour une production d'urgence

Dans ce contexte sanitaire inédit de pandémie de Covid-19, le chirurgien parisien Roman Khonsari et l'Assistance publique - hôpitaux de Paris (AP-HP) ont lancé Covid3D.org, une initiative, financée par l'université de Paris et le groupe de luxe Kering.

L'objectif initial : imprimer en urgence du matériel nécessaire aux soignants pour faire face au ralentissement des activités des centres de fabrication américains et chinois et à l'utilisation strictement locale de leur production. Outre les besoins liés au Covid-19, des objets d'importance vitale étaient nécessaires, incluant valves, matériel d'intubation, respirateurs, pousse-seringues, masques, et connecteurs médicaux.

Un parc de plus de 60 imprimantes 3D a alors été installé dans l'enceinte l'abbaye de Port-Royal, bâtiment historique de l'hôpital Cochin. Mis en place en mars 2020 par l'entreprise Bone 3D qui gère le parc, les machines d'impression 3D du fabricant Stratasys sont encore utilisées. Quid du contrôle qualité des pièces produites ?

Même s'il ne s'agit pas d'implants ni même de pièces complexes, ici, l'utilisation médicale des pièces exige les niveaux les plus élevés de qualité, de précision et de sécurité. Les équipes de l'APHP et de Bone 3D utilisent un scanner d'Artec 3D, le Artec Space Spider avec sa technologie de lumière bleue. Les scans permettent de comparer les objets venant d'être imprimés à leurs originaux. Si le scan démontre que le nouvel objet répond aux critères de qualité et que les caractéristiques clés de chaque objet sont maintenues, le lot réussit le test de contrôle qualité. S'il échoue, le lot entier est jeté. Pour les dispositifs où la précision des tubes intérieurs est requise, la tomographie à rayons X est utilisée conjointement avec Space Spider.

Tomographie

Les implants passés aux rayons X

Issue du domaine médical, la tomographie par rayons X sert aujourd'hui à contrôler certains dispositifs médicaux ! Le CT scan est l'examen privilégié des structures lattices fabriquées couche par couche via la fabrication additive. Entretien avec Philip Sperling, *Product Manager Additive Manufacturing*, chez Volume Graphics, éditeur de logiciels pour la tomographie à rayons X, et Younes Chahid, doctorant à l'université de Huddersfield, en Grande-Bretagne.

Philip Sperling
***Product Manager Additive Manufacturing*, chez Volume Graphics**

Younes Chahid
doctorant à l'université de Huddersfield, en Grande-Bretagne

Pour quelles raisons la fabrication additive s'est-elle imposée dans l'industrie médicale et la fabrication d'implants ?

Au cours des dernières années, la fabrication additive s'est imposée dans l'industrie médicale comme méthode de production d'implants orthopédiques, en particulier pour la fabrication de prothèses du genou et de la hanche. La fabrication additive par fusion de lit de poudre (ou *Powder Bed Fusion*, PBF) et plus spécifiquement des procédés par fusion de faisceau d'électrons (*Electron Beam Melting*, EBM) sont utilisés. La liberté de conception, l'absence d'outillage, les délais de réalisation courts, les coûts réduits de production ainsi qu'un suivi aisé des patients sont les atouts principalement mis en avant. Les structures en treillis, qui peuvent être adaptées à l'anatomie du patient, constituent une valeur ajoutée pour les implants issus de la fabrication additive même si dans le cas des prothèses de genoux et de hanches les cas d'implants personnalisés sont rares. Ces structures sont capables d'imiter des systèmes biologiques comme la structure osseuse pour permettre une meilleure croissance osseuse (ostéointégration) et la possibilité de se rétablir rapidement.

Pour quelles raisons utiliser la tomographie assistée par ordinateur ?

La mise en œuvre de structures complexes lattices se traduit par une récupération plus rapide, des contraintes mécaniques moins importantes et une meilleure fonctionnalité. Pour concevoir de telles structures, la porosité, l'épaisseur de la tige, la taille des cellules du réseau, etc., doivent être paramétrées avec précision par le fabricant. Les solutions logiciels de Volume Graphics permettent de mesurer et d'analyser les structures en treillis produites par fabrication additive afin de vérifier ces éléments. Pour une inspection approfondie des structures en treillis, de nombreuses caractéristiques et détails internes doivent être mesurés : à l'heure actuelle, la tomographie assistée par ordinateur basée sur les rayons X est la seule méthode permettant d'atteindre cet objectif. La tomographie à rayons X est capable de contrôler toutes les surfaces externes et internes et les caractéristiques géométriques, de trouver des défauts (comme la porosité, les inclusions ou les fissures), de détecter la poudre emprisonnée et les connexions manquantes entre les structures en treillis et les murs environnants.

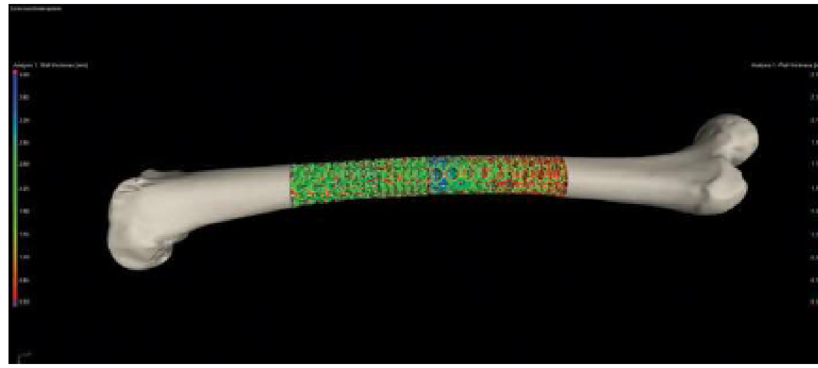

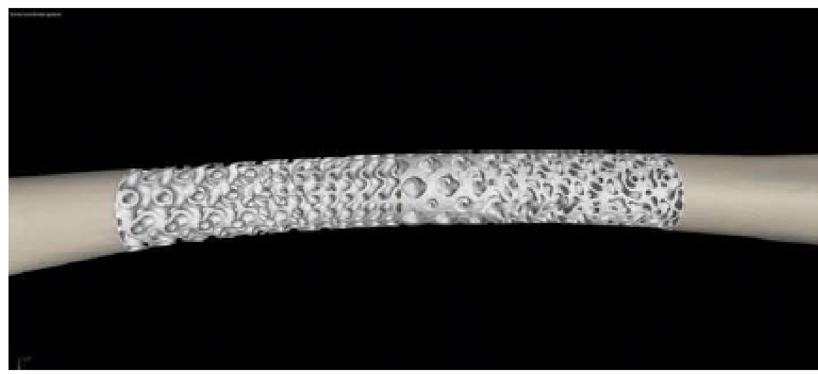

Structures lattices analysées grâce aux solutions éditées par Volume Graphics.

Quels sont les apports de vos logiciels ?

À titre d'exemple, prenons le cas de quatre structures TPMS mises en œuvre avec la plate-forme nTop, avec une épaisseur de paroi de 2 mm et une taille de cellule de 10 mm (TPMS signifiant « Triply Periodic Minimal Surface » pour surface minimale triplement périodique) : Gyroid, Diamond, Schwarz et Split P, quatre formes lattices bien précises souvent choisies dans les applications d'implants médicaux en raison de la moindre concentration de contraintes. Les mesures traditionnelles basées sur des éléments de géométrie standard sont très limitées pour ces structures complexes constituées principalement de surfaces de forme libre. La tomographie à rayons X, en tant que méthode d'inspection volumétrique, est capable de saisir toutes les surfaces et caractéristiques externes et internes. Avec un logiciel de tomographie assistée par ordinateur puissant comme, par exemple, VGStudioMax ou VGMetrology, toutes les surfaces et caractéristiques peuvent être mesurées conformément aux normes industrielles, et des analyses de surface comme l'analyse de l'épaisseur de paroi et la comparaison nominale-réelle sont possibles. Les procédures peuvent être entièrement automatisées. Les caractéristiques spécifiques des structures peuvent être mesurées. Nos applications offrent la possibilité de réaliser une grande variété d'analyses qui permettent de garantir une bonne qualité de l'implant ●

12.10. Appendix 10: Winner of Additive World 2020 DfAM Challenge organised by Additive Industries (Press release by Additive Industries)

Additive Industries

Accelerating Industrial Additive Manufacturing

Press release

Winners of 2020 Design for Additive Manufacturing Challenge, K3D and Younes Chahid, virtually announced

Designs of Additive Industries contest demonstrate unique industrial capabilities of 3D metal printing, honorable mention for SMS Group

Eindhoven (The Netherlands) – April 1, 2020

During the 8th edition of the Additive World Conference, Chairman of the Jury, Ultimaker's Steven van de Staak, announced K3D and Younes Chahid as winners of the Additive World Design for Additive Manufacturing Challenge 2020. All finalists, three in the student category and three professionals, pitched their designs in a video for the 6-member jury. After careful deliberation they made a unanimous and well-advised selection in both categories. The winning designs, a 'Laser Welding Head' and a 'Hip Implants Stem Design', are inspiring use cases of industrial 3D metal printing.

In the student category the first prize went to Younes Chahid from BiometicAM based in the United Kingdom with his Hip Implant Stem design. This noble and highly functional application improves patients' lives by shortening operation times as well as recovery times. The design of the structure is fully optimized with varying lattice densities and thicknesses for optimal bone ingrowth. Younes's story is complete and told with expertise and passion. The part can only be produced using metal additive manufacturing and in addition, is designed to print without supports, capable for being nested to maximise the total number of parts per build and therefore also lowering the total cost per part to allow for democratising this for patients around the world.

The winner of the professional category is K3D of The Netherlands, winning this contest the second year in the row. K3D CTO Jaap Bulsink presented the Laser Welding Head they developed for Hittech Bihca, supplier of precision components. Improved performance, functional integration, conformal cooling channels, light-weighting and optimized local porosities are all features that make this application a clear winner in a tough category this year with some other excellent case studies. The judges felt it refreshing to see that the K3D application made a strong business case and design in a real, industrial application, a category that isn't always well represented in design competitions. This design could not be produced in any other way than additive manufacturing and on top of that it can be printed without any supports in an efficient build setup, Design for Additive Manufacturing at its best.

An honorable mention is well deserved for Nina Uppenkamp, from the SMS Group in Germany. Her redesigned Media Block is a great design with a compelling business case which has been very well executed. A good demonstration of a manifold that is optimized for metal additive manufacturing. One of the things that makes her case even stronger is that both the original part and the redesigned part were functionally tested and compared. Her presentation was also amongst the best we have seen, very concise and professional.

All finalists get a free licence of Altair Inspire and Autodesk Netfabb software. Younes Chahid, as student winner, has won an Ultimaker 2+ printer while the team of K3D will receive an Ultimaker S3, both winners will also receive a 3D printing starter-pack from MakerPoint.

More information

More information on the winners and their designs can be found on the Press Page on the www.additiveindustries.com website.

Additive Industries b.v.
Achtseweg Zuid 155, NL 5651 GW Eindhoven, The Netherlands
P.O. Box 30160, NL 5600 GA Eindhoven, The Netherlands
www.additiveindustries.com

Contact
Irina Schatorjé, Marketing Manager
Mobile: +31 (0)646280407
E-mail: i.schatorje@additiveindustries.com

About Additive World
Additive World strives to connect the dots in industrial 3D printing. We want to create a platform to meet colleagues from your industry and experts in your field of use. To exchange insights, share experiences and accelerate the learning curve to a mature technology. Additive World is an initiative of Additive Industries.
www.additiveworld.com

About Design for Additive Manufacturing Challenge
In order to grow the number of examples and inspire many other industries to develop dedicated applications for industrial 3D printing, Additive Industries has launched the Additive World Design for Additive Manufacturing Challenge 2020 at the renowned Dutch Design Week in Eindhoven in October 2019. Competing in two categories, both professionals and students were encouraged to redesign an existing conventional part of a machine or product for 3D printing.

About Additive Industries

Additive Industries

Additive Industries is accelerating industrial additive manufacturing of high quality, functional, metal parts by offering a modular end-to-end 3D printing system including a seamlessly integrated information platform to high end and demanding industrial markets. With substantially improved reproducibility, productivity, and flexibility, Additive Industries redefines the business case for series production of additive manufacturing applications in aerospace, automotive, medical technology and high-tech equipment.

Jaap Bulsink (K3D): Laser Welding Head
Professional category winner

Design for Additive Manufacturing CHALLENGE 2020 Winners

Additive World

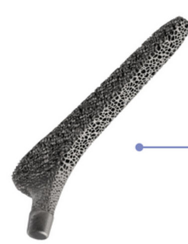

Younes Chahid (BiomimeticAM):
Hip implant stem design
Student category winner

12.11. Appendix 11: Selected in IMechE 2019 Rising Star - 25 under 35 (Published in iMeche Magazine Issue 2, 2019)

'It was a unique feeling to witness students hold in their hands the concepts they had thought up and designed – I was feeling like a magician for the first few months'

Younes Chahid

Younes Chahid

Additive manufacturing PhD researcher at University of Huddersfield, and co-founder of National 3D Printing Society

Age: 23 / Huddersfield

Why were you inspired to get into engineering?
When I was young, I would frequently read *Science et Vie Junior*, a children-friendly French science magazine. It was intriguing and simulating and led me to want to know how things worked.

The person who guided my thirst for knowledge was my brother-in-law. A great mechanical engineer who broadened my spectrum on the subject, he inspired me to join the field and is still my mentor today. This is very important in a country like my native Morocco, where the subject and degree course doesn't get the appreciation it deserves.

What's the most interesting role you've had?
Setting up the university's 3D printing society, even though it was hard to recruit the initial committee, convince the students' union and secure funding.

It was a unique feeling to witness students hold in their hands the concepts they had thought up and designed – I was feeling like a magician for the first few months. It was also inspiring to be able to influence students' career choices by helping them identify the right 3D printing field for them and finding them placements related to it.

I would love to see what we achieved on a small scale happen all across the UK. This is why I've recently co-founded the National 3D Printing Society, a social enterprise that will connect students, researchers and the additive manufacturing (AM) industry through an online platform, and assist students from any university to start their own 3D printing society.

What excites you about the potential of AM?
Instead of designing a part and iterating the process until you get the desired results, you set the constraints and requirements and see your design grow from scratch. This is exciting as it opens the door to a new generation of designs that are smart and adaptable.

What would you like to achieve in your career?
I'd love to play a part in accelerating the adoption of AM on a larger scale. This goal links into my AM metrology-related PhD, which is looking at the measurement challenges around structural integrity.

I'd also like to extend the National 3D Printing Society into a global one and broaden awareness of the impact the technology can have.